UNIVERSITY OF BEIRA INTERIOR
Engineering

Development of Computational Methodologies for Turbulence Transitional Flow Prediction

Rui Vizinho de Oliveira

Thesis submitted for the degree of Doctor of Philosophy in
Mechanical Engineering
(3rd Cycle of Studies)

Supervisor: Prof. Doutor José Carlos Páscoa Marques
Co-Supervisor: Prof. Doutor Miguel Ângelo Rodrigues Silvestre

Covilhã, Março 2016

To Ana, my sister Catarina, my mother Fernanda and my father António.

Acknowledgements

I would like to thank professor José Páscoa, for providing me with the opportunity to work and perform research under his careful supervision. For giving me guidance, and at the same time, freedom to work as I will. If I had a common supervisor, I would have probably never developed nothing new.
I also want to thank my co-supervisor professor Miguel Silvestre, for the interesting discussions we had on airfoil design and modeling.
At last but not at all the least, I want to deeply thank my friends, Mohammadmahdi Abdollahzadehsangroudi, João Morgado and José Luís Serra for everything. Words are not enough to express their support.
I also want to thank Amilcar Baptista for all the support and for managing and performing with excellence on all office and project issues.
I want to give special thanks to Galina Illieva for directly handling and managing project requirements, freeing us to perform our research work.
Finally I want to thank Jackson, Fred, Carlos and Shyam for all the support provided at work.

Support

The current Doctoral thesis was performed as part of Project MAAT, supported by European Union on course of the 7th Framework Programme, under Grant number 285602 and was also supported by C-MAST, Center for Mechanical and Aerospace Science and Technologies, Fundação para a Ciência e Tecnologia (FCT) research unit No.151.

Abstract

Turbulence transition modelling is still, albeit the past developments, an active research area of interest for various industry sectors. Its modelling can range from RANS based closures to full DNS computations. The former approach is of course the most feasible simulation methodology. Therefore, RANS based transition models have been developed for industry use. These, range from empirically correlated transition models to physics based phenomenological transition closures. Implementation and validation of these models resulted in a deeper understanding of the processes by which RANS based closures are able to predict turbulence transition onset. The research presented herein on the specific type of physics in which the transition models are based resulted in an accuracy improvement of an existing turbulence transition closure, the k-k$_l$-ω. Additionally, upon gaining a deeper understanding on the role of the pre-transitional flow region, a new turbulence transition model was devised. This is based on a never before applied concept of pre-transitional turbulent vortex deformation due to mean flow shear. This will induce the appearance of a small pre-transitional turbulent viscosity on the edge of the laminar boundary layer. The induced viscosity is a result from the predicted small negative pre-transitional $\overline{u'v'}$ values. Although experimentally verified, up until now, no model has ever been able to predict this turbulent feature based on a mechanical analogy. The transition V-model was then coupled to a turbulence model, the Spalart-Allmaras closure, resulting in the V-SA transition model. This was validated for a wide range of flow conditions and multiple geometries. It is concluded that the mechanical analogy based closure is a feasible concept with a promising future. Although the developed V-SA turbulence transition model is simple, it is able to predict complex transition phenomenon.

Keywords

Transition, Turbulence, RANS, OpenFoam, Fluent

Resumo

A modelação de transição para escoamento turbulento, continua a ser uma área de investigação activa, com interesse para vários sectores industriais. A sua modelação pode abranger desde modelos RANS a simulações DNS. A primeira abordagem é claramente a mais exequível forma de simular transição para turbulência. Como tal, modelos de transição RANS têm vindo a ser desenvolvidos para uso industrial. Estes podem variar desde modelos de correlação empírica a modelos fenomenológicos baseados na física do processo de transição. A implementação e validação destes modelos, resultou num aprofundamento do conhecimento sobre os processos a partir dos quais os modelos RANS têm a capacidade de prever a transição para a turbulência. Para além disto, a pesquisa sobre o tópico específico de modelos de transição baseados na física do processo de transição, resultou numa melhoria da exactidão de um modelo de transição existente, o k-k_l-ω. Adicionalmente, após adquirir um conhecimento mais detalhado sobre o papel do escoamento de pré-transição, foi desenvolvido um novo modelo de transição. Este é baseado num conceito nunca antes aplicado de deformação de vórtices presentes na região de pré-transição devido ao efeito de corte do escoamento médio. Isto irá induzir o aparecimento de uma pequena viscosidade de pré-transição na fronteira da camada limite laminar. Esta viscosidade é resultante da previsão de pequenos valores negativos de $\overline{u'v'}$ na região de pré-transição. Apesar de experimentalmente verificado, até agora, nenhum modelo conseguiu alguma vez prever este fenómeno turbulento baseando-se numa analogia mecânica. O modelo de transição V-model, foi então acoplado com um modelo de turbulência, o modelo Spalart-Allmaras, resultando no novo modelo de transição, o V-SA. Este foi validado para uma vasta gama de escoamentos assim como com múltiplas geometrias. Conclui-se que, o modelo baseado numa analogia mecânica é um conceito funcional com um futuro promissor. Apesar do modelo de transição desenvolvido, V-SA, ser simples, este tem a capacidade de prever fenómenos de transição complexos.

Palavras-chave

Transição, Turbulência, RANS, OpenFoam, Fluent

Contents

List of Figures

List of Tables

Nomenclature

Greek symbols

α	V-SA model vortex deformation angle along the shear stress tensor major axis
$\alpha^{'}$	V-SA model vortex deformation half angle along the shear stress tensor major axis
α_t	k-k$_l$-ω model effective turbulent diffusivity
α_t^{new}	k-k$_l$-ω-mod model effective turbulent diffusivity
β	V-SA model vortex deformation angle along the shear stress tensor minor axis
$\beta^{'}$	V-SA model vortex deformation half angle along the shear stress tensor minor axis
β_{bp}	k-k$_l$-ω model bypass transition threshold function
β_{nat}	k-k$_l$-ω model natural transition threshold function
β_{ts}	k-k$_l$-ω model Tollmien-Schlichting threshold function
γ	Turbulence intermittency
γ_{eff}	$\gamma - Re_\theta$ model effective turbulence intermittency
γ_{sep}	$\gamma - Re_\theta$ model separation induced transition turbulence intermittency
δ	$\gamma - Re_\theta$ model boundary layer thickness parameter
ε	Turbulent kinetic energy dissipation rate
ζ	Pressure loss coefficient
λ_θ	$\gamma - Re_\theta$ model pressure gradient parameter
λ_{eff}	k-k$_l$-ω model effective turbulent length scale
λ_t	k-k$_l$-ω model turbulent length scale
μ	Dynamic viscosity
μ_T	Turbulent dynamic viscosity
ν	Kinematic viscosity
ν_T	Turbulent kinematic viscosity
$\nu_{t,l}$	k-k$_l$-ω model large scale turbulent kinematic viscosity
$\nu_{t,s}$	k-k$_l$-ω model small scale turbulent kinematic viscosity
$\nu_{T_{uv}}$	V-SA model pre-transitional turbulent viscosity
$\tilde{\nu}_T$	Spalart-Allmaras model modified turbulent kinematic viscosity
Π	Pressure-strain redistribution component
ρ	Density
τ_{ij}	Reynolds stress tensor
ϕ_{bp}	k-k$_l$-ω model bypass transition limiting function
ϕ_{nat}	k-k$_l$-ω model natural transition limiting function
ϕ_{bp}^{new}	k-k$_l$-ω-mod model bypass transition limiting function
χ	Spalart-Allmaras model modified and turbulent kinematic viscosity ratio
Ω	Mean flow vorticity
Ω_{size}	V-SA model mean flow vorticity scale function
ω	Specific turbulent kinetic energy dissipation rate
ω_z	V-SA model pre-transitional vortex rotational velocity along z axis
$\tilde{\omega}$	V-SA model pre-transitional vortex general rotational velocity

Acronyms

AoA	Angle of Attack
CFD	Computational Fluid Dynamics
FSTI	Free-Stream Turbulence Intensity
MAAT	Multibody Advanced Airship for Transport
UBI	Universidade da Beira Interior
UDF	User Defined Function
SA	Spalart-Allmaras
V-SA	V-Spalart-Allmaras

Superscripts

$\vec{}$	Vector
$'$	Fluctuation flow value
$\overline{()}$	Reynolds time-average value

Subscripts

i	First order tensor indice
j	First order tensor indice
k	First order tensor indice
ij	Second order tensor indices
ijk	Third order tensor indices
inlet	Domain inlet boundary
outlet	Domain outlet boundary

Latin terms

A	V-SA model pre-transitional vortex surface area
C_{ijk}	Turbulence diffusion triple pressure-velocity correlation
D_{k_t}	k-ω-SST model turbulent kinetic energy destruction term
$\tilde{D_{k_t}}$	k-ω-SST model modified turbulent kinetic energy destruction term
D_t	k-k$_l$-ω model turbulent kinetic energy destruction term
D_l	k-k$_l$-ω model laminar fluctuations kinetic energy destruction term
$Dest_{k_p}$	V-SA model pre-transitional turbulent kinetic energy destruction term
$\tilde{D}_{k_t}$	$\gamma - Re_\theta$ model turbulent kinetic energy destruction term
$\frac{D}{D_t}$	Total derivative
E_γ	$\gamma - Re_\theta$ model turbulence intermittency destruction term
e_{cp}	V-SA model pre-transitional vortex specific kinetic energy
f_{v1}	Spalart-Allmaras model dimensionless function
f_{v2}	Spalart-Allmaras model dimensionless function
f_w	Spalart-Allmaras model dimensionless function
F_1	k-ω-SST model first blending function
F_{length}	$\gamma - Re_\theta$ model transition length function
F_{onset}	$\gamma - Re_\theta$ model transition onset function
F_{onset1}	$\gamma - Re_\theta$ model transition onset function
F_{onset2}	$\gamma - Re_\theta$ model transition onset function
F_{onset3}	$\gamma - Re_\theta$ model transition onset function
$F\left(\lambda_\theta\right)$	$\gamma - Re_\theta$ model pressure gradient function
$F_{\theta t}$	$\gamma - Re_\theta$ model blending function
F_{wake}	$\gamma - Re_\theta$ model flow wake identifier switch function
F_{turb}	$\gamma - Re_\theta$ model turbulence dimensionless function
$F_{reattach}$	$\gamma - Re_\theta$ model boundary layer re-attachment function
F_W	k-k$_l$-ω model kinematic wall effect damping function
F_ω	k-k$_l$-ω model boundary layer wake region damping function
F_{ss}	k-k$_l$-ω shear-sheltering damping function
F_{int}	k-k$_l$-ω model flow turbulence intermittency damping function
f_v	k-k$_l$-ω model viscous wall effect damping function
$f_{\tau,l}$	k-k$_l$-ω model time-scale damping function
$f_{nat,crit}$	k-k$_l$-ω model natural transition threshold control function
f_{int}^{new}	k-k$_l$-ω-mod model flow turbulence intermittency damping function
$f_{bp,crit}$	k-k$_l$-ω-mod model bypass transition threshold control function
F_{cent}	V-SA model pre-transitional vortex centrifugal force
F_{shear}	V-SA model shear force acting upon the pre-transitional vortex
F_{centA}	V-SA model pre-transitional vortex mechanical analogy centrifugal force on point A
F_{centB}	V-SA model pre-transitional vortex mechanical analogy centrifugal force on point B
F_x	V-SA model pre-transitional vortex mechanical analogy resulting force along x axis
F_y	V-SA model pre-transitional vortex mechanical analogy resulting force along y axis

F_S	V-SA model measure of mean flow shear scale and turbulent flow scale proximity
F_Ω	V-SA model measure of mean flow vorticity scale and turbulent flow scale proximity
h	V-SA model pre-transitional vortex mechanical analogy bar length
k	Turbulent kinetic energy
k_l	k-k_l-ω model laminar fluctuations kinetic energy
$k_{t,s}$	k-k_l-ω model small scale turbulent kinetic energy
$k_{t,l}$	k-k_l-ω model large scale turbulent kinetic energy
k_x	V-SA model pre-transitional vortex turbulent kinetic energy along x axis
k_y	V-SA model pre-transitional vortex turbulent kinetic energy along y axis
k_p	V-SA model pre-transitional turbulent kinetic energy
l	V-SA model pre-transitional vortex length
M_C	V-SA model pre-transitional vortex mechanical analogy resulting moment in turn of point C
P_{k_l}	k-k_l-ω model laminar fluctuations kinetic energy production term
P_{k_t}	k-ω-SST model turbulent kinetic energy production term
$\tilde{P_{k_t}}$	k-ω-SST model modified turbulent kinetic energy production term
P_k	k-k_l-ω model turbulent kinetic energy production term
$Prod_{k_p}$	V-SA model pre-transitional turbulent kinetic energy production term
P_{static}	Static pressure
P_{tot}	Total pressure
P_γ	$\gamma - Re_\theta$ model turbulence intermittency production term
P_{θ_t}	$\gamma - Re_\theta$ model transition momentum thickness Reynolds number production term
$\tilde{P_{k_t}}$	$\gamma - Re_\theta$ model turbulent kinetic energy production term
$ratio$	V-SA model ratio between pre-transitional vortex acting shear and centrifugal forces
r	Spalart-Allmaras model dimensionless function
r_{avg}	V-SA model average pre-transitional vortex radius
r_{local}	V-SA model pre-transitional vortex local radius of curvature
R_A	V-SA model pre-transitional vortex mechanical analogy reaction force on point A
R_B	V-SA model pre-transitional vortex mechanical analogy reaction force on point B
R_{bp}	k-k_l-ω model bypass transition energy transfer function
Re_{bp}^{new}	k-k_l-ω-mod model bypass transition energy transfer function
Re_t	k-k_l-ω model turbulent Reynolds number
Re_t^{new}	k-k_l-ω-mod model turbulent Reynolds number
Re_θ	$\gamma - Re_\theta$ model local momentum thickness Reynolds number
$Re_{\theta c}$	$\gamma - Re_\theta$ model empirical critical momentum thickness Reynolds number
$Re_{\theta t}$	$\gamma - Re_\theta$ model empirically correlated transition momentum thickness Reynolds number
$\overline{R_{e_{\theta c}}}$	$\gamma - Re_\theta$ model transported transition momentum thickness Reynolds number
Re_ν	$\gamma - Re_\theta$ model vorticity Reynolds number
Re_ω	$\gamma - Re_\theta$ model specific turbulent kinetic energy dissipation rate Reynolds number

Re_Ω	k-k$_l$-ω model vorticity based Reynolds number
R_{nat}	k-k$_l$-ω model natural transition energy transfer function
R_T	$\gamma - Re_\theta$ model turbulence Reynolds number
S	Mean flow shear
$\tilde{S}$	Spalart-Allmaras model production term
S_x	V-SA model pre-transitional vortex mechanical analogy shear force along x axis
S_y	V-SA model pre-transitional vortex mechanical analogy shear force along y axis
S_{size}	V-SA model mean flow shear scale function
$Sep_{Correct}$	V-SA model separation correction
$\vec{S}$	V-SA model pre-transitional vortex mechanical analogy shear force on point C
t_σ	$\gamma - Re_\theta$ model time scale
U	Mean flow velocity
U_{imp}	Imposed free-stream sinusoidal varying flow velocity
u	Flow velocity along x cartesian coordinate
V	V-SA model pre-transitional vortex volume
v	Flow velocity along y cartesian coordinate
x	x cartesian coordinate
y	y cartesian coordinate
y_w	Normal wall distance

xxx

Chapter 1

Introduction

1.1 Transition to Turbulence

Transition is a process that transforms a steady and organized laminar flow into an unsteady chaotic turbulent stream as exemplified in Fig.1.1. The transition regime can only be explained by first addressing turbulence itself. As such, turbulence can be roughly described as a collection of fractal flow patterns, such as vortex tubes and rings, with a high mixing capacity. It can be said that, in general all flows surrounding us develop under turbulent regime. This seems to be the case since most of these flows are exposed to a multitude of disturbances. These disturbances have their origin from sound, surface roughness, free-stream vorticity, thermal instability and more.

All of these factors have the potential to breed turbulence in an organized laminar flow, forcing it to go through a transition process. As such, turbulence and its transition understanding are fundamental for comprehension of the world around us, from the weather to the boiling water in a pan. Nevertheless, some flows are engineer to maintain their laminar properties. This is done in order to benefit from the low viscous drag characteristic of a non-turbulent flow.

1.2 MAAT Project

The MAAT project is an innovative concept of air transportation for goods and people. Transportation is achieved through means of two vehicles, the Feeder and Cruiser. The Feeder is mostly responsible for vertical freightage, between the ground stations and the second airborne vehicle. This last is then designated as the Cruiser. It was conceived to sustain flight for very long periods of time. For realizability reasons, both vehicles are airships. The docking of a Feeder inside the Cruiser is presented in Fig.1.2. As can be observed, the Cruiser airship is several times larger than the vertical transport Feeder. The operation altitude for the MAAT project vehicles is approximately 15 kilometers, which translates to stratospheric heights. The Cruiser will then carry at least two Feeders as shown in Fig.1.3. The disclosed configuration is expected to travel at a cruise velocity of 200 km/h. Although the cargo capacity of this transport is limited, its operation costs are reduced due to the fact that this project makes

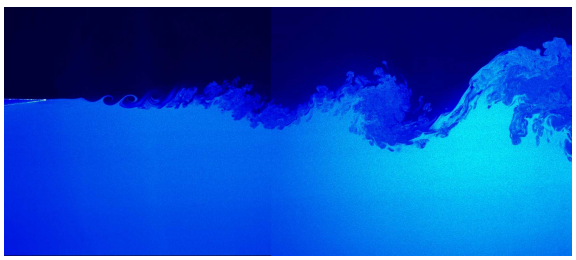

Figure 1.1: Transition to turbulence on a laminar mixing layer flow. Photo from experimental work of Parezanoviíc et al.[1].

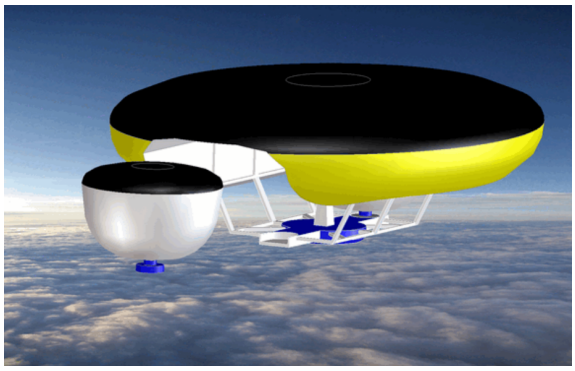

Figure 1.2: MAAT project vehicles. Feeder in docking operation near the Cruiser airship.

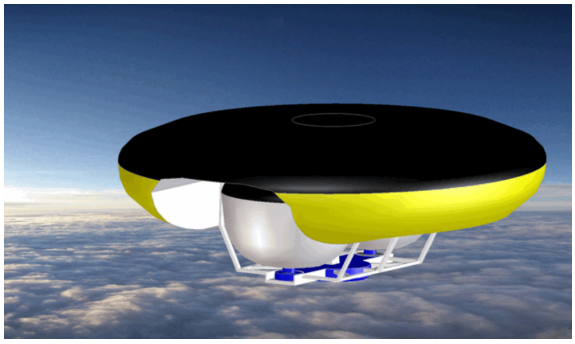

Figure 1.3: MAAT project vehicles. Cruiser carrying two Feeder airships.

use of solar powered vehicles without resorting to conventional commercial jet fuel such as Kerosene.

1.3 Objectives

The main motivation of the present work is the development of numerical models for prediction of laminar boundary layer transition to fully turbulent flow regime. These should be applied in a Reynolds Average Navier Stokes, RANS, work-frame. Therefore, the developed transition model should also be a RANS turbulence model or be coupled to one. The developed transition closures will be applicable for both bi-dimensional and three-dimensional geometries. These models will focus on the pre-transitional region of the laminar boundary layer depicted in Fig.1.4.

1.4 Thesis layout

The present work is divided in the next described chapters. Chapter two, or the bibliographic review, gives a summary of the known transition mechanisms and the impact of turbulence transition phenomenon over common geometries. It also includes a brief historical review of the considered main turbulence and transition experimental and numeric works related to the transition modeling subject. A description of approaches for transition modeling is performed. Also, a deeper exposition of two transition models is presented.

Chapter three, or the transition models development chapter, discloses the devised transi-

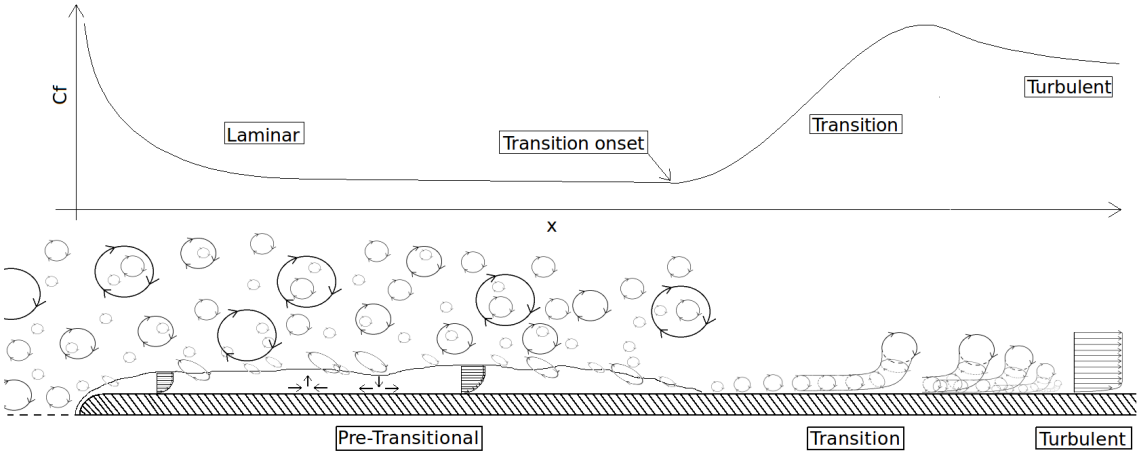

Figure 1.4: General overview of laminar boundary layer transition to turbulence. Some of the concepts of late transition depicted here were observed in the work of [2].

tion closures. An initial description of the first phenomenological model origin is presented. The current laminar fluctuation kinetic energy transition model is disclosed in detail. Afterwards, the laminar fluctuation kinetic energy transition model alteration is explained. The used empirically correlated transition closure formulation is exhibited. Following this exposition of the empirical RANS transition closure, a new turbulence transition model is presented. This is based on a never before used mechanical approximation for the effects of mean flow shear over turbulence characteristics. The development of this novel model is carefully described.

Chapter four, also designated as the ERCOFTAC test cases chapter, describes the validation of both developed transition models over the ERCOFTAC flat-plate benchmark test cases. This validation includes a comparison with numerical results obtained with two commercially available transition models and a turbulence closure. This begins then with the zero-pressure gradient flat-plate test cases. These are followed by the pressure-gradient experimental benchmark. The final validation is performed for the separation induced experimental test cases.

Chapter five, or the airfoil test cases chapter, presents a validation of the novel transition model with available experimental data. The latter is also compared to the results of a turbulence model. Initially a description of the motivation behind such validation is presented. This is followed by a short exposition over the purpose of the first used airfoil geometries. Afterwards three airfoil test cases are analyzed. Finally a turbine airfoil benchmark test case is studied.

Chapter six, designated as the three-dimensional test cases chapter, shows the application of the new transition closure over three-dimensional geometries. This analysis is compared with available experimental data and with the computational results from a turbulence model. The validation begins with a complex flow test case with cross flow effects over a prolate-spheroid. The following case is the flow over a wing under various angles of attack. The obtained numerical results with the developed novel transition model are compared to pictures from the experiment showing a naphthalene distribution over the top and bottom wing surfaces. The final analysis is on a transonic wing test case. The computational results from the newly developed transition closure were compared with experimental pressure coefficient distributions and transition patterns.

Chapter seven, or the conclusions chapter, presents a summary of what was done during the present work. Also, the main results obtained are presented along with problems encountered

during the development of the transition models. At the end of the chapter, future works are proposed for the continuous development of the transition closures.

Chapter 2

Bibliographic review

2.1 Transition mechanisms

The transition of laminar flow into fully turbulent regime is done through mainly three transition mechanisms. These are the natural, bypass and separation induced transition. Also a secondary fourth transition mechanism is increasingly being taken into consideration, the wake induced transition. This is normally observed within turbine and compressor engines where high turbulence intensity wakes are convected throughout the engine blades.

2.1.1 Natural transition

For flow with free-stream turbulence intensity $\leq 1\%$, natural transition is generally observed when the developing laminar flow reaches a critical Reynolds number value. After this critical stage of flow development, viscous wave instabilities named Tollmien-Schlichting waves begin to slowly grow, from small linear perturbations to non-linear disturbance waves. Having reach this point in the transition process, these non-linear waves create three dimensional disturbances and by means of inviscid mechanisms spots of turbulence begin to form randomly inside the laminar boundary layer. Some of these spots grow in size and downstream from where transition first began to develop, a process of fusion between these spots gives light to the fully turbulent boundary layer.

2.1.2 Bypass transition

It is commonly known that bypass transition can occur due to two sources of disturbances. One is surface roughness and the second high free-stream turbulence intensity, which translates to free-stream turbulence intensities $\geq 1\%$ [9]. Bypass transition is simply a natural transition process without the Tollmien-Schlichting wave development phase. When laminar flow suffers bypass transition the flow turns from laminar to the turbulent spot formation phase immediately. The subsequent development is equal to the natural transition process.

2.1.3 Separation induced transition

Boundary layer separation can be observed in flow development over airfoils with an high angle of attack or large leading edge radius surfaces. Due to the adverse-pressure-gradient, a separation bubble is formed and flow may or may not reattach closing the bubble. The process of reattachment is due to the transition of the separated laminar shear layer. This increased flow mixture capacity, originated by turbulence, allows for the shear layer to gain energy from the free-stream and reattach to the wall. During the transition process the free-stream turbulence intensity has an important role determining the separation bubble length [10]. This implies that for low free-stream turbulence intensity a longer transition process develops in the separated laminar shear boundary layer. After turbulence is reached the shear layer reattaches

creating a long length bubble. On the other hand, for high free-stream turbulence intensity, transition occurs faster implying shorter bubble length.

2.1.4 Wake induced transition

As previously mentioned, wake induced transition can be seen in turbine blade cascades. The appearance of turbulent spots on cascade blades can be due to the periodic passing wake, which has enhanced turbulence and creates a momentum deficit in the free-stream. As mentioned in Langtry et al. [11], the principal cause of the turbulent spot formation on the wake impinged blade surface is not known. Studies show that wakes can be seen as negative jets that destabilize the flow forming turbulent spots [12].

2.2 Impacts of transition

The use and general interest in transitional turbulence models in industrial engineering is steadily increasing [13, 11]. This also applies for the MAAT project [14, 15], a revolutionary concept of transportation. Due to its high altitude flight conditions air density and viscosity will greatly differ from sea-level values. Thus, the reigning Reynolds number flows and turbulence conditions will delay transition to turbulence. This implies that for the MAAT project vehicles, feeders and cruiser, large regions of laminar flow will be induced. Therefore, elements of the feeders and cruiser vehicles, such as propulsive systems, will be exposed to late transition and consequently considerable sized laminar flow regions. Possession of a turbulence model that can accurately predict transition onset as well as correctly calculate the transition length has become a must amongst CFD engineers who deal with transitional flows in a daily basis.

2.2.1 Wings stall conditions and turbulence transition effects

The effect of flow transition to turbulence over wings is a critical issue [16]. Investigation and modeling of airfoil flow characteristics is essential as shown in an Onera-A airfoil pre- and stall conditions evaluation using a finite volume method in [17] or the S809 airfoil laminar to turbulent transition modeling attempt using the standard k-ε turbulence model on [18] and others [19, 20]. In the beginning of aviation history, there were cases where airplanes suddenly lost all of the wings lift and or flight control. These unfortunate incidents typically happen under extreme off-flight envelope conditions such as very high angle of attack and low speed flight. This was later understood as the airplane wings stall state. Stall is a condition where the flow over the wing is fully separated and does not reattach. As such there is a pressure increase over the upper wing surface due to the presence of the separated flow vortices. Also, the wing's control surfaces will no longer operate since the low speed flow regions might not even flow in the designed direction due to the vortices imposed circulation. In commercial aviation, the airplane wings have small probes over the upper wing surface or "suction side" of the wing. These probes, also named as vortex generators, induce an axial vorticity which helps increasing the flow momentum near the wing's surface [21]. Additionally, these small structures will induce turbulence transition, again contributing to a higher momentum transfer rate to the wing's surface. It might be thought that the best solution for wing design is to force turbulence transition on the wing's leading edge, resulting in turbulent flow over the entire wing. Although this approach would improve the wing's stall angle of attack, fully turbulent

flow over the entire wing's surface will in fact reduce the wing's efficiency. This is so since turbulence affected surfaces are subjected to a higher drag due to the increase of surface momentum transfer. As such, turbulence transition control and prediction in wing design is of most importance [22].

2.2.2 Turbines turbulence transition characteristics

Contrary to compressor blade flow conditions, turbine blade flows normally have favorable-pressure-gradient characteristics. Such is the case since the purpose of turbines is the extraction of mechanical energy from the incoming flow. Typically the jet engine turbine stage can be found after its compressor and combustor stages. Therefore, turbines are exposed to various flow conditions such as high heat transfer [23], and high free-stream turbulence intensity [24]. These stages also have some regions of adverse-pressure-gradient on the suction side of the blade such as the T106. Also, despite the fact that high free-stream turbulence intensity induces an early transition to turbulence, these geometries have large laminar flow regions as shown in the work of Mayle [25]. This is due to the high favorable-pressure-gradient conditions found on the pressure side of the turbine blade. This induced flow acceleration inhibits laminar flow from turbulence transition. However, as shown in the experimental work of Volino and Simon [26, 27], the pressure side high free-stream turbulence intensity present at the edge of the boundary layer resulted only in its unsteadiness. As such, transition onset prediction is of vital importance in order to correctly estimate a turbine blade overall efficiency. The industrial usage of fully turbulent models will result in over-prediction of drag effects on the turbine blade. Additionally, the assumption of fully turbulent flow conditions from the leading edge of the turbine blade will produce optimistic stall angles of attack. Therefore a broader operational envelope will result from the flow calculations based on fully turbulent models. Some low-Reynolds turbulence models such as the Spalart-Allmaras, have the apparent ability of transition onset prediction due to their low-Reynolds formulation. However, as will be later explained this is only accidental in what regards bypass and natural transition mechanisms. For separation induced transition to turbulence these low-Reynolds turbulence models, such as the Spalart-Allmaras and the k-ω-SST turbulence closure, present reasonably good results [28].

2.2.3 Fuselages transition to turbulence considerations

Due to the typical large size of fuselages, turbulence transition onset does not present such significant impact on their overall behavior. Nonetheless, under low to medium speeds, laminar flow regions can extend for several meters over the fuselage. It will be later shown that for over almost half of a 2.4 meters long surface such as the prolate-spheroid the boundary layer flow remains laminar. Also, as shown in the work of Langtry and Menter [29], which presented a computation over the Eurocopter fuselage, it can be seen that the whole nose part of this geometry maintains laminar flow characteristics. This will result in a more accurate calculation of the resulting drag force acting upon the aircraft body. Unless the developing fuselage is exposed to very off-design conditions such as high angles of attack, the usage of a transition model will not be critical in defining the flight operational envelope. This is the case since in principal the fuselage does not contribute to flight control nor lift. There is, of course, the case of flying wing geometries where both wings and fuselage are bound together. In these special cases, fuselage and wing design cannot be considered as separated issues and transition to turbulence must be taken into account.

2.3 RANS throughout time

As presented in the historically detailed work of Schimtt [30], the development of a flow averaging process that could have resulted in the known Reynolds averaging was first incorrectly published by Boussinesq [31]. Citing the former publication: “here Boussinesq did not notice the apparition, through a temporal average of transport equations, of the tensor that will later be called Reynolds tensor”. It was then with the work of Reynolds [32], that the base for RANS models was developed. This enabled the creation of multiple types of turbulence models such as the second-order closures based on the Reynolds stress transport equations that were first closed by Rotta [33]. Most of the remaining RANS turbulence model types would not be feasible if not for the contribution of Boussinesq. The simplifying concept of a turbulent viscosity or eddy viscosity, was first presented in 1877 by Boussinesq [31]. Afterwards, the mixing-length theory was proposed by Prandtl [34]. The first algebraic, or zero-equation, turbulence models were based on this notion. However, some works dismissed the mixing-length theory as a viable theoretical basis for turbulence models development [35]. The simplest complete turbulence closure type is the two-equation turbulence model. This is so since these models are able to determine both turbulent velocity and length scales. These model types make use of two transport equations. Most, if not all, of these closures rely on the transport equation for the turbulent kinetic energy. The remaining second transport equation is used for the turbulence length scale calculation. The work of Jones and Launder [36], produced one of the best known and used two equation turbulence closure, the k-ε model. However, the first works on this particular model were presented by Chou [37] and others,[38, 39].

2.4 Transition throughout time

Experimental considerations on transition to turbulence were firstly addressed in 1937 by the pioneer work of Dryden [40]. Measurements in the boundary layer over a thin flat-plate were described and reviewed. Laminar to turbulent flow transition was observed in the performed experiment. It was acknowledged that increasing the free-stream turbulence intensity reduced the transitional Reynolds number considerably. Also, the effect of flow pressure-gradient on the transition Reynolds number was studied. For the same free-stream turbulence intensity, small variations on the flow pressure-gradient greatly changed the transition onset Reynolds number. Under a favorable-pressure-gradient, transition Reynolds number was increased. Streamwise velocity fluctuations were measured in both the laminar and turbulent flow regions. It was recorded that under free-stream turbulence intensity the laminar flow region over the flat-plate presented velocity fluctuations. The amplitude of these velocity fluctuations was considerably greater than that of the free-stream oscillations. The main reported difference in these velocity fluctuations between fully turbulent flow and the laminar state of motion was the fluctuations frequency. In laminar flow these velocity fluctuations presented a lower frequency in comparison to the fully turbulent state velocity fluctuations. Additionally it was concluded that it is impossible to determine if a flow is in a laminar or turbulent state just by considering the absence or presence of velocity fluctuations. This was the case since measurements in the laminar flow region, proved that under the influence of free-stream turbulence, a laminar boundary layer will develop considerable velocity fluctuations while maintaining a Blasius velocity profile.

Later in 1943, the experimental work of Schubauer and Skramstad [41], was performed with the main motivation of validating the then recently developed linear stability theory based

on exponential growth of small disturbances. The research effort focused on the effects of very low free-stream turbulence intensity. Measurements of turbulence, sound and transition were performed for the developing flow over a thin flat-plate. The reduction of the free-stream turbulence was performed gradually using damping screens in order to reduce this to the lowest possible value. It was concluded that the laminar boundary layer velocity oscillations are the velocity fluctuations induced by a wave traveling downstream within the boundary layer. This could be triggered by both free-stream turbulence or by sound. Also, it was concluded that a broad band random disturbance, under amplification and damping by the boundary layer, will isolate a limited frequency band close to the most highly amplified disturbance frequencies. This landmark experimental work provided the confirmation of Tollmien-Schlichting waves [42, 43], within the Blasius boundary layer. Later, other works presented experimental confirmation results of the T-S waves for channel flow and controlled boundary layer [44, 45].

In 1978, Arnal and Juillen showed that for free-stream turbulence intensity values higher than 0.5%, the main disturbances were not T-S waves [46]. Instead, a low frequency instability with maximum peak values at the middle of the laminar boundary layer was responsible. This fundamental instability, called the K-type instability, was identified in 1962 by Klebanoff et al. [47]. Later, other authors such as Craik [48], and Herbert [49], observed two different types of subharmonic instabilities. These were designated as the C-type and the H-type, after their authors names respectively. The fundamental instability was experimentally observed as an ordered pattern. On the other hand, subharmonic instabilities typically presented a staggered disposition. Both types of instabilities were observed in experimental works, such as Kozlov and Ramazanov [50], where a rectangular channel was used for visual inspection of the lambda shaped perturbations, and others [51, 52]. As discussed in the work of Leib et al. [53], Taylor noticed that these streamwise velocity fluctuations were related with thickening and thinning of the boundary layer [54]. Klebanoff in a later experimental work named these fundamental instabilities as breathing modes [4]. However, it was Kendall that renamed these as Klebanoff modes [55].

The experimental work of Bakewell and Lumley [56], reported measurements on the viscous sublayer of a turbulent boundary layer. It was concluded that the near wall region of the viscous sublayer was not a simple passive region dominated by viscous effects subjected to turbulence at its layer edge. Instead, together with the presence of a wall, it had an active role of generation and preservation of turbulence within the turbulent boundary layer. Also this layer had an active role in the transition process itself due to the close presence of the wall. The production of these streamwise velocity fluctuations $u^{'}$, are believed to be related to the wall-normal velocity oscillations $v^{'}$ through the "splat-mechanism" mentioned by Bradshaw [3], or by the concept of "inactive motion" proposed by Townsend [57] and Bradshaw [58]. As stated by Bradshaw [3], "the so-called inactive motion... is simple: the motion near the surface, ... results mainly from eddies actually generated near the surface, ... the contribution... to the shear stress -$\rho\overline{u^{'}v^{'}}$ is small". However, this small shear stress is critical for turbulence transition. The production of these fluctuations has particular characteristics. One of these is the boundary layer selectiveness of free-stream turbulent eddy scales that are filtered from the broad spectrum free-stream turbulence. This has been identified as "shear-sheltering" and was first described by Hunt et al. [59].

In the work of Jacobs and Durbin [60], the Orr-Sommerfeld equations were implemented using both their discrete and continuous modes. These were employed in order to correctly obtain the expansion into eigenfunctions of a general disturbance within a viscous flow. The fast decay phenomenon of the disturbances continuous modes in the boundary layer was observed.

This was related to the "shear-sheltering" effect which was demonstrated to be a general property of the continuous spectrum of the Orr-Sommerfeld equation. As such, continuous modes were eliminated from the main boundary layer region, being confined to the upper reaches of the laminar boundary layer. Also, it was concluded that the boundary layer depth reach of these disturbances was dependent on disturbance frequency and flow Reynolds number. A function relating these variables with penetration depth was developed. This was inversely proportional to the product of disturbance frequency with flow Reynolds number. The developed relation enforces the concept that only low frequency disturbances are amplified by shear in the pre-transitional laminar boundary layer region.

In the experimental work of Volino and Simon [61], spectra of fluctuating streamwise velocity $u^{'}$, wall-normal velocity $v^{'}$ and turbulent shear stresses $-u^{'}v^{'}$ were recorded. It was found noticeable values of $-u^{'}v^{'}$ in the pre-transitional boundary layer. This was also reported in the experimental work of Volino and Simon [27]. These were correlated with peak values of low-frequency wall-normal velocity fluctuations $v^{'}$ of the free-stream turbulence. As previously mentioned these $-u^{'}v^{'}$ values had lower energy and frequency than those found in fully turbulent boundary layer flow. Additionally, the experimental works of Volino and Simon [26, 27], measured heated flow conditions under high acceleration and curvature subject to high free-stream turbulence intensity. The experimental setup was designed to approximate the operational conditions of the downstream half of the pressure side of a gas turbine airfoil. Only a constant curvature wall was used in the experiment as the main test geometry. Other works on curvature effects in transition threshold can be found such as the report of Liepmann [62]. The obtained results documented flow transition to fully turbulent regime. The high free-stream turbulence intensity should impose an early transition. Nonetheless, due to the strong flow acceleration, transition was delayed. In this transitional region, significant unsteady effects and eddy advection were present. However, the near-wall turbulence production was suppressed due to the strong flow acceleration. The unsteadiness of this particular transitional flow was taken from the influence of the free-stream turbulence instead. This observation is similar to the first obtained laminar velocity fluctuation measurement experiment of Dryden in 1937 [40].

2.5 Approaches to transition modeling

2.5.1 DNS transition studies

Direct Numerical Simulation or DNS, is the direct calculation of the full Navier-Stokes equations, resolving all turbulence scales. The colossal computational requirements by this fully resolving turbulence method makes it almost impossible to apply in industrial relevant product development cases. One of the major limitations of DNS is its increasing requirements with higher Reynolds numbers. The increase in Reynolds number, decreases the size of the smallest turbulence scales. Therefore DNS simulations will require even more refined mesh conditions for increasing Reynolds number flows. Since the most relevant industrial flows have typically high values of Reynolds number, it is simply impractical to use such turbulence resolving methodology. Even though DNS is far from being considered a viable solution for industrial development, there is an increasing tendency of GPU parallel processing usage in CFD. This processing method largely increases computational processing speeds [63]. With time, this turbulence full scale resolving method might be used in industry.

Although nowadays DNS can only be practically applied to relatively simple geometries,

the outcome of these computer simulations deliver an insight in flow-physics never before seen in experimental conditions. This is due to the fact that, computational data can be thoroughly scrutinized, whereas experimental data outcome depth is dependent on the measuring technology available. Nevertheless, DNS is presently applied in a more numerical study approach such as the following presented work. The numerical investigation of Jacobs and Durbin [64], presented results of bypass simulation under free-stream turbulence. This was conducted through DNS. It was concluded that streaks of streamwise velocity fluctuations are triggered by low-frequency boundary layer breaching modes from free-stream turbulence. This turbulence spectrum is changed by a shear-layer non-linear process. The resulting spectrum has high energy in specific low-frequencies. This mechanism of frequency selection makes the resulting spectrum insensitive to details of inlet conditions. It was also concluded that the near wall streaks are relatively stable in the vicinity of the surface. When upwelling occurs, these streaks are pushed out of the lower part of the boundary-layer towards its edge. These, under the influence of the free-stream turbulence, become unstable and degenerate into turbulent spots. Other relevant DNS numerical study works related to transition can be found such as the work of Liu and Chen [2], where DNS modeling is applied to study the late stages of transition, and others [65, 66, 67].

2.5.2 LES transition applications

Large Eddy Simulation or LES, is being increasingly used in industrial applications thanks mainly to the parallel computational power enhancement of the last few years. However, product development and optimization using this type of turbulence modeling still presents a tremendous challenge in terms of computational costs. Turbulence modeling performed through LES resolves the larger scales of the turbulent vortices. The smaller scales are modeled using a RANS approach. This is so since in the small scale range the distribution of turbulent vortices approaches the isotropic and homogeneous state. As such, these are less influenced by the surrounding flow characteristics. On the other hand, the larger scaled turbulent vortices that have a longer life span, and thus are more exposed to flow history need to be fully resolved. This method was first successfully applied in 1970 by Deardorff in his turbulent channel flow simulation [68]. In order to model the small scale turbulence, Deardorff applied an eddy-viscosity model developed by Smagorinsky [69]. It goes without saying that LES simulation results are dependable on the selected small scale or sub-grid scale model as shown in the work of Schlatter [70]. Nevertheless, LES is applicable to turbulence transition modelling as shown in the laminar flow transition to fully turbulent regime over a flat-plate with a blowing and suction strip on [71] or the flow transition to turbulence on a channel flow from [72], and others [73, 74].

2.5.3 RANS based transition tools

2.5.3.1 Low-Reynolds turbulence models

Transition modeling is still not widely used in industrial flow computations, mainly due to several limitations of present day models. This seems to be the case since the available transition models tend to be complex. Thus, computation time is largely increased by the usage of a transition tool just to calculate an often small fraction of the relevant flow. It goes without saying that it is of vital importance to know where transition occurs. However, for some engineering problems this transition onset is overlooked and fully turbulent models are applied

instead [75]. Some of these, specifically low-Reynolds turbulence models, are sometimes used to predict transition onset. The first few serious efforts to evaluate transition modeling capabilities of used turbulence models were presented by Savill [76]. These low-Reynolds turbulence models derive their name from the fact that they resolve the turbulent boundary layer up to the wall, in the low Reynolds near wall region. This means that, instead of using a wall-function for resolving the near wall velocity distribution, the whole turbulent boundary layer, including the sub-laminar layer, is resolved. The near wall modeling is possible mainly due to damping functions. Some of these reduce the turbulence scale based on the calculation of the nearest wall distance. Others use the turbulent Reynolds number to reduce the turbulent viscosity in the near-wall region in order to simulate the sub-laminar layer of a turbulent boundary layer. The one-equation Spalart-Allmaras turbulence model is one such example of these low-Reynolds turbulence models.

Another low-Reynolds turbulence closure is the k-ω turbulence model, presented in the work of Wilcox [77]. This work exposed that after modifications on viscous damping functions, the k-ω model was able to reproduce sub-layer turbulent behavior details such as $k \sim y^2$ as y$\rightarrow 0$. These details also included maximum dissipation and peak value of k near the surface. Other low-Reynolds turbulence model developments were also presented by Chang et al. [78]. Chen et al. [79], presented a numerical work where three low-Reynolds turbulence models were validated for transitional flows. One of these turbulence closures was based on the linear eddy-viscosity relationship of Boussinesq [31]. The remaining two turbulence models had a non-linear eddy-viscosity formulation calculated through a cubic form. It was claimed that although the non-linear models presented better results than the linear relation closure, none of the tested models presented satisfactory transition results. Other related work was also published, such as the development of a cubic eddy-viscosity closure by Craft et al.[80], and others [81, 82]. Later, Hadzic and Hanjalic [10], presented a low-Reynolds second-moment turbulence closure applied to separation induced transition. This model was validated using the ERCOFTAC T3L test cases. It was shown that the second-moment turbulence model was able to correctly predict transition onset due to flow separation. Even though the model had difficulties predicting bypass transition for flows with lower turbulence intensity than $< 2.5\%$, it could predict the combination of laminar and turbulent flows in transitional separating flows.

Although some of these models have an apparent transition behavior, Rumsey [83], presented a work showing that this behavior is mere coincidence and can lead to design mistakes. This numerical work presented two very well known low-Reynolds turbulence models, the k-ω-SST and the Spalart-Allmaras turbulence closure. These were scrutinized for turbulence transition behavior. It was argued that the apparent transition behavior of these two turbulence models is simply accidental and to some degree undesirable since it might not be an accurate solution.

2.5.3.2 Empirical correlated transition models

The experimental work of Skramstad [41], resulted in one of the first empirical graphic correlation for transition onset. Dhawan and Narasimha [84], developed an experimental intermittency correlation that was used to determine transition onset. Later, the works of Abu-Ghannam and Shaw [85], Mayle [25], and others produced various empirical correlations for transition onset. Based on these empirical correlations transition to turbulence models were formulated such as the ones created by Cho et al.[86], applied on a turbine wake induced transition study, and others [87, 88]. Typically these first empirically correlated transition models were non-locally formulated, since they depended on integration of the boundary layer velocity profiles.

This was performed so as to obtain one of the parameters used by the empirical correlations. Most commonly this would be the local momentum thickness Reynolds number. The work of Anderson et al. [89], evaluated boundary layer upstream disturbances with higher spatial energy growths. It was found that the maximum spatial transient growth scales linearly with the Reynolds number, for values higher than 1×10^5. Taking into consideration the revealed linear relation, a scaling law for the transition Reynolds number was proposed. Using this, a simple transition onset prediction closure was developed. The latter correlated free-stream turbulence intensity and the transition Reynolds number. Later, Suzen and Huang [90], presented a new transport equation for turbulence intermittency. This was coupled to the Menter k-ω-SST turbulence model. The presented intermittency closure was a blended function from two other proposed intermittency models. The first was presented by Steelant and Dick [91], for streamwise intermittency evolution. The last used function was developed by Cho and Chung [92], for cross-stream intermittency distribution. The first locally formulated empirically correlated transition model was presented in 2005 by Langtry [29].

2.5.3.3 Non-empiric transition models

Besides the pure empirically correlated transition models, there is also the non-empiric closures that are either not dependent or semi-dependent on the applied empirical correlations. The cubic non-linear turbulence model proposed by Craft et al. [80], was modified in order to improve accuracy on flows far from equilibrium such as those characteristic of transition regions. The model enhancement included the inclusion of another transport equation for the second invariant of the stress anisotropy tensor [81]. It was concluded that the use of another parameter besides the turbulent Reynolds number was required for the correct calculation of the turbulence model coefficients. These were then formulated with dependence on the stress anisotropy second invariant as well as the turbulent Reynolds number. Another approach for turbulent transition modeling was proposed in the numerical work of Wang and Perot [93], which presented a turbulence potential model. This was validated under flat-plate transition and channel relaminarization.

Although it has been proven in the work of Rumsey [83], that low-Reynolds turbulence models transition capabilities are accidental, there still persists some works on the research effort of converting these models into transition tools. An example of such works was presented by Denissen et al. [94], where the k-ω-SST turbulence model was altered in order to correctly predict transition onset under high free-stream turbulence intensity. After calibration the model was validated with subsonic and hypersonic flow benchmark test cases.

In the work of Durbin [12], a new intermittency model was proposed for bypass transition onset prediction and length computation. The presented model is an intermittency transport equation. As all the intermittency models, this is coupled to the production term of the selected turbulence model. Transition onset is predicted by diffusion of the intermittency variable and the transition process is carried by a source term in the intermittency equation. This model does not require any external input data. Contrary to most models of this type, this does not use empirical correlations.

The recently developed transition to turbulence model by Rodio et al.[95], is based on the stress-ω model of Wilcox [96]. The transition closure was developed to predict natural transition phenomenon. It was concluded that the model was able to reliably predict the natural transition onset. However, for the cases of bypass and separation induced transition the model requires improvement.

2.5.3.4 Phenomenological transition models

Turbulent flow has always been distinguishable from its laminar state. Transition can be identified through an increase in skin-friction and velocity profile departure from a Blasius distribution. There used to be a certainty about the fact that only turbulent flow had velocity fluctuations. Laminar flow was considered to develop in a stationary fashion. This all changed with the work of Dryden [40]. The latter experimental work is considered to be the first attempt to successfully measure velocity fluctuations in the laminar flow region. Later on, the experimental work of Skramstad [41], also confirmed the presence of laminar fluctuations just before turbulence transition. To the best of our knowledge, and according to the award winning paper of Mayle and Schulz [97], the work of Lin [98], was the first to analytically evaluate the effects of laminar fluctuations over laminar velocity profiles. This study confirmed the possibility of having velocity fluctuations in a laminar flow, even when maintaining a Blasius velocity profile distribution. This fact was also documented by Dyban et al.[99] where a flat-plate was subjected to low speed flow with varying free-stream turbulence intensity from 0.3% to 25%, as well as on a heated flat-plate flow experimental configuration with a varying free-stream turbulence intensity from 0.4% to 6% by Sohn and Reshotko [100], and others [101, 102].

As previously mentioned, in the work of Mayle and Schulz [97], the LKE, or, Laminar-Kinetic-Energy theory was proposed. Following this development, a new tool for transition modeling was available. The first transition models based on LKE were developed by Lardeau et al. [103] and Walters and Leylek [104]. Others followed this trend, such as Vlahostergios et al. [105]. The work of Volino [106], presented a model that took into account the physical effects of free-stream turbulence in boundary layer calculation. The model computed a turbulent free-stream induced eddy-viscosity. This was attributed to the relation between the Klebanoff modes and the "splat-mechanism". The normal to the wall velocity fluctuations resulted in streamwise velocity oscillations. This model can be used in combination with any turbulence model. Therefore, besides the calculation of a turbulent eddy viscosity by the chosen turbulence closure, a free-stream induced eddy-viscosity is also used to calculate the total eddy viscosity of the flow. In 2000, the numerical work of Edwards et al. [107], claimed to have developed an unified one-equation turbulence transition model. The presented model was the result from blending two distinct turbulence closures. One of these is the very well known, low-Reynolds turbulence model, the Spalart-Allmaras closure. The other model was an eddy-viscosity transport equation for non-turbulent fluctuation growth. This was based on the work of Warren and Hassan [108]. The blending between these two closures was accomplished with a multi-dimensional intermittency function.

Walsh [109], evaluated the entropy production in the pre-transitional region. The production rate of entropy increased near the wall in the pre-transitional flow region and decreased downstream to the fully turbulent boundary layer distribution values. Although this work did not produce a new transition model, it will certainly be of critical importance for the development of a phenomenological transition model based on the physics of entropy generation rate near the transition onset region.

Another contribution to the ever increasing number of phenomenological transition to turbulence models is the recent modification of the k-k_l-ω model of Walters and Cokljat [110] by Fürst et al.[111]. This alteration was focused on the natural transition behavior of the transition closure under adverse-pressure-gradient conditions. The developed model was able to improve the transition onset prediction under adverse-pressure-gradient flows. Nevertheless, it was concluded that the transition closure still required improvement.

2.5.4 Linear stability models

The fundamental contributions made by Tollmien in [112] and [113] and Schlichting in [43] and [114], allowed the development of the currently known linear stability theory. Also the experimental works of Orszag and Patera [115] and Herbert [49], contributed for the validation of the linear stability theory.

Through the simultaneous work of Smith and Gamberoni [116] and Ingen [117], the e^n method was developed. This was initially conceived to be applied with viscous-inviscid codes such as the ISES [118]. However, the successful coupling of the e^n method with the Navier-Stokes equations became a growing trend [119]. Considered by some to be the state of the art in prediction of transition onset, it is a method based on the linear local stability theory. According to Ingen, "The linear stability theory considers a given laminar main flow upon which small disturbances are superimposed" [120]. The operation protocol of this method begins with the resolution of the laminar boundary layer velocity profiles. This is then used to calculate the growth rate of the superimposed linear instabilities within the flow by solving the linear stability equations. After completion of the latter, an integration of the obtained growth rates throughout the streamlines is performed. The resulting value will represent the amplification factor, n, of the instabilities. The disturbance amplitude ratio is then given by e^n. When this reaches a threshold, transition onset is assumed. Typical transition threshold values for e^n are obtained with n values between 7 to 9. The semi-empirical nature of the n factor determination, the high quality mesh requirements and its inherent two dimensional approach are some of the flaws of this transition calculation tool.

Nevertheless, the parallel computing works of Krimmelbein and Radspiel [121] and Krimmelbein and Krumbein [122], presented a three-dimensional solving methodology based on the e^n approach. This was derived from coupling multiple solving elements. These were a 3D Navier-Stokes solver, a transition module, a boundary layer code and a stability code. This method was applied to various three-dimensional geometries such as the 6:1 prolate-spheroid and a fuselage of a generic transport aircraft. It was demonstrated that a e^n based method for transition calculation on complex three-dimensional geometries using parallel computation is feasible.

2.6 The empirical correlated $\gamma - Re_\theta$ model

In the work presented by Langtry and Menter [29], where multiple geometries from airfoils to a full helicopter are analysed, along with the work of Menter et al.[123] with flat-plate validations including a three-dimensional transonic wing, and the following publications [124, 125, 126], a new transition model is introduced, the $\gamma - Re_\theta$. The turbulence transition closure is based on experimental data correlation with the possibility of user-defined empirical correlations. Typically these types of transition models require non-local information such as momentum thickness Reynolds number, which is calculated by boundary-layer velocity profile integration. However, the developed empirically correlated transition model is locally formulated. The authors proposed an alternative method to calculate the non-local variable of the momentum thickness Reynolds number. This was done by considering the approximation of the momentum thickness Reynolds number by the vorticity Reynolds number. The momentum thickness Reynolds number is then locally calculated using an algebraic relation based on the vorticity Reynolds number [127] and [128]. Although these two flow properties are not identical, it was shown that a relation between these was viable under a considerable range of flow favorable-pressure-gradients for which there is experimental transition data. Nonetheless,

under strong adverse-pressure-gradient and in nearly separated flows, the difference between vorticity Reynolds number and momentum thickness Reynolds number can be significant. The transition model is then constituted by two transport equations. One for the turbulence intermittency, γ, that is coupled to the selected turbulence model production term. The other equation is for the transition momentum thickness Reynolds number, Re_θ. This is computed in the free-stream according to the used empirical correlations applied by the model user. The transition momentum thickness Reynolds number is then diffused from the free-stream into the boundary layer. Within the boundary layer, the diffused transition momentum thickness Reynolds number is compared to the locally calculated momentum thickness Reynolds number. If the calculated value is equal to the diffused experimental data threshold then the intermittency production term is activated. Thus, transition to turbulence is triggered and fully turbulent flow is formed thereafter. This transition to turbulence closure is coupled with the k-ω-SST turbulence model of Menter [129]. However, according to the transition model authors, it is possible to use these transition components of the model with other turbulence models. The model was validated on two dimensional cases and three-dimensional cases including a full helicopter fuselage. The obtained results led the authors to conclude that the model was a reliable tool for industrial CFD calculation, able to capture the major transition effects.

The main problem with the work of Langtry [124], was the lacking of two key components of the model, due to proprietary reasons. However and thanks to the work of Suluksna and Juntasaro [130], which presented a first attempt of developing the critical momentum thickness Reynolds number and turbulence transition length functions, as well as others [131, 132, 133], these lacking terms were approximated by alternative functions. Nonetheless, later in 2009, Langtry and Menter, the original authors of the $\gamma - R_{e\theta}$ transition model, published all of the lacking terms [134]. This transition model, although having a promising future as an engineering tool, has too many transport equations. It delivers turbulent flow with transition calculation at the expense of a significant increase in processing time. These type of models are also non-universally formulated. They depend upon the used empirical correlations. This implies that whenever a new flow phenomenon is encountered the model might not work as it should. Following this work, You and Kwon [135], blended the SAS, Scale Adaptive Simulation, model and the empirical correlated transition closure of $\gamma - Re_\theta$ into one turbulence model. The model was tested on a circular cylinder at supercritical Reynolds number. The transition onset over the circular geometry predicted by the blended model was compared to the original stand-alone $\gamma - Re_\theta$ transition closure. The separated unsteady wake of the cylinder calculated by the blended model was compared to the original SAS model. Both of these results presented good agreement, thus, a new blended SAS empirically correlated transition turbulence model was developed. Also, Gorji [136], presented a comparison study with DNS results of an accelerated channel flow using ten eddy viscosity turbulence models. It was concluded that the k-ε turbulence model of Launder and Sharma [137] and the $\gamma - Re_\theta$ transition closure were the only models able to correctly capture the unsteady flow features.

2.7 The phenomenological k-k_l-ω model

As previously mentioned, based on the newly developed LKE theory, one of the first phenomenological turbulence transition models developed was presented by Walters and Leylek [104]. Later in 2008, a newly improved version of the transition model was published by Walters and Cokljat [110]. Some of the most significant differences between the two turbulence

transition models published versions was the turbulence length scale transport equation. For the Walters and Leylek [104], transition closure, a transport equation for turbulent kinetic energy dissipation rate was used. In the newer turbulence transition model of Walters and Cokljat [110], a transport equation for the specific turbulent kinetic energy dissipation rate was chosen instead. Besides this, there are many other changes between the two transition model versions. Nevertheless, both model versions share some interesting characteristics such as the division of turbulence into large and small scales. As discussed in the work of Volino [138], the experimental works of Moss and Oldfield [139] and Thole and Bogard [140], proved the existence of two different turbulence scales in fully turbulent boundary layers. Similar to the proposal presented by Walters and Leylek [104], the lower frequencies, or large scale fluctuations, were related to free-stream turbulence unsteady actuation on the boundary layer. The higher frequency, or small scale, is believed to be related to the near wall turbulence production. Also, in the work of Volino and Simon [141], it was once again concluded that the high amplitude low frequency velocity oscillations were related to the effect of free-stream turbulence. The effect of these low frequency perturbations are modeled by the k-k_l-ω transition model as laminar fluctuations kinetic energy. This is performed by the transition closure by dividing the total turbulent kinetic energy in the previously mentioned small and large turbulence scales. This division is only executed within the near wall region. The transition model then uses the laminar fluctuations kinetic energy to perform the transition process itself.

In 2007, Cutrone et al. [142], presented an improved turbulence transition closure based on the Walters and Leylek [104] and Walters and Leylek [143] versions of the k-k_l-ω transition model. Later, this same improved model was applied in the computation of turbo-machinery relevant flows by Cutrone et al. [6]. The numerical work of Reza et al. [144], changed some of the model constants used in the 2004 Walters and Leylek transition model. The changed model was compared with other turbulence models on some ERCOFTAC benchmark test cases and on the S809 two-dimensional wind turbine airfoil.

A low pressure turbine, LPT, computation with the 2004 Waters and Leylek transition model version was presented by Sanders et al. [145] and [146]. The study was divided in two parts, one for light loading conditions and the other for separated blade flow due to high blade loading level. It was concluded that the model presented reasonable results, although better experimental agreement was obtained for the light loading conditions. The experimental and numerical work of Genç et al. [147], performed an evaluation of the k-k_l-ω transition model for laminar separated bubbles over the NACA2415 airfoil. Also, the effect of separation bubble control was studied with the use of suction and blowing jet actuators. Other works related to this transition model were presented by Holloway et al.,[148] with an unsteady analysis of the flow behind a cylinder, Turner and Prosser [149] on a bypass transition validation over a flat-plate, Bernardini et al. [150] for the application of a zero-net mass flux actuator for turbine flow separation overthrow, and others [151, 152].

Chapter 3

RANS transition models

3.1 Transition models development

As previously mentioned, the main types of available RANS transition models are the empirical correlated transition closures and the phenomenological models. During the review effort on the available transition models the latter type was chosen as the main topic of research. This type of models was chosen for its physics modeling potential. The transition model study began with the implementation of a laminar kinetic energy theory based closure developed by Walters and Leylek [104]. The implementation was performed in the open-source software, OpenFoam. After some trials with this transition model, a second transition model was implemented. This was a newer version of the turbulence transition model developed by Walters and Cokljat [110]. During the model testing, some of its terms were changed for improvement on the turbulence transition accuracy. Afterwards, the final research effort in turbulence transition modeling resulted in a new transition closure. This is based on a mechanical approximation of the mean statistical effect of mean flow on the pre-transitional turbulence.

3.2 Origin of the laminar kinetic energy transition model

In the work of Mayle and Schulz [97], the Laminar-Kinetic-Energy theory was proposed. This is also known as the LKE theory. The transport equation for laminar kinetic energy was obtained in the same way the turbulent kinetic energy transport equation was obtained by Bradshaw [153]. The resulting equation obtained by Mayle is presented in (3.1).

$$\overline{u}\frac{\partial k_l}{\partial x}+\overline{v}\frac{\partial k_l}{\partial y}=-\left(\overline{u'v'}\right)\frac{\partial \overline{u}}{\partial y}-\frac{\partial}{\partial y}\left[\overline{v'k_l}-\nu\frac{\partial k_l}{\partial y}\right]-\varepsilon+\left(\overline{u'\frac{\partial U'_{imp}}{\partial t}}\right). \quad (3.1)$$

In this, the k_l represents the kinetic energy of laminar fluctuations. Although this transport equation is the corner stone of LKE theory, some models based on the theory do not make explicit use of it. Instead, only the concept of modeling laminar fluctuations kinetic energy is used to create new transition models. Some properties of the LKE theory transport equation are used in these newly developed models. For instance in (3.1), the k_l variable diffusion term takes only into account the fluid kinematic viscosity rather than adding this with the flow turbulent viscosity. An example of such model is presented in the following.

3.2.1 k-k_l-ε transition model

The first published version of a locally formulated laminar kinetic energy turbulence transition model was that of Walters and Leylek [104]. In this version of the transition closure the transported turbulent properties were the turbulent kinetic energy, k, the laminar kinetic energy, k_l, and the turbulent kinetic energy dissipation rate, ε. The transport equations are

then presented in (3.2-3.4).

$$\frac{Dk}{Dt} = P_k + R_{bp} + R_{nat} - \varepsilon - D_t + \frac{\partial}{\partial x_j}\left[\left(\nu + \frac{\alpha_t}{\sigma_k}\right)\frac{\partial k}{\partial x_j}\right], \quad (3.2)$$

$$\frac{Dk_l}{Dt} = P_{k_l} - R_{bp} - R_{nat} - D_l + \frac{\partial}{\partial x_j}\left[\nu\frac{\partial k_l}{\partial x_j}\right], \quad (3.3)$$

$$\frac{D\varepsilon}{Dt} = C_{\varepsilon 1}\frac{\varepsilon}{k}\left(P_k + R_{nat}\right) + C_{\varepsilon R}R_{bp}\frac{\varepsilon}{\sqrt{kk_l}} - C_{\varepsilon 2}\frac{\varepsilon^2}{k} - \frac{\varepsilon}{k}D_t + \frac{\partial}{\partial x_j}\left[\left(\nu + \frac{\alpha_t}{\sigma_\varepsilon}\right)\frac{\partial \varepsilon}{\partial x_j}\right]. \quad (3.4)$$

The terms $C_{\varepsilon R}$ and $C_{\varepsilon 1}$ are defined in (3.5) and (3.6) respectively.

$$C_{\varepsilon R} = 0.21\left(\frac{1.5\lambda_t}{\lambda_{eff}} - 1\right), \quad (3.5)$$

$$C_{\varepsilon 1} = 2\left[1 - \left(\frac{\lambda_{eff}}{\lambda_t}\right)^{\frac{4}{3}}\right] + 1.44\left(\frac{\lambda_{eff}}{\lambda_t}\right)^{\frac{4}{3}}. \quad (3.6)$$

Although the model was novel, soon after its disclosure in the literature, a new version of the model was developed in 2005 [143]. Afterwards, again a new version of the k-k$_l$-ω transition closure was presented in 2008 [110]. This turbulence transition closure version was modified and is presented in the following section.

3.3 k-k$_l$-ω phenomenological transition model

The work of Walters and Leylek [143], presented a new version of the laminar kinetic energy transition model based on their previously developed model in [104]. Albeit the similarities between both models, in the new model version the transport equation for turbulent kinetic energy dissipation rate, ε, was substituted by a transport equation for specific turbulent kinetic energy dissipation rate, ω. Later on, a new version of the k-k$_l$-ω transition model was released in 2008 by Walters and Cokljat [110]. The newly published transition model presented differences in some terms in relation to its previous version [143].

The model formulation of the 2008 version, is then constituted by a set of three transport equations. One for the laminar fluctuations kinetic energy (k_l), another for the turbulent kinetic energy (k), and the last one for the specific turbulent kinetic energy dissipation rate (ω). The transport equations for incompressible flow are shown in (3.7-3.9).

$$\frac{Dk}{Dt} = P_k + R_{bp} + R_{nat} - \omega k - D_t + \frac{\partial}{\partial x_j}\left[\left(\nu + \frac{\alpha_t}{\sigma_k}\right)\frac{\partial k}{\partial x_j}\right], \quad (3.7)$$

$$\frac{Dk_l}{Dt} = P_{k_l} - R_{bp} - R_{nat} - D_l + \frac{\partial}{\partial x_j}\left[\nu\frac{\partial k_l}{\partial x_j}\right], \quad (3.8)$$

$$\frac{D\omega}{Dt} = C_{\omega 1}\frac{\omega}{k}P_k + \left(\frac{C_{\omega r}}{f_W} - 1\right)\frac{\omega}{k}\left(R_{bp} + R_{nat}\right) - C_{\omega 2}\omega^2 + C_{\omega 3}f_\omega \alpha_t f_W^2 \frac{\sqrt{k}}{y^3} + \frac{\partial}{\partial x_j}\left[\left(\nu + \frac{\alpha_t}{\sigma_\omega}\right)\frac{\partial \omega}{\partial x_j}\right]. \quad (3.9)$$

The production components for the transport equations of turbulent kinetic energy, (3.7), and laminar fluctuations kinetic energy, (3.8), are based on velocity strain rate given by (3.10) and (3.11) respectively.

$$P_k = \nu_{t,s} S^2, \quad (3.10)$$

$$P_{k_l} = \nu_{t,l} S^2. \quad (3.11)$$

Additionally, it can be observed that these source terms, (3.10) and (3.11), are also dependent on a small and large scale turbulent viscosity, $\nu_{t,s}$ and $\nu_{t,l}$ respectively. Therefore, turbulence is divided in large and small scales. The former scale is limited by the wall and related to laminar fluctuations kinetic energy production through the "splat mechanism", as suggested by Volino [106]. The small scale is related to regular turbulence, and as observed in (3.10), it is also responsible for its production. As will be shown later, far from wall surfaces the small scale turbulent kinetic energy is equal to the free-stream turbulent kinetic energy.

Following the work of Walters and Leyleck [104], the definition of the turbulence dividing length scale, also designated as the effective turbulent length scale, is obtained from (3.12), where λ_t is the turbulent length scale presented in (3.13).

$$\lambda_{eff} = min\left(C_\lambda y, \lambda_t\right), \quad (3.12)$$

$$\lambda_t = \frac{\sqrt{k}}{\omega}. \quad (3.13)$$

The definition for the effective turbulence length scale, (3.12), implies that far from wall surfaces the dividing length scale is equal to the turbulence length scale. This presupposes that under these conditions, there is no dividing length scale, and as will be shown later, there is no turbulence large scale to begin with.

The small scale turbulent kinematic viscosity from the turbulent kinetic energy production term, (3.10), is computed according to equation (3.14).

$$\nu_{t,s} = f_\nu f_{int} C_\mu \sqrt{k_{t,s}} \lambda_{eff}. \quad (3.14)$$

This is calculated based on a series of damping functions that attempt to simulate various flow mechanisms. Also, there is a dependency on the effective turbulence length scale and on the small scale turbulent kinetic energy, $k_{t,s}$. This is calculated according to the relation presented in (3.15).

$$k_{t,s} = f_{ss} f_W k. \quad (3.15)$$

Two of the aforementioned damping functions are used to compute this small scale turbulent kinetic energy. The first of these functions serves as a model for the mechanism of shear-sheltering effect. According to the work of Jacobs and Durbin [60], this process is responsible for

the decay of the free-stream turbulence continuous modes inside a laminar boundary layer. This then results in a confinement of these perturbations modes to the edges of the laminar boundary layer. Within the k-k$_l$-ω model the shear-sheltering is obtained through (3.16).

$$f_{ss} = e^{\left[-\left(\frac{C_{ss}\nu\Omega}{k}\right)^2\right]}. \quad (3.16)$$

As can be observed, equation (3.16) is defined as an exponential function. This in turn is inversely proportional to the local turbulent kinetic energy. Due to the negative dependence of the exponential function, this implies that the larger the turbulent kinetic energy, the lower the shear-sheltering effect. Also, it must be remarked that this shear-sheltering term is defined with a direct proportionality to mean flow vorticity.

The second damping function is related to wall effects on turbulence. This is then the kinematic wall effect defined in (3.17).

$$f_W = \left(\frac{\lambda_{eff}}{\lambda_t}\right). \quad (3.17)$$

The kinematic wall effect is simply modeled as a relation between the turbulent length scale and its effective or dividing length scale. From relation (3.12), it can be concluded that in the vicinity of wall surfaces, there will be a decrease of the effective turbulence scale, λ_{eff}, in comparison with the turbulent length scale, λ_t. Hence, the kinematic wall effect damping function, (3.17), imposes a less than unity value in the vicinity of wall boundaries, whereby the free-stream equivalence of turbulent kinetic energy, k, and small scale turbulent kinetic energy, $k_{t,s}$, is lost. This gives room for the large scale turbulent kinetic energy, $k_{t,l}$, to first emerge in the flow. The large scale turbulent kinetic energy definition is exhibited in (3.18).

$$k_{t,l} = k - k_{t,s}. \quad (3.18)$$

The following damping function in equation (3.14), is the flow turbulence intermittency defined in (3.19).

$$f_{int} = min\left(\frac{k_l}{C_{int}k_{tot}}, 1\right). \quad (3.19)$$

The k_{tot} in equation (3.19) is equal to k plus k_l. This equation presents a linear relation with the laminar fluctuations kinetic energy, k_l. As will be shown later, this is a contradiction considering the fact that far from wall surfaces, k_l, is null. Therefore, this predicts a zero value for free-stream turbulence intermittency.

The last remaining damping function is again related to wall effects on turbulence. This is then the viscous wall effect damping function disclosed in (3.20).

$$f_\nu = 1.0 - e^{\left(-\frac{\sqrt{Re_t}}{A_\nu}\right)}. \quad (3.20)$$

Similar to the shear-sheltering damping function, this term is also an exponential based function. Nonetheless, the viscous wall effect damping function takes only into account the turbulent Reynolds number value.

For the particular model published in [110], the turbulent Reynolds number definition is not the same as other turbulence models. The k-k$_l$-ω transition closure turbulent Reynolds number

definition is disclosed in (3.21).

$$Re_t = \frac{f_W^2 k}{\nu\omega}. \quad (3.21)$$

Although this definition is similar to the most common turbulent Reynolds number relation, it presents an additional dependency on a damping function modeling the kinematic wall effect, f_W.

The last term within the small length scale turbulent kinematic viscosity, (3.14), is the fundamental relation between direct turbulence properties such as turbulent kinetic energy and specific turbulent kinetic energy dissipation rate with the turbulent viscosity, the C_μ. Taken to be constant within a turbulent boundary layer under equilibrium conditions, this coefficient takes the value of 0.09 for such cases. However, under non-equilibrium turbulent flows, such as turbulence transition stages, C_μ no longer presents the aforementioned constant value. Also and in order to satisfy realizability, C_μ is instead a function of flow and turbulence properties, calculated according to (3.22).

$$C_\mu = \frac{1}{A_0 + A_s \left(\frac{S}{\omega}\right)}. \quad (3.22)$$

This expression for C_μ is a simplified version of its original form according to the work of Shih and Zhu [154], and Shih et al. [155].

As mentioned earlier, the laminar fluctuations kinetic energy production component, (3.11), is a function of the large scale turbulent kinematic viscosity, $\nu_{t,l}$. This is related to the transition onset process and it is defined according to (3.23).

$$\nu_{t,l} = min\left\{ f_{\tau,l} C_{11} \left(\frac{\Omega \lambda_{eff}^2}{\nu}\right) \sqrt{k_{t,l}} \lambda_{eff} + \beta_{ts} C_{12} Re_\Omega y^2 \Omega, \frac{0.5\left(k_l + k_{t,l}\right)}{S} \right\}. \quad (3.23)$$

The imposed minimum limit term ensures the realizability constraint through the right hand side of the minimum function, $0.5\left(k_l + k_{t,l}\right)/S$. Within the left hand side of the minimum term, the first component accounts for the bypass transition mechanism while the second component treats the natural transition process. Similar to the small scale turbulent viscosity, $\nu_{t,s}$, the bypass transition element is a function of the effective turbulence length scale. Nevertheless, the bypass term has a dependency on the large scale turbulent kinetic energy, $k_{t,l}$, instead of the small scale, $k_{t,s}$. Also, this bypass transition function applies a time-scale damping function, $f_{\tau,l}$. The definition for the latter relation is disclosed in (3.24).

$$f_{\tau,l} = 1 - e^{\left[-C_{\tau,l} \frac{k_{t,l}}{\lambda_{eff}^2 \Omega^2}\right]}. \quad (3.24)$$

Although there is some resemblance between this damping function and the viscous wall effect, (3.20), the former uses mean flow vorticity and the large scale turbulent kinetic energy, $k_{t,l}$, while the viscous wall effect is based on the turbulent Reynolds number.

Furthermore, the bypass term is a function of mean flow vorticity. The component responsible for handling the natural transition process is dependent on a Tollmien-Schlichting threshold function. The definition of this threshold is disclosed in (3.25).

$$\beta_{ts} = 1 - e^{\left(-\frac{max\left(Re_\Omega - C_{ts,crit}, 0\right)^2}{A_{ts}}\right)}. \quad (3.25)$$

Additionally, the previous equation and the natural transition component of (3.23), make use of the vorticity based Reynolds number, Re_Ω. This is defined in (3.26).

$$Re_\Omega = \frac{y^2\Omega}{\nu}. \quad (3.26)$$

Finally, the natural transition element is also dependent on mean flow vorticity and on wall distance.

Besides the turbulent kinetic energy destruction term, ωk, there is also the near wall anisotropic destruction terms in the laminar fluctuations and turbulent kinetic energy transport equations, (3.8) and (3.7). These are computed according to the relations disclosed in (3.27) and (3.28) respectively.

$$D_l = \nu \frac{\partial\sqrt{k_l}}{\partial x_j}\frac{\partial\sqrt{k_l}}{\partial x_j}, \quad (3.27)$$

$$D_t = \nu \frac{\partial\sqrt{k}}{\partial x_j}\frac{\partial\sqrt{k}}{\partial x_j}. \quad (3.28)$$

The laminar fluctuations kinetic energy transport equation, (3.8), does not have any turbulent diffusion. This is in agreement with the pioneer work published in the award winning paper of Mayle and Schulz [97]. However, resembling with most if not all turbulence models, the turbulent kinetic energy transport equation, (3.7), has turbulent diffusion. As such, the effective turbulent diffusivity is computed according to equation (3.29).

$$\alpha_t = f_\nu C_{\mu,std}\sqrt{k_{t,s}}\lambda_{eff}. \quad (3.29)$$

It must be noted that for this relation the $C_{\mu,std}$, is not the same as the previous C_μ from the small scale turbulent viscosity, (3.14). The k-k$_l$-ω transition model published in [110], assumes a constant value for $C_{\mu,std}$ of 0.09.

Contrary to the empirically correlated transition closure, instead of using an intermittency function to activate turbulence production, the k-k$_l$-ω transition model uses energy transfer. The transition process is mainly conducted through the transfer of energy from the laminar fluctuations kinetic energy to the turbulent kinetic energy. Therefore, there is a flux of turbulent kinetic energy from the large scales to the turbulence small length scales. This energy transfer is done through R_{bp} or R_{nat}. These two energy transfer functions are defined in (3.30) and (3.31) respectively.

$$R_{bp} = C_r\beta_{bp}k_l\frac{\omega}{f_W}, \quad (3.30)$$

$$R_{nat} = C_{r,nat}\beta_{nat}k_l\Omega. \quad (3.31)$$

For bypass transition, energy transfer is conducted by R_{bp}, on the other hand, for natural transition this transfer is operated through R_{nat}. These two components do not change the overall total turbulent kinetic energy. This is the case since these terms are added to the turbulent kinetic energy transport equation, (3.7), while being subtracted from the laminar fluctuations kinetic energy equation, (3.8). Both, R_{bp} and R_{nat}, are dependent on the laminar fluctuations kinetic energy, k_l, in order to assure that the energy transfer process does not

Table 3.1: k-k$_l$-ω turbulence transition model constants.

$A_0 = 4.04$	$A_s = 2.12$	$A_\nu = 6.75$	$A_{bp} = 0.6$	$A_{nat} = 200$
$A_{ts} = 200$	$C_{bp,crit} = 1.2$	$C_{nc} = 0.1$	$C_{nat,crit} = 1250$	$C_{int} = 0.75$
$C_{ts,crit} = 1000$	$C_{r,nat} = 0.02$	$C_{11} = 3.4 \times 10^{-6}$	$C_{12} = 1.0 \times 10^{-10}$	$C_r = 0.12$
$C_{ss} = 1.5$	$C_{\tau,l} = 4360$	$C_{\omega 1} = 0.44$	$C_{\omega 2} = 0.92$	$C_{\omega 3} = 0.3$
$C_{\omega r} = 1.5$	$C_\lambda = 2.495$	$C_{\mu,std} = 0.09$	$\sigma_k = 1$	$\sigma_\omega = 1.17$

exceed its source value. Also, the latter transition energy transfer terms make use of threshold functions β_{bp} and β_{nat} for bypass and natural transition respectively. These are presented in (3.32) and (3.33).

$$\beta_{bp} = 1.0 - e^{\left(-\frac{\phi_{bp}}{A_{bp}}\right)}, \quad (3.32)$$

$$\beta_{nat} = 1.0 - e^{\left(-\frac{\phi_{nat}}{A_{nat}}\right)}. \quad (3.33)$$

These threshold functions still require additional limiting functions defined in (3.34), (3.35) and (3.36).

$$\phi_{bp} = max\left[\left(\frac{k}{\nu\Omega} - C_{bp,crit}\right), 0\right], \quad (3.34)$$

$$\phi_{nat} = max\left[\left(Re_\Omega - \frac{C_{nat,crit}}{f_{nat.crit}}\right), 0\right], \quad (3.35)$$

$$f_{nat,crit} = 1.0 - e^{\left(-C_{nc}\frac{\sqrt{k_l}y}{\nu}\right)}. \quad (3.36)$$

The elements in ϕ_{bp} and ϕ_{nat} are the crucial keys for turbulence bypass and natural transition control accordingly. These control the onset of transition.

The last consideration over the set of transport equations presented in (3.7-3.9), is the f_ω term. This is only used in the specific turbulent kinetic energy dissipation rate transport equation, (3.9). The f_ω component is then a damping function related to the boundary layer wake region. This is responsible for the stabilization of the length scale of turbulent flows in stagnation and separated flow regions. The f_ω function is then calculated in (3.37).

$$f_\omega = 1.0 - e^{\left[-0.41\left(\frac{\lambda_{eff}}{\lambda_t}\right)^4\right]}. \quad (3.37)$$

As observed, this stabilization length scale term uses the same ratio present in the kinematic wall effect damping function, f_W. Nonetheless, contrary to relation (3.17), in equation (3.37), the f_w term uses this ratio within an exponential function instead of a direct linear relation.

Conclusively, the k-k$_l$-ω transition model resulting total turbulent kinematic viscosity is the sum of the large and small scale kinematic viscosities as presented in (3.38).

$$\nu_t = \nu_{t,s} + \nu_{t,l}. \quad (3.38)$$

The model constants are disclosed in table 3.1.

3.3.1 k-k$_l$-ω modifications for transition onset prediction improvement

The model implementation as published by Walters and Cokljat [110], presented some issues when tested on experimental test cases. Some authors have attempted to alter these laminar kinetic energy transition models. Cutrone et al. [142], and Cutrone et al. [6], developed a modified version of the transition model based on the work of Walters and Leylek [104] and Walters and Leylek [143]. Turner [151], wrote her PhD. thesis on the alteration of the Walters and Cokljat [110], transition model. Therefore, an attempt to find the reasons for such discrepancies was carried out. The alteration of some of the original terms resulted in an improvement on the results of the published model. Through careful analysis of the model behavior, and using an educated guess based on knowledge of the flow physics, several modifications to the original model are proposed. The process by which such corrections were analyzed was based on comparing results with the same boundary conditions on equal numerical meshes run in Ansys Fluent and OpenFoam. The published model from [110] and its corrected version, described in the present section, were implemented in OpenFoam, whereas the assumed same model is available in the commercial software Ansys Fluent. The new variant of the k-k$_l$-ω transition model from [110], is presented by highlighting the relevant changes to the original one.

The proposed first modification of the model is made to the function f_{int} (3.19). Without this correction the original model predicts zero turbulent viscosity in the free-stream. This is due to the fact that, (k_l), exists only near wall surfaces. The corrected term is then (3.39).

$$f_{int}^{new} = min\left(\frac{k}{C_{int}k_{tot}}, 1\right). \quad (3.39)$$

This was also confirmed by Turner [151].

The second relevant change, in relation to the original model, is a definition of the turbulence Reynolds number, Re_t (3.21), without the non-dimensional function, f_W (3.17). The literature definition of turbulent Reynolds number is the same amongst several turbulence models such as Chang et al. [78], Craft et al. [81] and Lardeau et al. [103]. Removing the dimensionless damping function (3.17), responsible for the kinematic wall effect, resulted in a correction of the asymptotic skin-friction coefficient behavior along the fully turbulent region of the flow. Such effect was observed in the flat-plate test cases during the model's correction stage. This is to be expected since f_W reduces the value of Re_t near the wall. This in turn increases the viscous wall effect of (3.20), decreasing the small-scale turbulent viscosity near the wall. By doing so, it excessively decreases the influence of turbulence near the wall. Thus decreasing the rate of momentum transfer to the wall surface. The proposed term is presented in (3.40). The small-scale turbulent viscosity distribution due only to the last correction is presented in Fig.3.1.

$$Re_t = \frac{k}{\nu\omega}, \quad (3.40)$$

Further, it was observed that in the original model, the destruction term of turbulent kinetic energy specific dissipation rate, $-C_{\omega 2}\omega^2$, presents an excessive effect near the wall. It was identified that the turbulence model of Craft et al. [80], presents a set of equations that have a very similar behavior to the present model. This is mostly related to the turbulent kinetic energy (k) and also for the specific turbulent kinetic energy dissipation rate (ω). In that work, instead of (ω), the transported quantity is the turbulent kinetic energy dissipation

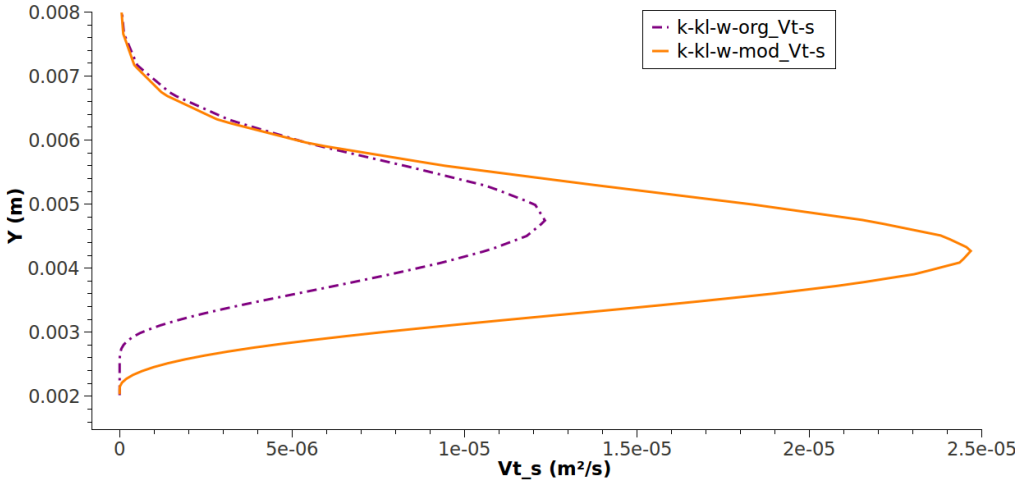

Figure 3.1: Flat-plate small-scale turbulent viscosity profile near the wall. Results computed with the OpenFoam implemented original k-k_l-ω-org transition closure and its modified version the k-k_l-ω-mod transition model.

rate ($\tilde{\varepsilon}$). The interest on this model lies on the used $C_{\varepsilon 2}$ function. This function is multiplied to the term responsible for the destruction of the turbulent kinetic energy dissipation rate. The $C_{\varepsilon 2}$ purpose is then to reduce the influence of the turbulent kinetic energy dissipation rate destruction term near the wall. In this regard, Turner [151], proposed a change by which $-C_{\omega 2}\omega^2$ is multiplied by the square of f_W, (3.17). Although this modification was implemented, it was identified that the transition process of the flow over a flat-plate presented some issues regarding transition onset. In the present version of the model a linear relation with f_W was applied instead. This resulted in better flow transition development. This term is presented in the third element, on the right side of (3.41).

$$\begin{aligned}\frac{D\omega}{Dt} &= C_{\omega 1}\frac{\omega}{k}P_{k_\omega} + \left(\frac{C_{\omega r}}{f_W} - 1\right)\frac{\omega}{k}\left(R_{bp} + R_{nat}\right) - C_{\omega 2}\omega^2 f_W \\ &\quad + C_{\omega 3} f_\omega \alpha_t f_W^2 \frac{\sqrt{k}}{y^3} + \frac{\partial}{\partial x_j}\left[\left(\nu + \frac{\alpha_t}{\sigma_\omega}\right)\frac{\partial \omega}{\partial x_j}\right], \end{aligned} \tag{3.41}$$

As might have been noticed, the previous (ω) transport equation production term is different from the original equation in (3.9). The production component of the transport equation for specific turbulent kinetic energy dissipation rate, is based on the velocity vorticity field as exhibited in (3.42).

$$P_{k_\omega} = \nu_{t,s}\Omega^2, \tag{3.42}$$

The published version of the k-k_l-ω in [110] specifies that turbulence diffusivity, α_t (3.29), is calculated using the $C_{\mu,std}$ constant equal to 0.09. This value is typically found in the inertial sublayer of a turbulent boundary layer of flow over a flat-plate. Therefore, it is assumed an equilibrium state of turbulence over the entire flow region, transition included. Though, turbulence is far from equilibrium in the transition region. The use of the small and large scale turbulent kinematic viscosity provided a more physically correct model for the turbulence diffusivity (3.43).

$$\alpha_t^{new} = \nu_{t,s} + \nu_{t,l}. \tag{3.43}$$

The R_{bp} term in (3.30), is a key parameter to control the extension of the transition region. Herein it is propose that (3.30) should not be a function of the kinematic wall effect f_W, in (3.17). This induces an excessive energy transfer from the laminar to turbulent kinetic energy. The proposed modification for R_{bp} is (3.44).

$$R_{bp}^{new} = C_r \beta_{bp} k_l \omega. \quad (3.44)$$

The bypass transition term ϕ_{bp} (3.34), shows that vorticity plays an important role determining transition onset. Taking into account dimensional reasoning, it is proposed the use of the specific turbulence dissipation rate instead of the mean flow vorticity. By applying this, the dependence on the turbulence Reynolds number is enforced. The resulting corrected function is presented in (3.45).

$$\phi_{bp}^{new} = max\left[\left(Re_t - \frac{C_{bp,crit}}{f_{bp,crit}}\right), 0\right]. \quad (3.45)$$

In (3.45), there is an additional function $f_{bp,crit}$. During the model's corrections, it was observed that using only a threshold constant for bypass transition onset in (3.34) was impractical. In the original natural transition onset function (3.35) the constant, $C_{nat,crit}$, is divided by, $f_{nat.crit}$. As such, an analogous function was implemented on the bypass transition onset term, (3.45). This improved the computed transition onset results. The applied function is presented in (3.46).

$$f_{bp,crit} = 1.0 - e^{\left(-C_{bp}\frac{\sqrt{k_l}y}{\nu}\right)}. \quad (3.46)$$

As observed in (3.46), an additional constant is required, namely $C_{bp} = 0.05$. Some modifications were also applied to the model's original constants such as $C_{bp,crit} = 120$, $C_r = 0.18$ and $C_{nat,crit} = 2500$. These last modifications were performed through calibration with the ERCOFTAC zero-pressure-gradient flat-plate test case T3A.

3.4 $\gamma - Re_\theta$ empirical transition model

The first locally formulated empirically correlated turbulence transition model was developed by Langtry and Menter in [29]. The full description of the model was published in [134]. The developed transition model was coupled to the k-ω-SST turbulence model. Nevertheless, the set of equations constituting the transition tool can be coupled to any other turbulence model as long as an intermittency factor can be applied to the production and destruction terms of the turbulence closure. The transition model has two transport equations, one for turbulence intermittency and the second for the transition momentum thickness Reynolds number. The transport equation for turbulence intermittency, γ, is then presented in (3.47).

$$\frac{\partial \rho\gamma}{\partial t} + \frac{\partial\left(\rho U_j \gamma\right)}{\partial x_j} = P_\gamma - E_\gamma + \frac{\partial}{\partial x_j}\left[\left(\mu + \frac{\mu_t}{\sigma_f}\right)\frac{\partial \gamma}{\partial x_j}\right]. \quad (3.47)$$

This equation production component is disclosed in (3.48).

$$P_\gamma = F_{length} c_{a1} \rho S \left[\gamma F_{onset}\right]^{0.5} \left(1 - c_{e1}\gamma\right). \quad (3.48)$$

This is based on the mean flow shear, S. The onset and length of transition is controlled through the dimensionless functions F_{onset} and F_{length}. The onset function is presented in (3.49).

$$F_{onset} = max\left(F_{onset2} - F_{onset3}, 0\right). \quad (3.49)$$

As observed, this function in turn depends on secondary onset functions. These are presented in (3.50) and (3.51).

$$F_{onset2} = min\left(max\left(F_{onset1}, {F_{onset1}}^4\right), 2.0\right). \quad (3.50)$$

$$F_{onset3} = max\left(1 - \left(\frac{R_T}{2.5}\right)^3, 0\right). \quad (3.51)$$

The second onset function, F_{onset2}, itself relies on the first onset function, F_{onset1} defined in (3.52).

$$F_{onset1} = \frac{Re_\nu}{2.193 Re_{\theta c}}. \quad (3.52)$$

This primary dimensionless onset term depends on the main innovation brought to light by Menter et al. [128], the locally formulated momentum thickness Reynolds number, Re_θ. This relation is defined in (3.53).

$$Re_\theta = \frac{Re_\nu}{2.193}. \quad (3.53)$$

The usage of this relation in the primary onset function results in (3.54).

$$\begin{aligned} F_{onset1} &= \frac{2.193 Re_\theta}{2.193 Re_{\theta c}} \\ &= \frac{Re_\theta}{Re_{\theta c}}. \end{aligned} \quad (3.54)$$

Therefore, the main purpose of F_{onset1}, is to compare the locally calculated momentum thickness Reynolds number with the empirically obtained critical momentum thickness Reynolds number, $Re_{\theta c}$. It must be noted that $Re_{\theta c}$, is the critical Reynolds number at which turbulence intermittency, γ, begins to increase within the boundary layer. Therefore, this process takes place upstream of the transported transition momentum thickness Reynolds number, $\overline{Re_{\theta t}}$.

The vorticity Reynolds number, Re_ν, is originally defined according to (3.55). However, the used definition is shear based. The applied vorticity Reynolds number is then disclosed in (3.56).

$$Re_{\nu_{org}} = \frac{\rho y^2 \Omega}{\mu}, \quad (3.55)$$

$$Re_\nu = \frac{\rho y^2 S}{\mu}. \quad (3.56)$$

The fundamental correlations for the critical momentum thickness Reynolds number, $Re_{\theta c}$, and the transition length function, F_{length}, were missing on the first publication of the $\gamma - Re_\theta$ transition model. Therefore, publications with alternative functions for these two components

flourish. An example of these from the work of Paul [132] are shown in (3.57) and (3.58) respectively.

$$Re_{\theta c} = min\left(0.625\overline{Re_{\theta t}} + 62, \overline{Re_{\theta t}}\right), \quad (3.57)$$

$$F_{length} = min\left[0.01e^{\left(-0.022\overline{Re_{\theta t}}+12\right)} + 0.57, 300\right]. \quad (3.58)$$

Nevertheless, the originally applied correlations published by the original authors of the $\gamma - Re_\theta$ transition closure are available in [134]. The empirical correlation for the critical momentum thickness Reynolds number is then formulated according to relation (3.59).

$$Re_{\theta c} = \begin{cases} \overline{Re_{\theta t}} - (396.035 \times 10^{-2} + \left(-120.656 \times 10^{-4}\right)\overline{Re_{\theta t}} + \left(868.230 \times 10^{-6}\right)\overline{Re_{\theta t}}^2 \\ + \left(-696.506 \times 10^{-9}\right)\overline{Re_{\theta t}}^3 + \left(174.105 \times 10^{-12}\right)\overline{Re_{\theta t}}^4), & \overline{Re_{\theta t}} \leq 1870 \\ \overline{Re_{\theta t}} - \left(593.11 + \left(\overline{Re_{\theta t}} - 1870\right) \times 0.482\right). & \overline{Re_{\theta t}} > 1870 \end{cases}. \quad (3.59)$$

The original transition length dimensionless function, F_{length}, is then disclosed in (3.60).

$$F_{length} = \begin{cases} 398.189 \times 10^{-1} + \left(-119.270 \times 10^{-4}\right)\overline{Re_{\theta t}} + \left(-132.567 \times 10^{-6}\right)\overline{Re_{\theta t}}^2, & \overline{Re_{\theta t}} < 400 \\ 263.404 + \left(-123.939 \times 10^{-2}\right)\overline{Re_{\theta t}} + \left(194.548 \times 10^{-5}\right)\overline{Re_{\theta t}}^2 \\ + \left(-101.695 \times 10^{-8}\right)\overline{Re_{\theta t}}^3, & 400 \leq \overline{Re_{\theta t}} < 596 \\ 0.5 - \left(\overline{Re_{\theta t}} - 596\right) \times 3 \times 10^{-4}, & 596 \leq \overline{Re_{\theta t}} < 1200 \\ 0.3188. & 1200 \leq \overline{Re_{\theta t}} \end{cases}. \quad (3.60)$$

Both of these empirical correlations are polynomials based on the transported transition momentum thickness Reynolds number, $\overline{Re_{\theta t}}$.

The third onset function, F_{onset3}, is based on the turbulent Reynolds number defined in (3.61).

$$R_T = \frac{\rho k}{\mu \omega}. \quad (3.61)$$

The destruction term of the intermittency transport equation, (3.47), is defined in (3.62).

$$E_\gamma = c_{a2}\rho\Omega\gamma F_{turb}\left(c_{e2}\gamma - 1\right). \quad (3.62)$$

Contrary to the intermittency production term, (3.48), this is based on mean flow vorticity, Ω. The turbulence dimensionless function, F_{turb}, is also a function of, R_T. This is then presented in (3.63).

$$F_{turb} = e^{-\left(\frac{R_T}{4}\right)^4}. \quad (3.63)$$

The transition momentum thickness Reynolds number, $\overline{Re_{\theta t}}$, is calculated and convected along the free-stream. This is then diffused into the boundary layer where the aforementioned functions will evaluate the local transition threshold conditions. The transition momentum thickness Reynolds number transport equation is then shown in (3.64).

$$\frac{\partial\left(\rho\overline{Re_{\theta t}}\right)}{\partial t} + \frac{\partial\left(\rho U_j\overline{Re_{\theta t}}\right)}{\partial x_j} = P_{\theta t} + \frac{\partial}{\partial x_j}\left(\sigma_{\theta t}\left(\mu + \mu_t\right)\frac{\partial\overline{Re_{\theta t}}}{\partial x_j}\right). \quad (3.64)$$

The source term of the transition momentum thickness Reynolds number transport equation, $P_{\theta t}$, is disclosed in (3.65).

$$P_{\theta t} = c_{\theta t} \frac{\rho}{t} \left(Re_{\theta t} - \overline{Re_{\theta t}} \right) (1.0 - F_{\theta t}) . \quad (3.65)$$

As can be observed, this source component is designed to force $\overline{Re_{\theta t}}$ to be equal to the empirically correlated $Re_{\theta t}$. It must be noticed that, the latter empirical value can be calculated using diverse empirical correlations. The originally used empirical correlation is presented in (3.66).

$$Re_{\theta t} = \begin{cases} 1173.51 - 589.428 T_u + \frac{0.2196}{T_u{}^2} F(\lambda_\theta), & T_u \leq 1.3 \\ 331.5 \left[T_u - 0.5658 \right]^{-0.671} F(\lambda_\theta). & T_u > 1.3 \end{cases} . \quad (3.66)$$

These correlations make use of the turbulence intensity, T_u, and of a pressure gradient function, $F(\lambda_\theta)$. The definition of $F(\lambda_\theta)$ is disclosed in (3.67).

$$F(\lambda_\theta) = \begin{cases} 1 - \left[-12.986 \lambda_\theta - 123.66 \lambda_\theta^2 - 405.689 \lambda_\theta^3 \right] e^{-\left[\frac{T_u}{1.5} \right]^{1.5}}, & \lambda_\theta \leq 0 \\ 1 + 0.275 \left[1 - e^{[-35 \lambda_\theta]} \right] e^{\left[\frac{-T_u}{0.5} \right]}. & \lambda_\theta > 0 \end{cases} . \quad (3.67)$$

The latter component is a function of the pressure gradient parameter, λ_θ. This is defined according to (3.68).

$$\lambda_\theta = \frac{\rho \theta^2}{\mu} \frac{dU}{ds}. \quad (3.68)$$

The term, dU/ds, is the calculated flow acceleration through the streamwise direction.

In order to allow the diffusion of the transition momentum thickness Reynolds number, $\overline{Re_{\theta t}}$, from the forced free-stream value to the latent boundary layer, a switch function is required. This is performed through the usage of the blending function, $F_{\theta t}$. This takes a unity value within the boundary layer and assumes a null value in the flow free-stream The blending function is then defined in (3.69).

$$F_{\theta t} = min \left(max \left(F_{wake} e^{-\left(\frac{y}{\delta} \right)^4}, 1.0 - \left(\frac{\gamma - \frac{1}{c_{e2}}}{1.0 - \frac{1}{c_{e2}}} \right)^2 \right), 1.0 \right) . \quad (3.69)$$

This switch utility should not take a zero value within a flow wake region. Therefore, another switch function is required in order to distinguish within the shear flow conditions, if these correspond to a boundary layer or a flow wake. The used wake identifier is then the F_{wake} parameter disclosed in (3.70).

$$F_{wake} = e^{-\left(\frac{Re_\omega}{1 \times 10^5} \right)^2}. \quad (3.70)$$

This parameter uses a turbulent kinetic energy specific dissipation, ω, Reynolds number defined in (3.71).

$$Re_\omega = \frac{\rho \omega y^2}{\mu}. \quad (3.71)$$

The blending function, $F_{\theta t}$, also makes use of a boundary layer thickness parameter, δ. This is

locally calculated according to the following equations (3.72), (3.73) and (3.74).

$$\delta = \frac{50\Omega y}{U}\delta_{BL}, \quad (3.72)$$

$$\delta_{BL} = \frac{15}{2}\theta_{BL}, \quad (3.73)$$

$$\theta_{BL} = \frac{\overline{Re_{\theta t}}\mu}{\rho U}. \quad (3.74)$$

The last considered term in the $\overline{Re_{\theta t}}$ transport equation production component, (3.65), is a time scale, t. This is applied for correct dimensional characteristics. The latter scale is defined in (3.75).

$$t = \frac{500\mu}{\rho U^2}. \quad (3.75)$$

Unlike the turbulence intermittency transport equation, (3.47), the transport equation (3.65), does not require a destruction term. This is the case since, the existing production term only assures that the convected $\overline{Re_{\theta t}}$ value is the same as the empirically determined transition threshold value of the momentum thickness Reynolds number, $Re_{\theta t}$. In order to account for the separation induced transition an effective turbulence intermittency is calculated according to (3.76).

$$\gamma_{eff} = max\left(\gamma, \gamma_{sep}\right). \quad (3.76)$$

This operates by comparing the maximum value of the convected intermittency from the transport equation, (3.47), and the intermittency function related to separation induced transition. This is defined according to relation (3.77).

$$\gamma_{sep} = min\left(s_1 max\left[0, \left(\frac{Re_\nu}{3.235 Re_{\theta c}}\right) - 1\right] F_{reattach}, 2\right) F_{\theta t}. \quad (3.77)$$

The separation intermittency parameter, γ_{sep}, makes use of a boundary layer re-attachment function disclosed in (3.78).

$$F_{reattach} = e^{-\left(\frac{R_T}{20}\right)^4}. \quad (3.78)$$

This parameter in turn only evaluates the turbulent conditions through the turbulent Reynolds number, (3.61).

As already mentioned, the empirically correlated turbulence transition model, $\gamma - Re_\theta$, was coupled to the low-Reynolds turbulence closure the k-ω-SST. Therefore, the effective intermittency is applied to this classical k-ω-SST turbulence model according to the modified equation set (3.79-3.82).

$$\frac{\partial \rho k}{\partial t} + \frac{\partial \rho U_j k}{\partial x_j} = \tilde{P}_{k_t} - \tilde{D}_{k_t} + \frac{\partial}{\partial x_j}\left(\left(\mu + \sigma_k \mu_t\right)\frac{\partial k}{\partial x_j}\right), \quad (3.79)$$

Table 3.2: γ-Re$_\theta$ turbulence transition model constants.

$c_{e1} = 1.0$	$c_{a1} = 2.0$	$\sigma_f = 1.0$	$\sigma_{\theta t} = 2.0$
$c_{e2} = 50$	$c_{a2} = 0.06$	$c_{\theta t} = 0.03$	$s_1 = 2.0$

$$\frac{\partial \rho\omega}{\partial t} + \frac{\partial \rho U_j \omega}{\partial x_j} = \frac{\gamma_{SST}}{\nu_t} P_{k_t} - D_\omega + \frac{\partial}{\partial x_j}\left[\left(\mu + \sigma_\omega \mu_t\right)\frac{\partial \omega}{\partial x_j}\right] + 2\rho\left(1 - F_1\right)\sigma_{\omega 2}\frac{1}{\omega}\frac{\partial k}{\partial x_j}\frac{\partial \omega}{\partial x_j}, \quad (3.80)$$

$$\tilde{P}_{k_t} = \gamma_{eff} P_{k_t}, \quad (3.81)$$

$$\tilde{D}_{k_t} = min\left(max\left(\gamma_{eff}, 0.1\right), 1.0\right) D_{k_t}. \quad (3.82)$$

In (3.81-3.82) P_{k_t} and D_{k_t} are the original production and destruction terms of the k-ω-SST turbulence closure. The turbulence transition model constants are presented in the table 3.2.

3.5 Introduction of the V-model transition closure

The V-model is not able to compute turbulence. Instead it determines the transition threshold region. For this reason, the V-model transition closure was coupled to the Spalart-Allmaras turbulence model. Transition onset prediction is performed by computing the viscosity induced by the predicted pre-transitional $\overline{u'v'}$ values described throughout this work. The modus-operandi of the V-SA model is depicted in Fig.3.2.

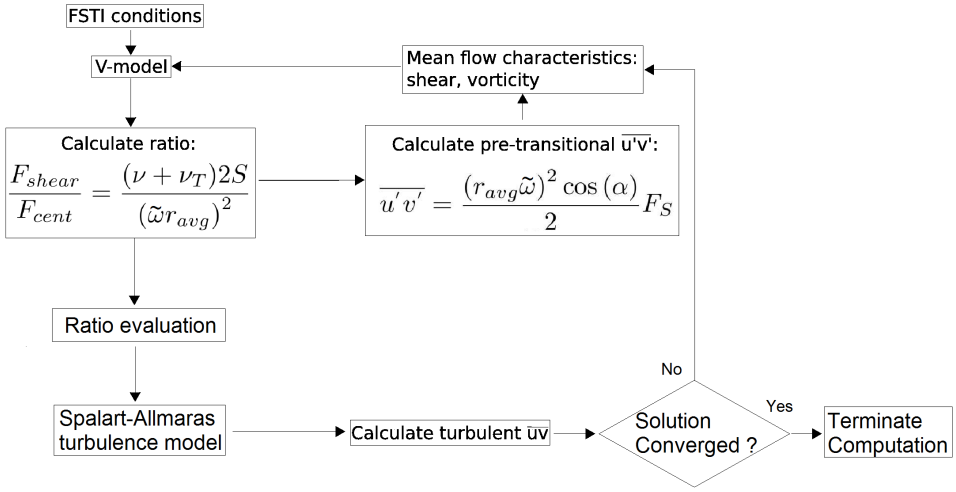

Figure 3.2: V-SA model architecture, by coupling the transition V-model to the Spalart-Allmaras turbulence model.

3.5.1 Mechanical model approximation rational

The rational behind the development of the transition V-model is herein presented, including the flow physics on which it is supported. Before the mechanical approximation disclosure, some considerations need to be taken into account and explained. It is here assumed that pre-transitional turbulence is isotropic in a strain-less free-stream, in the sense that $k_x = k_y = k_z = k_p$. This is in agreement with the flow physics of transition such as presented in the work of [97]. However, under the effect of flow shear the model will predict

small pre-transitional negative values of $\overline{u'v'}$ related to non-isotropic turbulence conditions. A bi-dimensional analysis is here described. Nevertheless, the V-model transition closure is applicable to three-dimensional cases as will be later presented. This is the case since the main three orthogonal shear deformation planes are all accounted for in the computation of the local shear magnitude. As such, a global effect of three-dimensionality is taken into account in the computation of the pre-transitional $\overline{u'v'}$.

3.5.1.1 Pre-transitional turbulent kinetic energy considerations

Pre-transition velocity fluctuations wave forms, for a specific frequency, have seldom a regular shape. Although this is true for most cases, the modeling of the pre-transition region, see works such as [60], requires both discrete and continuum modes. Citing [60], "The eigensolutions to the Orr-Sommerfeld equation in an unbounded domain are classified into two spectra: the first is a finite set of discrete modes; the second is an infinite continuum of modes. The latter are weakly damped and are irrelevant to classical linear stability analysis. Unstable modes are only members of the discrete spectrum." As previously stated, the modes used in classical linear stability analysis are the discrete spectrum components. However, the present transition model will attempt to model the effects on the continuum spectrum of modes. Citing [60], "The eigenfunction of the discrete modes decays exponentially with distance above the boundary layer. The eigenfunction of the continuous modes is sinusoidal in that region." Therefore and in order to simplify the following exposure, a sinusoidal wave shape was considered to model the free-stream pre-transition continuum spectrum. It is here assumed that sinusoidal wave forms represent the time evolution of velocity fluctuations due to pre-transitional turbulence. Admitting that a particle is stuck inside one of these special pre-transitional turbulent vortices, its movement follows that of the vortex. Considering then a cross sectional plane of the bi-dimensional vortex, the equations of motion for the particle imprisoned in the small pre-transitional vortex can be obtained. The equations of motion for $x^{'}$ and $y^{'}$ are then defined by (3.83) and (3.84) respectively. These were obtained considering as a frame of reference the center of the pre-transitional vortex itself.

$$x^{'} = -r_{avg}\cos\left(\tilde{\omega}t + \frac{\alpha}{2}\right), \quad (3.83)$$

$$y^{'} = -r_{avg}\cos\left(\tilde{\omega}t - \frac{\alpha}{2}\right). \quad (3.84)$$

The time derivative of the latter will introduce the equations of the velocity fluctuations $u^{'}$ and $v^{'}$ represented by (3.85) and (3.86).

$$u^{'} = r_{avg}\tilde{\omega}\sin\left(\tilde{\omega}t + \frac{\alpha}{2}\right), \quad (3.85)$$

$$v^{'} = r_{avg}\tilde{\omega}\sin\left(\tilde{\omega}t - \frac{\alpha}{2}\right). \quad (3.86)$$

As already mentioned, it should be noted that these last four laws of motion are deduced assuming a frame of reference of the vortex itself. From the presented equations (3.83-3.86), consideration of the α values must be taken. It can be seen that for $\alpha = \frac{\pi}{2}$ these laws of motion describe a circular motion as shown in Fig.3.3. This motion can be interpreted as a circular non-deformed pre-transitional vortex. Nonetheless, for $\alpha = \frac{\pi}{4}$ and $\alpha = \frac{3\pi}{4}$ the described

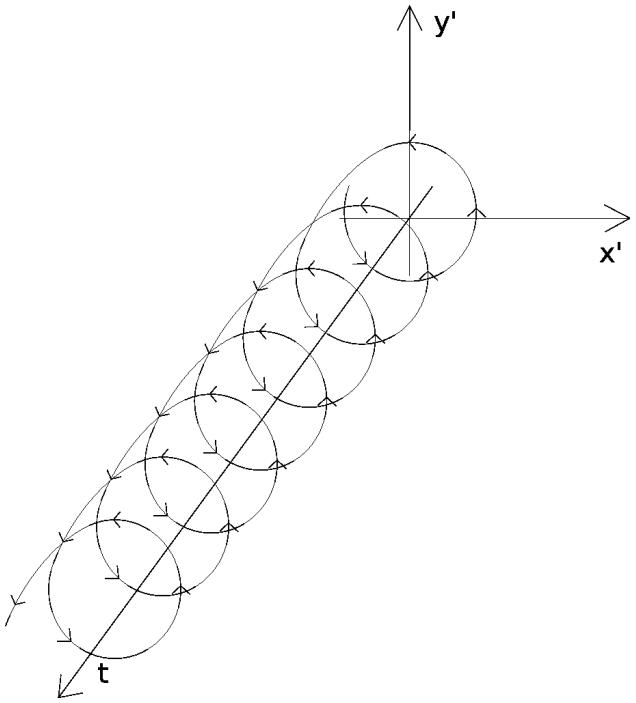

Figure 3.3: Particle trajectory describing a circular path through time.

motion will be elliptical. The limiting cases are obtained for $\alpha = 0$ and $\alpha = \pi$, where although the motion is periodical, it is also linear.

The pre-transitional vortex will have its turbulent kinetic energy. This can be related to a more simple definition of kinetic energy. In order to perform the analogy, we take another look at the clinging particle under the effect of the circular pre-transitional vortex. This circular motion analogy is considered under a bi-dimensional plane coincident with the xy Cartesian frame of reference positioned within the vortex center. Considering Fig.3.4, the animated particle in point P will have a certain amount of specific kinetic energy defined as, $e_{c_P} = U^2/2$. This same particle will have a mean turbulent kinetic energy since it follows the pre-transitional vortex rotational motion. The latter is defined as the sum of the mean turbulent kinetic energy along xx's axis and the mean turbulent kinetic energy along yy's axis. Assuming a circular vortex, and taking this into consideration, through (3.87), a relation can be obtained in order to characterize the value of rotational velocity and radius of the pre-transitional vortex. The resulting relation is then (3.88).

$$k_x + k_y = \frac{1}{2}\overline{u'u'} + \frac{1}{2}\overline{v'v'} = e_{c_P} = \frac{(\omega_z r_{avg})^2}{2}, \quad (3.87)$$

$$\sqrt{2\,(k_x + k_y)} = \omega_z r_{avg}. \quad (3.88)$$

In (3.88), ω_z represents the vortex rotational speed and r_{avg} is the average pre-transitional vortex radius in the xy cross section plane.

An equivalence of turbulent kinetic energy and kinetic energy was just performed. Besides the assumption of a circular pre-transitional vortex, up until this point no approximation has been used. However, in order to close this particular system an approximation must be performed.

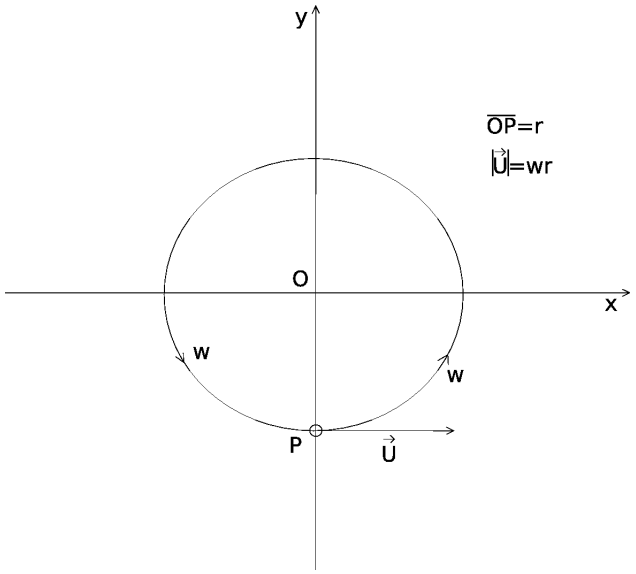

Figure 3.4: The pre-transitional turbulent vortices can be generated at the interface between the free-stream turbulence and the pre-transitional laminar boundary layer due to ”inactive motion“ [3]. It is here presented a cut-section of a circular pre-transitional vortex.

Either the average radius of the vortices is approximated or the rotational velocity of the vortices, ω_z. The approach of rotational velocity approximation was chosen. The used relation was defined on the assumption that, rotational velocity of the pre-transitional turbulent vortices should be proportional to its pre-transitional turbulent kinetic energy. Also, the rotational velocity of pre-transitional vortices should be inversely proportional to the flow kinematic viscosity. This is further related to the fact that for a fixed turbulent large scale, the small turbulence sizes, such as the Kolmogorov scales, are reduced with increasing Reynolds number flows. This scale reduction is also related to an increase of the turbulent vortices rotational velocities due to angular momentum conservation. Therefore, the lower the fluid kinematic viscosity, the higher the flow Reynolds number and consequently the higher the turbulent vortices rotational velocities. Besides this, dimensional analysis of the used relation confirms its correct dimensional characteristics. The selected approximation is then presented in (3.89).

$$\omega_z = \frac{k_x + k_y}{\nu}. \quad (3.89)$$

Throughout the remaining model exposure $\omega_z = \tilde{\omega}$. Therefore, since $k_x + k_y = 2k_p$, the value of $\tilde{\omega}$ is now computed using the relation presented in (3.90).

$$\tilde{\omega} = \frac{2k_p}{\nu}. \quad (3.90)$$

From this relation and equation (3.88), the value of r_{avg} is calculated in (3.91).

$$r_{avg} = \frac{\sqrt{4k_p}}{\tilde{\omega}}. \quad (3.91)$$

In order to compute terms such as $\overline{u'u'}$ or $\overline{u'v'}$ a time average of these fluctuating values must be performed according to equation (3.92).

$$\overline{u'u'} = \lim_{T\to\infty} \frac{1}{T} \int_0^T u'u'dt. \quad (3.92)$$

It was then assumed a sinusoidal function for these fluctuating velocities. This purports that these fluctuations have a periodicity. Therefore this implies that a finite value for T is possible. A plausible value for T could be the periodicity of these sinusoidal functions. This assumption results in (3.93).

$$\overline{u'u'} = \frac{\tilde{\omega}}{2\pi} \int_0^{\frac{2\pi}{\tilde{\omega}}} u'u'dt. \quad (3.93)$$

Using the explicit formulations of u' and v', the calculation of $\overline{u'u'}$ and $\overline{u'v'}$ should be done according to (3.94) and (3.95) respectively.

$$\overline{u'u'} = \frac{\tilde{\omega}}{2\pi} \int_0^{\frac{2\pi}{\tilde{\omega}}} \left[r_{avg}\tilde{\omega} \sin\left(\tilde{\omega}t + \frac{\alpha}{2}\right)\right]^2 dt, \quad (3.94)$$

$$\overline{u'v'} = \frac{\tilde{\omega}}{2\pi} \int_0^{\frac{2\pi}{\tilde{\omega}}} r_{avg}\tilde{\omega} \sin\left(\tilde{\omega}t + \frac{\alpha}{2}\right) r_{avg}\tilde{\omega} \sin\left(\tilde{\omega}t - \frac{\alpha}{2}\right) dt. \quad (3.95)$$

The $\overline{u'u'}$ value is directly obtained through (3.96). It can be seen that for isotropic pre-transitional turbulence, $k_x = k_y$, equation (3.96) is in accordance with the kinetic energy relations of (3.87) and (3.88).

$$\overline{u'u'} = \frac{r_{avg}^2\tilde{\omega}^2}{2}. \quad (3.96)$$

The $\overline{u'v'}$ value is then calculated using relation (3.97). It should be noted that r_{avg} is the mean radius of the undeformed pre-transitional vortex. As can be seen in (3.97), there is a dependence with α. This α represents the phase shift between the two velocity components u' and v'. It also represents the deformation angle of the pre-transitional vortex. For α equal to $\frac{\pi}{2}rad$ or 90° the pre-transitional vortex has a circular undeformed shape. Also, for this value of α, according to (3.97), the Reynolds shear stresses, $\overline{u'v'}$, will be zero for an undeformed pre-transitional vortex.

$$\overline{u'v'} = \frac{r_{avg}^2\tilde{\omega}^2\cos(\alpha)}{2}. \quad (3.97)$$

3.5.1.2 Mechanical model for pre-transitional turbulent velocity fluctuation components under mean shear

The fact that $\overline{u'v'}$ has a trend to present negative values under shear influence is commonly accepted. The reasoning begins by considering a no-slip wall constrained velocity profile. Under this scenario, a positive vertical velocity fluctuation away from the wall, such that $v' > 0$, will induce a reduction of the flow momentum. The excited particle tends to maintain its

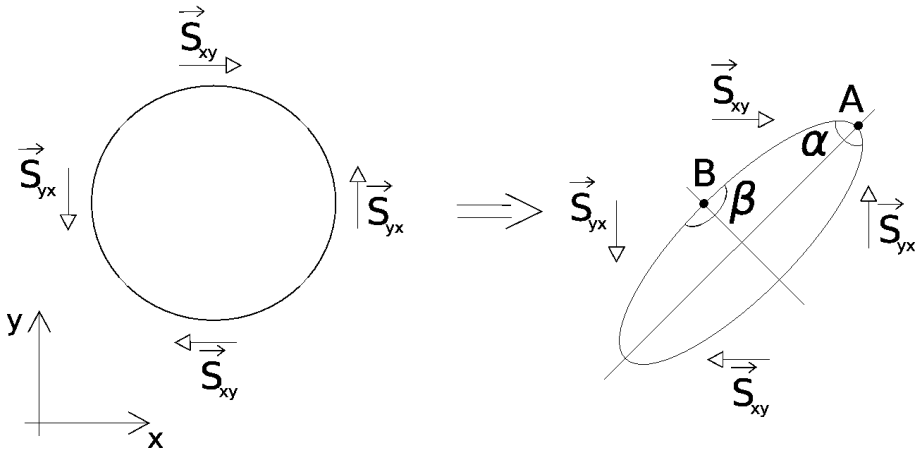

Figure 3.5: The deformation of a large scale vortical structure due to mean flow shear assumes the presented shape. Also, this is the expected pre-transitional vortex deformation shape under mean flow shear.

momentum, this is lower than the new surrounding fluid due to the presence of the wall no-slip condition. This will then imply that $u^{'} < 0$, since the relative velocity of the new low momentum fluid is lower than the surroundings. The reverse case is also applicable, that is for $v^{'} < 0$ a value of $u^{'} > 0$ will follow. Therefore $\overline{u'v'}$ has a negative value.

Consider then the case where an initially circular pre-transitional vortex is deformed by mean shear as in Fig.3.5. It must be noted that the presented schematic only demonstrates what is to be expected, not what the mechanical model predicts. Due to shear deformation, there will be an alteration of path curvature along the vortex surface. The centrifugal force distribution along the pre-transitional vortex will change accordingly. These centrifugal forces defined in (3.98), will act as pseudo non-linear springs of the pre-transitional vortex. These will act on the vortex when shear is present. The effect of the vortex deformation is reflected on the centrifugal forces computation, (3.98), through the local curvature radius, r_{local}.

$$F_{cent} = \frac{U^2 \rho V}{r_{local}}. \quad (3.98)$$

In order to compute the centrifugal forces, (3.98), the local radius of curvature, r_{local}, needs to be calculated. The change of the vortex curvature is dependent on the predicted deformation angle, α. As such, a relation between the local radius of curvature and the angle of deformation of the system is required. This relation was developed so as to deliver the requirements in,

$$\alpha = \pi \Rightarrow r_{local} = \infty, \quad (3.99)$$

$$\alpha = 0 \Rightarrow r_{local} = 0, \quad (3.100)$$

$$\alpha = \frac{\pi}{2} \Rightarrow r_{local} = r_{avg}. \quad (3.101)$$

The requirement presented in (3.99) is representative of an absolute flat vortex with orientation depicted in Fig.3.9. The following requirement in (3.100) represents the scenario of a perfectly flat vortex with orientation depicted in Fig.3.5. The final requirement in (3.101) represents the undeformed circular vortex. Also, the calculation of local radius will depend on the average

radius of the vortex and its deformation angle, α. The developed relation was then,

$$r_{local} = r_{avg}\frac{\alpha}{\pi - \alpha}. \quad (3.102)$$

This relation enforces the requirements in (3.99-3.101).
The shear force acting upon the vortex is defined in (3.103). In this equation, S, is mean flow shear magnitude. The A and V terms in both the equations (3.98) and (3.103), represent surface area and volume of the pre-transitional vortex respectively. These are defined in (3.104) and (3.105). The l is here considered as the length of the pre-transitional vortex. A value for this is not required since l will cancel itself in the upcoming model development.

$$F_{shear} = (\mu + \mu_T)SA, \quad (3.103)$$

$$A = 2\pi r_{avg} l, \quad (3.104)$$

$$V = \pi r_{avg}^2 l. \quad (3.105)$$

This non-linear spring feature of the centrifugal forces can be modeled by a relatively simple mechanical system shown in Fig.3.6. The non-linear spring mechanical behavior is given by the centrifugal force physical characteristics as disclosed in (3.98). The r_{local} represents the local curvature radius of the pre-transitional vortex. In Fig.3.6, the left picture represents the expected statistical mean shape of a pre-transitional vortex under the effect of mean flow shear. Normally the shear tensor main axes are aligned $45\ ^\circ$ with the local flow direction. The presented α and β angles in this left picture of Fig.3.6 are representative of the vortex deformation angles located in the directions of the shear stress tensor major axis and minor axis. Also, this α angle represents the phase shift in the motion equations (3.83-3.86). The right schematic in Fig.3.6, is the approximation of the continuum vortex shown in the left picture by a discrete system composed of four elements. In this schematic, the $\alpha^{'}$ and $\beta^{'}$ angles are the half values of the original α and β angles. Therefore, the angle relations in this problem are shown in (3.106) and (3.107).

$$\alpha = 2\alpha^{'}, \quad (3.106)$$

$$\beta^{'} = \frac{\pi}{2} - \alpha^{'}. \quad (3.107)$$

The solution of the mechanical dynamic problem presented in the right schematic of Fig.3.6 can be simplified by considering only one quarter of the system. This is possible due to the double symmetry along the shear stress tensor major axis and minor axis coincident with the axes of the ellipse resulting from the deformed circular pre-transitional vortex. With this in mind, the final mechanical model approximation is then shown in Fig.3.7. The presented orientation is in accordance to Fig.3.5.
The attempt to solve the mechanical system in Fig.3.7 will produce a relation between vortex deformation and mean shear. In order to solve the mechanical problem presented in Fig.3.7,

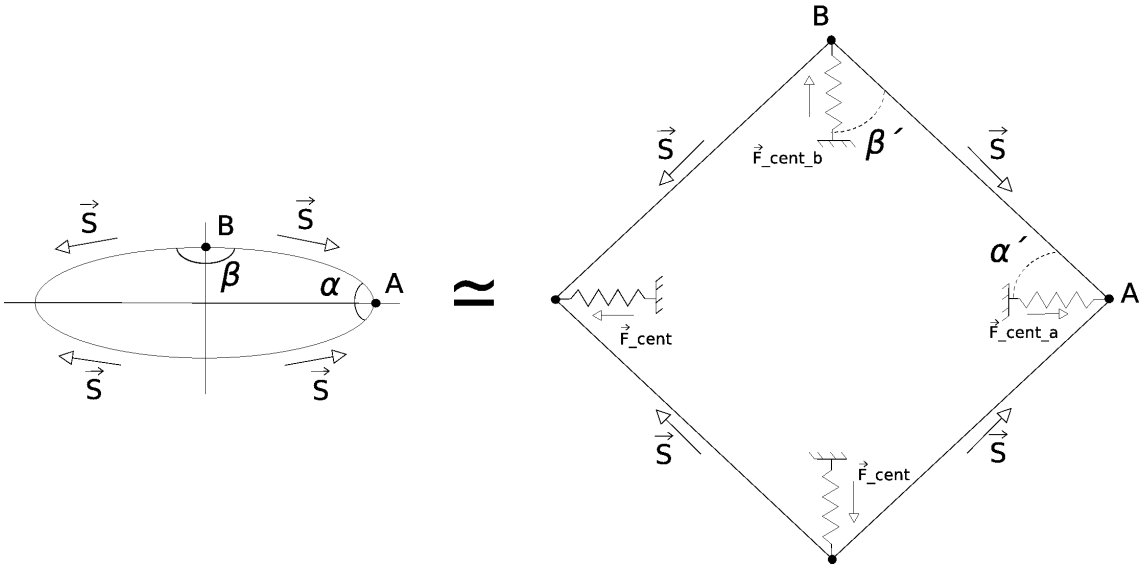

Figure 3.6: The pre-transitional boundary layer oscillations due to shear known as Klebanoff modes were first observed and named ”breathing modes“ by [4]. This behavior of the pre-transitional turbulent vortices can be accounted for by the mechanical model approximation. The depicted mechanical model approximation makes use of a fictitious non-linear spring analogy to describe the internal forces acting on the vortex.

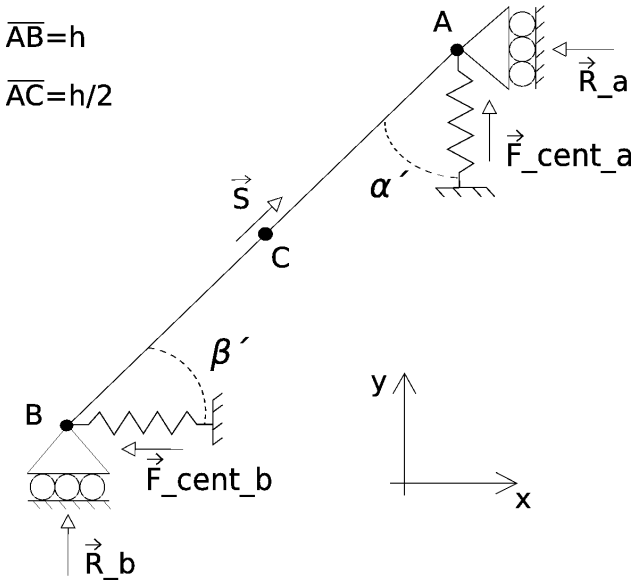

Figure 3.7: The shear force, $\vec{S}$, effect on pre-transitional eddies is approximated by this mechanical model for one quarter of a circular vortex. The mechanical approximation depicted here is applied to pre-transitional turbulent vortices in the upper zones of the laminar boundary layer.

classical mechanical system solving procedures must be taken. First an equilibrium of the system moments in relation to point "C" is in order. The resulting equation is presented in (3.108).

$$\Sigma M_C = R_A \frac{h}{2} cos(\alpha^{'}) + F_{centA} \frac{h}{2} sin(\alpha^{'}) - R_B \frac{h}{2} sin(\alpha^{'}) - F_{centB} \frac{h}{2} cos(\alpha^{'}) = 0. \quad (3.108)$$

The shear force depicted in Fig.3.7 by an $\vec{S}$, is decomposed in the x and y axes directions resulting in S_x and S_y presented in (3.109) and (3.110) respectively.

$$S_x = \vec{S} sin(\alpha^{'}), \quad (3.109)$$

$$S_y = \vec{S} cos(\alpha^{'}). \quad (3.110)$$

From this, the following required equation is the equilibrium of forces in the y axis direction. The obtained equation is disclosed in (3.111).

$$\Sigma F_y = R_B + F_{centA} + S_y = 0 \Leftrightarrow R_B = -F_{centA} - S_y. \quad (3.111)$$

The final required system equation is the x axis direction forces equilibrium equation. The resulting equation is shown in (3.112).

$$\Sigma F_x = -R_A - F_{centB} + S_x = 0 \Leftrightarrow R_A = -F_{centB} + S_x. \quad (3.112)$$

Substitution of the obtained relations (3.111) and (3.112) in the moment equilibrium equation (3.108) will result in (3.113).

$$\begin{aligned} &- F_{centB} \frac{h}{2} cos(\alpha^{'}) + S_x \frac{h}{2} cos(\alpha^{'}) + F_{centA} \frac{h}{2} sin(\alpha^{'}) \\ &+ F_{centA} \frac{h}{2} sin(\alpha^{'}) + S_y \frac{h}{2} sin(\alpha^{'}) - F_{centB} \frac{h}{2} cos(\alpha^{'}) = 0. \end{aligned} \quad (3.113)$$

From the relations (3.109) and (3.110), equation (3.113) turns to (3.114).

$$F_{centA} h sin(\alpha^{'}) - F_{centB} h cos(\alpha^{'}) + \vec{S} h sin(\alpha^{'}) cos(\alpha^{'}) = 0. \quad (3.114)$$

From this, the following step is presented in,

$$\frac{F_{centB} cos(\alpha^{'}) - F_{centA} sin(\alpha^{'})}{sin(\alpha^{'}) cos(\alpha^{'})} = \vec{S}. \quad (3.115)$$

According to equations (3.98), (3.102), (3.106) and (3.107), the centrifugal forces in points "A" and "B" are defined in,

$$F_{centA} = \frac{1}{4} \frac{U^2 \rho V}{r_{avg}} \frac{\pi - 2\alpha^{'}}{2\alpha^{'}}, \quad (3.116)$$

$$F_{centB} = \frac{1}{4} \frac{U^2 \rho V}{r_{avg}} \frac{2\alpha^{'}}{\pi - 2\alpha^{'}}. \quad (3.117)$$

The value of the shear force depicted by an $\vec{S}$ in Fig.3.7 is equal to a quarter of the total shear

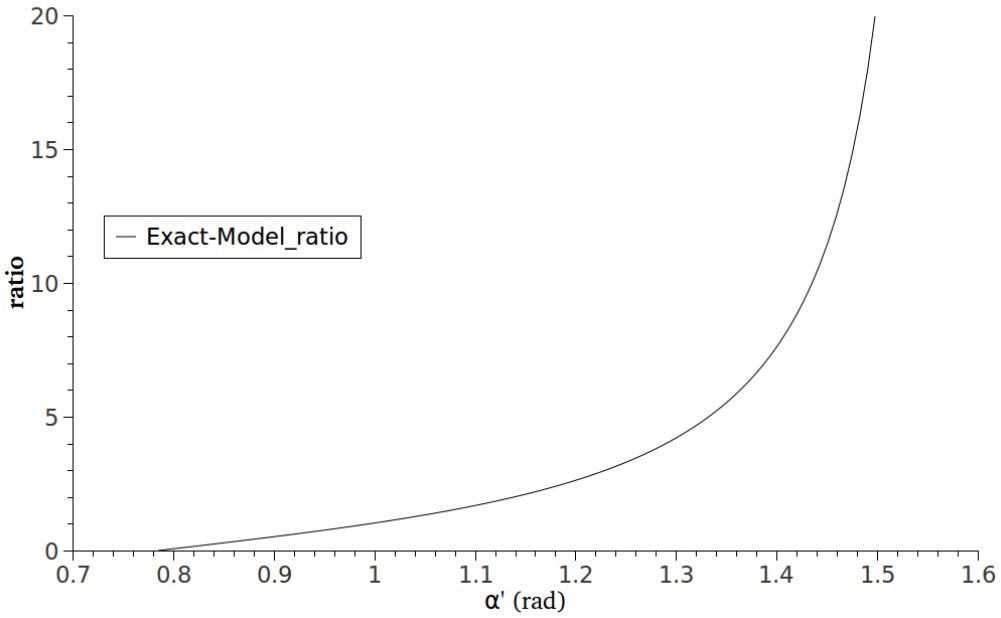

Figure 3.8: Ratio evolution with $\alpha^{'}$ according to the mechanical system solution (3.122).

force acting upon the pre-transitional vortex defined in (3.103). Therefore, $\vec{S}$ is defined in,

$$\vec{S} = \frac{1}{4}(\mu + \mu_T)SA. \quad (3.118)$$

As such, from these relations the resulting equation from (3.115) is disclose in,

$$\frac{U^2 \rho V}{r_{avg}} \left[\frac{\left(\frac{2\alpha^{'}}{\pi - 2\alpha^{'}}\right)\cos\left(\alpha^{'}\right) - \left(\frac{\pi - 2\alpha^{'}}{2\alpha^{'}}\right)\sin\left(\alpha^{'}\right)}{\sin\left(\alpha^{'}\right)\cos\left(\alpha^{'}\right)} \right] = (\mu + \mu_T)SA. \quad (3.119)$$

From the mean linear velocity of the pre-transitional vortex defined in (3.120) and from the definition of area, “A“, and volume, “V“, defined in (3.104) and (3.105) respectively, the ratio between pre-transitional vortex acting shear and centrifugal forces is given in (3.121).

$$U = \tilde{\omega} r_{avg}, \quad (3.120)$$

$$ratio = \frac{F_{shear}}{F_{cent}} = \frac{(\nu + \nu_T)2S}{\left(\tilde{\omega} r_{avg}\right)^2}. \quad (3.121)$$

The solution of this system in terms of angle $\alpha^{'}$ is then,

$$\left[\frac{\left(\frac{2\alpha^{'}}{\pi - 2\alpha^{'}}\right)\cos\left(\alpha^{'}\right) - \left(\frac{\pi - 2\alpha^{'}}{2\alpha^{'}}\right)\sin\left(\alpha^{'}\right)}{\sin\left(\alpha^{'}\right)\cos\left(\alpha^{'}\right)} \right] = ratio. \quad (3.122)$$

The evolution of ratio to $\alpha^{'}$ of the exact solution (3.122) is presented in Fig.3.8. According to relation (3.122) and observing Fig.3.8, an unexpected evolution of the angle $\alpha^{'}$ is predicted by the mechanical model. Based on (3.122), this solution of the mechanical model approximation

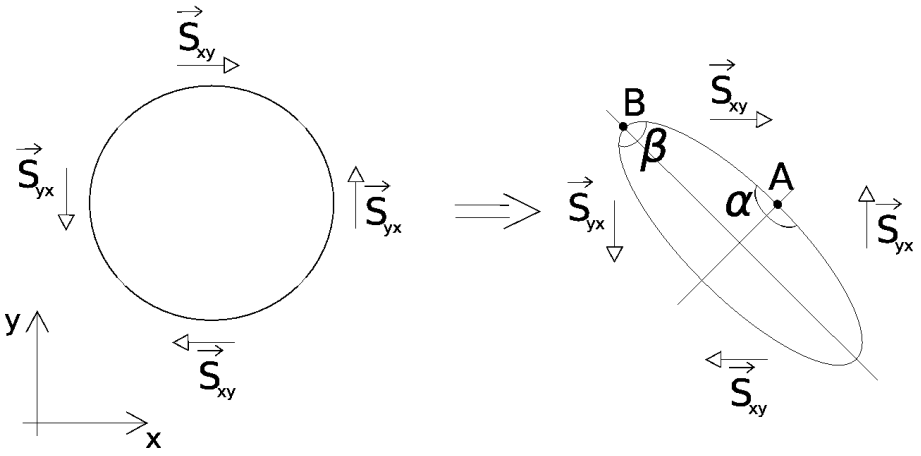

Figure 3.9: The derived relation (3.122) for computation of the $\alpha^{'}$ deformation angle is used to calculate the α deformation angle through (3.106). The former relation predicts an α angle increase with shear, instead of the expected angle decrease as depicted in Fig.3.5. As the mean flow shear increases so does the ratio calculated according to (3.121). The predicted pre-transitional vortex deformation under mean flow shear is presented here.

used in this work predicted an increase of the angle $\alpha^{'}$ with increasing shear. This in turn means that according to (3.97) and (3.106), the calculated values of $\overline{u^{'}v^{'}}$ will be negative. The α angle increases from $\frac{\pi}{2}$ to its limiting value π. This also signifies that the correct pre-transitional vortex shape under the effect of shear is the one presented in Fig 3.9. Since the relation (3.122) is far too complex to be use in a numerical transition closure, a simpler function is used instead. The used function is a good approximation of the exact relation and is presented in,

$$tan\left[1.8\left(\alpha^{'}-\frac{\pi}{4}\right)^{0.7}\right]=ratio. \quad \text{(3.123)}$$

The used mechanical approximation function in the transition V-model numerical implementation is here presented in (3.124). This is done in order to simplify implementation attempts by the reader.

$$\alpha^{'}=min\left[\left(\frac{tan^{-1}\left(ratio\right)}{1.8}\right)^{1.42857}+\frac{\pi}{4},\frac{\pi}{2}\right]. \quad \text{(3.124)}$$

In (3.124), the minimum function is applied since the maximum value of $\alpha^{'}$ is $\frac{\pi}{2}$. This correspond to a perfectly flat pre-transitional vortex deformation angle. For values of $ratio=0$ the minimum value of $\alpha^{'}$ is $\frac{\pi}{4}$. This represents an undeformed circular pre-transitional vortex.

3.5.2 The transition V-model transport equation

The Reynolds stress transport equations were first closed by [33], setting the foundations for second order turbulence models. The transport equations are here presented in (3.125) as presented by [77].

$$\frac{\partial\tau_{ij}}{\partial t}+U_k\frac{\partial\tau_{ij}}{\partial x_k}=-\tau_{ik}\frac{\partial U_j}{\partial x_k}-\tau_{jk}\frac{\partial U_i}{\partial x_k}+\varepsilon_{ij}-\Pi_{ij}+\frac{\partial}{\partial x_k}\left[\nu\frac{\partial\tau_{ij}}{\partial x_k}+C_{ijk}\right], \quad \text{(3.125)}$$

$$\varepsilon_{ij} = \overline{2\mu \frac{\partial u_i^{'}}{\partial x_k} \frac{\partial u_j^{'}}{\partial x_k}}, \quad (3.126)$$

$$\Pi_{ij} = \overline{p^{'} \left(\frac{\partial u_i^{'}}{\partial x_j} + \frac{\partial u_j^{'}}{\partial x_i} \right)}, \quad (3.127)$$

$$C_{ijk} = \overline{\rho u_i^{'} u_j^{'} u_k^{'}} + \overline{p^{'} u_i^{'}} \delta_{jk} + \overline{p^{'} u_j^{'}} \delta_{ik}. \quad (3.128)$$

In (3.125), $\tau_{ij} = -\overline{\rho u_i^{'} u_j^{'}}$, represents the Reynolds stress tensor. The presented terms on the right hand side of (3.125), are from left to right, two terms of production, one for turbulent dissipation presented in (3.126), another for pressure-strain shown in (3.127) and finally the molecular and turbulent diffusion. This last term is presented in (3.128). Considering the normal Reynolds stresses transport equations, that is, the trace components of the stress tensor, the number of terms is reduced resulting in (3.129). Through the condition imposed by the equation of continuity applied to turbulent velocity fluctuations the pressure-strain term is null.

$$\frac{\partial \tau_{ii}}{\partial t} + U_k \frac{\partial \tau_{ii}}{\partial x_k} = -2\tau_{ik} \frac{\partial U_i}{\partial x_k} + \overline{2\mu \frac{\partial u_i^{'}}{\partial x_k} \frac{\partial u_i^{'}}{\partial x_k}} + \frac{\partial}{\partial x_k} \left[\nu \frac{\partial \tau_{ii}}{\partial x_k} + \overline{\rho u_i^{'} u_i^{'} u_k^{'}} + 2\overline{p^{'} u_i^{'}} \delta_{ik} \right]. \quad (3.129)$$

Since $k = \frac{1}{2}\overline{u_i^{'} u_i^{'}}$, considering then the relation that, $\tau_{ii} = -2\rho k$, we obtain the following transport equation for turbulent kinetic energy in (3.130).

$$\frac{\partial k}{\partial t} + U_k \frac{\partial k}{\partial x_k} = -\overline{u_i^{'} u_k^{'}} \frac{\partial U_i}{\partial x_k} - \overline{\nu \frac{\partial u_i^{'}}{\partial x_k} \frac{\partial u_i^{'}}{\partial x_k}} + \frac{\partial}{\partial x_k} \left[\nu \frac{\partial k}{\partial x_k} - \frac{1}{2}\overline{\rho u_i^{'} u_i^{'} u_k^{'}} - \overline{p^{'} u_i^{'}} \delta_{ik} \right]. \quad (3.130)$$

The proposed transition model pre-transition turbulent kinetic energy transport equation components are based on some terms of equation (3.130). The transition closure production term was obtained by analyzing the first term in (3.130). This analysis will be performed considering a flat-plate flow far from its leading edge region. Within the shear region of the flow, $\overline{u_1^{'} u_2^{'}}$ or, $\overline{u^{'} v^{'}}$, will be negative. The shear value of $\partial U_1 / \partial x_2$ will be positive. Thus, this term is a production term in mean flow shear conditions. The mean flow shear magnitude, S, is used as the mean flow property that drives pre-transitional turbulence production. It must be noted that for clarity reasons, a term was omitted in the previously presented $\overline{u^{'} v^{'}}$ calculation in (3.97). The term is a function responsible for the evaluation of the mean flow and turbulent scales proximity, F_S. This is defined in (3.131).

$$F_S = 1 - min \left(mag \left(\frac{S_{size} - r_{avg}}{max\left(S_{size}, r_{avg}\right)} \right), 1 \right). \quad (3.131)$$

The used mean flow shear scale function, S_{size}, is defined in (3.132).

$$S_{size} = \sqrt{\frac{\nu}{S}}. \quad (3.132)$$

The $\overline{u'v'}$ computation is then performed according to,

$$\overline{u'v'} = \frac{(r_{avg}\tilde{\omega})^2 \cos(\alpha)}{2} F_S. \quad (3.133)$$

The production term used is presented in,

$$Prod_{k_p} = -C_{P_k} S \overline{u'v'}. \quad (3.134)$$

In this equation, C_{P_k} is the V-model calibration constant equal to 0.8335. The C_{P_k} calibration constant was obtained by considering the experimental validation with the ERCOFTAC zero-pressure-gradient flat-plate test case T3A.

The second term on the RHS of (3.130) will be used to obtain the dissipation term of the presented transition model transport equation. The calculation of the cross partial derivatives from this term reveals a fundamental result. In order to simplify the partial derivatives calculation, the following assumption is required. The definitions in equations (3.83) and (3.84) impose a phase shift between $x^{'}$ and $y^{'}$. For an undeformed pre-transitional vortex, implying $\alpha = \frac{\pi}{2}$, and summing a phase shift value of $\frac{\pi}{4}$ to both equations, (3.83) and (3.84), we obtain the same phase shift imposition through (3.137) and (3.138) respectively. A detailed explanation of the process is presented in (3.135) and (3.136).

$$x^{'} = -r_{avg} \cos\left(\tilde{\omega}t + \frac{\frac{\pi}{2}}{2} + \frac{\pi}{4}\right) = r_{avg} \sin(\tilde{\omega}t), \quad (3.135)$$

$$y^{'} = -r_{avg} \cos\left(\tilde{\omega}t - \frac{\frac{\pi}{2}}{2} + \frac{\pi}{4}\right) = -r_{avg} \cos(\tilde{\omega}t), \quad (3.136)$$

$$x^{'} = r_{avg} \sin(\tilde{\omega}t), \quad (3.137)$$

$$y^{'} = -r_{avg} \cos(\tilde{\omega}t). \quad (3.138)$$

The new velocity fluctuations $u^{'}$ and $v^{'}$ are then represented by (3.139) and (3.140) respectively.

$$u^{'} = r_{avg}\tilde{\omega} \cos(\tilde{\omega}t), \quad (3.139)$$

$$v^{'} = r_{avg}\tilde{\omega} \sin(\tilde{\omega}t). \quad (3.140)$$

Considering then a cross partial derivative where the length scale of ∂y is comparable to the length scale of $\partial y^{'}$ resulting in,

$$\frac{\partial u^{'}}{\partial y} \approx \frac{\partial u^{'}}{\partial y^{'}} = \frac{\partial r_{avg}\tilde{\omega} \cos(\tilde{\omega}t)}{\partial y^{'}}. \quad (3.141)$$

It can be observed that apparently the latter partial derivative can not be easily solved. How-

ever, the $\tilde{\omega}t$ dependence can be written as,

$$y^{'} = -r_{avg}\cos\left(\tilde{\omega}t\right) \Leftrightarrow \tilde{\omega}t = arcos\left(\frac{-y^{'}}{r_{avg}}\right). \quad (3.142)$$

By doing so the cross partial derivative becomes then,

$$\frac{\partial u^{'}}{\partial y^{'}} = \frac{\partial r_{avg}\tilde{\omega}\cos\left(arcos\left(\frac{-y^{'}}{r_{avg}}\right)\right)}{\partial y^{'}} = \frac{\partial \tilde{\omega} r_{avg}\frac{-y^{'}}{r_{avg}}}{\partial y^{'}}. \quad (3.143)$$

The resulting cross partial derivative is presented in (3.144).

$$\frac{\partial u^{'}}{\partial y^{'}} = -\frac{\partial \tilde{\omega} y^{'}}{\partial y^{'}} = -\tilde{\omega}. \quad (3.144)$$

Therefore the cross partial derivative of the dissipation term (3.126) is equal to a form of rotational velocity of the undeformed pre-transitional turbulent vortices, $\tilde{\omega}$. It must be noted that due to the assumption of $\partial y \approx \partial y^{'}$, a scale proximity between turbulent and mean flow must exist. The non-cross partial derivatives of (3.126) were not considered. The resulting dissipation term in the V-model transport equation is then presented in (3.145). It must be noted that although the cross partial derivative, (3.144), of the dissipation term, (3.126), has a negative sign, the dissipation term makes use of the square of this cross partial derivative.

$$Dest_{k_p} = \nu\Omega^2 F_\Omega \approx \nu\overline{\frac{\partial u_i^{'}}{\partial x_k}\frac{\partial u_i^{'}}{\partial x_k}}. \quad (3.145)$$

Similar to the used "shear-sheltering" effect function presented in the work of [110], mean flow vorticity, Ω, is used as a form of rotational velocity instead of the pre-transitional vortex rotational speed, $\tilde{\omega}$, for the destruction effect within the boundary layer. Citing from the work of [110], "Shear-sheltering refers to the damping of turbulence dynamics that occurs in thin regions of high vorticity...". This is also done in order to allow the mean flow characteristics to control transition onset as depicted in Fig.3.2. Also, mean flow vorticity can be related to stabilization effects of turbulence, which can be interpreted as a turbulence sink. Such can be observed in relaminarization experiments of turbulent flow inside tube coils as presented by the work of [156]. This was also calculated with DNS [157]. The F_Ω function assures the aforementioned assumption of $\partial y \approx \partial y^{'}$. F_Ω can also be interpreted as a measure of the mean and turbulent flow scale proximity. This is defined in (3.146).

$$F_\Omega = 1 - min\left(mag\left(\frac{\Omega_{size} - r_{avg}}{max\left(\Omega_{size}, r_{avg}\right)}\right), 1\right). \quad (3.146)$$

The used mean flow vorticity scale function, Ω_{size}, is defined in (3.147).

$$\Omega_{size} = \sqrt{\frac{\nu}{\Omega}}. \quad (3.147)$$

The turbulent diffusion component of the transport equation was chosen to be equal to a common turbulent kinetic energy transport equation such as the model of [80]. The resulting pre-transitional turbulent kinetic energy transport equation is then presented in,

$$\frac{Dk_p}{Dt} = Prod_{k_p} - Dest_{k_p} + \frac{\partial}{\partial x_j}\left[\left(\nu + \nu_T\right)\frac{\partial k_p}{\partial x_j}\right]. \quad (3.148)$$

From the transition V-model, the pre-transition turbulent kinetic energy will apply an induced viscosity defined in (3.149).

$$\nu_{Tuv} = \frac{-\overline{u'v'}}{mag\left(\nabla U\right)}. \quad (3.149)$$

This will then be the small effect of the pre-transitional turbulent kinetic energy on the viscosity within the pre-transitional region of the laminar boundary layer.

3.5.3 Coupling of the transition V-model to Spalart-Allmaras turbulence closure

The Spalart-Allmaras is a well known one-equation turbulence model. It was first presented by [158]. As stated before, the transition V-model was coupled to the Spalart-Allmaras turbulence closure version presented in [159]. This was performed by simply adding a control function in the production term of the turbulence model. This control function depends upon the ratio value obtained by the mechanical model approximation in (3.121). The performed implementation is shown in (3.150).

$$\begin{aligned}\frac{D\tilde{\nu_T}}{Dt} &= C_{b1}\tilde{S}\tilde{\nu_T}exp\left(-C_{\tilde{\nu_T}}ratio\right) - C_{w1}f_w\left(\frac{\tilde{\nu_T}}{y}\right)^2 \\ &+ \frac{\partial}{\partial x_j}\left[\left(\frac{\tilde{\nu_T}+\nu}{\sigma}\right)\frac{\partial\tilde{\nu_T}}{\partial x_j}\right] + \frac{C_{b2}}{\sigma}\frac{\partial\tilde{\nu_T}}{\partial x_i}\frac{\partial\tilde{\nu_T}}{\partial x_i}. \quad (3.150)\end{aligned}$$

As can be seen in the first component of the RHS of (3.150), the control function is an exponential term. The $C_{\tilde{\nu_T}}$ constant is equal to 0.5. Also in order to account for the effect of the pre-transitional viscosity, (3.149), the Spalart-Allmaras turbulence model production term is slightly changed to,

$$\tilde{S} = \frac{\Omega}{\sqrt{2}} + \frac{\tilde{\nu_T}}{\left(\kappa y\right)^2}f_{v2}. \quad (3.151)$$

The total turbulent viscosity that the V-SA transition model predicts is a sum of the obtained turbulent viscosity from the SA model and the transition V-model. This is presented in (3.152).

$$\nu_T = \nu_{Tuv} + f_{v1}\tilde{\nu_T}. \quad (3.152)$$

3.5.4 Fine tuning the V-SA transition model

Due to the model initial validation, some issues were encountered related to calibration of the V-SA model. Also, under separation induced transition conditions the model presented transition onset delays. As such, a separation correction for the model was devised. This is presented in (3.153).

$$Sep_{Correct} = exp\left(-max\left(C_{sep}\left(\frac{\Omega - S}{\tilde{\omega}}\right), 0\right)\right). \quad (3.153)$$

The proposed correction is based on the observation that the main flow region where the pre-transitional turbulent kinetic energy is excessively destroyed is on vorticity dominated flows. Therefore, the use of an exponential function with negative dependency on the subtraction of the mean flow vorticity field by the mean flow shear value ensures that for flow regions with

vorticity dominating effects, the destruction term will be diminished. This separation correction will force the destruction term, (3.145), to be almost zero if the vorticity field is very intense. The applied maximum function imposes that for low vorticity flows, where the main strain feature is pure shear, the correction function will not affect the destruction term. This is the case since the subtraction result will be negative. The correction function is then applied to the destruction term in the V-model transport equation. This results in equation (3.154).

$$\frac{Dk_p}{Dt} = Prod_{k_p} - Dest_{k_p} Sep_{Correct} + \frac{\partial}{\partial x_j}\left[(\nu + \nu_T)\frac{\partial k_p}{\partial x_j}\right]. \quad (3.154)$$

The constant C_{sep} within equation (3.153) has a value of 10. The C_{sep} calibration constant was obtained by considering the experimental A-airfoil validation and the ERCOFTAC zero-pressure-gradient flat-plate test case T3A.

Afterwards, further validation with airfoils and wings exposed a critical flaw of the separation corrected transition model, the V-SA-Sep-Correct. This model version presented an abnormal behavior on the fully turbulent flow region. Under adverse-pressure-gradient conditions, the turbulent boundary layer would prematurely separate. This would not be of concern if the base turbulence closure, that is the Spalart-Allmaras model, also computed flow separation at the same critical regions. However, the turbulence model did not behave as such.

As previously stated, the V-SA turbulence transition model is composed of the transition V-model and the Spalart-Allmaras turbulence closure. The applied Spalart-Allmaras turbulence model is not the standard version on [158]. Instead, the initially implemented turbulence closure version was the one published on [159]. This was the case due to the fact that the V-SA model, being developed on OpenFOAM, used the available Spalart-Allmaras implementation. Also, the original coupling between the transition V-model and the turbulence closure was straightforward. This focused solely on the production term of the turbulence model as shown in (3.150).

The V-SA-Sep-Correct model improvement starts by reconsidering the coupling between its two components. A more dynamic linkage is implemented according to the recommendations on [158]. The resulting model coupling is disclosed in (3.155).

$$\begin{aligned}\frac{D\tilde{\nu_T}}{Dt} = {} & C_{b1}\tilde{S}\tilde{\nu_T}C_t exp\left(-ratio\right) - \left[C_{w1}f_w - \left\{1 - C_t exp\left(-ratio\right)\right\}\frac{C_{b1}}{\kappa^2}f_w\right]\left(\frac{\tilde{\nu_T}}{d}\right)^2 \\ & + \frac{\partial}{\partial x_j}\left[\left(\frac{\tilde{\nu_T} + \nu}{\sigma}\right)\frac{\partial \tilde{\nu_T}}{\partial x_j}\right] + \frac{C_{b2}}{\sigma}\frac{\partial \tilde{\nu_T}}{\partial x_i}\frac{\partial \tilde{\nu_T}}{\partial x_i}. \end{aligned} \quad (3.155)$$

The C_t constant is equal to 1.1 and the original $C_{\tilde{\nu_T}}$ constant is removed. Further, the proposed coupling takes into consideration not only the production term of the Spalart-Allmaras model, but also its destruction element. Along with this modification, the production term of the turbulence model is changed to the following form in (3.156).

$$\tilde{S} = \Omega + \frac{\tilde{\nu_T}}{\left(\kappa d\right)^2} f_{v2}. \quad (3.156)$$

Additionally the f_{v2} function is modified to its original form in [158]. The altered formulation is disclosed in (3.157).

$$f_{v2} = 1 - \frac{\chi}{1 + \chi f_{v1}}. \quad (3.157)$$

Finally the last modification is done on the V-SA model pre-transitional turbulent kinetic energy,

k_p, transport equation, (3.154). Its production constant in (3.134), C_{Pk}, is changed from its original 0.8335 value to 0.83. The final C_{Pk} calibration constant was obtained by considering the experimental T3A test case validation of the ERCOFTAC zero-pressure-gradient flat-plate benchmark.

Chapter 4

ERCOFTAC benchmark

The ERCOFTAC, or European Research Community on Flow, Turbulence and Combustion, has a large data set on transition threshold experimental test cases along with many other experiments related to turbulence. The flat-plate benchmark cases were chosen for the validation of the developed turbulence transition models due to their availability, data information depth and simple implementation.

4.1 Flat-plate test cases

During the transition model's development stage, experimental bi-dimensional test cases were used. These were selected because of computational simplicity and fast convergence. Some of these cases are geometrically simple, such as the zero-pressure-gradient flat-plate ERCOFTAC T3A, T3A- and T3B cases. However, the pressure-gradient flat-plate ERCOFTAC T3C test cases have a more complex geometry. This is due to the required flow acceleration. The top surface of the pressure-gradient flat-plate test cases, is shaped in order to reproduce the experimental acceleration and deceleration rates. Finally the T3L separation induced transition flat-plate test cases were considered. These test cases have a similar geometry to the zero-pressure-gradient flat-plate case. Yet, these have a larger leading edge radius to induce flow separation.

All of the obtained results for the Spalart-Allmaras turbulence model, henceforward designated as SA, the V-SA transition closure versions, the originally implemented and the modified versions of the k-k$_l$-ω transition model, herein referred to as k-k$_l$-ω-org and k-k$_l$-ω-mod respectively, were computed using the open-source software OpenFoam. The considered cases were all steady-state and incompressible. These were performed with a constant density of $\rho = 1.2\,(kg/m^3)$. The results calculated with OpenFoam were run with a pressure based solver SIMPLE, linear discretization for Laplacian terms and second order linear-upwind stabilized transport, or LUST, discretization scheme for divergence terms. All of the obtained results with the empirical transition model γ-$R_{e\theta}$ and the phenomenological k-k$_l$-ω model were computed using Ansys Fluent 13.0. The used discretization scheme was the second order upwind, SOU, and for pressure the linear setting was applied. Unless stated otherwise, the presented numerical cases make use of an air kinematic viscosity of $\nu = 1.5 \times 10^{-5}\,(m^2/s)$.

The V-SA turbulence transition model applied to the tested cases has two calibrations. These are performed based upon the experimental transition onset data from the ERCOFTAC T3A test case and the computational flat-plate geometry with the corresponding leading edge radius size. Therefore, for flat-plate cases using a leading edge radius of 0.002 meters, the applied V-SA closure was calibrated using the computational flat-plate geometry with a leading edge radius size of 0.002 meters. Subsequently, test cases using a flat-plate geometry with a leading edge radius of 0.00075 meters, will have a V-SA transition model calibrated with the transition threshold data from the ERCOFTAC T3A test case using a computational flat-plate geometry with a leading edge radius size of 0.00075 meters. It should be noted that, although

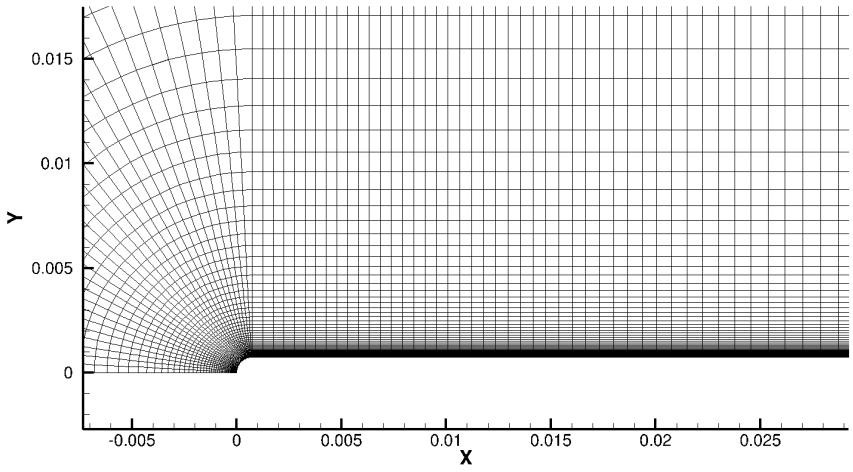

Figure 4.1: Zero-pressure-gradient flat-plate leading edge mesh view.

the experimental ERCOFTAC flat-plate geometry had a leading edge radius of 0.00075 meters, the analysis of the leading edge radius effect on the V-SA transition models calibration, the developed k-k$_l$-ω-mod transition closure and the existing k-k$_l$-ω and γ-$R_{e\theta}$ transition models, was considered to be pertinent. However, the original k-k$_l$-ω implementation on OpenFoam, the k-k$_l$-ω-org, is only evaluated on the flat-plate geometries with a leading edge radius of 0.00075 meters and on the separation flat-plate test cases.

The previously proposed corrections in section, "Fine tuning the V-SA transition model", were only applied to the V-SA transition model calibrated with the ERCOFTAC T3A flat-plate test case using a geometry with leading edge radius of 0.00075 meters. As such, the flat-plate results obtained for the leading edge radius size of 0.002 meters will not include results from the separation corrected V-SA transition model herein defined as V-SA-Sep-Correct. This also applies for the second correction implemented on the V-SA model. Using the V-SA-Sep-Correct closure as the base model, the correction was focused on the coupling between the transition V-model and the SA turbulence closure. The resulting model is then the improved V-SA transition closure henceforward designated as V-SA-Improved.

4.1.1 Zero-Pressure-Gradient test cases

The experimental values from Coupland [160], obtained for a flat-plate under zero-pressure-gradient were considered in this validation study. As already mentioned, the present geometry is simple. For the zero-pressure-gradient test case the flat-plate mesh used was structured and had y^+ values below 0.1. It is constituted by a flat-plate with 1.7 meters of extension with 200 mesh points over its surface. The flat-plate leading edge has a circular shape. The leading edge radius can vary from 0.00075 to 0.002 meters. This is done so as to show the effect of the leading edge radius on the overall results. Along the circular leading edge the geometry has 30 mesh points. A detail view of the zero-pressure-gradient flat-plate leading edge mesh is shown in Fig.4.1. The wall perpendicular spacing of the first layer of cells over the flat-plate is 1×10^{-5} meters. The top surface of the geometry is located at approximately 0.15 meters above the flat-plate. This vertical length has 110 mesh points along it. The inlet is positioned 0.15 meters before the flat-plate leading edge. It has a height of 0.15 meters. The bottom surface

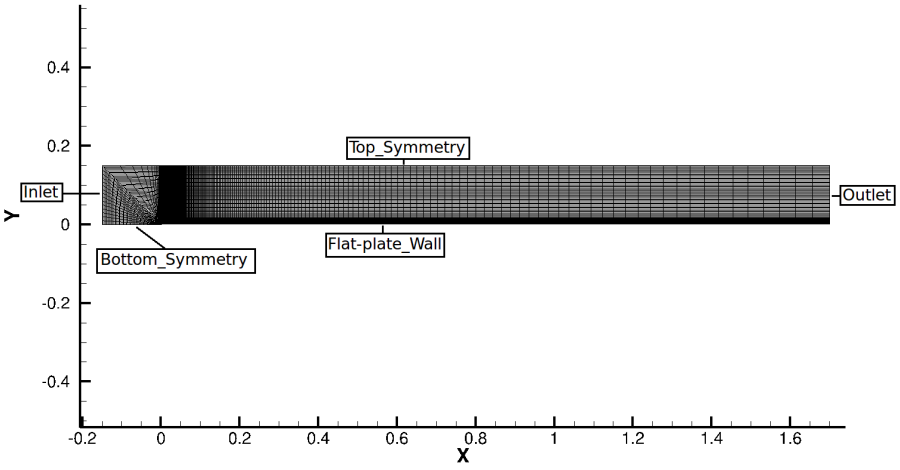

Figure 4.2: General overview of zero-pressure-gradient flat-plate mesh with 25000 nodes.

Table 4.1: ERCOFTAC Zero-Pressure-Gradient Flat-Plate Upstream Conditions

$Case$	$Tu(\%)$	$U(m/s)$
$T3A$	3.0	5.4
$T3B$	6.0	9.4
$T3A-$	0.9	19.8

upstream of the flat-plate leading-edge, will be considered as a symmetry boundary condition. This is done in order to generate a natural stagnation region as well as a correct initial boundary layer development [110]. This short extension has 110 mesh nodes. The top surface has also a symmetry boundary condition [104] [110] and [132]. The zero-pressure-gradient flat-plate geometry mesh is disclosed in Fig.4.2.

The outlet surface of the geometry has a Neumann boundary condition of $\frac{\partial x}{\partial \eta} = 0$, where x represents any flow variable except for fluid static pressure. For the latter flow variable, the outlet surface has a Dirichlet boundary condition. The flat-plate and leading edge radius are assigned with no-slip wall conditions. As such, for all tested turbulence and transition models a first type boundary condition was applied to the turbulent kinetic energy $k = 0$, the pre-transitional turbulent kinetic energy $k_p = 0$, the laminar kinetic energy $k_l = 0$ and the modified turbulent viscosity $\tilde{\nu_t} = 0$. The wall boundary condition for the specific turbulent kinetic energy dissipation rate is equal to a second type boundary condition for the k-k$_l$-ω phenomenological model of Walters [110], the original implementation in OpenFoam, k-k$_l$-ω-org, and its modified version the k-k$_l$-ω-mod. For the empirically correlated transition model, γ-$R_{e\theta}$, coupled to the k-ω-SST turbulence model, this same variable has a wall function as reported by Menter [129].

According to the ERCOFTAC database, the upstream flow conditions for the zero-pressure-gradient test cases are presented in table 4.1.

4.1.1.1 T3A flat-plate validation

The first flat-plate zero-pressure-gradient transition test case considered was the ERCOFTAC T3A case. This case was designed to evaluate bypass transition type. The used inlet boundary conditions for all tested transition and turbulence models are presented in table 4.2. It must

Table 4.2: ERCOFTAC T3A Flat-plate Inlet Boundary Conditions

Model	$U(m/s)$	$k(m^2/s^2)$	$k_p(m^2/s^2)$	$\omega(s^{-1})$	$\tilde{\nu_t}(m^2/s)$
SA	5.4	N/A	N/A	N/A	4.5×10^{-5}
V-SA	5.4	N/A	0.03936	N/A	4.5×10^{-5}
V-SA-Sep-Correct	5.4	N/A	0.03936	N/A	4.5×10^{-5}
V-SA-Improved	5.4	N/A	0.03936	N/A	4.5×10^{-5}
k-k_l-ω-org	5.4	0.12	N/A	65	N/A
k-k_l-ω-mod	5.4	0.12	N/A	65	N/A
k-k_l-ω	5.4	0.12	N/A	65	N/A
γ-Re_θ	5.4	0.12	N/A	700	N/A

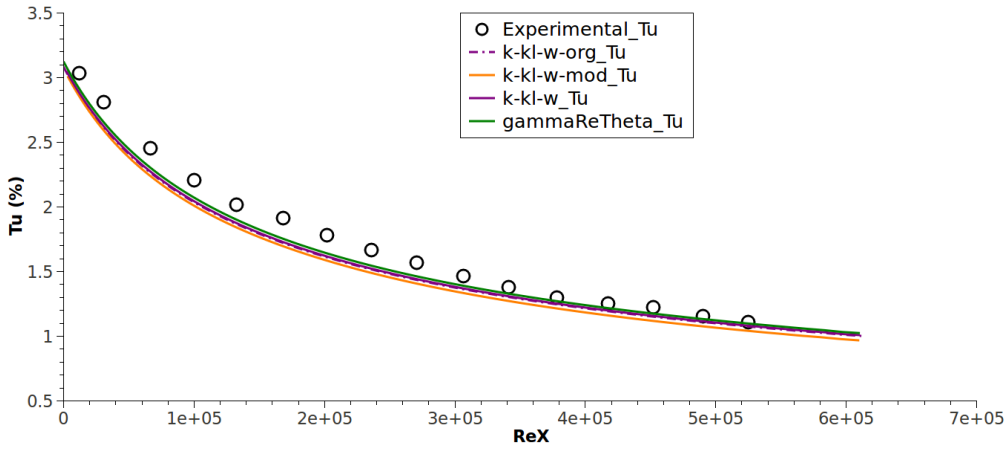

Figure 4.3: Flat-plate T3A turbulence intensity decay.

be noted that, although not referenced in this table, the used inlet boundary conditions for the V-SA-Fluent-Implementation were the same as the V-SA transition models. This transition model implementation is only evaluated on flat-plate test cases with leading edge radius size of 0.00075 meters and on the T3L separation induced transition flat-plate cases. This is the case for all of the following disclosed results.

The analysis of the free-stream turbulence intensity decay rate is vital for turbulence transition models such as k-k_l-ω, k-k_l-ω-org, k-k_l-ω-mod, and γ-Re_θ. This is so, since it is a method to analyze the free-stream turbulence characteristics such as the turbulent kinetic energy and its length scale. The free-stream turbulence intensity decay rate is shown in Fig.4.3. As can be seen, the imposed inlet boundary conditions allow a correct free-stream turbulence decay. The V-SA closures and the SA model do not require such validation. The SA model does not make use of a transport equation for turbulent kinetic energy nor its specific dissipation rate. The V-SA models, although having a transport equation for pre-transitional turbulent kinetic energy, this is not allowed to decay in the free-stream. Specification of the correct leading edge turbulence intensity and modified turbulent viscosity, $\tilde{\nu_t}$, will suffice for the correct behavior of these turbulence transition models.

The skin-friction coefficient along the flat-plate is presented in Fig.4.4. The presented results were obtained for the flat-plate with leading edge radius of 0.002 meters. The k-k_l-ω-mod, k-k_l-ω and γ-Re_θ transition models predict a slightly earlier transition onset compared to the experimental data. This behavior is believed to be related to the leading edge radius size. The V-SA model was calibrated using the transition onset point of this same case for this leading edge radius size. As such, it is to be expected that the model is able to predict the transition

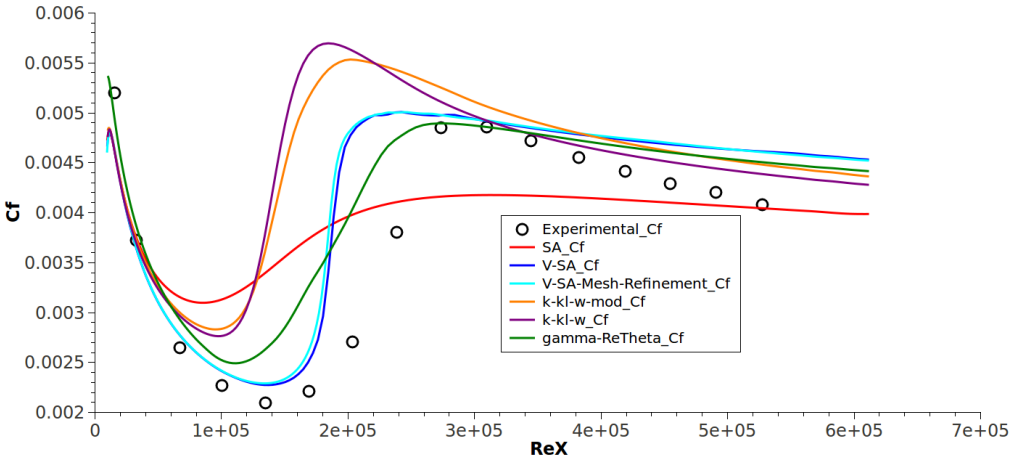

Figure 4.4: Comparison of experimental data from ERCOFTAC T3A flat-plate test case skin-friction coefficient distribution with the turbulence SA closure and the transition V-SA, k-k$_l$-ω-mod, k-k$_l$-ω and γ-Re_θ models. The used structured computational light and refined grids for the mesh refinement study had the respective sizes of 110×340 and 220×680 nodes. The flat-plate leading edge radius size is 0.002 meters.

onset correctly. The SA turbulence model predicts an early transition. Also a mesh independence result is shown using the V-SA model. This was obtained by calculating the same case with a computational mesh with the double number of nodes. As can be seen the presented results have mesh independence. The effect of using a smaller leading edge radius on this case is presented in Fig.4.5. As expected the k-k$_l$-ω-mod, k-k$_l$-ω and γ-Re_θ transition models improve on the transition onset prediction. However, the k-k$_l$-ω-mod and k-k$_l$-ω closures compute the transition onset earlier than the empirically correlated γ-Re_θ transition model. The k-k$_l$-ω-org predicts an even earlier turbulence transition with a low skin-friction coefficient on the fully turbulent region of the flat-plate. The applied V-SA, V-SA-Sep-Correct, V-SA-Improved and the V-SA-Fluent-Implementation transition models were calibrated using this test case. Therefore, the initiation of transition is correctly computed. The SA turbulence model still presents a very early transition.

As already mentioned, the V-model transition closure calculates small pre-transitional negative values of $\overline{u'v'}$. This is shown for the region near the leading edge and for the transition onset zone of the T3A test case in Fig.4.6. As can be seen, when the mean flow characteristics are ideal the V-model predicts the piercing of the laminar boundary layer by the pre-transitional $\overline{u'v'}$. This then activates the turbulence model production term. The proposed mechanical model approximation for pre-transitional turbulent vortex deformation predicts the distribution of $\overline{u'v'}$ in the pre-transitional boundary layer region. A comparison is performed between the experimental ERCOFTAC database of $\overline{u'v'}$ and the V-model predicted values. These comparisons are performed from the leading edge to the transition onset point. The last comparison is one station in the middle of the transition region. The results are presented in Figs.4.7, 4.8, 4.9, 4.10, 4.11 and 4.12. These represent the axial positions in meters of 0.095, 0.195, 0.295, 0.395, 0.495 and the transition section 0.595 respectively. The latter axial positions correspond to the Reynolds numbers of 3.24×10^4, 6.70×10^4, 10.06×10^4, 13.48×10^4, 16.92×10^4 and the transition section 20.35×10^4 respectively. As can be seen, the V-model predicts an overshoot of $\overline{u'v'}$ near the leading edge. However, the results greatly improve along the pre-transitional region. Within the laminar boundary layer, the scale functions, F_S and F_Ω, are null in the near wall

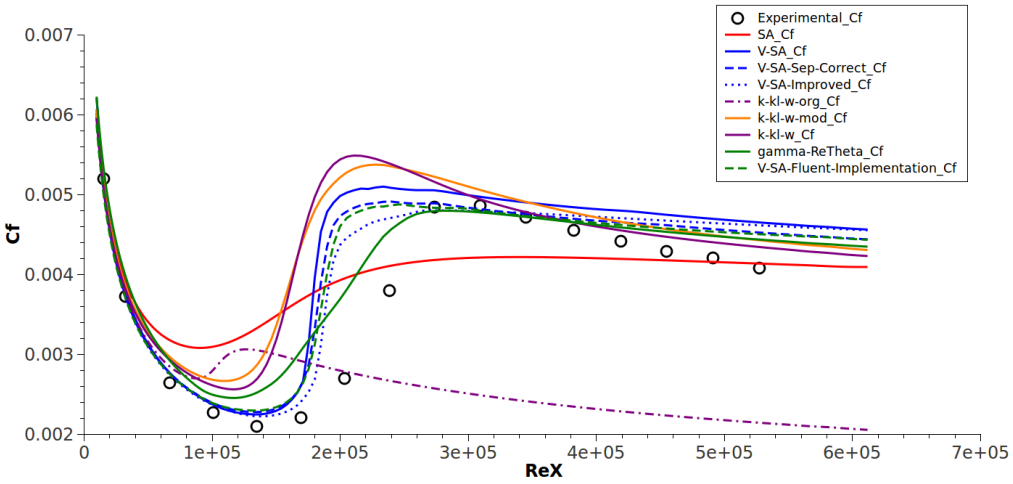

Figure 4.5: Comparison of experimental data from ERCOFTAC T3A flat-plate test case skin-friction coefficient distribution with the turbulence SA closure and the transition V-SA, V-SA-Sep-Correct, V-SA-Improved, V-SA-Fluent-Implementation, k-k$_l$-ω-org, k-k$_l$-ω-mod, k-k$_l$-ω and γ-Re_θ models. The flat-plate leading edge radius size is 0.00075 meters.

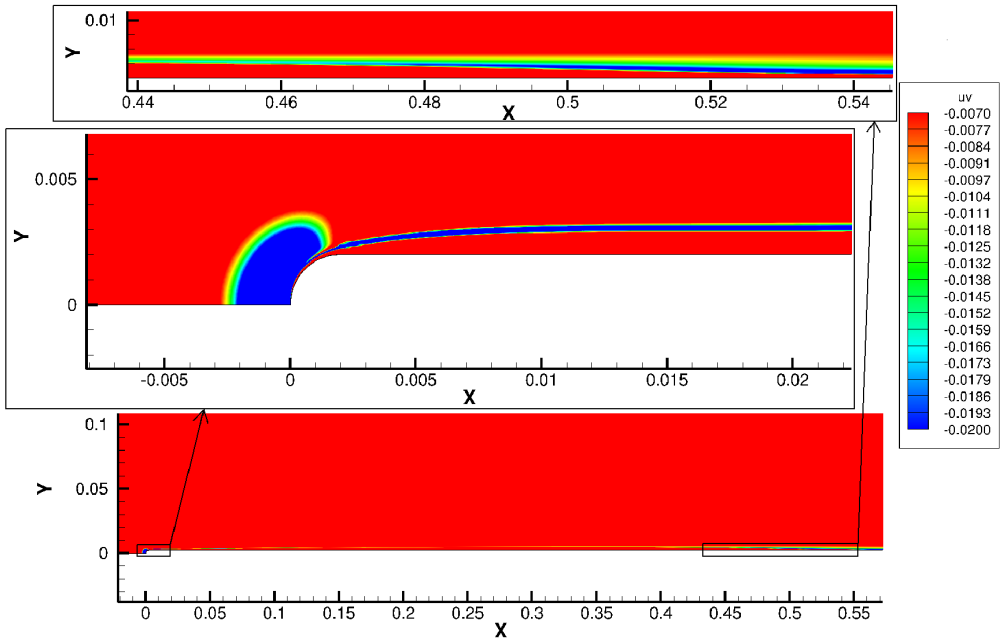

Figure 4.6: Contour map of $\overline{u'v'}$ values with detailed results near the leading edge and transition onset zone of the T3A flat-plate test case.

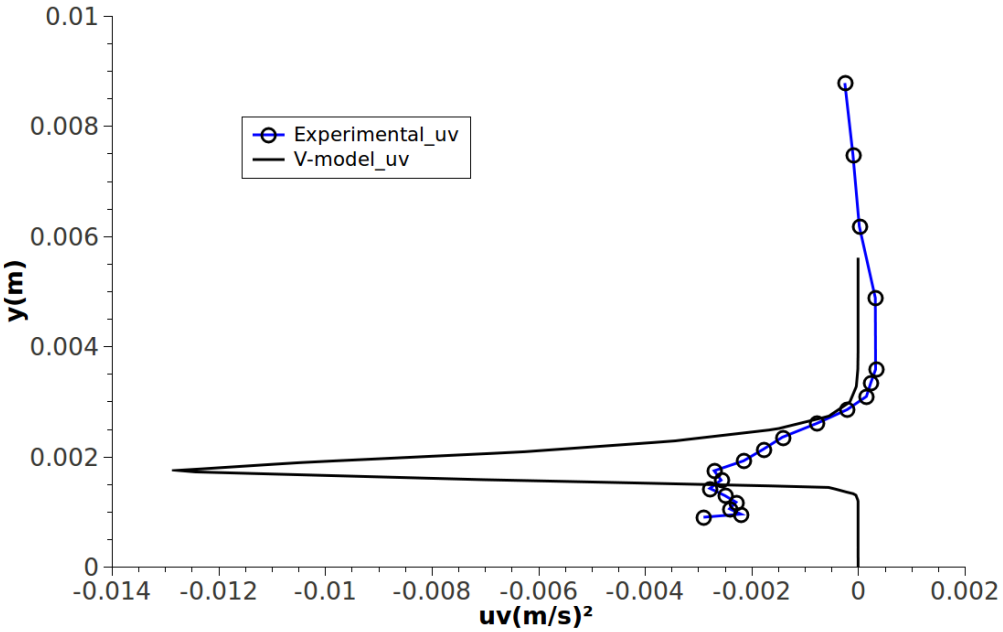

Figure 4.7: Comparison of ERCOFTAC flat-plate T3A experimental $\overline{u'v'}$ values with those predicted by the transition V-model in the axial position of 0.095 meters or Rex of 3.24×10^4. The negative pre-transitional $\overline{u'v'}$ values were related to ”splat-mechanism“ or ”inactive-motion“ by [3].

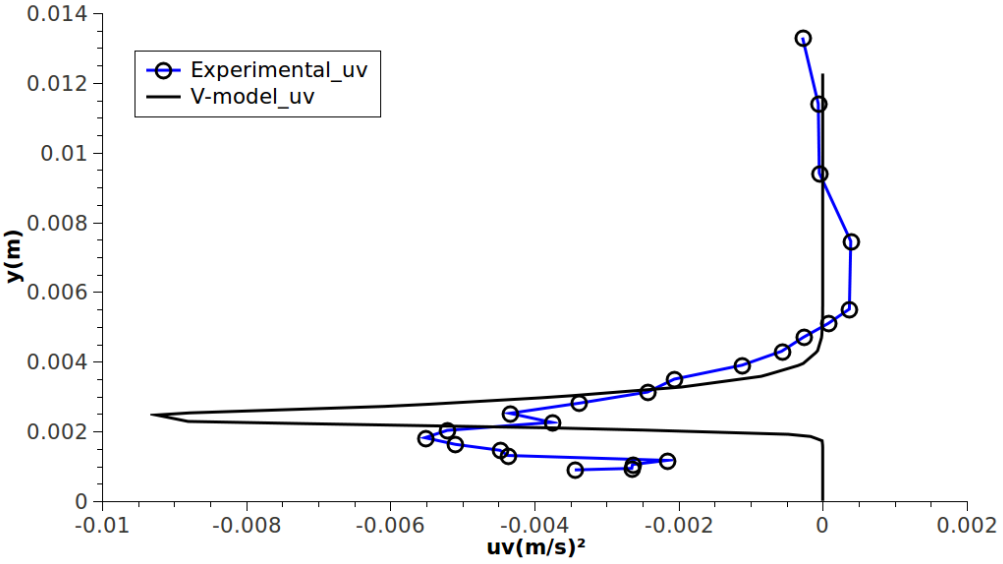

Figure 4.8: Comparison of ERCOFTAC flat-plate T3A experimental $\overline{u'v'}$ values with those predicted by the transition V-model in the axial position of 0.195 meters or Rex of 6.70×10^4.

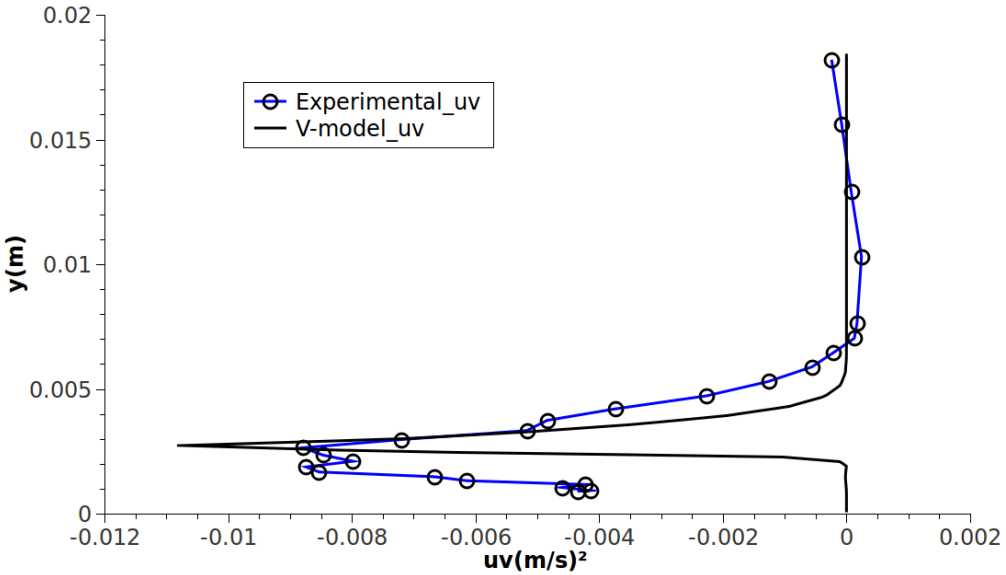

Figure 4.9: Comparison of ERCOFTAC flat-plate T3A experimental $\overline{u'v'}$ values with those predicted by the transition V-model in the axial position of 0.295 meters or Rex of 10.06×10^4.

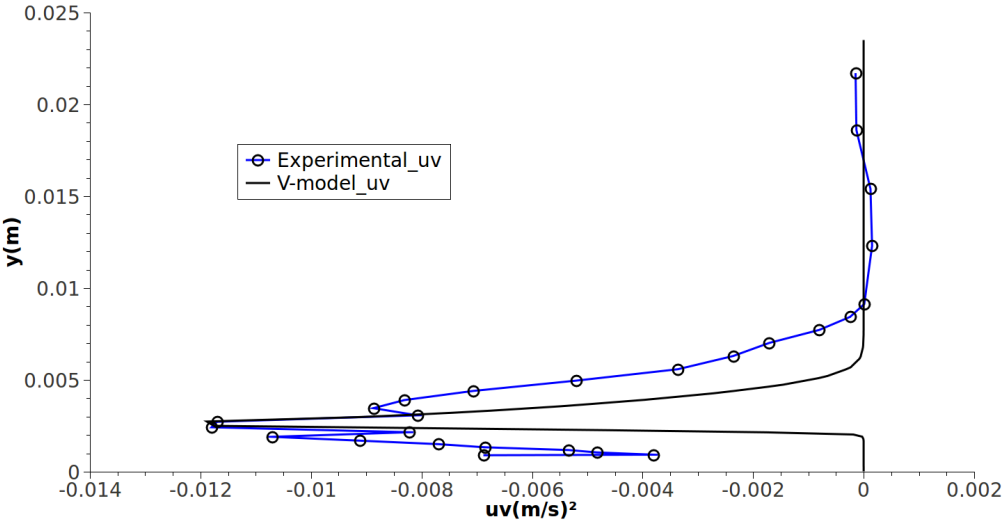

Figure 4.10: Comparison of ERCOFTAC flat-plate T3A experimental $\overline{u'v'}$ values with those predicted by the transition V-model in the axial position of 0.395 meters or Rex of 13.48×10^4.

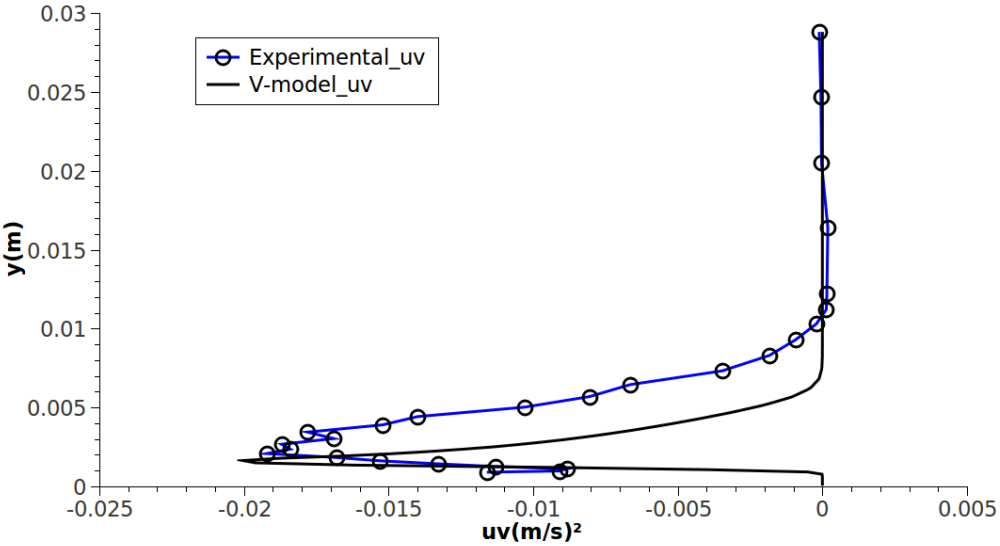

Figure 4.11: Comparison of ERCOFTAC flat-plate T3A experimental $\overline{u'v'}$ values with those predicted by the transition V-model in the axial position of 0.495 meters or Rex of 16.92×10^4.

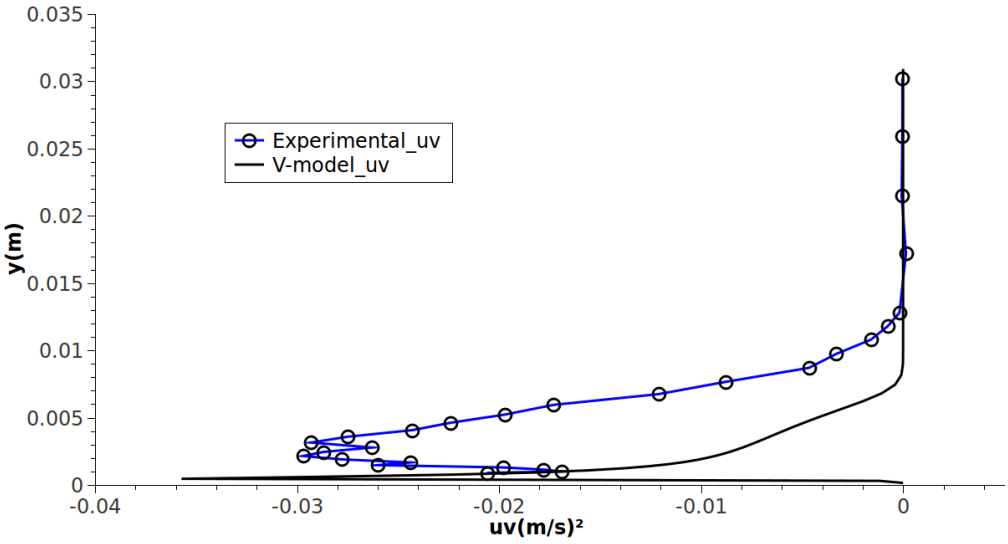

Figure 4.12: Comparison of ERCOFTAC flat-plate T3A experimental $\overline{u'v'}$ values with those predicted by the transition V-model in the axial position of 0.595 meters or Rex of 20.35×10^4.

Table 4.3: ERCOFTAC T3B Flat-plate Inlet Boundary Conditions

Model	$U(m/s)$	$k(m^2/s^2)$	$k_p(m^2/s^2)$	$\omega(s^{-1})$	$\tilde{\nu}_t(m^2/s)$
SA	9.4	N/A	N/A	N/A	4.5×10^{-5}
V-SA	9.4	N/A	0.4771	N/A	4.5×10^{-5}
V-SA-Sep-Correct	9.4	N/A	0.4771	N/A	4.5×10^{-5}
V-SA-Improved	9.4	N/A	0.4771	N/A	4.5×10^{-5}
k-k_l-ω-org	9.4	1.0736	N/A	65	N/A
k-k_l-ω-mod	9.4	1.0736	N/A	65	N/A
k-k_l-ω	9.4	1.0736	N/A	65	N/A
γ-Re_θ	9.4	1.05	N/A	700	N/A

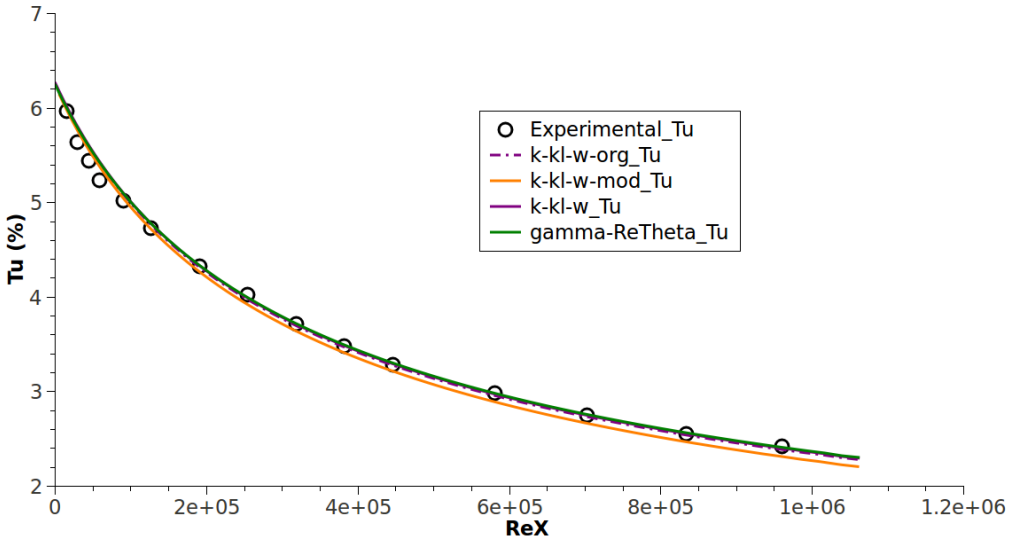

Figure 4.13: Flat-plate T3B turbulence intensity decay.

region. Although the calculated pre-transition $\overline{u'v'}$ values are zero in this zone, the near wall experimental measured $\overline{u'v'}$ values are not zero. The results in Fig.4.12, corresponding to a station in the middle of the transition length region, show that the model predictions deviate from the measured values.

4.1.1.2 T3B flat-plate validation

The ERCOFTAC T3B flat-plate zero-pressure-gradient test case is similar to the T3A. However, both the free-stream turbulence intensity and the free-stream velocity are roughly doubled imposing a very early transition onset. This case was designed to evaluate bypass transition type closer to the flat-plate leading edge. The applied inlet boundary conditions for all tested transition and turbulence models are presented in table 4.3. The free-stream turbulence intensity decay rate is presented in Fig.4.13. As observed, the imposed inlet boundary conditions allow for a correct free-stream turbulence development. An initial attempt to run the transition and turbulence models under the flow conditions imposed on table 4.3 was performed. This computation was done using a geometry with leading edge radius of 0.002 meters. The results for the flat-plate T3B ERCOFTAC test case presented in Fig.4.14, show that all models predict transition earlier than expected. This is due to the leading edge curvature radius, low fluid kinematic viscosity and high velocity conditions that induce flow separation at the beginning of the flat-plate. Therefore, the transition closures predict an early separation induced transition

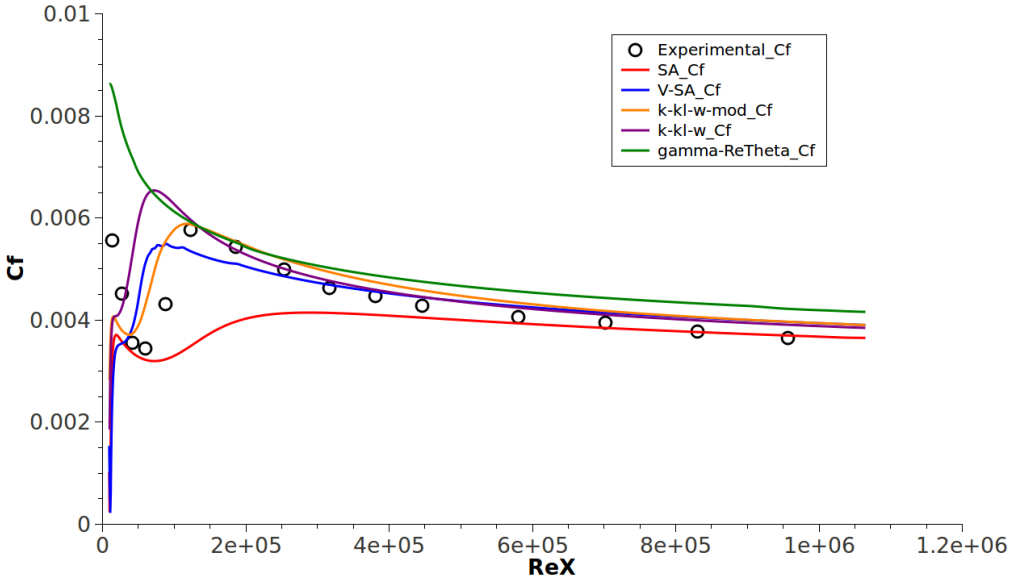

Figure 4.14: Comparison of experimental data from ERCOFTAC T3B flat-plate test case skin-friction coefficient distribution with the turbulence SA closure and the transition V-SA, k-k$_l$-ω-mod, k-k$_l$-ω and γ-Re_θ models. The flat-plate leading edge radius size is 0.002 meters.

instead of a bypass transition type as was meant to be. The separation bubble can be seen in Fig.4.15. In order to evaluate the transition turbulence models capacity to correctly predict bypass transition for the T3B test case conditions, another computation was performed. The inlet boundary conditions were maintained but the fluid kinematic viscosity was increased to double its standard value to $\nu = 3 \times 10^{-5}\,(m^2/s)$ for this particular case. This was performed in order to avoid flow separation at the leading edge of the flat-plate. As shown in Fig.4.16, avoiding the separation bubble the V-SA transition model is able to correctly predict transition onset. Also the k-k$_l$-ω-mod, k-k$_l$-ω and γ-Re_θ transition closures are able to predict a transition inception closer to the experimental data. The γ-Re_θ transition model computes a larger laminar skin-friction coefficient value than what is to be expected. This condition is anomalous, and has not been observed in the transition model publications. The SA model predicts transition later than expected. The effect of reducing the leading edge radius to 0.00075 meters should dispose of the need to apply a higher fluid kinematic viscosity. As such, the results for the T3B test case with the original kinematic viscosity of $\nu = 1.5 \times 10^{-5}\,(m^2/s)$ are presented in Fig.4.17. The presented results show that the anomalous behavior of the γ-Re_θ transition closure remains unchanged. The SA turbulence model predicts transition onset later than the experimental data. The V-SA, V-SA-Sep-Correct, V-SA-Improved and V-SA-Fluent-Implementation transition closures predict the transition threshold slightly earlier than the experiment. The most accurate models are the k-k$_l$-ω-mod and the k-k$_l$-ω transition models. The implemented original formulation of the k-k$_l$-ω transition model, the k-k$_l$-ω-org, does not predict any transition to turbulence over the flat-plate geometry.

4.1.1.3 T3A- flat-plate validation

The last flat-plate zero-pressure-gradient test case is the T3A-. This case was conceived to evaluate natural transition type. This is so, since its upstream turbulence intensity is less

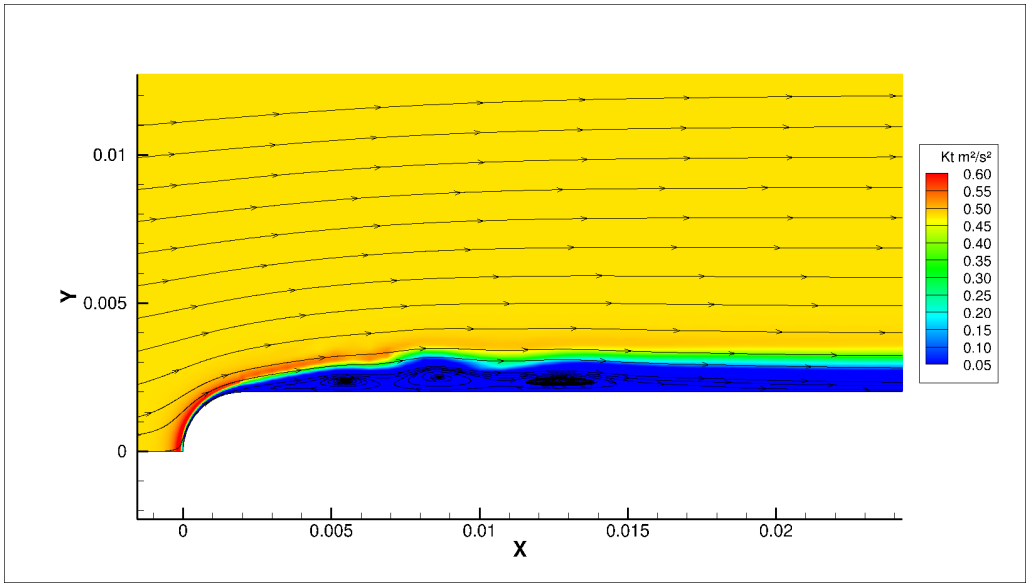

Figure 4.15: Separation bubble from the T3B V-SA computational case. Flow stream-lines are displayed over the contour of pre-transitional turbulent kinetic energy.

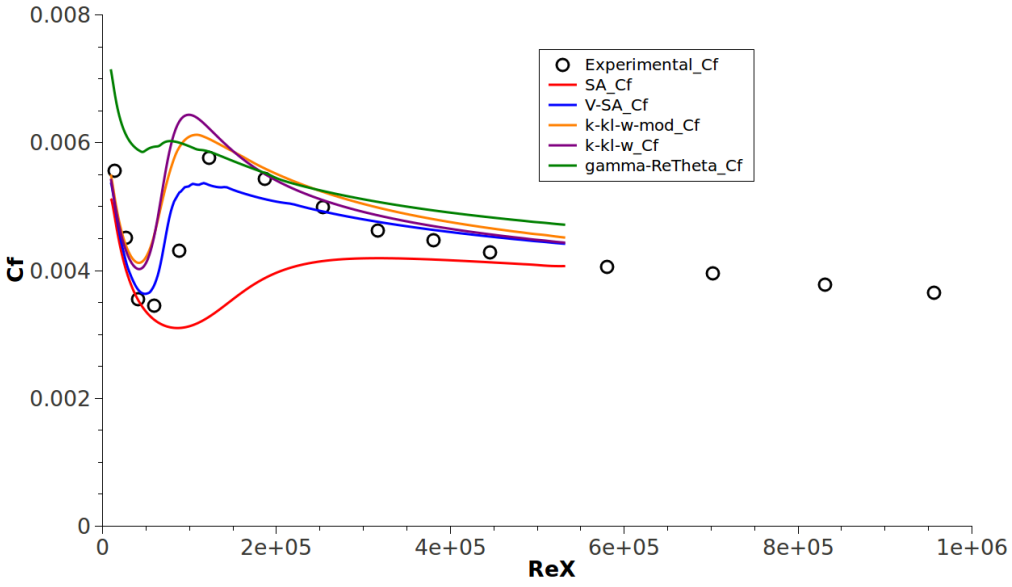

Figure 4.16: Comparison of experimental data from ERCOFTAC T3B flat-plate test case skin-friction coefficient distribution with the turbulence SA closure and the transition V-SA, k-k_l-ω-mod, k-k_l-ω and γ-Re_θ models. The used fluid kinematic viscosity was $\nu = 3 \times 10^{-5}\,(m^2/s)$. The flat-plate leading edge radius size is 0.002 meters.

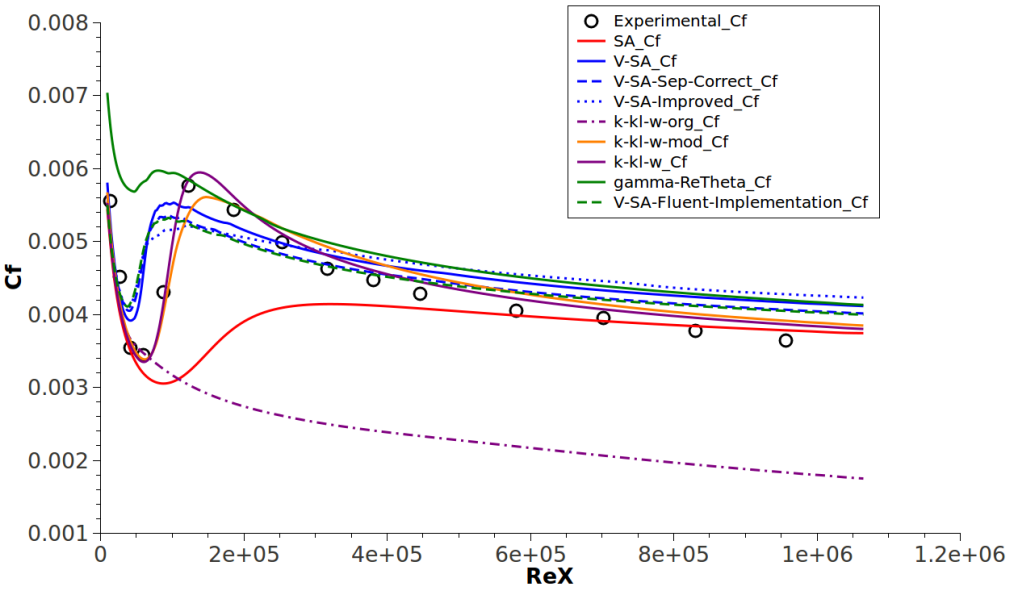

Figure 4.17: Comparison of experimental data from ERCOFTAC T3B flat-plate test case skin-friction coefficient distribution with the turbulence SA closure and the transition V-SA, V-SA-Sep-Correct, V-SA-Improved, V-SA-Fluent-Implementation, k-k_l-ω-org, k-k_l-ω-mod, k-k_l-ω and γ-Re_θ models. The used fluid kinematic viscosity was $\nu = 1.5 \times 10^{-5}\,(m^2/s)$. The flat-plate leading edge radius size is 0.00075 meters.

Table 4.4: ERCOFTAC T3A- Flat-plate Inlet Boundary Conditions

Model	$U(m/s)$	$k(m^2/s^2)$	$k_p(m^2/s^2)$	$\omega(s^{-1})$	$\tilde{\nu_t}(m^2/s)$
SA	19.8	N/A	N/A	N/A	4.5×10^{-5}
V-SA	19.8	N/A	0.0476	N/A	4.5×10^{-5}
V-SA-Sep-Correct	19.8	N/A	0.0476	N/A	4.5×10^{-5}
V-SA-Improved	19.8	N/A	0.0476	N/A	4.5×10^{-5}
k-k_l-ω-org	19.8	0.08	N/A	65	N/A
k-k_l-ω-mod	19.8	0.08	N/A	65	N/A
k-k_l-ω	19.8	0.08	N/A	65	N/A
γ-Re_θ	19.8	0.078	N/A	700	N/A

than 1%. It must be noted that although the free-stream turbulence intensity is decreased, the free-stream velocity is approximately four times higher than the imposed velocity in the T3A test case as presented in table 4.1. This will cause flow separation at the flat-plate leading edge. The applied inlet boundary conditions for all tested transition and turbulence models are presented in table 4.4. The computed free-stream turbulence intensity decay over the flat-plate is disclosed in Fig.4.18. The applied inlet turbulent boundary conditions reproduce a correct free-stream turbulence development. As already mentioned, a first computation with the presented inlet conditions resulted in flow separation at the leading edge of the flat-plate as presented in Fig.4.19. The latter will then again result in an earlier separation induced transition. The skin-friction coefficient plot results are presented in Fig.4.20. In order to eliminate or greatly reduce the flow separation at the leading edge of the flat-plate, the fluid kinematic viscosity was again increased. For the case of T3A-, the fluid kinematic viscosity was increased from its standard value to $\nu = 8 \times 10^{-5}\,(m^2/s)$. This larger increase in fluid kinematic viscosity was required since the upstream velocity was much higher than that of the T3B test case. The inlet boundary conditions were maintained but the used computational mesh was augmented.

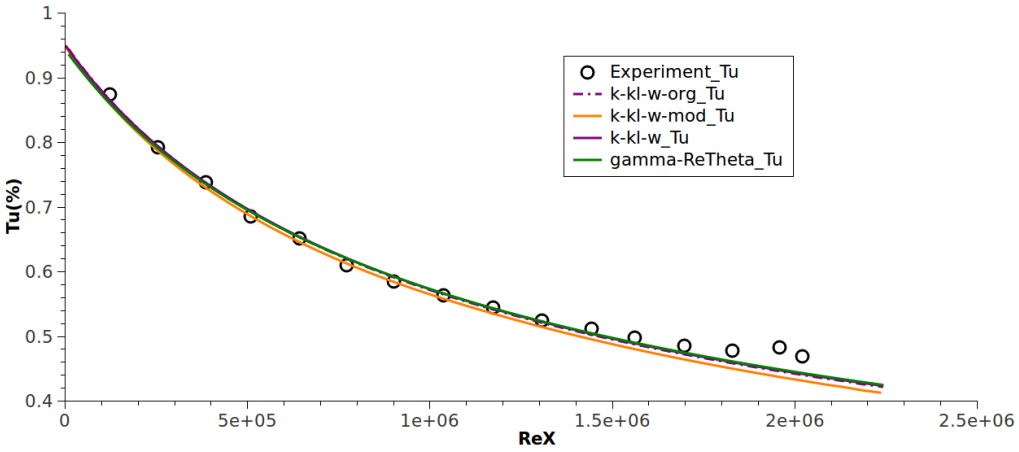

Figure 4.18: Flat-plate T3A- turbulence intensity decay.

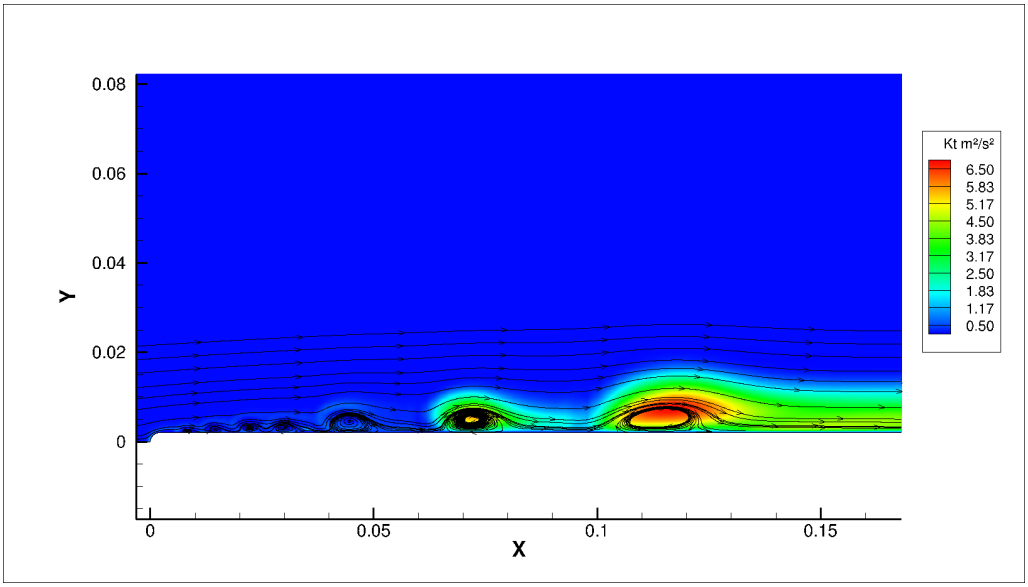

Figure 4.19: Separation bubble from the T3A- V-SA computational case. Flow stream-lines are displayed over the contour of pre-transitional turbulent kinetic energy.

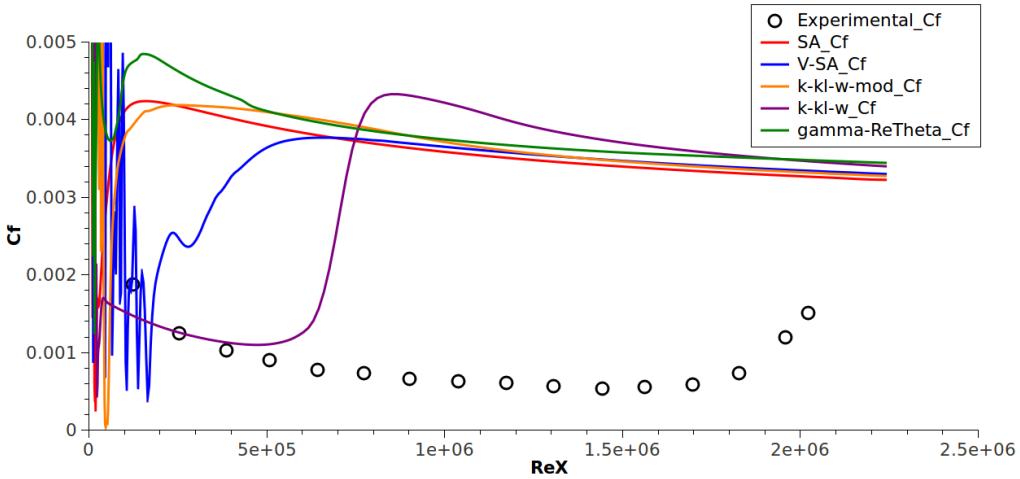

Figure 4.20: Comparison of experimental data from ERCOFTAC T3A- flat-plate test case skin-friction coefficient distribution with the turbulence SA closure and the transition V-SA, k-k_l-ω-mod, k-k_l-ω and γ-Re_θ models. The flat-plate leading edge radius size is 0.002 meters.

For this particular case, the used mesh is almost the same as the previous described mesh for the zero-pressure-gradient flat-plate test cases. The difference of the applied mesh is then the larger flat-plate extension of 9.0 meters long. The number of nodes along the flat-plate were 400. The remaining characteristics of the mesh are the same as the one used for both the T3A and T3B test cases. As can be seen in Fig.4.21, the V-SA model is able to correctly calculate the transition onset. The transition point is very close to the minimal experimental value of skin-friction coefficient. Although the V-SA model correctly predicts transition onset, the transition extension is relatively shorter than that of the experimental data. The SA model predicts transition onset far too early. The k-k_l-ω-mod and k-k_l-ω transition closures behave in a similar manner, predicting turbulence transition slightly earlier than the experiment. The empirically correlated γ-Re_θ transition model does not predict turbulence transition. This does not imply that the model cannot predict transition under these conditions. This means that the model was not able to predict natural transition under the maximum flat-plate length of 9.0 meters. Similar to the ERCOFTAC T3B test case, the use of a smaller leading edge radius will avoid the need of resort to computations with higher kinematic viscosity. The obtained skin-friction coefficient distribution results are disclosed in Fig.4.22. Again the SA turbulence model predicts a very early transition. The V-SA, V-SA-Sep-Correct and V-SA-Improved transition models predict an early transition onset, with the improved version of the model predicting the best result. The V-SA-Fluent-Implementation closure computes a transition threshold closer to the original V-SA transition model. With the exception of the V-SA-Improved transition model, the k-k_l-ω-org predicts a more accurate transition threshold region than the V-SA model versions. However, the k-k_l-ω-org computed skin-friction coefficient in the fully turbulent region is below the correct values. The k-k_l-ω-mod, k-k_l-ω and γ-Re_θ transition closures predict the transition threshold closer to the experimental data. Nevertheless, the best numerical result is obtained with the γ-Re_θ and the worst with the k-k_l-ω-mod.

4.1.2 Pressure-Gradient test cases

The experimental data from Coupland [161], for a flat-plate subjected to flow pressure-gradient was considered. The present geometry is slightly more complex than the zero-pres-

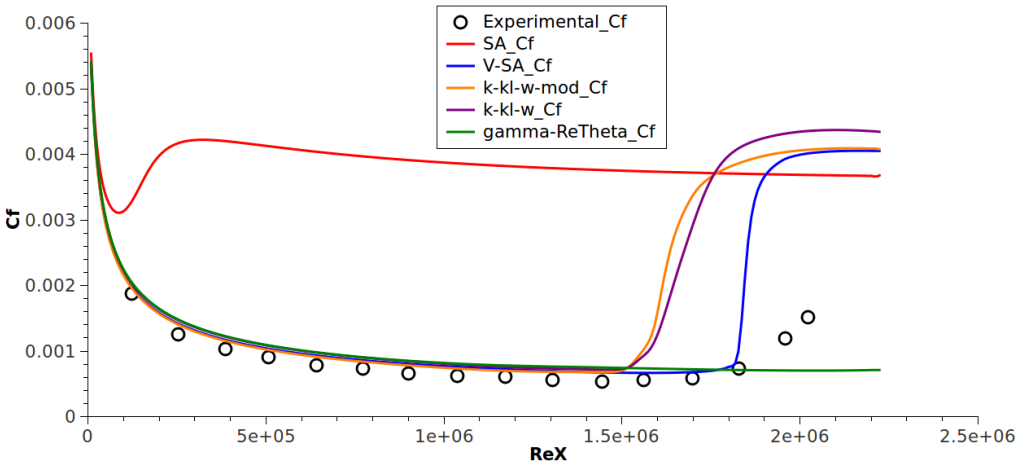

Figure 4.21: Comparison of experimental data from ERCOFTAC T3A- flat-plate test case skin-friction coefficient distribution with the turbulence SA closure and the transition V-SA, k-k_l-ω-mod, k-k_l-ω and γ-Re_θ models. The used fluid kinematic viscosity was $\nu = 8 \times 10^{-5}\,(m^2/s)$. The flat-plate leading edge radius size is 0.002 meters.

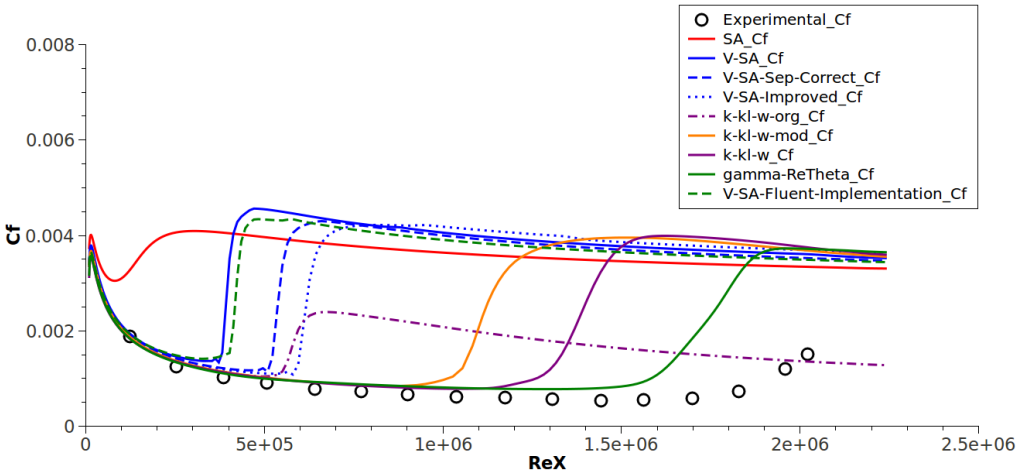

Figure 4.22: Comparison of experimental data from ERCOFTAC T3A- flat-plate test case skin-friction coefficient distribution with the turbulence SA closure and the transition V-SA, V-SA-Sep-Correct, V-SA-Improved, V-SA-Fluent-Implementation, k-k_l-ω-org, k-k_l-ω-mod, k-k_l-ω and γ-Re_θ models. The used fluid kinematic viscosity was $\nu = 1.5 \times 10^{-5}\,(m^2/s)$. The flat-plate leading edge radius size is 0.00075 meters.

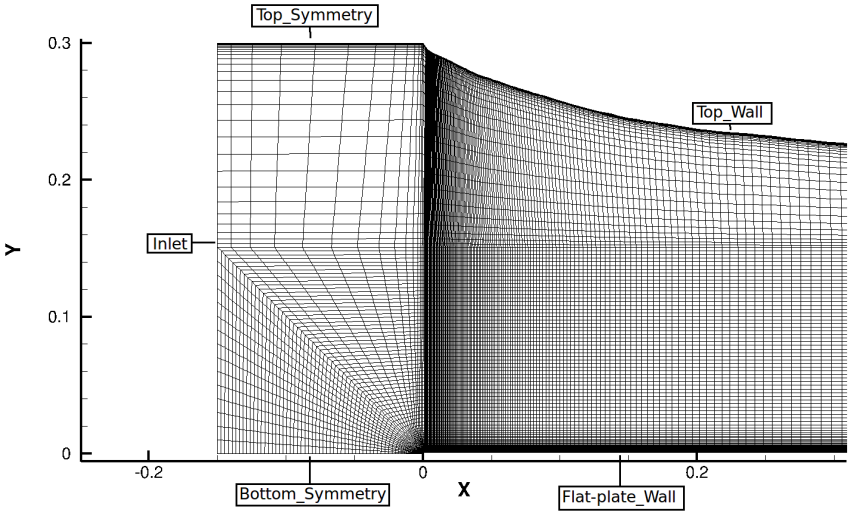

Figure 4.23: Pressure-gradient flat-plate inlet mesh view.

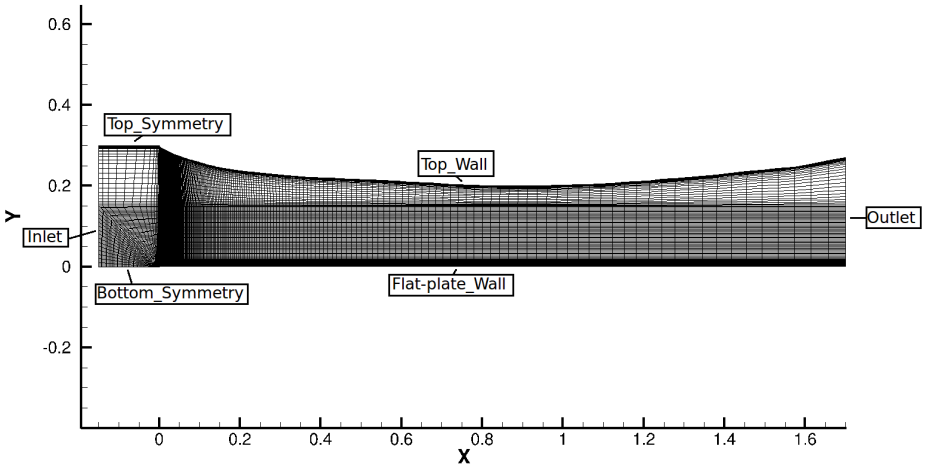

Figure 4.24: General overview of pressure-gradient flat-plate mesh with 31000 nodes.

sure-gradient test cases. It can be said that the bottom part of this geometry is equal to the latter exposed cases. The top surface of the geometry is curved and it extends over the entire flat-plate 1.7 meters. The curved surface has 200 mesh points along it. The mesh points cluster near this surface resulting in a distance of 1×10^{-4} meters for the first layer of cells. This top section of the mesh has 30 nodes along its vertical connectors. Summing this with the previous bottom part of the mesh makes a total of 140 mesh points in the vertical direction over the flat-plate. Similar to the first flat-plate geometry, the inlet is located 0.15 meters before the flat-plate leading edge. This has a height of 0.3 meters. A detail view of the pressure-gradient geometry inlet mesh is given in Fig.4.23. The remaining characteristics of the used computational mesh are similar to the zero-pressure-gradient cases. The pressure-gradient flat-plate full geometry mesh is presented in Fig.4.24. In the present case, the top surface is a no-slip wall boundary condition. As such, this surface has equal boundary conditions to the bottom flat-plate. Also, the effect of different leading edge radius of 0.00075 and 0.002 meters will be

Table 4.5: ERCOFTAC T3C Pressure-Gradient Flat-Plate Upstream Conditions

$Case$	$Tu(\%)$	$U(m/s)$
$T3C1$	6.6	5.9
$T3C2$	3.0	5.0
$T3C3$	3.0	3.7
$T3C4$	3.0	1.2
$T3C5$	3.0	8.4

Table 4.6: ERCOFTAC T3C1 Flat-plate Inlet Boundary Conditions

Model	$U(m/s)$	$k(m^2/s^2)$	$k_p(m^2/s^2)$	$\omega(s^{-1})$	$\tilde{\nu}_t(m^2/s)$
SA	5.9	N/A	N/A	N/A	4.5×10^{-5}
V-SA	5.9	N/A	0.22745	N/A	4.5×10^{-5}
V-SA-Sep-Correct	5.9	N/A	0.22745	N/A	4.5×10^{-5}
V-SA-Improved	5.9	N/A	0.22745	N/A	4.5×10^{-5}
k-k$_l$-ω-org	5.9	11	N/A	1075	N/A
k-k$_l$-ω-mod	5.9	11	N/A	1075	N/A
k-k$_l$-ω	5.9	11	N/A	1075	N/A
γ-Re_θ	5.9	11	N/A	11576	N/A

studied. The free-stream turbulence intensity and velocity are measured in an horizontal line along the geometry at the vertical distance of 0.15 meters above the flat-plate.

From the ERCOFTAC database, the upstream flow conditions for the T3C pressure-gradient flat-plate test cases are presented in table 4.5.

4.1.2.1 T3C1 flat-plate validation

The first considered flat-plate pressure-gradient transition test case was the ERCOFTAC T3C1. This is used for benchmarking favorable-pressure-gradient conditions for bypass transition type. The specified inlet boundary conditions for all tested transition and turbulence models are presented in table 4.6. The free-stream turbulence intensity decay rate for the used turbulence and transition models is disclosed in Fig.4.25. The results for the flat-plate T3C1 ERCOFTAC test case are presented in Fig.4.26. Among these, there is also a mesh refinement study similar to the one performed for the T3A test case. The used refined mesh has double number of nodes of the previously described computational mesh. The mesh refinement study indicates that the obtained results are mesh independent. It should be noted that the calculation of skin-friction coefficient for these pressure-gradient test cases is performed using the local free-stream velocity. This implies that the free-stream velocity used for calculating the latter coefficient varies along the plate due to flow pressure-gradient. The discrepancies in the skin-friction coefficient in the laminar region over the flat-plate are probably due to an incorrect velocity non-dimensionalization. As can be seen, the SA turbulence model predicts transition onset later than expected. The V-SA transition model is able to predict transition onset very close to the experimentally determined transition Reynolds number. The modified laminar kinetic energy transition model, k-k$_l$-ω-mod, predicts transition closer to the experimental data than the original k-k$_l$-ω closure. The empirical transition model, γ-Re_θ, presents again an anomalous behavior. This occurrence is apparently related to near leading edge bypass transition flow conditions. Reduction effects of the flat-plate leading edge radius to 0.00075 meters, are presented in Fig.4.27. The disposition of the computed skin-friction coefficient curves by the previously applied turbulence and transition models is almost unchanged. Nonetheless, there is a slight improvement of the transition onset prediction by both the k-k$_l$-ω-mod and

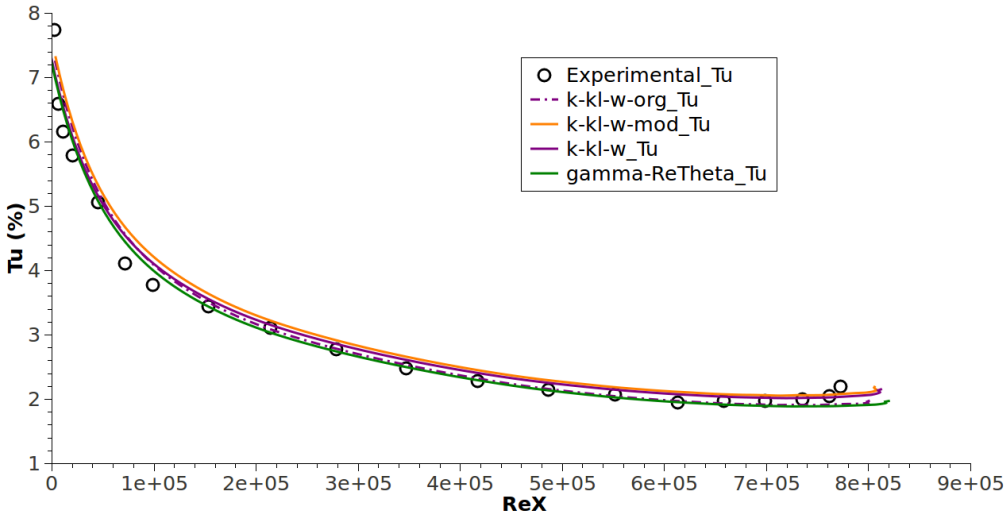

Figure 4.25: Flat-plate T3C1 turbulence intensity decay.

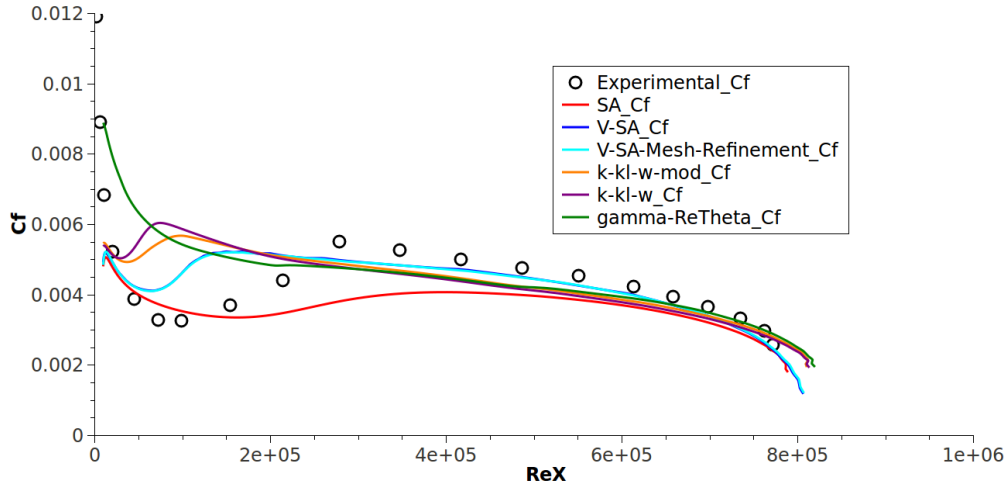

Figure 4.26: Comparison of experimental data from ERCOFTAC T3C1 flat-plate test case skin-friction coefficient distribution with the turbulence SA closure and the transition V-SA, k-k_l-ω-mod, k-k_l-ω and γ-Re_θ models. The used structured computational light and refined grids for the mesh refinement study had the respective sizes of 140×340 and 280×680 nodes. The flat-plate leading edge radius size is 0.002 meters.

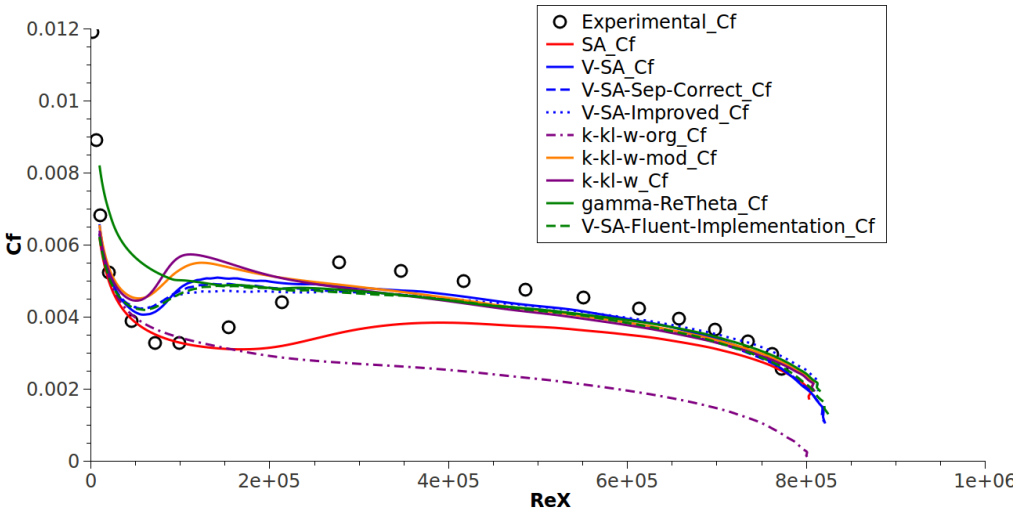

Figure 4.27: Comparison of experimental data from ERCOFTAC T3C1 flat-plate test case skin-friction coefficient distribution with the turbulence SA closure and the transition V-SA, V-SA-Sep-Correct, V-SA-Improved, V-SA-Fluent-Implementation, k-k$_l$-ω-org, k-k$_l$-ω-mod, k-k$_l$-ω and γ-Re_θ models. The flat-plate leading edge radius size is 0.00075 meters.

Table 4.7: ERCOFTAC T3C2 Flat-plate Inlet Boundary Conditions

Model	$U(m/s)$	$k(m^2/s^2)$	$k_p(m^2/s^2)$	$\omega(s^{-1})$	$\tilde{\nu}_t(m^2/s)$
SA	5	N/A	N/A	N/A	4.5×10^{-5}
V-SA	5	N/A	0.03375	N/A	4.5×10^{-5}
V-SA-Sep-Correct	5	N/A	0.03375	N/A	4.5×10^{-5}
V-SA-Improved	5	N/A	0.03375	N/A	4.5×10^{-5}
k-k$_l$-ω-org	5	0.08	N/A	55	N/A
k-k$_l$-ω-mod	5	0.08	N/A	55	N/A
k-k$_l$-ω	5	0.08	N/A	55	N/A
γ-Re_θ	5	0.08	N/A	592	N/A

k-k$_l$-ω transition closures. The k-k$_l$-ω-org transition model does not predict any transition onset, remaining laminar the whole extension of the plate. The V-SA-Sep-Correct, V-SA-Improved and V-SA-Fluent-Implementation transition models, compute the transition threshold region on the same transition Reynolds number as the V-SA model. However, the minimum skin-friction coefficient value of the V-SA model is slightly lower than all the other V-SA transition closure versions.

4.1.2.2 T3C2 flat-plate validation

The following analyzed flat-plate pressure-gradient transition test case was the ERCOFTAC T3C2 case. The present experiment has the purpose to provide data regarding bypass transition on the minimum cross-section station of the T3C experimental benchmark setup. Therefore, the experimental transition onset is observed in the point where the pressure-gradient condition changes from favorable to adverse. The specified inlet boundary conditions for all tested transition and turbulence models are presented in table 4.7. These inlet boundary conditions are validated for the turbulence decay affected models. The turbulence intensity decay rate is presented in Fig.4.28. As observed in Fig.4.29, the results for the T3C2 test case show that the V-SA model is able to predict transition onset correctly. However, the V-SA model cal-

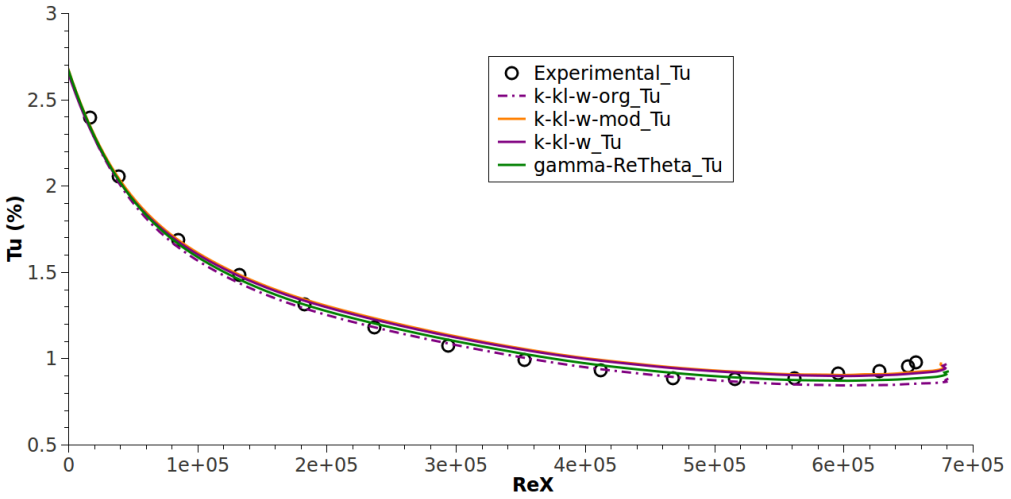

Figure 4.28: Flat-plate T3C2 turbulence intensity decay.

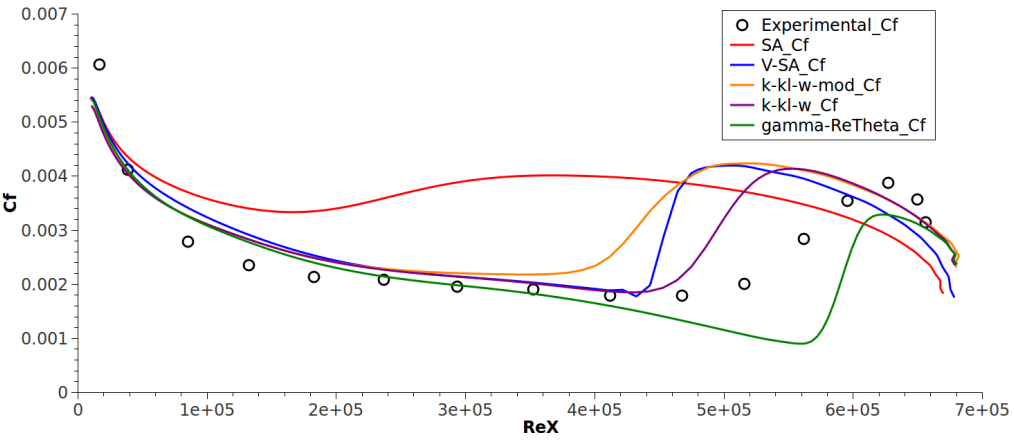

Figure 4.29: Comparison of experimental data from ERCOFTAC T3C2 flat-plate test case skin-friction coefficient distribution with the turbulence SA closure and the transition V-SA, k-k_l-ω-mod, k-k_l-ω and γ-Re_θ models. The flat-plate leading edge radius size is 0.002 meters.

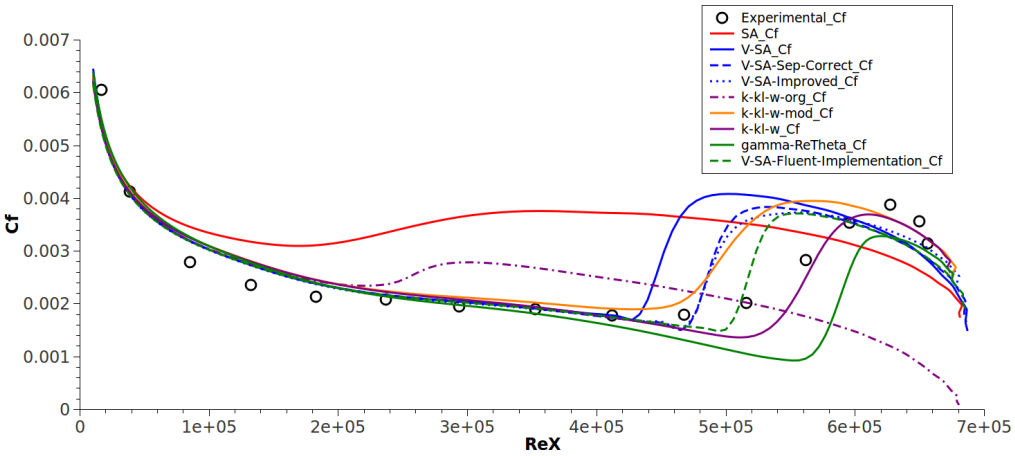

Figure 4.30: Comparison of experimental data from ERCOFTAC T3C2 flat-plate test case skin-friction coefficient distribution with the turbulence SA closure and the transition V-SA, V-SA-Sep-Correct, V-SA-Improved, V-SA-Fluent-Implementation, k-k$_l$-ω-org, k-k$_l$-ω-mod, k-k$_l$-ω and γ-Re_θ models. The flat-plate leading edge radius size is 0.00075 meters.

culates a short transition extension when compared to the experimental data. The SA model predicts transition onset much earlier than the experimental results. The k-k$_l$-ω model presents the best transition behavior of all tested models. This shows a very accurate transition onset point with a large transition length. Yet, the latter is still shorter than the experimentally determined transition extension. The modified k-k$_l$-ω-mod model predicts transition earlier than its original version. Nevertheless, it must be reminded that the leading edge geometry size is not the experimentally used one. The γ-Re_θ empirical model, predicts transition later than expected, without the anomalous behavior previously reported. The leading edge radius shrinkage effect can be visualized in Fig.4.30. Similar to the earlier obtained results of the T3C1 case, in general, the skin-friction coefficient curves remain mostly in the same positions with some exceptions described in the following. The V-SA-Sep-Correct and the V-SA-Improved transition models improve on the transition threshold point compared to the original V-SA model. The V-SA-Fluent-Implementation computes a slightly later transition onset. The original k-k$_l$-ω closure, predicts a later transition onset in comparison to the experimental skin-friction coefficient distribution. The initial OpenFoam implementation of this model, the k-k$_l$-ω-org, predicts a very early transition onset with a low value of skin-friction coefficient on the turbulent flat-plate region. The k-k$_l$-ω-mod transition model with the correct experimental leading edge radius, is able to accurately predict the transition onset for the T3C2 test case conditions.

A similar analysis, of the predicted pre-transitional $\overline{u'v'}$ values, presented for the zero-pressure-gradient T3A test case was also applied to the T3C2. This evaluation was also done using the experimental ERCOFTAC database of $\overline{u'v'}$. Again this analysis was executed from the leading edge to the transition onset point including a station in the middle of the transition length. The results are presented in Figs.4.31, 4.32, 4.33, 4.34, 4.35, 4.36, 4.37, 4.38, 4.39 and 4.40. These represent the axial positions in meters of 0.095, 0.195, 0.295, 0.395, 0.495, 0.595, 0.695, 0.795, 0.895 and the transition section 0.995 respectively. The latter axial positions correspond to the Reynolds numbers of 3.85×10^4, 8.50×10^4, 13.21×10^4, 18.26×10^4, 23.69×10^4, 29.37×10^4, 35.25×10^4, 41.16×10^4, 46.75×10^4 and the transition section 51.59×10^4 respectively.
The initial behavior of the V-model mechanical approximation for $\overline{u'v'}$ calculation is similar to the zero-pressure-gradient flat-plate test case development. There is an overshot in the cal-

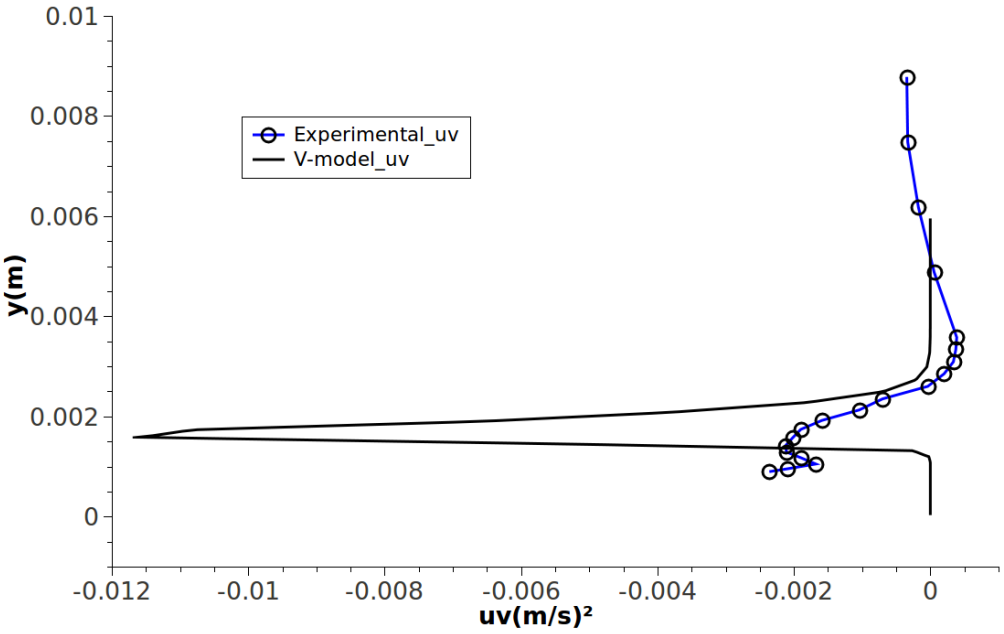

Figure 4.31: Comparison of ERCOFTAC flat-plate T3C2 experimental $\overline{u'v'}$ values with those predicted by the transition V-model in the axial position of 0.095 meters or Rex of 3.85×10^4.

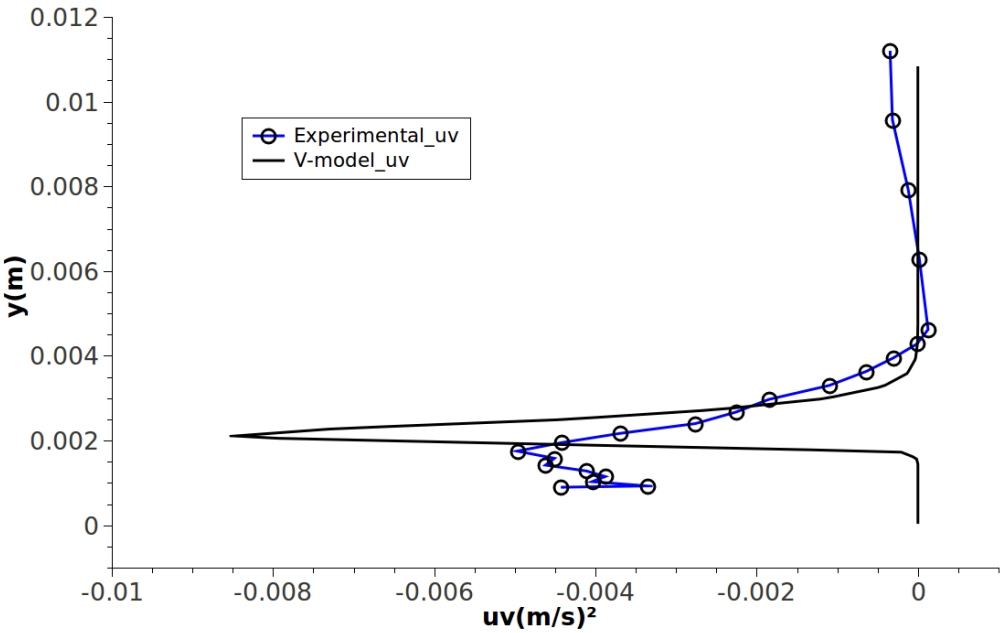

Figure 4.32: Comparison of ERCOFTAC flat-plate T3C2 experimental $\overline{u'v'}$ values with those predicted by the transition V-model in the axial position of 0.195 meters or Rex of 8.50×10^4.

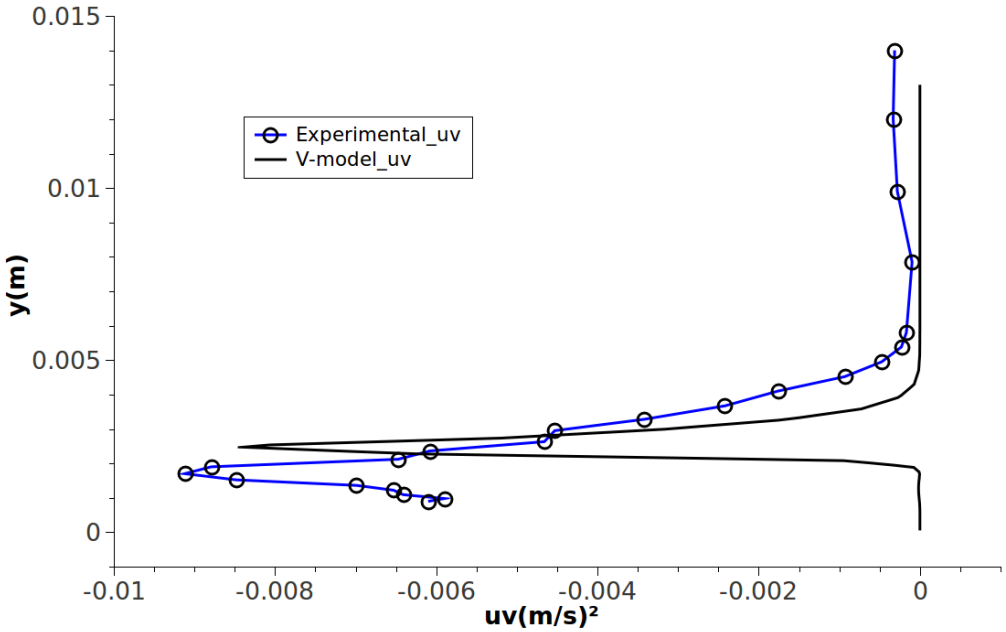

Figure 4.33: Comparison of ERCOFTAC flat-plate T3C2 experimental $\overline{u'v'}$ values with those predicted by the transition V-model in the axial position of 0.295 meters or Rex of 13.21×10^4.

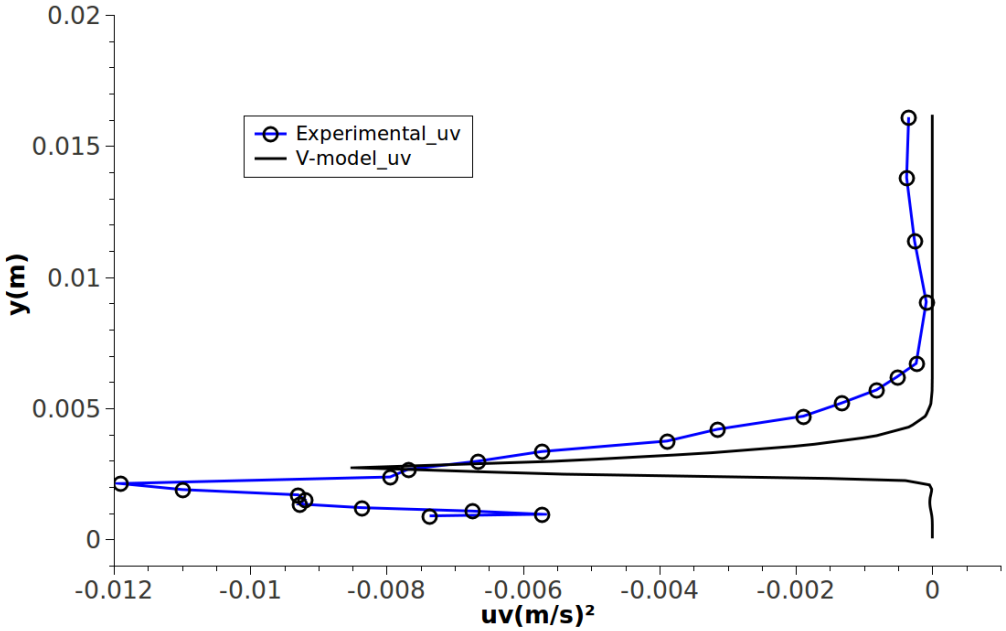

Figure 4.34: Comparison of ERCOFTAC flat-plate T3C2 experimental $\overline{u'v'}$ values with those predicted by the transition V-model in the axial position of 0.395 meters or Rex of 18.26×10^4.

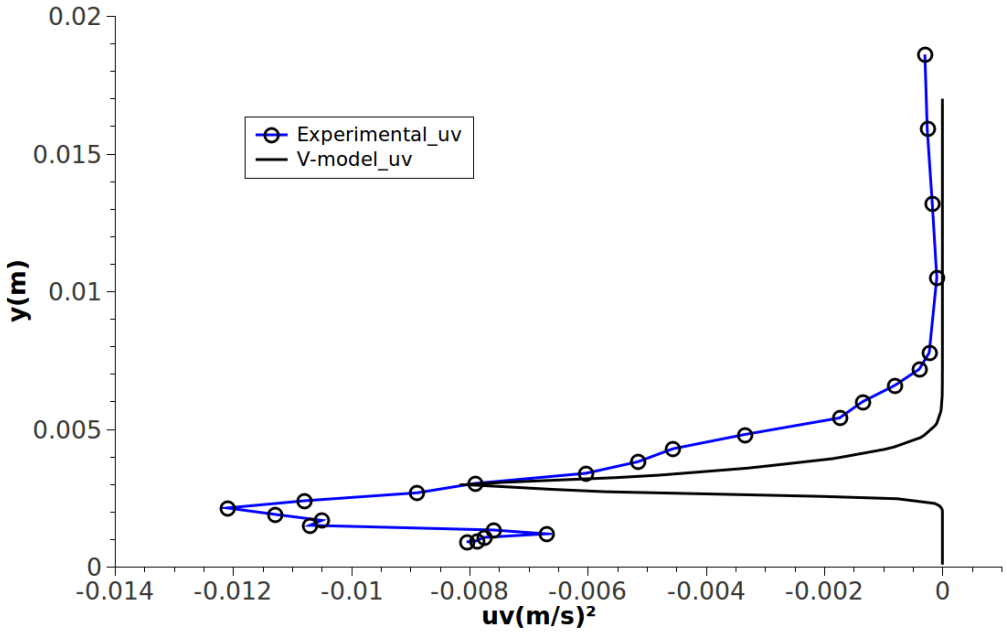

Figure 4.35: Comparison of ERCOFTAC flat-plate T3C2 experimental $\overline{u'v'}$ values with those predicted by the transition V-model in the axial position of 0.495 meters or Rex of 23.69×10^4.

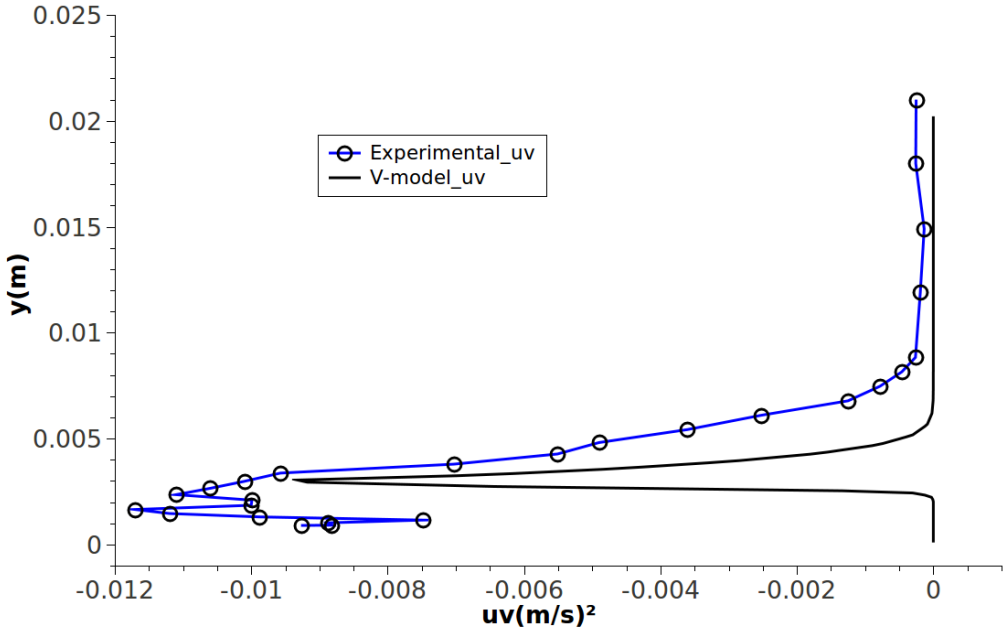

Figure 4.36: Comparison of ERCOFTAC flat-plate T3C2 experimental $\overline{u'v'}$ values with those predicted by the transition V-model in the axial position of 0.595 meters or Rex of 29.37×10^4.

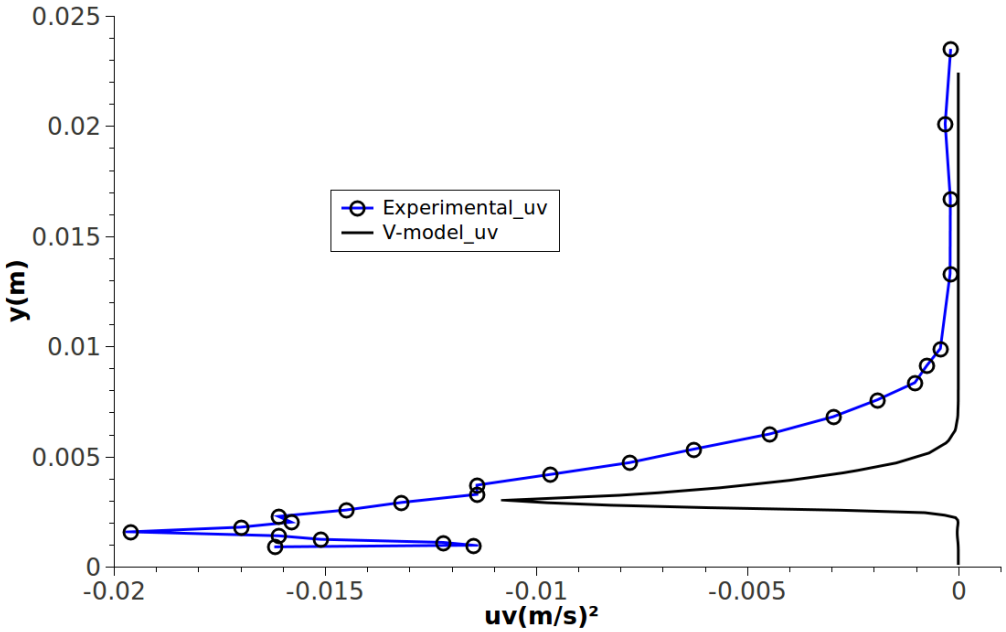

Figure 4.37: Comparison of ERCOFTAC flat-plate T3C2 experimental $\overline{u'v'}$ values with those predicted by the transition V-model in the axial position of 0.695 meters or Rex of 35.25×10^4.

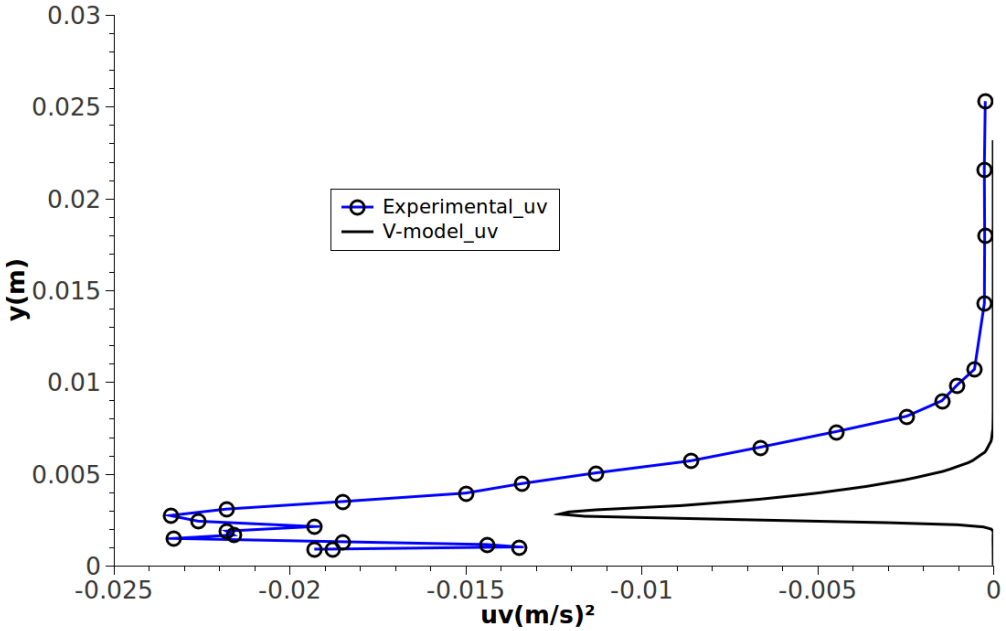

Figure 4.38: Comparison of ERCOFTAC flat-plate T3C2 experimental $\overline{u'v'}$ values with those predicted by the transition V-model in the axial position of 0.795 meters or Rex of 41.16×10^4.

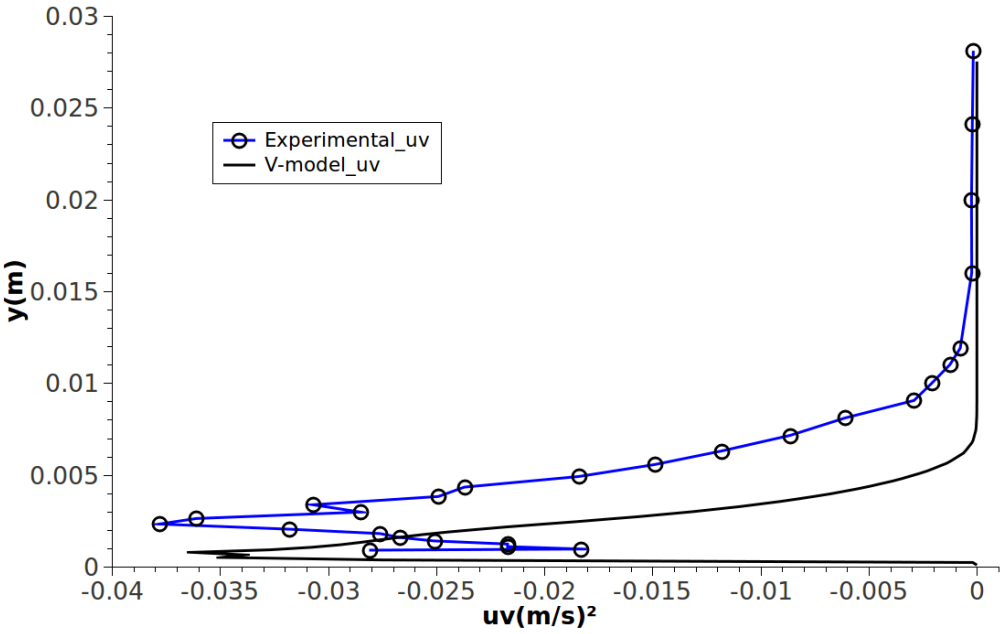

Figure 4.39: Comparison of ERCOFTAC flat-plate T3C2 experimental $\overline{u'v'}$ values with those predicted by the transition V-model in the axial position of 0.895 meters or Rex of 46.75×10^4.

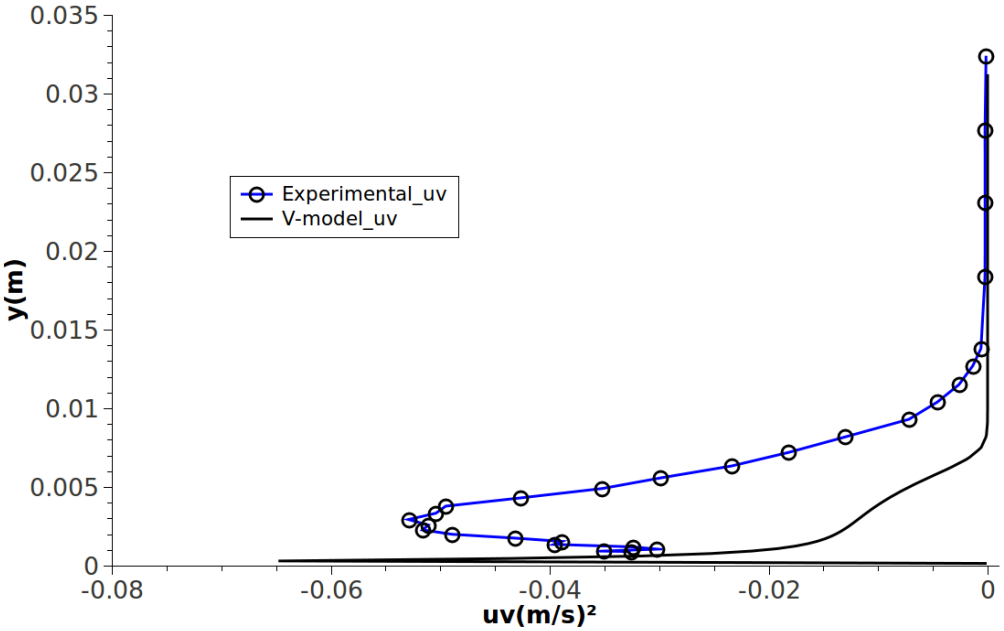

Figure 4.40: Comparison of ERCOFTAC flat-plate T3C2 experimental $\overline{u'v'}$ values with those predicted by the transition V-model in the axial position of 0.995 meters or Rex of 51.59×10^4.

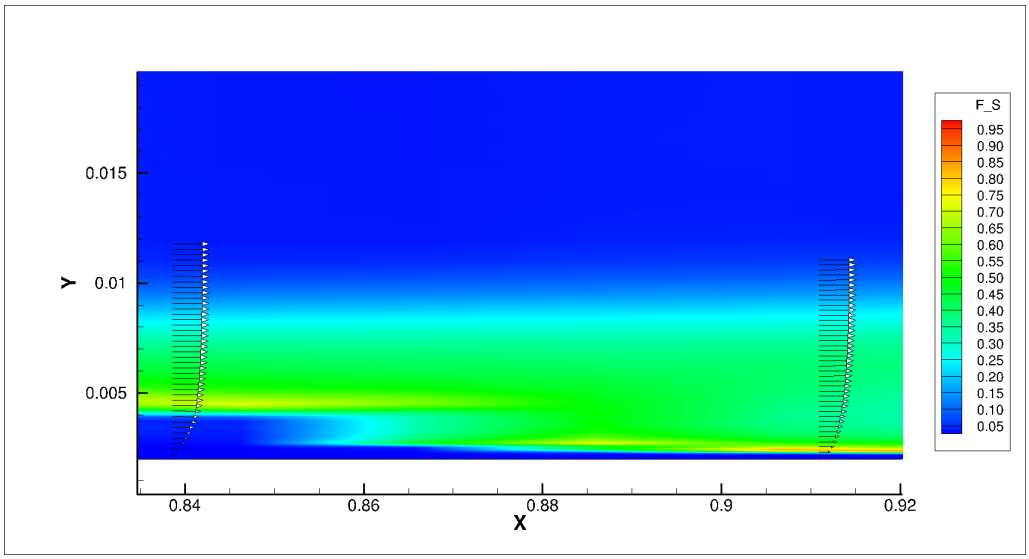

Figure 4.41: Evolution on the transition onset region of the scale function between mean flow shear and turbulence scales.

culated pre-transitional $\overline{u'v'}$ distribution near the leading edge of the flat-plate. The V-model then approaches to the experimental data measurements up until Rex of 13.21×10^4. From the measurements at Rex of 18.26×10^4 until the station of transition onset, the V-model predicts a lower maximum peak value of $\overline{u'v'}$. This under prediction evolution by the V-model was not observed in the zero-pressure-gradient analyzed T3A test case. However, the V-model restores the maximum peak value of $\overline{u'v'}$, on the measuring station located at Rex of 46.75×10^4. This corresponds to the region where the V-model has already predicted the laminar boundary layer piercing by the $\overline{u'v'}$ values, in other words, the transition onset. At this stage, there is a large band in the transition boundary layer where the scale functions are closer to unity. Otherwise, it can be said that the turbulent and mean flow scales are similar in almost all over the boundary layer wall-normal extension. This can be observed in Fig.4.41. The presented scale function is related to the mean flow shear.

4.1.2.3 T3C3 flat-plate validation

The flat-plate pressure-gradient transition test case considered here was the ERCOFTAC T3C3 case. The experimentally applied turbulent flow conditions were performed in order to observe turbulent bypass transition under adverse-pressure-gradient. The turbulence transition onset was set to happen prior to flow separation on the diverging region of the T3C experimental benchmark configuration. The specified inlet boundary conditions for all tested transition and turbulence models are presented in table 4.8. The turbulence intensity decay rate for the specified inlet boundary conditions is presented in Fig.4.42. The results for the T3C3 test case are presented in Fig.4.43. Again the discrepancy between the computed and experimental values of skin-friction coefficient are due to an incorrect value of free-stream velocity used on the process of non-dimensionalization. As can be observed, the V-SA model's transition onset prediction is in accordance with the experimental data. This is calculated at the correct transition Reynolds number prior to flow separation. Nonetheless, the skin-friction coefficient of the critical point is lower than the experimental data. Again, this might be related to the aforementioned free-stream velocity applied on the process of non-dimensionalization. The SA turbulence closure transits to fully turbulent regime earlier than expected. The empiri-

Table 4.8: ERCOFTAC T3C3 Flat-plate Inlet Boundary Conditions

Model	$U(m/s)$	$k(m^2/s^2)$	$k_p(m^2/s^2)$	$\omega(s^{-1})$	$\tilde{\nu_t}(m^2/s)$
SA	3.7	N/A	N/A	N/A	4.5×10^{-5}
V-SA	3.7	N/A	0.01848	N/A	4.5×10^{-5}
V-SA-Sep-Correct	3.7	N/A	0.01848	N/A	4.5×10^{-5}
V-SA-Improved	3.7	N/A	0.01848	N/A	4.5×10^{-5}
k-k_l-ω-org	3.7	0.05	N/A	55	N/A
k-k_l-ω-mod	3.7	0.05	N/A	55	N/A
k-k_l-ω	3.7	0.05	N/A	55	N/A
γ-Re_θ	3.7	0.05	N/A	592	N/A

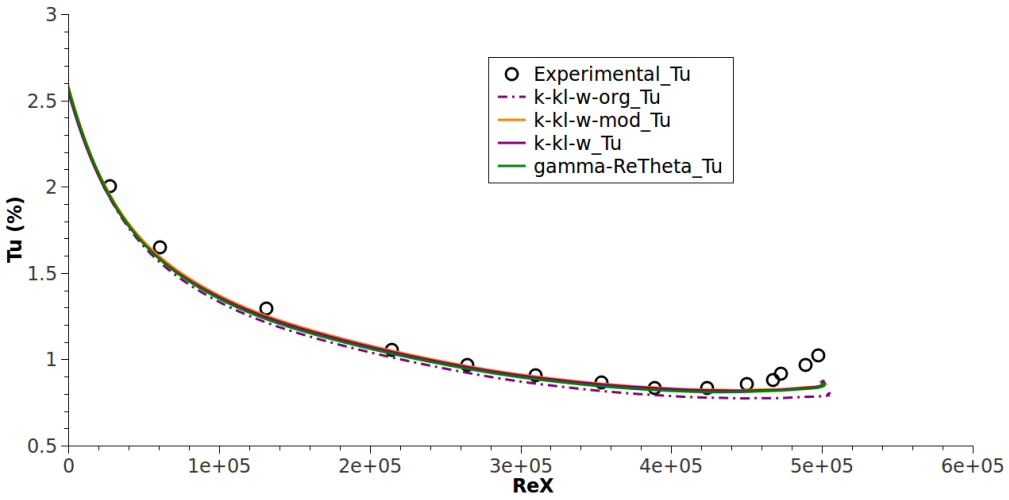

Figure 4.42: Flat-plate T3C3 turbulence intensity decay.

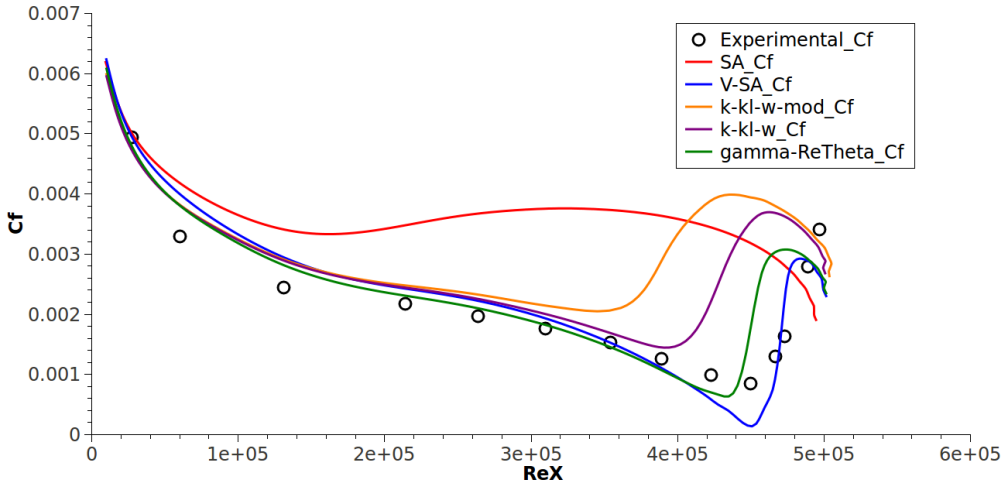

Figure 4.43: Comparison of experimental data from ERCOFTAC T3C3 flat-plate test case skin-friction coefficient distribution with the turbulence SA closure and the transition V-SA, k-k$_l$-ω-mod, k-k$_l$-ω and γ-Re_θ models. The flat-plate leading edge radius size is 0.002 meters.

cally correlated, γ-Re_θ, transition model also displays a good transition onset prediction. The phenomenological, k-k$_l$-ω-mod and k-k$_l$-ω, transition closures compute an early beginning of transition. The modified version predicts the earliest result of the two models. The usage of a smaller flat-plate leading edge radius of 0.00075 meters alters the previously presented results. These are then displayed in Fig.4.44. The SA turbulence model results remain unchanged. The V-SA closure computes a slightly earlier transition onset, whereas the V-SA-Sep-Correct model predicts a later transition onset. The latter is computed after flow separation. This is not in accordance to the experimental data, since this test case is suppose to detect bypass transition prior to flow separation. The V-SA-Fluent-Implementation model presents a similar behavior to the V-SA-Sep-Correct closure. On the other hand, the V-SA-Improved turbulence transition model correctly predicts the bypass transition prior to flow separation at the exact transition Reynolds number. It can be noticed that the k-k$_l$-ω transition model greatly improves on the computed transition point. Yet, its modified version predicts transition onset earlier than expected. Nevertheless, the k-k$_l$-ω-org predicts a low skin-friction coefficient turbulent region with a transition onset even earlier than both the k-k$_l$-ω transition model versions. Also, the γ-Re_θ closure apparently is unaffected by the reduction of the flat-plate leading edge radius, as it computes transition onset at almost the same position.

4.1.2.4 T3C4 flat-plate validation

The following flat-plate pressure-gradient transition benchmark is the ERCOFTAC T3C4. This case has the particular characteristic of testing transition under strong adverse-pressure-gradient conditions. The flow actually separates before turbulence transition onset as will be observed in both numerical results and experimental data. The specified inlet boundary conditions for all tested transition and turbulence models are presented in table 4.9. The decay rate of the free-stream turbulence intensity over the flat-plate obtained with the applied inlet boundary conditions in table 4.9, is disclosed in Fig.4.45. This validates the used inlet free-stream turbulent characteristics. Shown in Fig.4.46, the results for the pressure-gradient T3C4 test case demonstrate that the V-SA model predicts transition onset near the experimen-

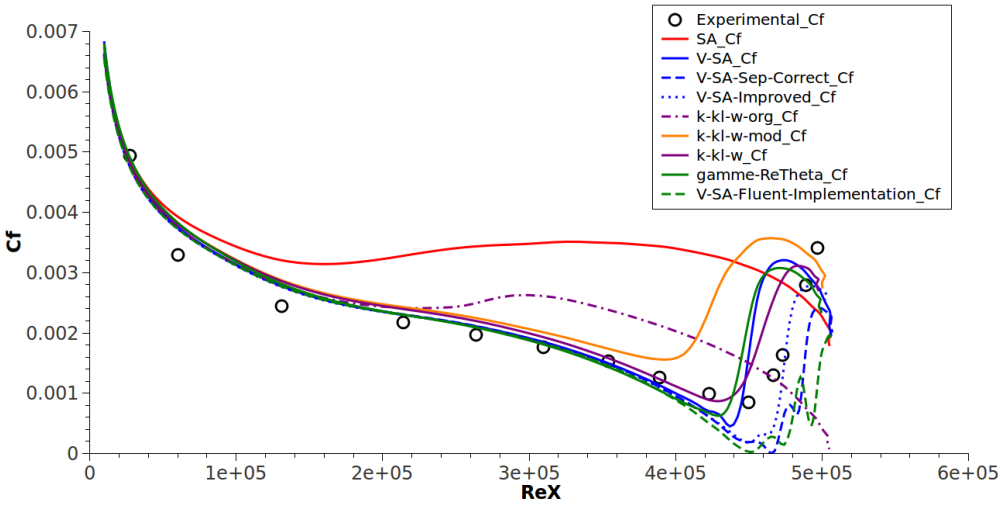

Figure 4.44: Comparison of experimental data from ERCOFTAC T3C3 flat-plate test case skin-friction coefficient distribution with the turbulence SA closure and the transition V-SA, V-SA-Sep-Correct, V-SA-Improved, V-SA-Fluent-Implementation, k-k_l-ω-org, k-k_l-ω-mod, k-k_l-ω and γ-Re_θ models. The flat-plate leading edge radius size is 0.00075 meters.

Table 4.9: ERCOFTAC T3C4 Flat-plate Inlet Boundary Conditions

Model	$U(m/s)$	$k(m^2/s^2)$	$k_p(m^2/s^2)$	$\omega(s^{-1})$	$\tilde{\nu_t}(m^2/s)$
SA	1.2	N/A	N/A	N/A	4.5×10^{-5}
V-SA	1.2	N/A	0.001944	N/A	4.5×10^{-5}
V-SA-Sep-Correct	1.2	N/A	0.001944	N/A	4.5×10^{-5}
V-SA-Improved	1.2	N/A	0.001944	N/A	4.5×10^{-5}
k-k_l-ω-org	1.2	0.02	N/A	55	N/A
k-k_l-ω-mod	1.2	0.02	N/A	55	N/A
k-k_l-ω	1.2	0.02	N/A	55	N/A
γ-Re_θ	1.2	0.02	N/A	592	N/A

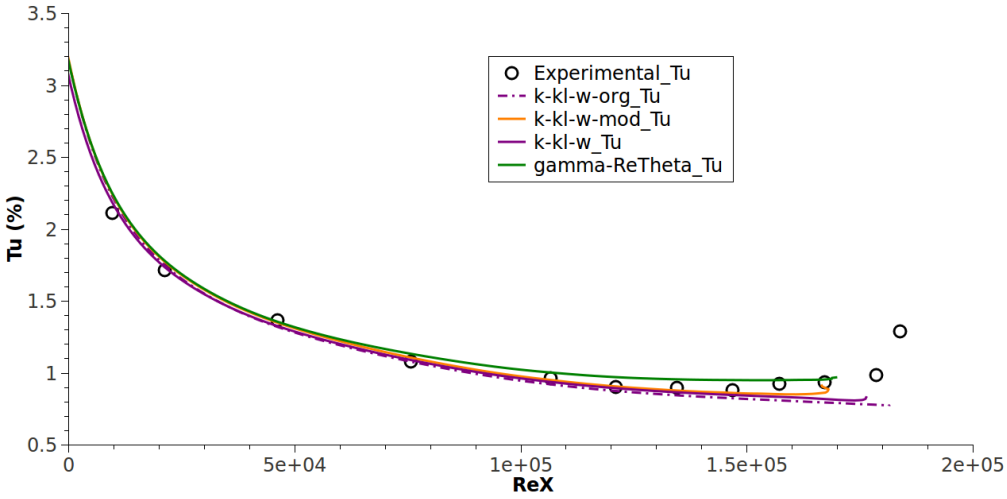

Figure 4.45: Flat-plate T3C4 turbulence intensity decay.

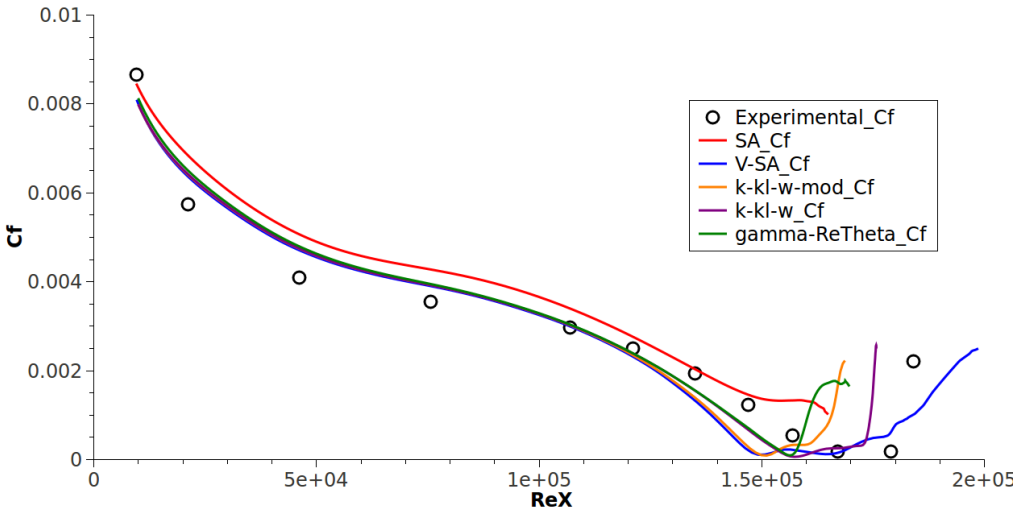

Figure 4.46: Comparison of experimental data from ERCOFTAC T3C4 flat-plate test case skin-friction coefficient distribution with the turbulence SA closure and the transition V-SA, k-k_l-ω-mod, k-k_l-ω and γ-Re_θ models. The flat-plate leading edge radius size is 0.002 meters.

tal measurements. The V-SA model correctly predicts separation induced transition at the very end of the flat-plate. This behavior is also observed in the results obtained with the γ-Re_θ, k-k_l-ω and the k-k_l-ω-mod. However, the V-SA model displays a slightly sluggish turbulent ramp up of skin-friction coefficient to the experimentally recorded values. The SA model does not predict flow separation over the flat-plate. As can be seen in the results, the SA model plot-line has a shorter length than the V-SA. Although both models were computed in the same mesh, the local free-stream velocities are different. For the V-SA model, since flow separates, the apparent cross-section of the duct is reduced, thus the local free-stream velocity is higher than the attached flow computation from the SA closure. This will then result in different end Reynolds numbers for the plots. The overall effect of the usage of a reduced leading edge radius is presented in Fig.4.47. As expected, the flat-plate leading edge radius does not greatly influence the results. This is the case since the radius reduction does not influence the imposed pressure-gradient conditions. Taking into consideration the fact that, in the present benchmark test case, transition is triggered by flow separation and this in turn is conditioned by flow adverse-pressure-gradient conditions, therefore the transition onset should remain unchanged for a leading edge radius reduction. There is of course the case of a considerable leading edge radius increase, which might force the flow to separate prematurely, causing an earlier separation induced transition. Nonetheless, the V-SA transition model improved the transition length when compared to the computed results of the larger radius test case. The V-SA-Sep-Correct and V-SA-Improved models calculate a similar skin-friction coefficient curve to the V-SA computed result. The V-SA-Fluent-Implementation transition closure displays an extensive and delayed transition threshold region. The k-k_l-ω-org closure presents a similar behavior to the original k-k_l-ω transition model.

4.1.2.5 T3C5 flat-plate validation

The last flat-plate pressure-gradient transition test case was the ERCOFTAC T3C5. Similar to the T3C1, this case evaluates bypass transition for favorable-pressure-gradients. However, the

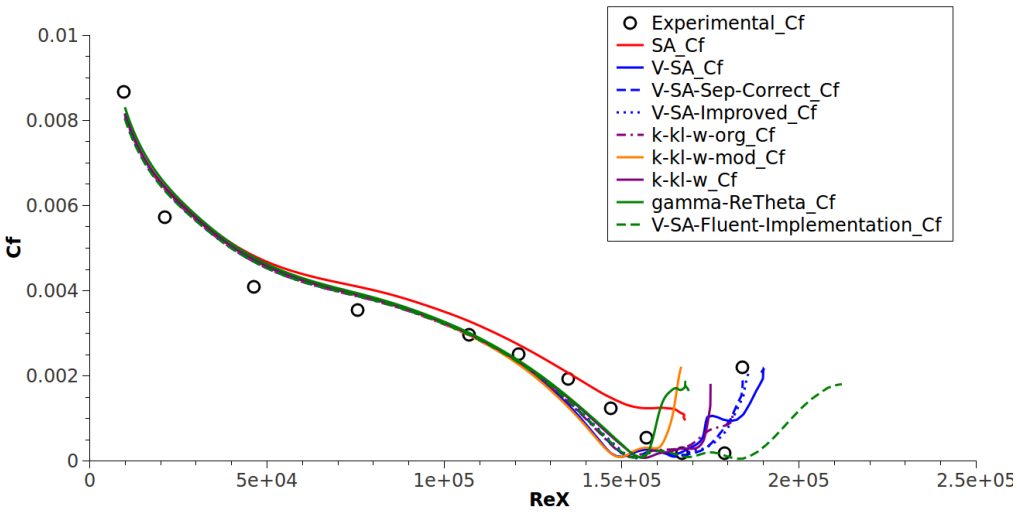

Figure 4.47: Comparison of experimental data from ERCOFTAC T3C4 flat-plate test case skin-friction coefficient distribution with the turbulence SA closure and the transition V-SA, V-SA-Sep-Correct, V-SA-Improved, V-SA-Fluent-Implementation, k-k_l-ω-org, k-k_l-ω-mod, k-k_l-ω and γ-Re_θ models. The flat-plate leading edge radius size is 0.00075 meters.

Table 4.10: ERCOFTAC T3C5 Flat-plate Inlet Boundary Conditions

Model	$U(m/s)$	$k(m^2/s^2)$	$k_p(m^2/s^2)$	$\omega(s^{-1})$	$\tilde{\nu_t}(m^2/s)$
SA	8.4	N/A	N/A	N/A	4.5×10^{-5}
V-SA	8.4	N/A	0.09525	N/A	4.5×10^{-5}
V-SA-Sep-Correct	8.4	N/A	0.09525	N/A	4.5×10^{-5}
V-SA-Improved	8.4	N/A	0.09525	N/A	4.5×10^{-5}
k-k_l-ω-org	8.4	0.22	N/A	85	N/A
k-k_l-ω-mod	8.4	0.22	N/A	85	N/A
k-k_l-ω	8.4	0.22	N/A	85	N/A
γ-Re_θ	8.4	0.22	N/A	915	N/A

free-stream velocity is much higher and the turbulence intensity is approximately half of the first flat-plate pressure-gradient example. The specified inlet boundary conditions for all tested transition and turbulence models are presented in table 4.10. The free-stream turbulence intensity decay rate using these inlet turbulent flow characteristics is shown in Fig.4.48. The T3C5 skin-friction coefficient experimental and numerical results are presented in Fig.4.49. The empirically correlated model, γ-Re_θ, displays the previously mentioned anomalous transition behavior. The phenomenological models, k-k_l-ω and k-k_l-ω-mod, are able to calculate transition close to the experimental data. The modified closure version computes transition earlier than its original model. As can be seen, the V-SA model predicts transition onset to turbulence close to the experimental data, similar to the result of k-k_l-ω. The SA turbulence closure computes fully turbulent flow regime early near the flat-plate leading edge. The obtained results for the same case with the flat-plate leading edge radius of 0.00075 meters are presented in Fig.4.50. Although the γ-Re_θ closure delays transition inception compared to the bigger radius flat-plate result, this delay is too large. For the present case, this transition model shows high sensitivity to the used leading edge radius of the flat-plate. Despite the fact that the k-k_l-ω transition closure presents a delay on transition prediction, its modified version, the k-k_l-ω-mod, predicts transition onset close to the experimental data. The k-k_l-ω-org transition model computes an early transition with a low value of skin-friction coefficient on the turbulent region. The

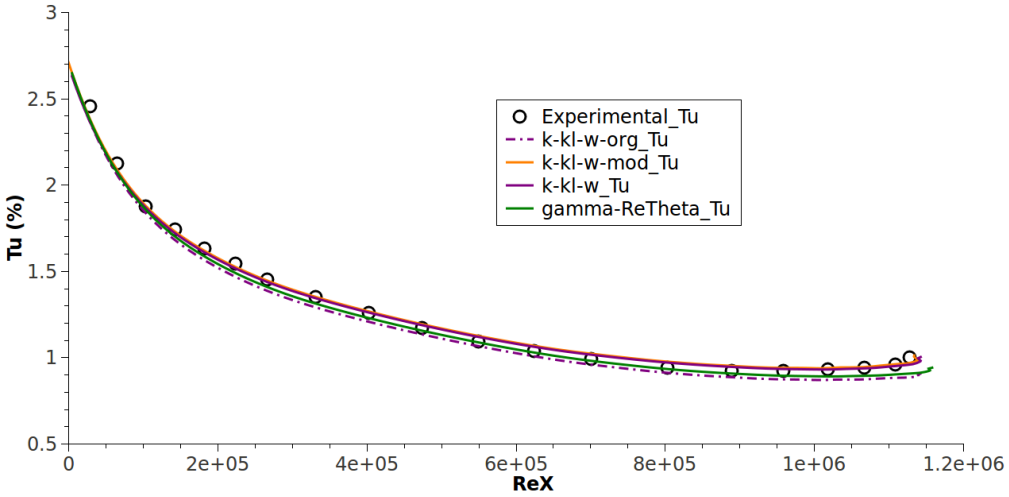

Figure 4.48: Flat-plate T3C5 turbulence intensity decay.

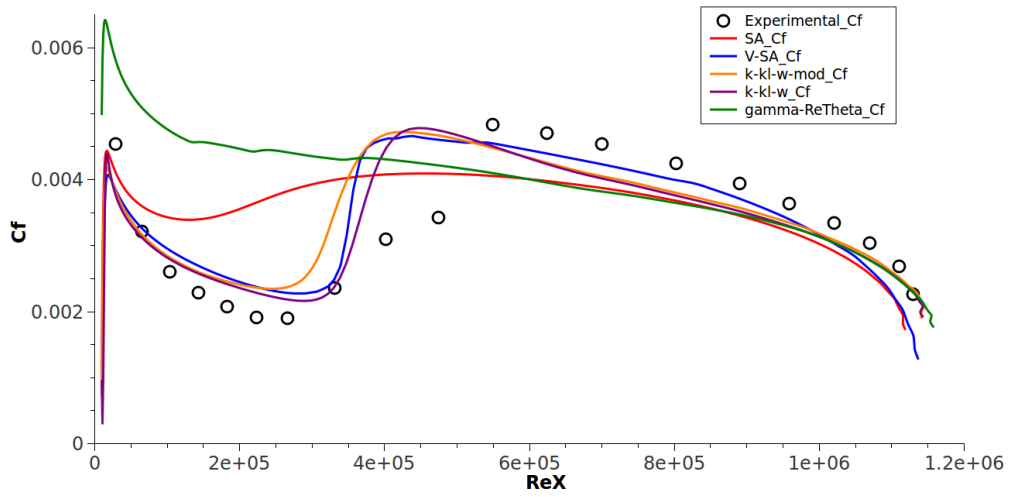

Figure 4.49: Comparison of experimental data from ERCOFTAC T3C5 flat-plate test case skin-friction coefficient distribution with the turbulence SA closure and the transition V-SA, k-k_l-ω-mod, k-k_l-ω and γ-Re_θ models. The flat-plate leading edge radius size is 0.002 meters.

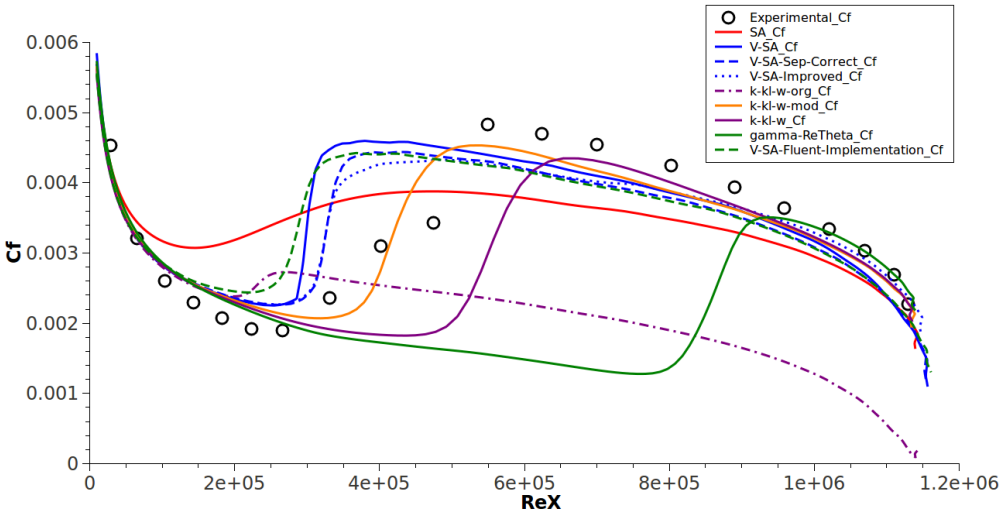

Figure 4.50: Comparison of experimental data from ERCOFTAC T3C5 flat-plate test case skin-friction coefficient distribution with the turbulence SA closure and the transition V-SA, V-SA-Sep-Correct, V-SA-Improved, V-SA-Fluent-Implementation, k-k_l-ω-org, k-k_l-ω-mod, k-k_l-ω and γ-Re_θ models. The flat-plate leading edge radius size is 0.00075 meters.

Table 4.11: ERCOFTAC T3L Flat-Plate Upstream Conditions

$Case$	$Tu(\%)$	$U(m/s)$
$T3L1$	0.2	5.0
$T3L3$	2.3	5.0
$T3L5$	2.3	2.5

V-SA transition closure predicts the transition Reynolds number near the experimental value. Both the V-SA-Sep-Correct and the V-SA-Improved transition models, are able to compute an accurate transition onset Reynolds number compared to the experimental recorded Reynolds number value. Compared to these three transition models, the V-SA-Fluent-Implementation closure discloses a slightly earlier transition onset prediction. Finally, the SA turbulence closure computes an early developed fully turbulent boundary layer.

4.1.3 Separation test cases

As mentioned earlier, the ERCOFTAC T3L test cases of separation induced transition were considered for validation purposes. The importance of such validation is made clear in the work of Hadzic and Hanjalic [10]. The experimental results from Coupland and Brierley [162], were used for the present validation. Flow separation will be highly influenced by the fluid properties. As such, the fluid kinematic viscosity used was the experimental value of $\nu = 1.6 \times 10^{-5}\,(m^2/s)$. The mesh geometry is similar to the zero-pressure-gradient test cases. The main difference is in the flat-plate leading edge. The leading edge has a curvature radius of 0.005 meters, which is in accordance with the experimental setup. Along the leading edge the mesh has 60 nodes. The separation induced transition flat-plate geometry leading edge mesh is presented in Fig.4.51. The geometry boundary condition types distribution is identical to the used mesh for the zero-pressure-gradient test cases. The upstream conditions for the considered test cases are presented in table 4.11. The following inlet boundary conditions tables will only display a single entry for the V-SA transition model. These should be interpreted

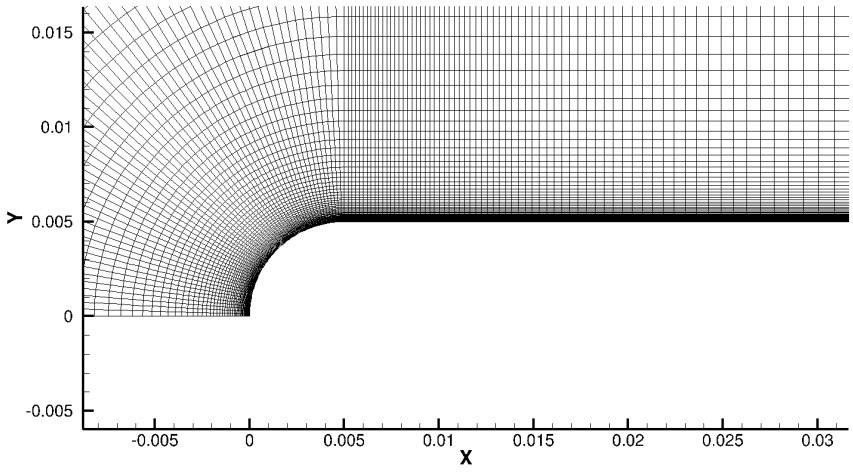

Figure 4.51: Separation induced transition flat-plate leading edge mesh view.

Table 4.12: ERCOFTAC T3L1 Flat-plate Inlet Boundary Conditions

Model	$U(m/s)$	$k(m^2/s^2)$	$k_p(m^2/s^2)$	$\omega(s^{-1})$	$\tilde{\nu}_t(m^2/s)$
SA	5	N/A	N/A	N/A	8×10^{-5}
V-SA	5	N/A	1.5×10^{-4}	N/A	8×10^{-5}
k-k$_l$-ω-org	5	2×10^{-4}	N/A	5	N/A
k-k$_l$-ω-mod	5	2×10^{-4}	N/A	5	N/A
k-k$_l$-ω	5	2×10^{-4}	N/A	5	N/A
γ-Re_θ	5	2×10^{-4}	N/A	100	N/A

as the applied conditions for all of the used V-SA transition model variants.

4.1.3.1 T3L1 flat-plate validation

The presently analyzed separation induced transition test case is the T3L1. This experimental case setup was devised in order to capture separation triggered transition onset for very low free-stream turbulence intensity. As can be observed in table 4.11, this is far below 1%. The specified inlet boundary conditions for all tested transition and turbulence models are presented in table 4.12. The results for this case are presented in Fig.4.52. A mesh refinement study is performed using a mesh with the double number of nodes. The computations where done using the SA turbulence model. The refine mesh results show that the turbulence closure transition onset is slightly delayed. Nevertheless, the fully turbulent region is the same as the regular mesh results. Although the SA model refine mesh results present a transition shift, this is small. Therefore the results can be considered to be mesh independent. The flat-plate leading edge oscillations of skin-friction coefficient are due to laminar-boundary layer separation. The Spalart-Allmaras low-Reynolds turbulence closure predicts transition onset in accordance to the experimental values. Nonetheless, the model shows low values for skin-friction coefficient in both transition and fully turbulent region. Both the V-SA-0-002 and V-SA-0-00075, calibrated with the flat-plate leading edge radius of 0.002 and 0.00075 meters respectively, are unable to predict the transition onset after the initial separation bubble formation. Still, both of these models eventually compute transition onset far later over the flat-plate. The presented results exposed a problem with the V-model based transition closures under these turbulence and flow

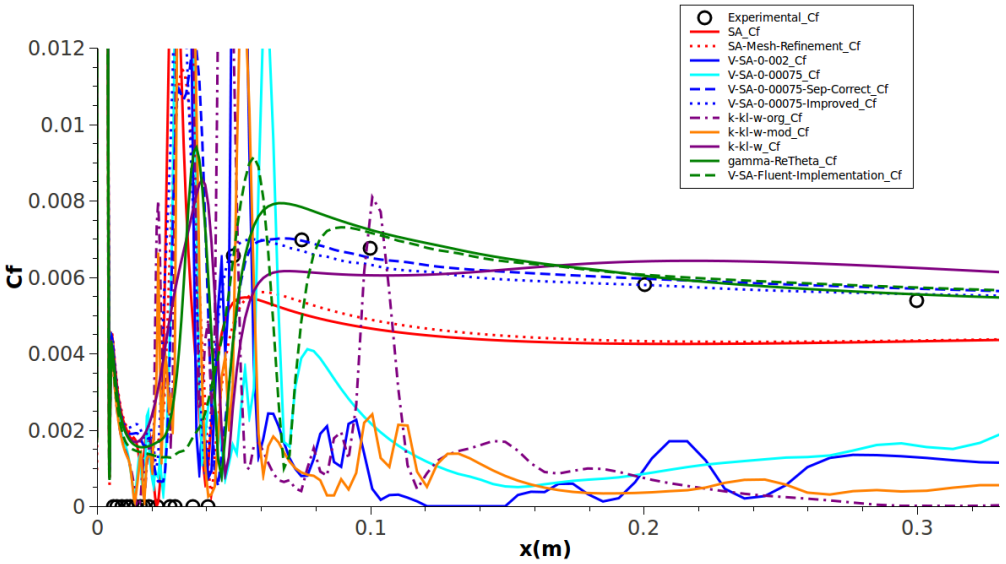

Figure 4.52: Comparison of experimental data from ERCOFTAC T3L1 flat-plate test case skin-friction coefficient distribution with the turbulence SA closure and the transition V-SA-0-002, V-SA-0-00075, the V-SA-0-00075 separation corrected, improved and fluent implementation versions, k-k_l-ω-org, k-k_l-ω-mod, k-k_l-ω and γ-Re_θ models. The flat-plate leading edge oscillations of skin-friction coefficient are due to flow separation.

conditions. This issue has been understood as an excessive effect of the V-model destruction term $-\Omega^2 \nu F_\Omega$. Due to the turbulence and flow conditions of very low speed and low turbulence intensity the resulting pre-transitional turbulence kinetic energy is very small. Consequently the vorticity field, generated by the leading edge induced flow separation, will obliterate the existing pre-transitional turbulent kinetic energy. Therefore, a separation correction was devised and applied to the V-SA-0-00075 transition model. This correction diminishes the effect of the V-model destruction term in flow regions where mean flow vorticity is higher than mean flow shear. The obtained results with this correction have been previously shown throughout the present chapter as the V-SA-Sep-Correct results. As can be seen in Fig.4.52, the corrected model is able to predict the transition onset accurately. It also shows one of the best behavior after transition threshold amongst the tested models. Since the V-SA-Fluent-Implementation model is the V-SA-Sep-Correct closure implemented on Fluent through an UDF, this is able to compute the separation induced transition. Nevertheless, this is predicted later than the OpenFoam implementation. The V-SA-Improved transition model presents a transition behavior very similar to the V-SA-Sep-Correct closure. The k-k_l-ω phenomenological transition model is also accurate in determining the streamwise position of turbulence transition. Still, this model shows an abnormal distribution of skin-friction coefficient afterwards and high values within the fully turbulent region. Even though the k-k_l-ω-org and k-k_l-ω-mod transition models are not based on the V-model, these fail to capture separation induced transition near the experimental data. Both of these closures predict turbulence transition far later over the flat-plate. The γ-Re_θ empirical transition closure presents a correct transition onset prediction compared to the experimental data. Although the model shows higher values of skin-friction coefficient in the transition peak, the fully turbulent region is correctly computed.

Table 4.13: ERCOFTAC T3L3 Flat-plate Inlet Boundary Conditions

Model	$U(m/s)$	$k(m^2/s^2)$	$k_p(m^2/s^2)$	$\omega(s^{-1})$	$\tilde{\nu_t}(m^2/s)$
SA	5	N/A	N/A	N/A	8×10^{-5}
V-SA	5	N/A	0.0198	N/A	8×10^{-5}
k-k$_l$-ω-org	5	0.0235	N/A	5	N/A
k-k$_l$-ω-mod	5	0.0235	N/A	5	N/A
k-k$_l$-ω	5	0.0235	N/A	5	N/A
γ-Re_θ	5	0.0235	N/A	60	N/A

4.1.3.2 T3L3 flat-plate validation

The second separation induced transition test case considered has a higher turbulence intensity than that of the T3L1 experimental conditions. The specified inlet boundary conditions for all tested transition and turbulence models are presented in table 4.13. The T3L3 ERCOFTAC flat-plate test case results are presented in Fig.4.53. Again the flat-plate leading edge oscillations of skin-friction coefficient are due to boundary layer separation. The Spalart-Allmaras turbulence model computes a late turbulence transition compared to the experiment. Furthermore, the model generally presents lower values of skin-friction coefficient both in the transition region and fully turbulent flow extension. The V-SA-0-002, V-SA-0-00075 and its separation corrected and improved versions predict transition onset on the same streamwise position as the Spalart-Allmaras turbulence model. Therefore all of these models display a late turbulence transition threshold compared to the experimental data. However, the V-SA-0-00075 transition model, the separation correction variant, V-SA-0-00075-Sep-Correct, and its improved version, V-SA-0-00075-Improved, compute a fully turbulent skin-friction coefficient distribution closer to the experimental data. Again the V-SA-Fluent-Implementation presents a delayed transition prediction compared to its OpenFoam implementation, V-SA-0-00075-Sep-Correct. The k-k$_l$-ω turbulence transition closure computes the latest transition threshold. Further, this model presents an irregular behavior after its computed transition onset as can be seen in its fully turbulent extension of Fig.4.53. The k-k$_l$-ω-mod transition closure, shows a similar behavior to the original k-k$_l$-ω model, however, the transition onset is slightly earlier and its skin-friction coefficient peak value is lower. The k-k$_l$-ω-org model presents an initial behavior similar to the SA turbulence model, however, the turbulent skin-friction coefficient value is low. The γ-Re_θ transition model is able to precisely account for the separation induced turbulence transition onset. Notwithstanding, this closure computes higher values of skin-friction coefficient in the presented results. This is especially evident in the transition onset skin-friction coefficient peak value. However, the model presents the most accurate transition length compared to the remaining numerical results. Besides the Spalart-Allmaras turbulence closure and the k-k$_l$-ω-org, all of the turbulence transition models present a distribution of skin-friction coefficient values higher than the experimental data within the fully turbulent boundary layer.

4.1.3.3 T3L5 flat-plate validation

The last considered separation induced transition experimental benchmark is the T3L5. The specified inlet boundary conditions for all tested transition and turbulence models are presented in table 4.14. The T3L5 test case results are presented in Fig.4.54. For all the presented turbulence and transition models, the flat-plate leading edge oscillations of skin-friction coefficient are due to flow separation. Contrary to the T3L1 numerical results, the presently discussed plot shows that for all tested models there is less oscillation of the skin-friction

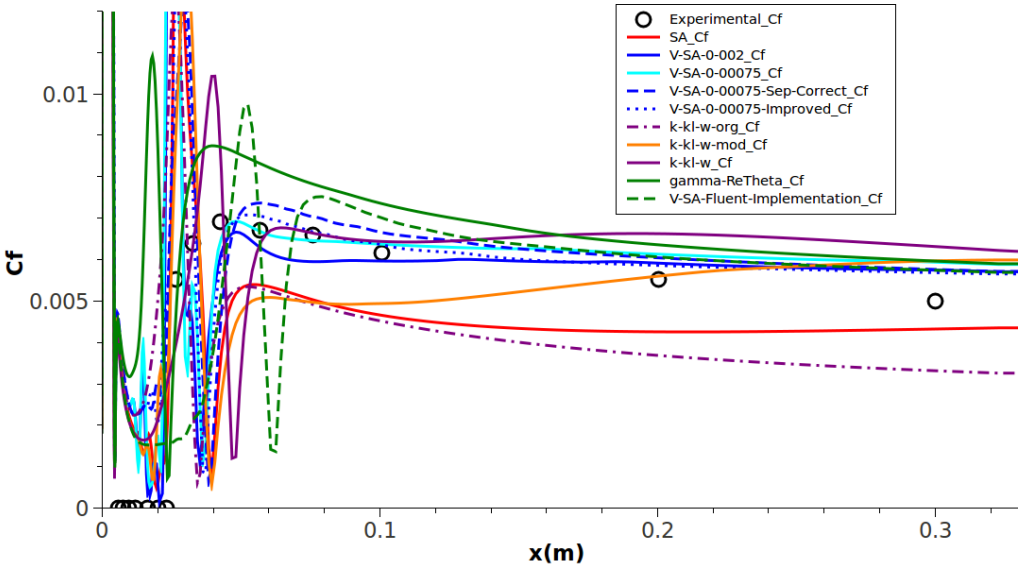

Figure 4.53: Comparison of experimental data from ERCOFTAC T3L3 flat-plate test case skin-friction coefficient distribution with the turbulence SA closure and the transition V-SA-0-002, V-SA-0-00075, the V-SA-0-00075 separation corrected, improved and fluent implementation versions, k-k_l-ω-org, k-k_l-ω-mod, k-k_l-ω and γ-Re_θ models. The flat-plate leading edge oscillations of skin-friction coefficient are due to flow separation.

Table 4.14: ERCOFTAC T3L5 Flat-plate Inlet Boundary Conditions

Model	$U(m/s)$	$k(m^2/s^2)$	$k_p(m^2/s^2)$	$\omega(s^{-1})$	$\tilde{\nu_t}(m^2/s)$
SA	2.5	N/A	N/A	N/A	8×10^{-5}
V-SA	2.5	N/A	0.00496	N/A	8×10^{-5}
k-k_l-ω-org	2.5	0.0065	N/A	5	N/A
k-k_l-ω-mod	2.5	0.0065	N/A	5	N/A
k-k_l-ω	2.5	0.0065	N/A	5	N/A
γ-Re_θ	2.5	0.0065	N/A	50	N/A

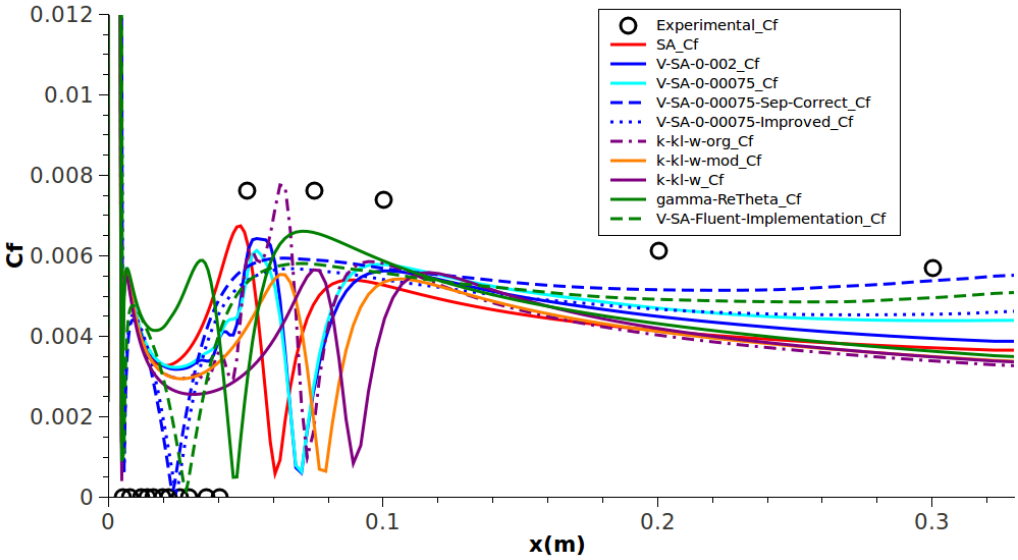

Figure 4.54: Comparison of experimental data from ERCOFTAC T3L5 flat-plate test case skin-friction coefficient distribution with the turbulence SA closure and the transition V-SA-0-002, V-SA-0-00075, the V-SA-0-00075 separation corrected, improved and fluent implementation versions, k-k_l-ω-org, k-k_l-ω-mod, k-k_l-ω and γ-Re_θ models. The flat-plate leading edge oscillations of skin-friction coefficient are due to flow separation.

coefficient values within the separated flow region. This is due to the formation of a single separation bubble. The Spalart-Allmaras turbulence closure predicts a slightly longer separation bubble, thus a later transition to turbulence compared to the experimental measurements. The V-SA-0-002 turbulence transition closure obtained results show that the closure predicts transition onset later than the Spalart-Allmaras model. The V-SA-0-00075 transition model displays an almost identical transition behavior to the V-SA-0-002 closure. This same turbulence transition model with the separation correction, V-SA-0-00075-Sep-Correct, predicts the transition onset earlier than any other turbulence transition closure. Although this corrected transition model has an apparent early transition threshold, its streamwise position of transition skin-friction coefficient peak value occurs very close to the experimentally recorded data. Both the V-SA-Improved and V-SA-Fluent-Implementation transition models disclose a similar behavior to the V-SA-0-00075-Sep-Correct closure with a small delay. The k-k_l-ω turbulence transition model predicts the largest separation bubble, followed by its modified version the k-k_l-ω-mod and the original implementation, the k-k_l-ω-org. Therefore these models predict the latest separation induced transition onset points. As for the empirically-correlated transition model, γ-Re_θ, this presents the best behavior in predicting the beginning of transition. Also, the model predicts the highest skin-friction coefficient peak value closest to the experimental data. It can be said that in general all of the turbulence and transition models have a similar behavior in the fully turbulent region. Nonetheless, taking into consideration the experimental distribution of skin-friction coefficient, all of the models predict a lower value than the recorded data both in the transition and fully turbulent flow region. Yet, all transition and turbulence closures will develop the previously mentioned abnormal behavior of the k-k_l-ω model. This is an increase of the skin-friction coefficient after the transition onset. The V-SA-0-00075-Sep-Correct is the first model to display this distribution. The remaining models late skin-friction coefficient increase is disclosed in Fig.4.55.

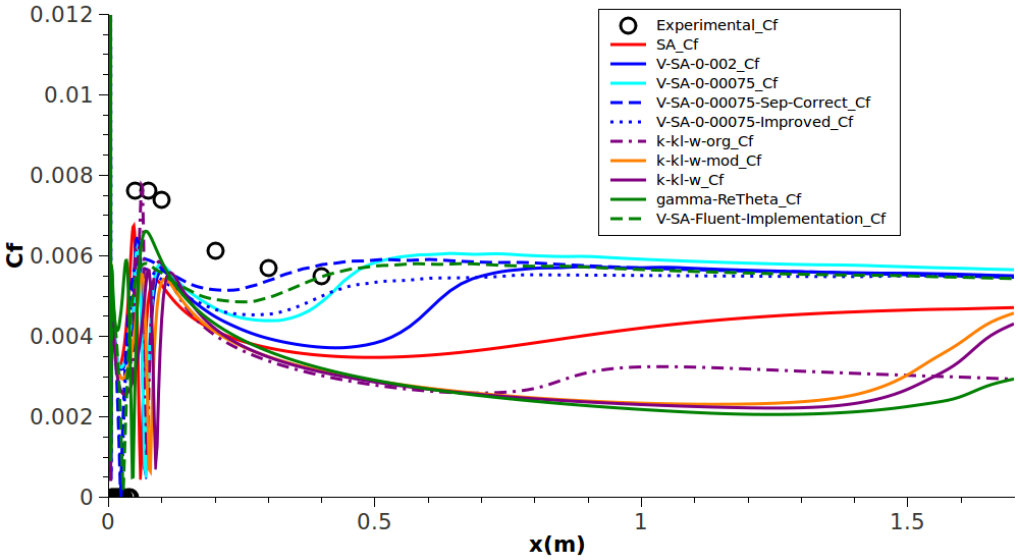

Figure 4.55: Comparison of experimental data from ERCOFTAC T3L5 flat-plate test case skin-friction coefficient distribution with the turbulence SA closure and the transition V-SA-0-002, V-SA-0-00075, the V-SA-0-00075 separation corrected, improved and fluent implementation versions, k-k_l-ω-org, k-k_l-ω-mod, k-k_l-ω and γ-Re_θ models. The flat-plate leading edge oscillations of skin-friction coefficient are due to flow separation. Full flat-plate extension.

4.1.4 Summary of results

A turbulence model and a selection of transition models available in the commercial software, Ansys Fluent 13.0, were tested together with the developed transition closures. This evaluation was performed making use of the flat-plate transition test case collection of ERCOFTAC.

It was concluded that altering small geometrical characteristics affects most of the presented numerical results. The change of the flat-plate leading edge radius from 0.002 meters to the experimentally used value of 0.00075 meters has a profound effect on the development of the pre-transitional region. In general, the leading edge radius reduction induces a later transition onset prediction by the tested transition models.

The empirical transition model, γ-Re_θ, shows an abnormal behavior for bypass transition near the flat-plate leading edge. Also the model shows high sensitivity to the leading edge radius under the ERCOFTAC T3C5 flat-plate test case. Nevertheless, this closure presents the best behavior for the separation induced transition test cases of the T3L benchmark study. In general, the commercial software transition models, γ-Re_θ and the k-k_l-ω, are reliable transition tools.

The modified version of the k-k_l-ω phenomenological model, k-k_l-ω-mod, was developed with the intent of predicting transition similar to the k-k_l-ω. This objective has been partially achieved, as the model follows the behavioral trends of the k-k_l-ω transition closure with a far better performance than its original implementation, k-k_l-ω-org. However, this still requires further development in order to be considered as reliable as its original transition model.

The developed V-SA transition model was evaluated for two calibrations. Also corrections were applied to the model in order to overcome the difficulties encountered in separated flow conditions. The V-SA model variants apparently fail to correctly predict natural transition. For

the remaining tested flat-plate cases, this transition model displays reasonable transition onset results. The applied separation correction is effective and has a reduced effect on the overall performance of the model.

Although the prediction of the pre-transitional $\overline{u'v'}$ values is not perfect, it is close to the experimentally measured data. As such, it can be concluded that the proposed V-SA transition model is indeed able to capture some of the pre-transition physical phenomenons.

Chapter 5

Airfoil benchmark

The purpose of this chapter is to present the first application of the developed transition model to some of the most significant geometries in the aeronautic industry, the airfoils. These are the cornerstone of any aeronautic endeavor.

5.1 Two-dimensional airfoil test cases

After the developed transition models validation over the simplistic, but fundamental, flat-plate test cases, more complex geometries were chosen to further validate the developed transition to turbulence detection tools. For all presented airfoil results, the used computational mesh was structured and had y^+ values below 0.1 over the entire airfoil surface. With exception of the T106 turbine blade, the following mesh description is valid for all presented airfoil test cases. The chord length of all airfoils is of 1 meter. The number of mesh points along the surface of the airfoils is 800 nodes. This is divided between the upper and lower sides of the airfoils. The computational mesh nodes are more densely distributed near the leading and trailing edges of the airfoils. The mesh far-field is located at approximately 15 chords away from the airfoil. The number of mesh nodes along the direction normal to the airfoil and far-field surfaces is of 150 points. These cluster near the airfoils surface resulting in a wall perpendicular spacing of the first layer of cells of 1×10^{-6} meters. An overview of the airfoil's surrounding farfield geometry mesh topology is shown in Fig.5.1.

The used wall boundary conditions for the applied turbulence and transition models follow the same settings presented in the "ERCOFTAC benchmark" chapter. The applied numerical and fluid characteristics for all tested cases, with exception of the T106 turbine blade test case, are the same as those disclosed in section "Flat-plate test cases".

5.1.1 NREL airfoils for HAWTs

The development of specialized airfoils for HAWTs, or horizontal-axis wind-turbines, began in 1984 with the National Renewable Energy Laboratory, NREL, and the Airfoils, Incorporated [163]. Most of the previously used HAWT airfoils were initially developed for airplane wings. These were designed according to requirements of the National Advisory Committee for Aeronautics (NACA) and National Aeronautics and Space Administration (NASA). Therefore, an effort to create an airfoil specifically for horizontal-axis wind turbine use was required. This resulted in the Eppler Airfoil Design and Analysis Program [164] and [165]. The latter produced multiple airfoil concepts such as the S805 and S809. These airfoils were studied theoretically and experimentally verified. This was performed in the lowest turbulence intensity wind tunnel available at the time. The experiment took place at the Delft University of Technology Low Speed Laboratory, The Netherlands. This was a low turbulence intensity wind tunnel with a maximum free-stream turbulence intensity of less than 0.05%. Thus the reported results were obtained in free-atmospheric conditions.

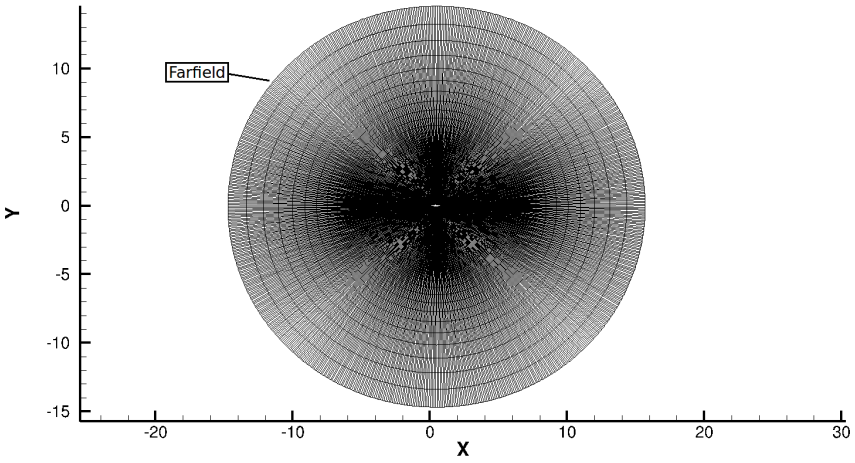

Figure 5.1: General overview of airfoil far-field mesh topology with 120000 nodes.

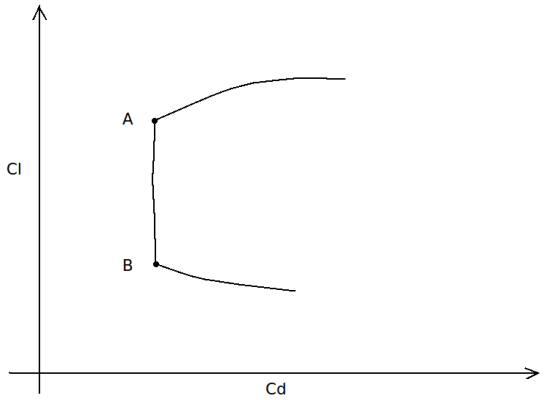

Figure 5.2: Bucket shape drag polar characteristics. Points A and B delimit the low drag region of the operational envelope for the airfoil. Adapted from [5].

5.1.1.1 S805 airfoil validation

The S805 airfoil is mainly used in wind turbine energy generation. The airfoil design was conducted in order to fulfill two main objectives. The first design objective for this airfoil was a characteristic moderate low maximum lift coefficient. The second objective was the constraint of a low drag-profile under a minimum and maximum lift coefficient range of 0.5 to 0.9 for the Reynolds number of 1×10^6. Therefore, the design philosophy of these type of airfoils is based on the concept of producing a bucket shape drag polar such as the one shown in Fig.5.2. The airfoil design and experimental data presented here was obtained from the technical report of Somers [5].

As reported in [166], the wind tunnel at the Delft University of Technology Low Speed Laboratory presented a variation range of turbulence intensity levels from 0.02% to 0.04% for the velocities of $10m/s$ and $60m/s$ respectively. As such, since the used free-stream velocities were $15m/s$ and $30m/s$, an approximate low-free-stream turbulence intensity value of 0.03% was chosen to represent the wind tunnel test conditions. The test case computation was conducted using the SA turbulence closure and the V-SA transition model with the separation correction and its improved version. The used transition closure is then the one calibrated for the ERCOFTAC flat-plate leading edge radius of 0.00075 meters. This particular calibration was

Table 5.1: NREL S805 Airfoil Inlet Boundary Conditions

Model	$U(m/s)$	$k_p(m^2/s^2)$	$\tilde{\nu}_t(m^2/s)$
SA	15	N/A	1×10^{-4}
V-SA-Sep-Correct	15	3.038×10^{-5}	1×10^{-4}
V-SA-Improved	15	3.038×10^{-5}	1×10^{-4}
SA	30	N/A	1×10^{-4}
V-SA-Sep-Correct	30	1.22×10^{-4}	1×10^{-4}
V-SA-Improved	30	1.22×10^{-4}	1×10^{-4}

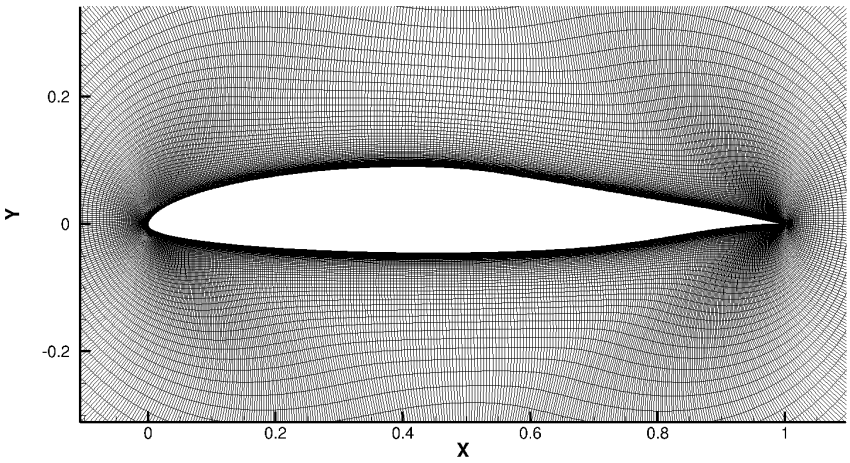

Figure 5.3: S805 airfoil detail mesh view. The airfoil has 800 nodes over its surface with a total number of mesh points of 120000.

selected since it represents a more authentic calibration based on the experimental geometry specifications. The used inlet boundary conditions for all tested angles of attack over the S805 airfoil are presented in table 5.1.

A mesh independence test was performed using a computational mesh with double number of nodes. The S805 airfoil near surrounding mesh is shown in Fig.5.3. The results of this validation were focused on the distribution of skin-friction coefficient over the top surface of the airfoil. These are presented in Fig.5.4. As can be observed, there is almost no change from the used mesh to the refined case. Therefore, this geometry computational results are considered mesh independent.

The flow transition threshold points over the upper and lower surfaces of the airfoil were obtained by inspection of the skin-friction coefficient curve over these. The obtained distribution of transition points for flow Reynolds number of 1×10^6, is presented in Fig.5.5. The SA turbulence model presents a distribution of the transition onset points that vary with the flow AoA. These transition points are not in accordance with the experimental data. With exception of extreme AoA values, the SA model predicts earlier transition regions over the airfoil upper and lower surfaces. The V-SA-Sep-Correct transition closure is able to predict with some accuracy most of the transition onset points in accordance with the experiment. However, this does not include the fast transition point movement over the upper surface of the airfoil. The V-SA-Improved transition model presents a very similar transition onset prediction behavior to the separation corrected V-SA model.

The airfoil drag polar distribution for the same flow Reynolds number is presented in Fig.5.6.

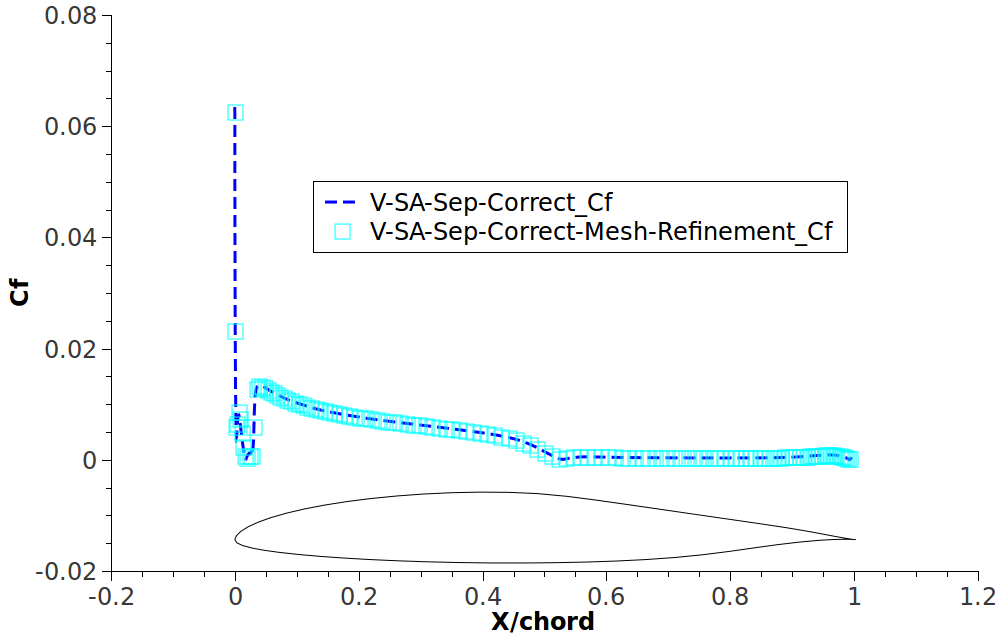

Figure 5.4: Mesh independence test using skin-friction coefficient value distribution over the S805 airfoil top surface at an AoA of 12° for Reynolds number of 1×10^{6}.

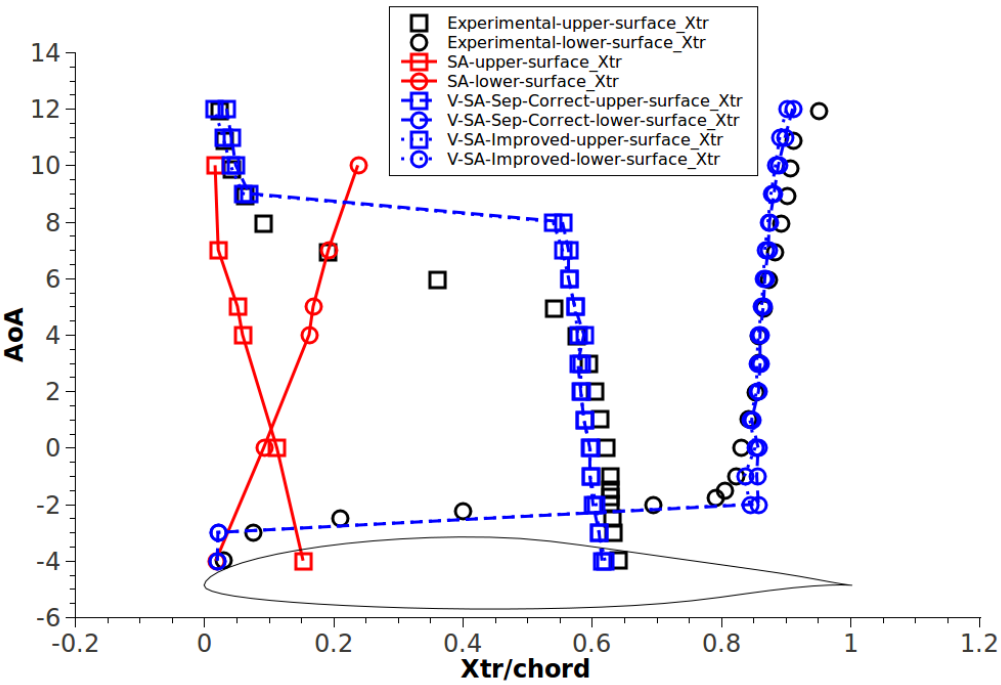

Figure 5.5: Experimental data comparison of transition onset points over the S805 airfoil upper and lower surfaces with computed results from the turbulence SA closure and the transition V-SA-Sep-Correct and V-SA-Improved models. The flow Reynolds number is 1×10^{6}.

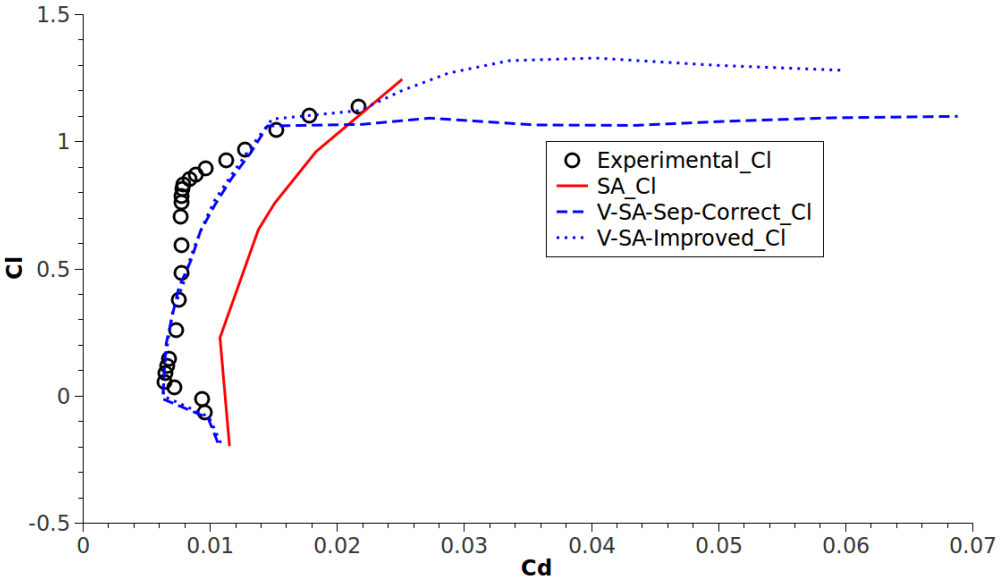

Figure 5.6: Experimental data comparison of the drag polar of the S805 airfoil with computed results from the turbulence SA closure and the transition V-SA-Sep-Correct and V-SA-Improved models. The flow Reynolds number is 1×10^6.

The experimental drag polar has the desired bucket shape. The V-SA-Sep-Correct model is able to correctly predict the lift to drag coefficient ratio for most of the tested angles. For the upper branch of the drag polar, the V-SA-Sep-Correct closure predicts slightly higher values of drag coefficient than those obtained in the experiment. The V-SA-Improved model computes a drag polar similar to the V-SA-Sep-Correct closure, showing only some improvement on the drag polar upper tip extension. For the SA turbulence model case, the computed drag polar presents a shape with higher drag coefficient values.

It should be noticed that the computed V-SA-Sep-Correct drag polar presents an apparent down shift in comparison to the experimental data for the high values of lift coefficient, as if the predicted lift coefficient is less than the expected. For this reason, an evaluation of the lift coefficient with AoA is presented in Fig.5.7. As can be seen, the V-SA-Sep-Correct transition model does indeed predict slightly lower values of lift coefficient. This is more pronounced for the higher AoA range, approximately between 9° and 15°. However, for the same AoA range, the V-SA-Improved transition model computes higher values of lift coefficient than was expected. The SA turbulence closure predicts the highest values of lift coefficient.

Although the latter analysis clarifies the V-SA model variants computed lift coefficients, this can not account for the large deviation from the experimental data at high angles of attack of both the V-SA transition models within the lift to drag plot results of Fig.5.6. As such, another analysis of the drag coefficient with AoA is disclosed in Fig.5.8. As can be seen, for the range of AoA from -4° to 8°, the V-SA-Sep-Correct model predicts a lower drag coefficient over the airfoil than the SA turbulence model. This is to be expected, since the V-SA-Sep-Correct transition closure predicts an initial laminar boundary layer extension over the airfoil while the SA closure assumes fully turbulent boundary layer flow from the leading edge region of the geometry. Nevertheless, for higher angles of attack, the V-SA-Sep-Correct transition model increases drastically its computed drag coefficient, surpassing even that predicted by the SA model at an AoA of 10°. The V-SA-Improved transition model improves on this issue. In order to understand what is causing this behavior a flow-field view at the AoA of 10° is disclosed in Fig.5.9. It is

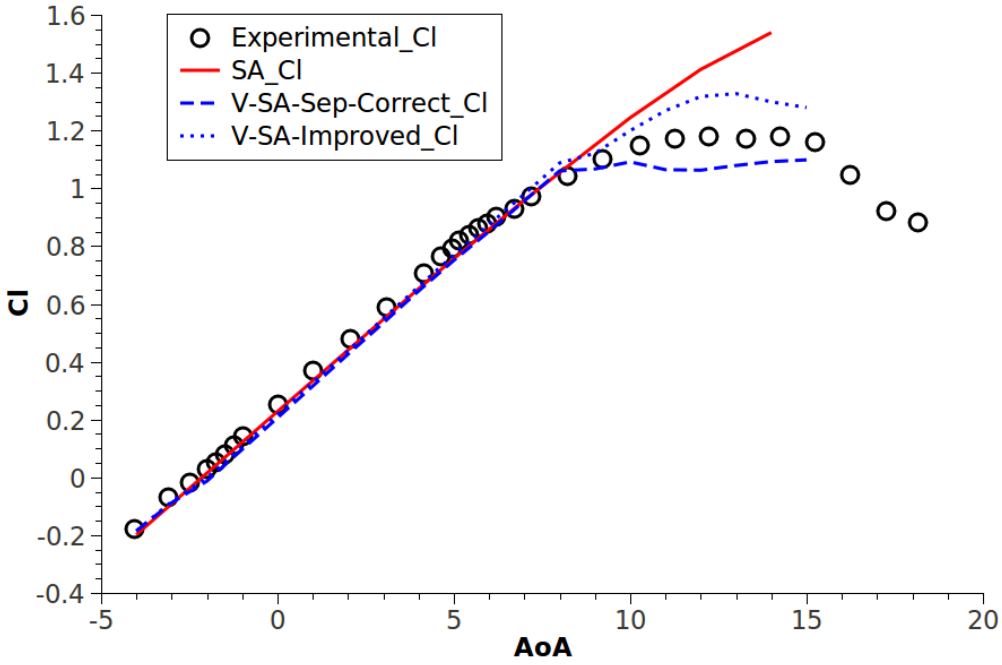

Figure 5.7: Experimental data comparison of lift coefficient with AoA for the S805 airfoil with computed results from the turbulence SA closure and the transition V-SA-Sep-Correct and V-SA-Improved models. The flow Reynolds number is 1×10^6.

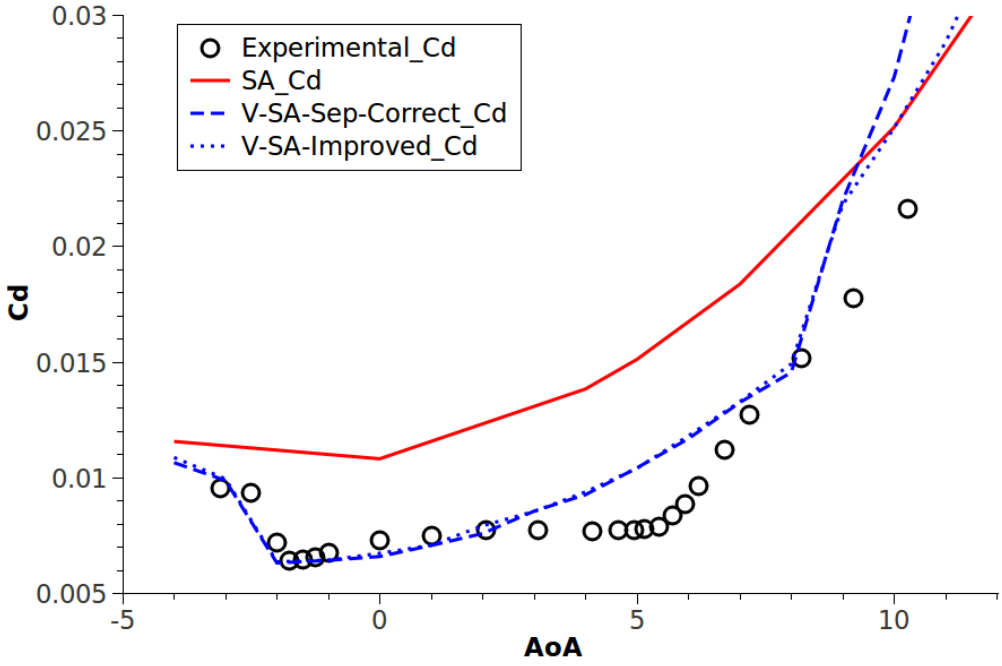

Figure 5.8: Experimental data comparison of drag coefficient with AoA for the S805 airfoil with computed results from the turbulence SA closure and the transition V-SA-Sep-Correct and V-SA-Improved models. The flow Reynolds number is 1×10^6.

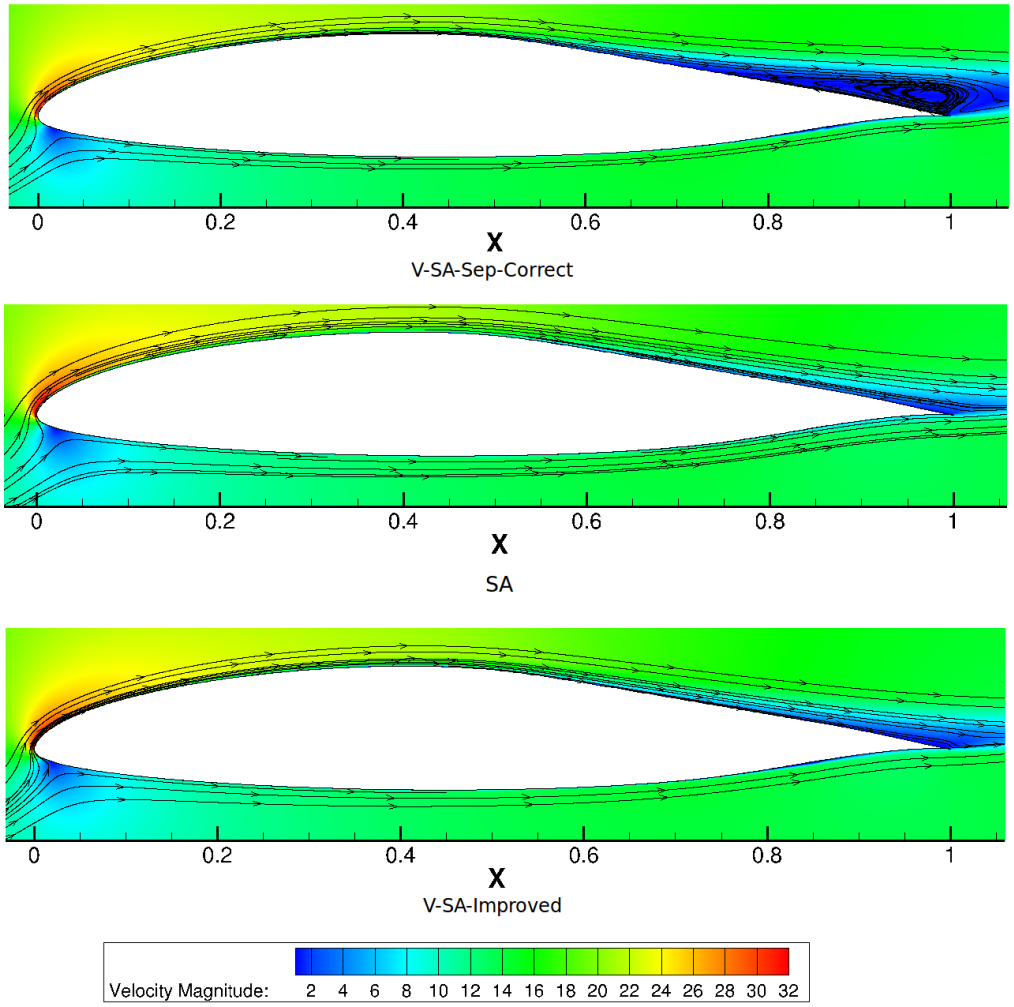

Figure 5.9: Comparison of flow stream-lines with velocity magnitude contour under an AoA of 10° for the S805 airfoil between computed results from the turbulence SA closure and the transition V-SA-Sep-Correct and V-SA-Improved models. The flow Reynolds number is 1×10^6.

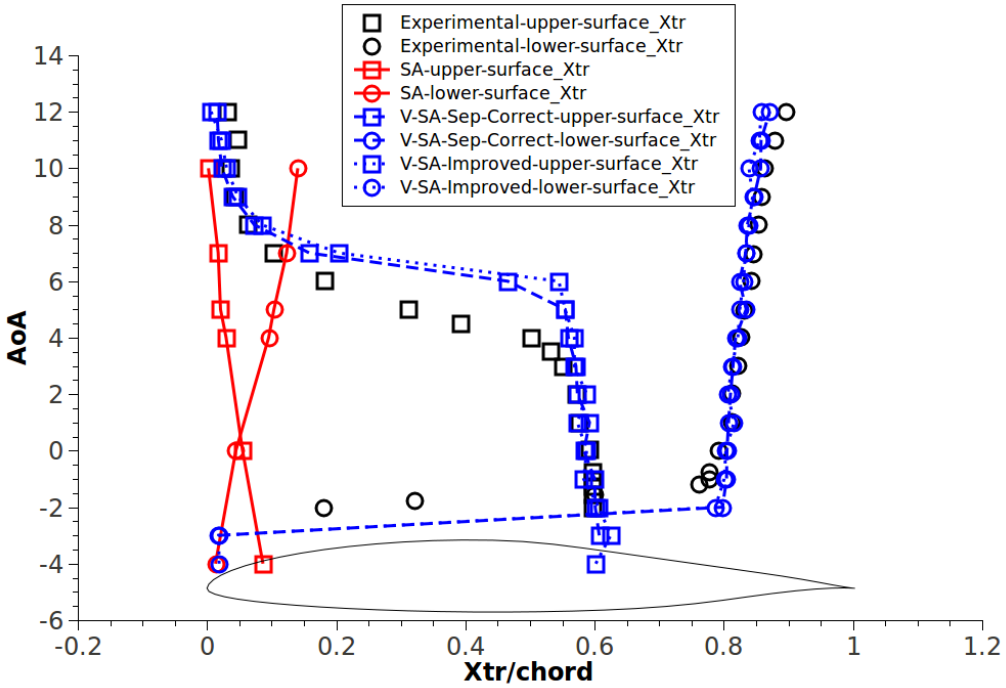

Figure 5.10: Experimental data comparison of transition onset points over the S805 airfoil upper and lower surfaces with computed results from the turbulence SA closure and the transition V-SA-Sep-Correct and V-SA-Improved models. The flow Reynolds number is 2×10^6.

possible to conclude that, at the AoA of $10\,^\circ$ or higher, the reason why the V-SA-Sep-Correct turbulence transition model increases its drag coefficient is due to flow separation as shown in Fig.5.9. Although the transition closure is already under full turbulent regime, it predicts flow separation. However, the SA turbulence model computes an attached flow over the entire airfoil surface. The V-SA-Improved model computes the flow turbulent extension as attached to the airfoil surface. Additionally, for the AoA range of $3\,^\circ$ to $7\,^\circ$, both transition models present higher values of drag coefficient when compared to experimental data. This is due to the delay presented by both transition models, that were not able to correctly capture the fast transition shift over the upper surface of the airfoil as disclosed in Fig.5.5.

For comparison purposes, the transition onset evolution and drag polar results were also obtained for flow Reynolds number of 2×10^6. Therefore, the upper and lower airfoil surface evolution of transition threshold points with angle of attack is presented in Fig.5.10. Similar conclusions to the latter lower Reynolds number case can be withdrawn from the comparison between experimental and numerical results. Nonetheless, it must be noted that for both the V-SA-Sep-Correct and V-SA-Improved transition models the fast transition shift over the airfoil upper surfaces is predicted with a smaller delay in relation to the experimental data, with a slightly larger delay by the improved transition model version.

The S805 airfoil drag polar for flow Reynolds number of 2×10^6 is presented in Fig.5.11. The experimental results for the flow Reynolds number of 2×10^6 differ slightly from the lower Reynolds number flow of 1×10^6 test case. The most pronounced difference regards the maximum lift coefficient value of the top corner from the bucket shape base of the drag polar. For the low Reynolds flow case this value of lift coefficient is 0.9, while for the high Reynolds case this is roughly 0.7. The SA turbulence model predicts a drag polar again with larger values of drag coefficient. Both the V-SA-Sep-Correct and V-SA-Improved transition models are able to

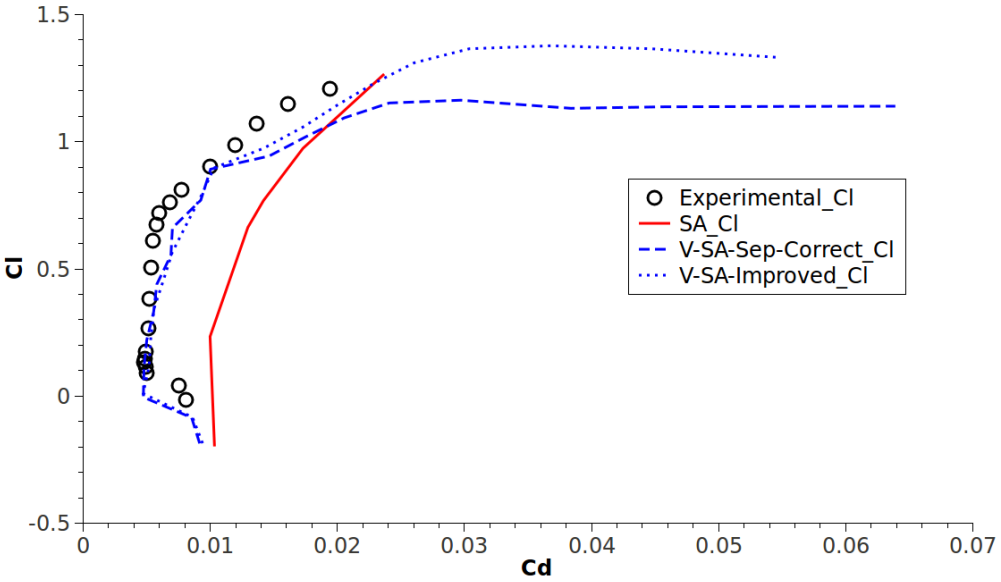

Figure 5.11: Experimental data comparison of the drag polar of the S805 airfoil with computed results from the turbulence SA closure and the transition V-SA-Sep-Correct and V-SA-Improved models. The flow Reynolds number is 2×10^6.

Table 5.2: NREL S809 Airfoil Inlet Boundary Conditions

Model	$U(m/s)$	$k_p(m^2/s^2)$	$\tilde{\nu}_t(m^2/s)$
SA	30	N/A	1×10^{-4}
V-SA-Sep-Correct	30	1.22×10^{-4}	1×10^{-4}
V-SA-Improved	30	1.22×10^{-4}	1×10^{-4}

predict a reasonable drag polar compared to the experimental data. However, for the higher lift coefficient range the lift to drag ratio, computed by the V-SA-Sep-Correct transition closure, deviates more noticeably from the experimental data. The V-SA-Improved turbulence transition model presents results closer to the experimental data at this high AoA range.

5.1.1.2 S809 airfoil validation

Similar to the S805 airfoil, the S809 was created for wind turbine energy generation. The airfoil design was also conducted in order to fulfill the objectives of a characteristic moderate low maximum lift coefficient and a constant low drag-profile for a lift coefficient range. The main difference between the S809 and the S805 airfoil is on the second objective characteristics. This is then the imposition of a low drag-profile under a minimum and maximum lift coefficient range of 0.2 to 0.8 for the Reynolds number of 2×10^6. The disclosed airfoil design and experimental data was obtained from the technical report of Somers [167]. Other sources of data can also be found in the experimental work of Ramsay et al. [168, 169].

Analogous to the previous S805 airfoil case, this benchmark test case computation was performed using the SA turbulence closure and the separation corrected and improved V-SA transition model versions, V-SA-Sep-Correct and V-SA-Improved. The applied inlet boundary conditions for all tested angles of attack over the S809 airfoil are presented in table 5.2.

Resembling the previous airfoil test case, a mesh refinement validation was also performed for the S809 airfoil. This was executed using a computational mesh which has the double

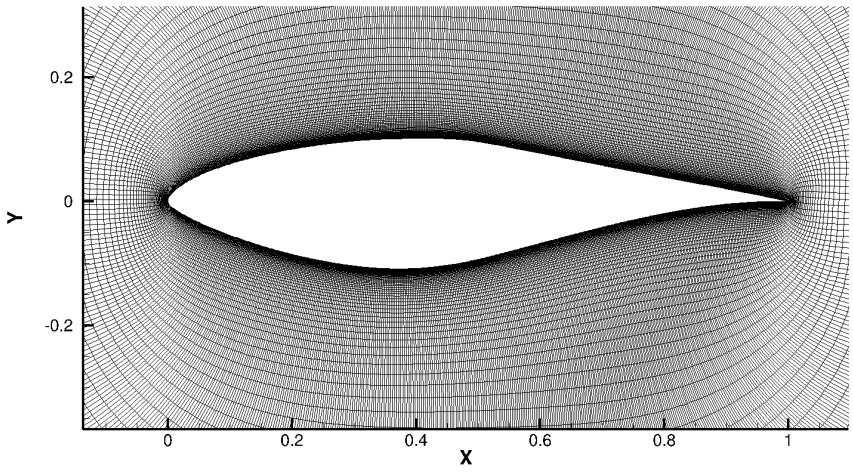

Figure 5.12: S809 airfoil detail mesh view. The airfoil has 800 nodes over its surface with a total number of mesh points of 120000.

number of nodes. The S809 airfoil neighboring mesh is disclosed in Fig.5.12. The computed results of skin-friction coefficient over the top surface of the airfoil are disclosed in Fig.5.13. Although there is a small skin-friction coefficient value deviation at the leading edge of the airfoil, the remaining surface results are equal. The refined mesh predicts a slightly lower value of skin-friction coefficient at the leading edge. As such, the S809 airfoil computational mesh results are considered to be mesh independent.

For flow Reynolds number of 2×10^6, the transition onset regions were recorded for both upper and bottom sides of the airfoil. The obtained results are presented in Fig.5.14. In general the SA turbulence model predicts transition onset points earlier than the experimental recorded data. The V-SA-Sep-Correct closure is able to predict most of the transition onset regions close to the experimental data points. The improved V-SA transition model, V-SA-Improved, computes the transition threshold points similar to the V-SA-Sep-Correct closure. Although the V-SA-Improved model computes the upper surface transition shift with a very small delay, the lower surface transition behavior shows an improvement when compared to the V-SA-Sep-Correct closure.

The obtained airfoil drag polar is presented in Fig.5.15. The SA turbulence closure shows a drag polar with higher drag coefficient values compared to the experimental data. The V-SA-Sep-Correct transition model computes an accurate drag polar for most of its extent, with exception for the very low negative AoA range. The improved V-SA transition model, V-SA-Improved, computes better results at these negative AoA values. The remaining drag polar plot is almost equal to the V-SA-Sep-Correct transition closure.

5.1.2 Aerospatiale A-airfoil validation

The Aerospatiale A-airfoil has mostly been used for turbulence research [170]. The presented experimental data was obtained by ONERA in the F1 and F2 wind tunnels [171]. Additionally, works such as [172] [173] and [174], constitute some of the experimental data sources for this airfoil. Most of the numerical works focus mainly on validation of RANS turbulence models and LES simulations [175] [176] and [177]. The considered experiment was the F2 wind tunnel airfoil test case. This was conducted over the Aerospatiale A-airfoil for an angle of attack of $13.3\,^{\circ}$.

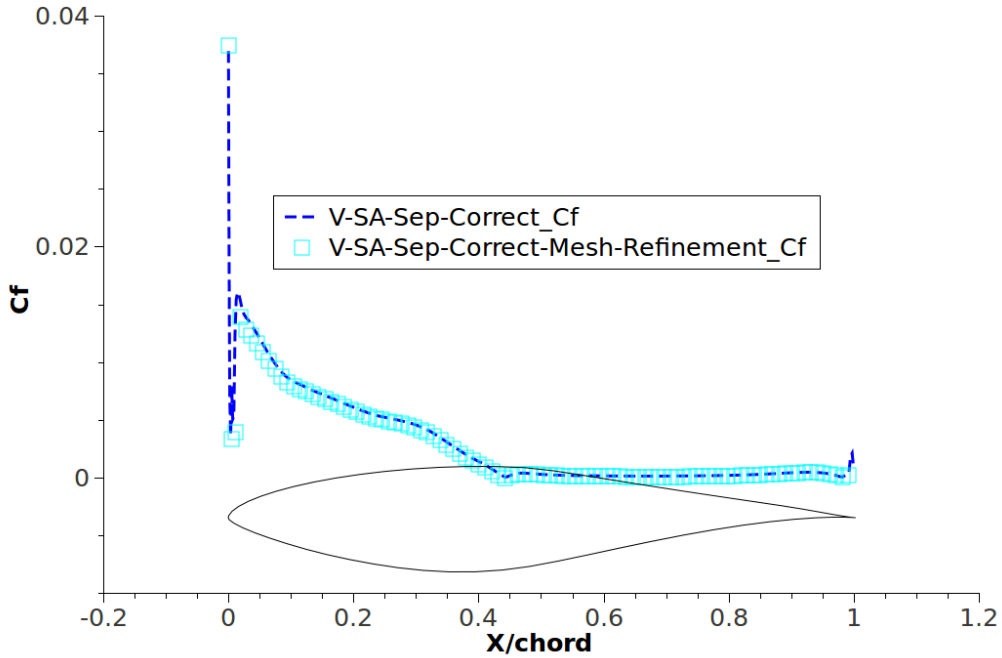

Figure 5.13: Mesh independence test using skin-friction coefficient value distribution over the S809 airfoil top surface at an AoA of 15° for Reynolds number of 2×10^6.

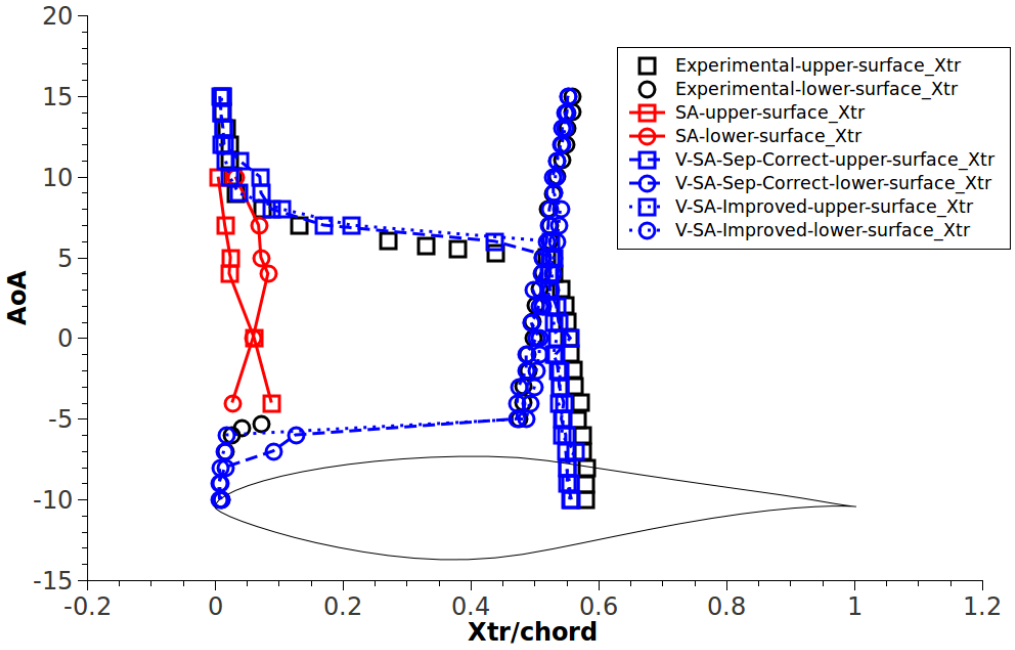

Figure 5.14: Experimental data comparison of transition onset points over the S809 airfoil upper and lower surfaces with computed results from the turbulence SA closure and the transition V-SA-Sep-Correct and V-SA-Improved models. The flow Reynolds number is 2×10^6.

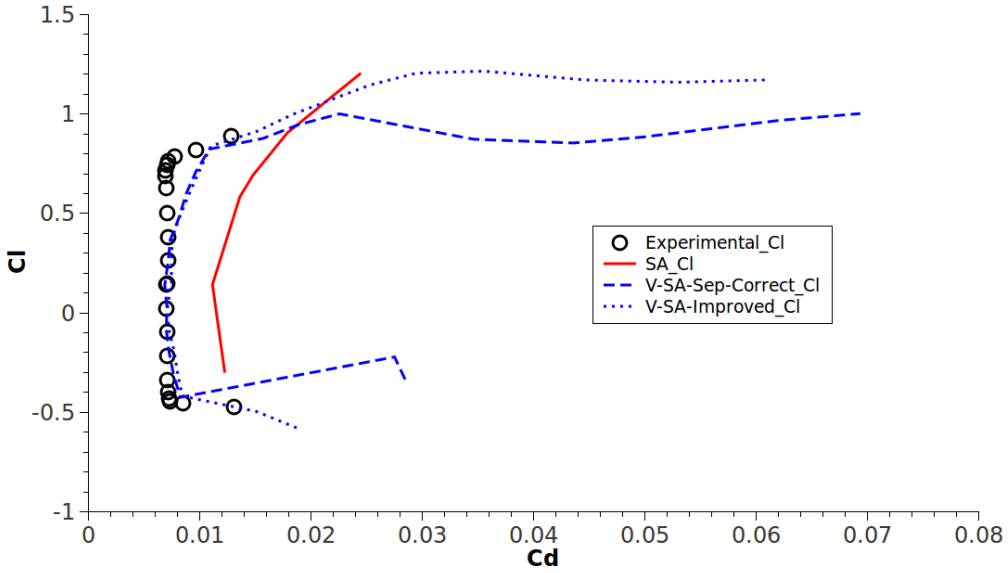

Figure 5.15: Experimental data comparison of the drag polar of the S809 airfoil with computed results from the turbulence SA closure and the transition V-SA-Sep-Correct and V-SA-Improved models. The flow Reynolds number is 2×10^6.

Table 5.3: Aerospatiale A-airfoil Inlet Boundary Conditions

Model	$U(m/s)$	$k_p(m^2/s^2)$	$\tilde{\nu}_t(m^2/s)$
SA	30	N/A	1×10^{-4}
V-SA-Sep-Correct	30	1.22×10^{-4}	1×10^{-4}
V-SA-Improved	30	1.22×10^{-4}	1×10^{-4}

The experimental chord Reynolds number was 2×10^6. The F2 wind tunnel experimental test conditions presented free-stream turbulence intensity values lower than 0.05%. Therefore, a turbulence intensity value of 0.03% was applied in the presented computational results. The SA turbulence model, the separation corrected V-SA transition closure, V-SA-Sep-Correct, and its improved version, V-SA-Improved, were used in the Aerospatiale A-airfoil test case computation. The used inlet boundary conditions for the tested AoA over the A-airfoil are presented in table 5.3.

In order to assure that the obtained results will not vary much with the selected computational mesh, an independence validation was performed. Again, the computed numerical mesh had a double number of nodes. The Aerospatiale A-airfoil surface nearby mesh is presented in Fig.5.16. For this validation, skin-friction coefficient distribution over the airfoil top surface for the used computational mesh and its refined version, was evaluated. Therefore, a skin-friction coefficient plot over the upper surface of the airfoil is presented together with experimental data in Fig.5.17. The refined mesh skin-friction coefficient distribution presents a slightly earlier development of the flow behavior compared to the used mesh. Turbulence transition and flow separation are predicted slightly earlier than the obtained results with the regular mesh. Nonetheless, this is a small deviation considering the increase in node distribution, therefore the results are considered to be mesh independent.

As discussed in the numerical work of Dahlström and Davidson [178], for the F2 wind tunnel test, the flow over the upper surface of the A-airfoil transits to turbulence at 12% chord length. Afterwards, the flow develops under adverse-pressure-gradient until its separation point

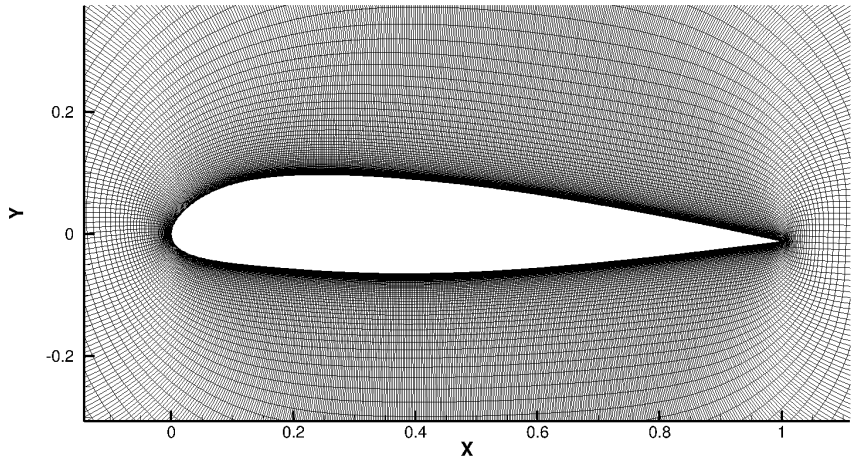

Figure 5.16: Aerospatiale A-airfoil detail mesh view. The airfoil has 800 nodes over its surface with a total number of mesh points of 120000.

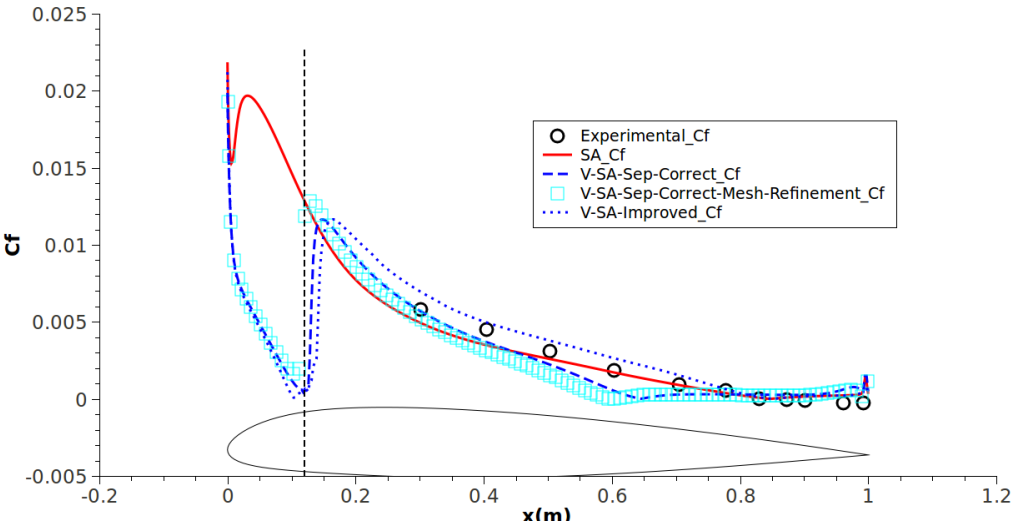

Figure 5.17: Aerospatiale A-airfoil upper surface skin-friction coefficient experimental data comparison with computed results from the turbulence SA closure and the transition V-SA-Sep-Correct and V-SA-Improved models. A mesh refinement study using a mesh with double number of nodes is presented. The experimental transition threshold is marked by the vertical dashed line. The zero skin-friction coefficient value is marked by the horizontal dotted line. The flow Reynolds number is 2×10^6.

Table 5.4: T106 Turbine Blade Test Conditions

$Tu(\%)$	$k_p(m^2/s^2)$	$\tilde{\nu_t}(m^2/s)$
1	1.41135	4.563×10^{-6}
2	5.6454	1.732×10^{-5}
3	12.7022	1.197×10^{-5}
4	22.5816	4.120×10^{-6}
5	35.2838	9.678×10^{-7}
6	50.8086	1.785×10^{-7}
6.7	64.6863	4.958582×10^{-8}

located at roughly 82.5% of the chord length. As observed in the obtained numerical results, the SA turbulence model captures correctly the experimental flow separation point. However, the flow transition threshold is predicted to occur right at the leading edge of the airfoil. The V-SA-Sep-Correct transition closure is able to accurately predict the experimental transition point at 12% of the chord. Nonetheless, the V-SA-Sep-Correct closure predicts an earlier flow separation at approximately 65% of the chord. The improved transition model, V-SA-Improved, computes an accurate transition onset. Also, the computed separation point is in accordance with the experimental data, similar to the SA turbulence model.

5.1.3 T106 turbine blade airfoil

The knowledge of flow losses in turbine cascades is critical to evaluate the latter mechanical efficiency. This is mostly related to the behavior of the laminar boundary layer transition to turbulence. It is then of great interest to delay the boundary layer transition onset. As stated by Hoheisel et al. [179], "An important aspect of turbine aerodynamic design is the question of optimum profile shape to reduce the losses. With respect to the boundary layer state of actual turbo-machinery blades, it is essential to find velocity distributions with the laminar-turbulent transition point as far downstream as possible.".

One of the first works to evaluate the effects of turbulence on turbine cascades performance was presented by Hebbel [180]. However, the first work to carefully consider the effects of varying free-stream turbulence intensity was presented by Hoheisel et al. [179]. The T106 linear turbine cascade blade experimental data from [179] was used to evaluate the improved V-SA transition model version.

In order to have access to a fast implicit density based solver, the V-SA-Improved transition model was implemented in Ansys Fluent. Evaluation of the separation, transition onset and flow re-attachment over the suction side of the T106 turbine blade was performed. This was performed for the Reynolds number value of $Re = 11 \times 10^5$. A variation of the free-stream turbulence intensity from $Tu = 1\%$ to $Tu = 6.7\%$ was considered. A compressible fluid was used with perfect gas law for density calculation. The applied fluid kinematic viscosity was set to a constant value of $\nu = 1.809 \times 10^{-5} \left(m^2/s\right)$. The inlet flow angle was 37.7° and the outlet flow Mach number was 0.59. The test conditions are disclosed in table 5.4.

The used numerical mesh was both structured and unstructured with y^+ values below 0.3 for the entire T106 geometry. This mesh had a blade chord of 0.1 meters with 400 mesh nodes around the turbine airfoil. The first layer of cells had a wall normal distance of 1×10^{-6} meters. In order to model a linear turbine cascade, linear periodic boundary conditions were applied above and below the blade with a separating distance equal to the cascade pitch of 0.0799 meters. The geometry inlet was located a pitch distance before the leading edge of the turbine

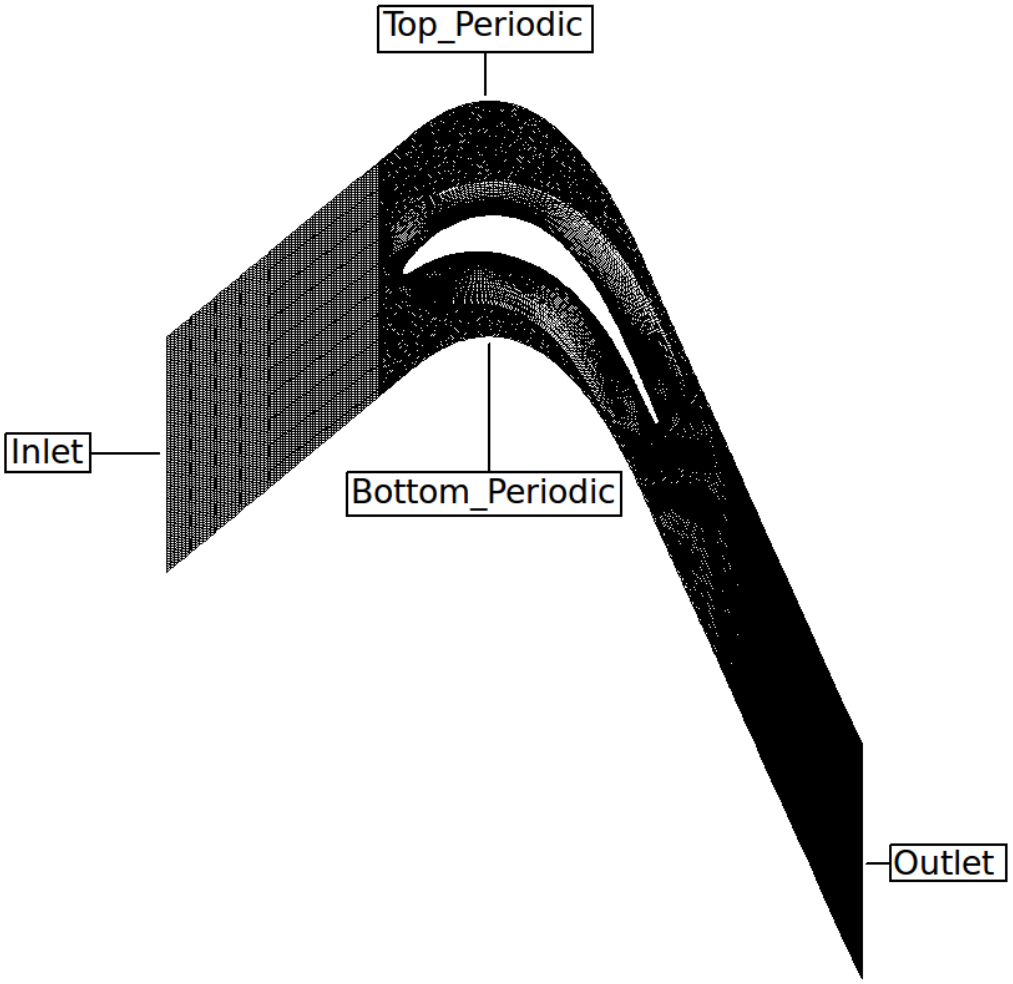

Figure 5.18: General overview of the T106 turbine blade airfoil mesh. The total number of mesh points is 52000.

blade and the geometry outlet was located at two pitch distances after the blade leading edge. The applied boundary conditions can be observed on the general mesh overview presented in Fig.5.18. The unstructured mesh portion was used as an interface between the structured mesh regions as shown in Fig.5.19.

A mesh validation was performed using a computational mesh with double number of nodes. The considered analysis concerns the skin-friction coefficient distribution along the suction side of the T106 geometry. This is disclosed in Fig.5.20. Although the mesh validation shows a small deviation, it can be considered that the obtained results are mesh independent.

The results for the flow Reynolds number of $Re = 11 \times 10^5$ are presented in Fig.5.21. As can be observed, turbulence transition onset is driven by bypass transition or separation induced transition depending on the free-stream turbulence intensity. For lower values of turbulence intensity, less than $Tu = 3\%$, the dominant transition process is separation induced transition. For higher values of free-stream turbulence intensity, turbulence transition is performed through bypass transition mechanisms. The V-SA-Improved transition model is able to capture this shift of transition process from separation induced transition to bypass transition. However, the V-SA-Improved closure computes flow separation later than the experimental record. This is also observed for the transition onset curve with exception for the bypass transition onset curve section where the V-SA-Improved transition model predicts a slightly earlier transition on-

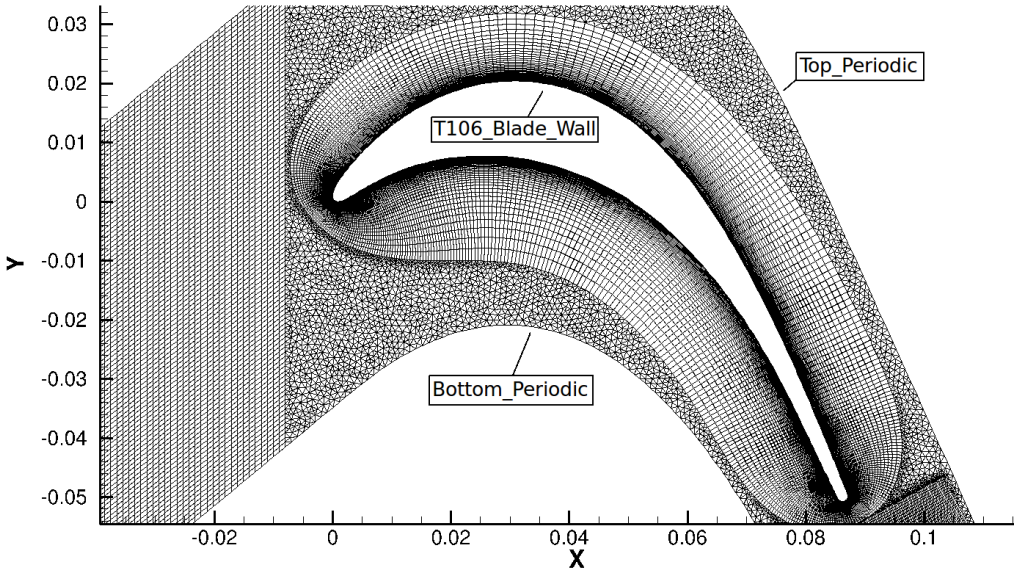

Figure 5.19: T106 turbine blade airfoil detail mesh view. The airfoil has 400 nodes over its surface.

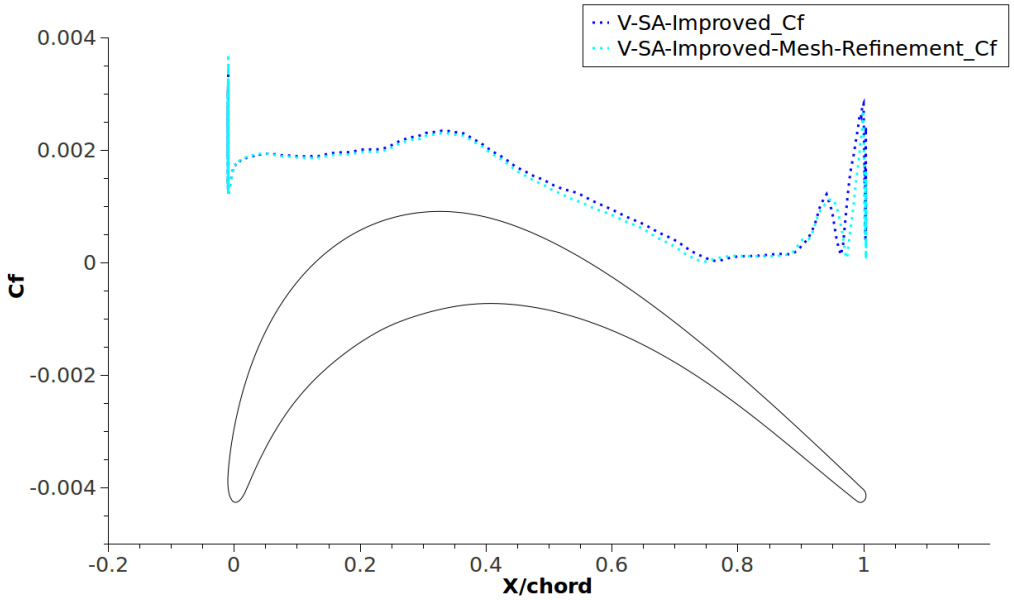

Figure 5.20: Mesh independence test using skin-friction coefficient value distribution over the T106 turbine blade airfoil suction side surface, under flow Reynolds number of $Re = 11 \times 10^5$ with free-stream turbulence intensity of $Tu = 1\%$.

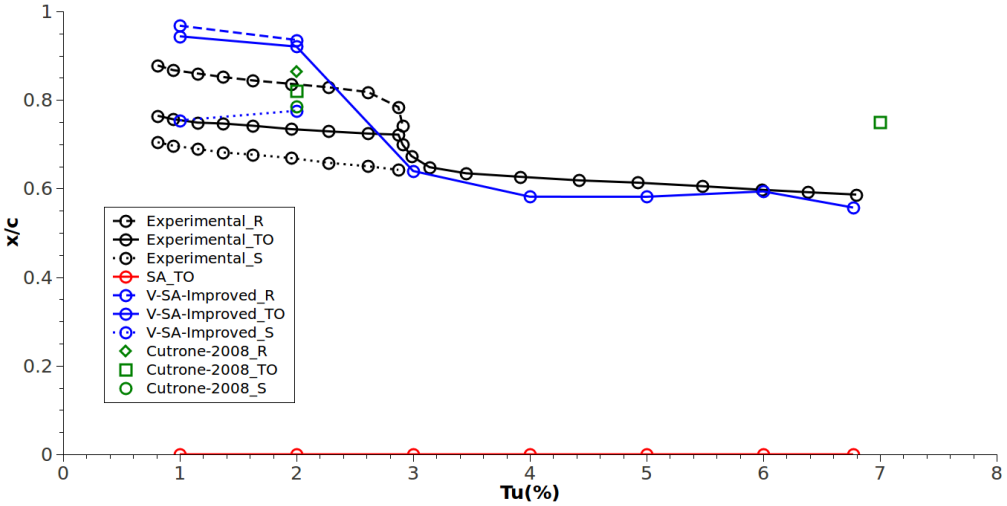

Figure 5.21: Experimental data comparison of laminar boundary layer evolution over the T106 turbine blade airfoil under flow Reynolds number of $Re = 11 \times 10^5$. The separated regions are represented by "S", transition onset points are disclosed by "TO" and flow re-attachment zones are designated by "R". The improved V-SA transition model, V-SA-Improved, was used for comparison along with results from the SA turbulence closure and the numerical work of Cutrone et al. [6].

set than the experimental data curve. The numerical work of Cutrone et al. [6], presents very little data on this specific result. Nonetheless, for the lower turbulence intensity of $Tu = 2\%$, the presented numerical data is similar to the V-SA-Improved computed separation point. The remaining transition onset and re-attachment points are in better agreement with experimental data than the V-SA-Improved model. However, for the case of high free-stream turbulence intensity of $Tu = 7\%$, the numerical data of Cutrone et al., presents a late turbulent transition onset point. The SA turbulence model computes a turbulence transition threshold at the leading edge of the T106 turbine blade.

In order to evaluate the efficiency of a turbine blade a total pressure loss coefficient is calculated according to the work of [179]. This is disclosed in (5.1).

$$\zeta = \frac{Ptot_{inlet} - Ptot_{outlet}}{Ptot_{inlet} - Pstatic_{outlet}} \quad (5.1)$$

The obtained total pressure loss coefficient with varying free stream turbulence intensity is presented in Fig.5.22. The experimental data validation indicates that the V-SA-Improved transition closure is able to accurately compute the pressure losses for lower turbulence intensities than $Tu = 2\%$ and larger turbulence intensities than $Tu = 6\%$. The transition model over-predicts the pressure losses on the bypass transition turbulence intensity range of $Tu = 3\%$ to $Tu = 5\%$. From the previously presented transition onset analysis this is related to the transition process shift from separation induced transition to bypass transition mechanisms. This shift forces the transition threshold to move towards the leading edge of the turbine blade, or in other words, it imposes an earlier transition onset. Nevertheless, the V-SA-Improved transition model predicted pressure-loss coefficient values are closer to the experimental data than the SA turbulence closure computed coefficients.

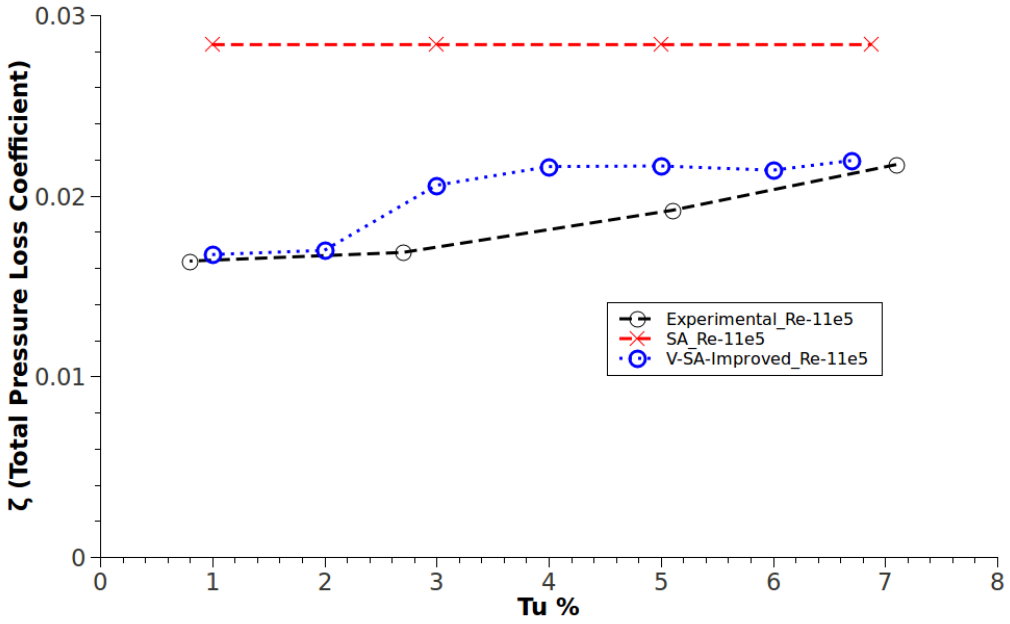

Figure 5.22: Experimental data comparison of total pressure loss coefficient of the T106 turbine blade airfoil under flow Reynolds number of $Re = 11 \times 10^5$. This is evaluated within a range of free-stream turbulence intensity values of $Tu = 0.8\%$ to $Tu = 7.1\%$. The V-SA-Improved transition model was used for comparison along with results from the Spalart Allmaras turbulence model.

5.1.4 Summary of results

The separation corrected V-SA transition model is able to predict with some accuracy the transition threshold regions for various airfoil geometries. However, the analysis performed with the S805 airfoil and the Aerospatiale A-airfoil revealed a problem with the V-SA-Sep-Correct. Under adverse pressure gradient flow, the model computes fully turbulent boundary layer separation earlier than the experimental data. Although the V-SA-Sep-Correct closure makes use of the SA model as its turbulent component, this early separation is also sooner than what the SA turbulence model computes.

The improvements applied to the V-SA-Sep-Correct model, resulting in the V-SA-Improved transition closure, enabled the model to correctly compute fully turbulent attached flow features under adverse-pressure-gradient conditions similar to the SA turbulence closure. Also, the implemented modifications do not significantly change the transition onset prediction behavior of the V-SA-Sep-Correct model.

The validation with the T106 turbine blade airfoil presented some issues regarding the flow correct separation point and the transition onset within the separated flow extension. For the lower free-stream turbulence intensity numerical runs, the V-SA-Improved transition model systematically predicts delayed flow separation and transition onset points in comparison with the experiment.

For the increased free-stream turbulence intensity, the transition process shifts for bypass, and the transition onset region predicted by the V-SA-Improved model approaches that of the experimental data. However, for this case the bypass transition onset is predicted slightly earlier than the experiment. When compared to the SA turbulence closure, the use of the V-SA-Improved model allows a more accurate calculation of the turbine pressure losses.

Chapter 6

Three-dimensional transition flow benchmark

A complete validation of any turbulence transition model for industry use should include real-world geometries. Therefore, three-dimensional geometry validation test cases must be used in order to perceive the developed model's capacity of predicting complex three-dimensional transition flows.

6.1 Three-dimensional geometry test cases

The selected cases were a simple 6:1 Prolate-spheroid geometry, which resembles a fuselage shape, the Onera-M6 wing geometry and the compressible benchmark test case the DLR-F5 wing. The used wall boundary conditions for the applied turbulence and transition models follow the same settings presented in chapter "ERCOFTAC benchmark". Unless stated otherwise, the applied numerical and fluid characteristics for all tested cases are the same as those disclosed in section "Flat-plate test cases".

6.1.1 The 6:1 Prolate-spheroid test case

The incompressible three-dimensional geometry of a 6:1 prolate-spheroid was computed using SA, V-SA, the V-SA with separation correction, its improved model version, V-SA-Improved, and the empirical correlation transition model of Ansys Fluent, the $\gamma - R_{e\theta}$.

These test cases were performed using the experimental data of [7]. This was obtained through a personal communication with Dr. Kreplin. The latter experimental work has many test cases, however only some of these were considered for validation purposes. The selected three test cases had significant transition effects. The upstream conditions for these test cases are presented in table 6.1. The experimental setup comprised of a 6:1 prolate-spheroid with a major and minor axis lengths of 2.4 and 0.4 meters respectively. For the considered test cases the experimental flow velocity was $45\,(m/s)$. The experimental fluid kinematic viscosity was $\nu = 1.7 \times 10^{-5}\,\left(m^2/s\right)$. In order to perform validation using these test cases experimental data, an equal three-dimensional geometry was used with the same dimensions.

The used prolate-spheroid mesh was structured and had y^+ values below 0.6 over the entire surface. Along the surface major axis the mesh had 400 computational nodes. In the azimuth orientation, the prolate-spheroid cross-section had 100 mesh nodes. The total value of grid points over the prolate-spheroid surface was 40000. The total number of mesh points is of 2.8 million. From these a value of 1.6 million cells belong to the boundary layer region.

Table 6.1: 6:1 Prolate-spheroid Test Conditions

AoA	$Tu(\%)$	Re
5°	0.1	6.5×10^6
15°	0.1	6.5×10^6
30°	0.1	6.5×10^6

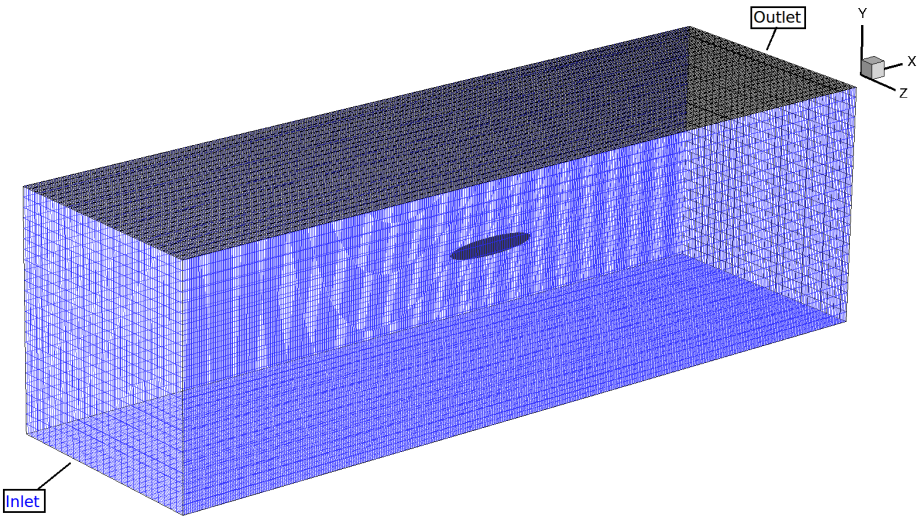

Figure 6.1: General overview of the 6:1 Prolate-spheroid mesh. The inlet and outlet surfaces are indicated and colored with the corresponding surface name color. The spheroid computational grid has a total number of 2800000 mesh points.

Table 6.2: 6:1 Prolate-spheroid Inlet Boundary Conditions

Model	$U(m/s)$	$k(m^2/s^2)$	$k_p(m^2/s^2)$	$\omega(s^{-1})$	$\tilde{\nu}_t(m^2/s)$
SA	45	N/A	N/A	N/A	4.5×10^{-5}
V-SA	45	N/A	0.003038	N/A	4.5×10^{-5}
V-SA-Sep-Correct	45	N/A	0.003038	N/A	4.5×10^{-5}
V-SA-Improved	45	N/A	0.003038	N/A	4.5×10^{-5}
γ-Re_θ	45	0.003038	N/A	1	N/A

The first layer of cells over the spheroid surface were distanced at 1×10^{-5} meters. The 6:1 Prolate-spheroid surrounding structured mesh is disclosed in Fig.6.1. A detail view of the 6:1 Prolate-spheroid tip surface mesh is presented in Fig.6.2.

The inlet boundary conditions for these test cases of transition under cross-flow effects over a 6:1 prolate-spheroid are presented in table 6.2. The applied inlet boundary conditions for the Fluent transition model $\gamma - R_{e\theta}$, were selected in order to simulate the same turbulence intensity in the free-stream as presented in table 6.1. The used fluid kinematic viscosity was the experimental value of $\nu = 1.7 \times 10^{-5}\,(m^2/s)$.

A mesh independence validation test case was computed using a computational grid with 6 million cells. A skin-friction coefficient contour map shows the refinement effect on the transition region oscillations in Fig.6.3. The refined mesh oscillations present smaller amplitudes. The transition onset region is mostly the same, thus the computed results can be considered to be mesh independent.

Cut-section plots of skin-friction coefficient for the obtained results is performed. The cut-section plane is perpendicular to the 6:1 prolate-spheroid minor axis and contains the latter volume center point. This section cuts the 6:1 prolate-spheroid in the x-z plane as shown in Fig.6.4.

The results for the $5\,^\circ$ angle of attack, AoA, test case are presented in Fig.6.5. The experimental data for the prolate-spheroid tips is not available. Thus, these have been assigned with a zero value of skin-friction coefficient in all presented results. Nevertheless, for all AoA the flow separates at the trailing edge of the prolate-spheroid. As can be seen, the SA closure determines transition onset right at the leading edge of the prolate-spheroid. The

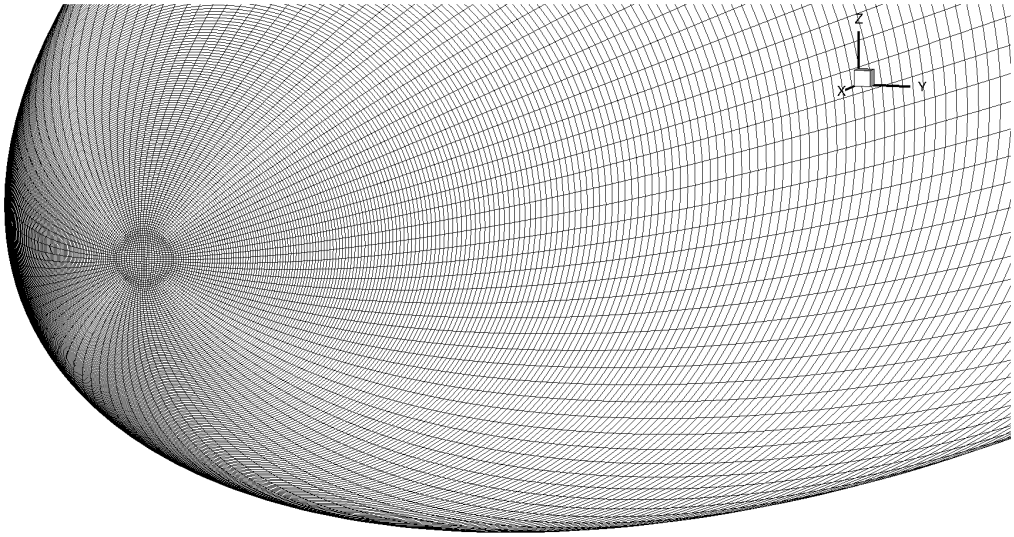

Figure 6.2: The 6:1 Prolate-spheroid leading edge detail mesh view. The Prolate-spheroid has 40000 nodes over its surface.

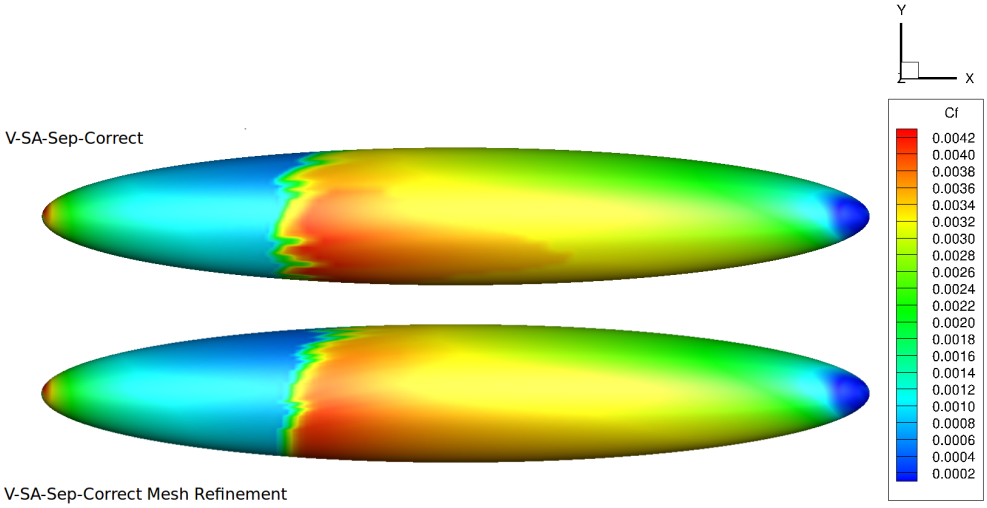

Figure 6.3: Prolate-spheroid mesh independence validation with AoA 5°. The V-SA-Sep-Correct transition model calculated skin-friction coefficient contour map is used as surface contour. The top contour represents the 2.8 million cells mesh result and the bottom contour shows the refinement effect of the usage of a 6 million cell computational grid.

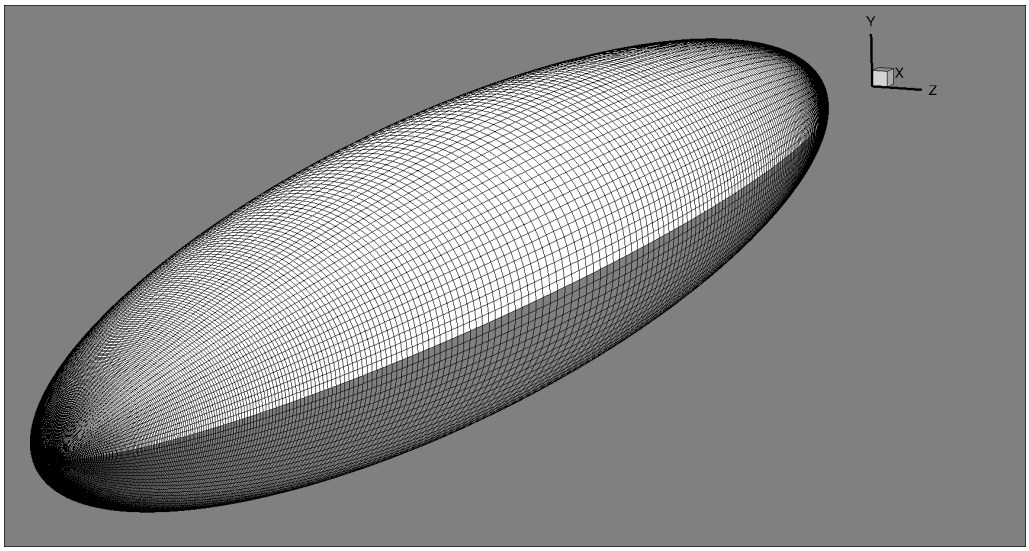

Figure 6.4: X-Z cut-section of 6:1 prolate-spheroid for skin-friction coefficient plots. The cutting plane is perpendicular to the 6:1 prolate-spheroid minor axis and contains its origin point. The presented structured mesh has the size of 100×400 nodes.

V-SA transition model predicts transition onset near to the experimental result. It should be noted that, the transition length of the V-SA is shorter than the experimental data. However, the transition onset position is quite close to the experimental measurements. The separation corrected V-SA model version predicts a slightly earlier transition threshold compared to the base V-SA transition closure. The V-SA-Improved transition model displays a transition onset behavior similar to the experimental recorded data. The $\gamma - R_{e\theta}$ transition model predicts the transition onset correctly but the transition line along the surface has an incorrect angle. A skin-friction coefficient plot from a top x-z cutting plane parallel to the one presented in Fig.6.4 is presented in Fig.6.6. It is shown that the $\gamma - R_{e\theta}$ empirical transition model is able to correctly predict transition onset as well as the late transition value of skin-friction coefficient. For this top cut section, it is seen that the separation corrected version of the V-SA model presents a weaker behavior than its original version for these flow conditions. The V-SA-Improved transition model computes a transition region close to the experimental data.

The central x-z cutting plane results are presented in Fig.6.7. The presented results confirm the reliability of the V-SA model and the fact that the separation corrected version of the transition model predicts a slightly earlier transition onset. The V-SA-Improved closure computes a correct transition onset compared to the experimental data. Although the computed initial skin-friction coefficient distribution along the fully turbulent flow length is accurate, the calculated skin-friction coefficient values over the Prolate-spheroid rear tip is slightly over-predicted.

The results for the AoA 15° test case shown in Fig.6.8 expose the fact that the SA model predicts transition at the leading edge of the geometry. The V-SA closure is able to predict transition onset near the experimental values although with some delay. The separation corrected V-SA closure presents a similar transition pattern to the original transition model. The V-SA-Improved transition model predicts the transition onset later than both the V-SA and V-SA-Sep-Correct closures. Again the $\gamma - R_{e\theta}$ transition model predicts the transition onset very close to the experimental data but the transition zone shape is incorrect. In the work of [181], similar numerical results were obtained with the $\gamma - R_{e\theta}$ transition model for these last two test cases.

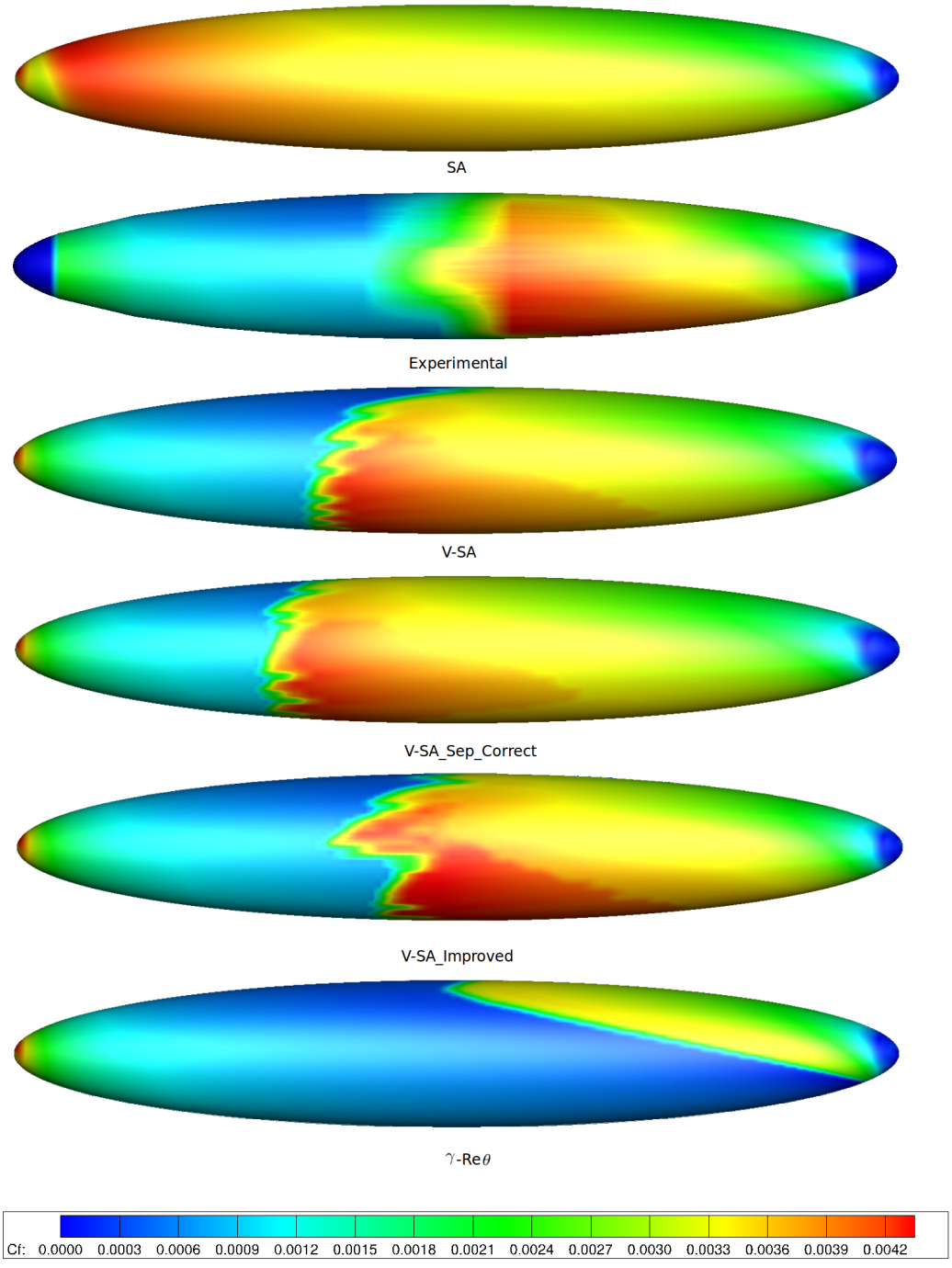

Figure 6.5: Comparison of experimental data from [7] for skin-friction coefficient contour map of 6:1 prolate-spheroid with AoA 5° with numerical results from the turbulence SA closure and the transition V-SA, V-SA-Sep-Correct, V-SA-Improved and γ-Re_{θ} models.

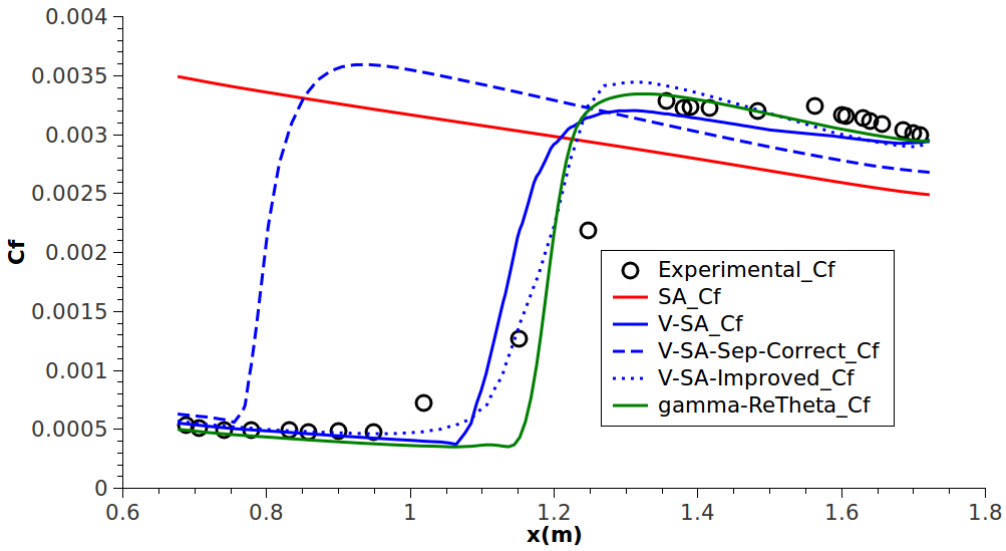

Figure 6.6: Comparison of experimental skin-friction coefficient along a top X-Z cutting plane over the 6:1 prolate-spheroid with AoA 5° with numerical results from the turbulence SA closure and the transition V-SA, V-SA-Sep-Correct, V-SA-Improved and γ-Re_θ models.

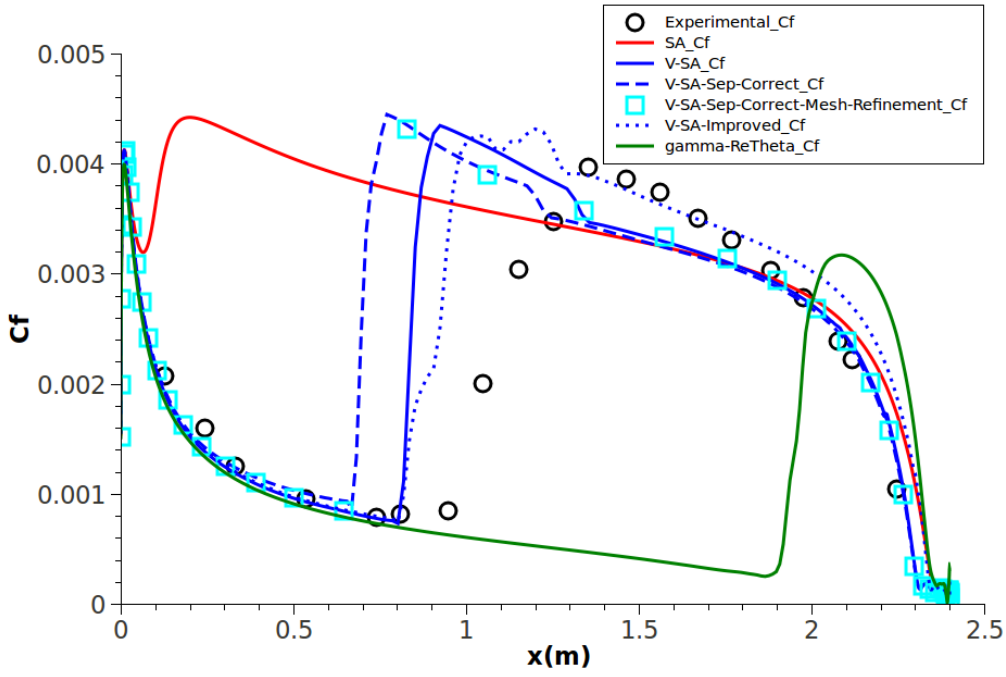

Figure 6.7: Comparison of experimental skin-friction coefficient along the X-Z cutting plane over the 6:1 prolate-spheroid with AoA 5° with numerical results from the turbulence SA closure and the transition V-SA, V-SA-Sep-Correct, V-SA-Improved and γ-Re_θ models.

The x-z cutting plane results are presented in Fig.6.9. As can be seen, the V-SA model predicts transition onset close to the experimental data with a slight delay. However, due to the separation corrected V-SA model earlier transition threshold prediction behavior, this computes the transition onset point closer to the experimental data. Both of the transition models predicted a transition skin-friction coefficient peak value lower than that of the experimental data. The V-SA-Improved transition closure computes the transition threshold later than expected, displaying a slightly higher value of skin-friction coefficient over the fully turbulent region when compared to the remaining turbulence and transition models. The evolution of flow streamlines and $\overline{u'v'}$ iso-surfaces over the spheroid are presented in Fig.6.10. As can be observed, there is flow separation at the trailing edge of the spheroid. Also, the leading edge $\overline{u'v'}$ iso-surfaces patterns are quite interesting. There seems to be two sets of $\overline{u'v'}$ fluctuations over the spheroid nose. This can also be observed in the front view of the 6:1 prolate-spheroid $\overline{u'v'}$ iso-surface patterns. These are presented in Fig.6.11. In the fully turbulent flow region these patterns cease to exist. Instead a constant iso-surface covers the remaining extension of the prolate-spheroid. These fluctuations are related to the Klebanoff modes.

The final 6:1 prolate-spheroid validation test case was performed with an AoA of $30\ ^{\circ}$. As can be seen in the results of Fig.6.12, the V-SA model's transition onset prediction is in accordance with the experimental measurements. The V-SA transition closure can even predict the saw-tooth shape behavior of the transition onset line very similar to the experimental data. A resembling saw-tooth shape transition pattern is also predicted by the separation corrected V-SA model. Although the V-SA-Improved transition closure calculates an almost equal transition pattern to the one computed by the original V-SA model, this is predicted slightly later. The SA turbulence model predicts transition onset at the beginning of the prolate-spheroid. The $\gamma - R_{e\theta}$ exhibits a similar behavior to the last two test cases presented here.

The x-z cutting plane results are presented in Fig.6.13. As shown the V-SA model is able to predict transition onset near the experimental data and calculates the transition process with a saw-tooth shape. The latter shape is due to strong cross-flow effects during turbulence transition. This effect is visible in the regions marked by the letters A, B, C and D in Fig.6.12. Although the separation corrected V-SA transition model predicts the transition onset point coincident with the experimental data, the transition development shows a less satisfactory skin-friction coefficient value distribution along the transition length. This shows skin-friction coefficient spikes that overshoot the experimental data distribution. Since the V-SA-Improved transition model predicts the transition threshold slightly later, the skin-friction coefficient plot line crosses over only the last spike of the cross-flow induced transition saw-tooth shape region. Therefore, the V-SA-Improved skin-friction coefficient plot presents a transition onset prediction slightly later than the experimental data, showing only one of the transition spikes prior to the fully turbulent flow region.

6.1.2 The Onera-M6 wing test case

The following three-dimensional geometry studied was the Onera-M6 wing. This has a single type of wing section defined by the Onera D symmetrical airfoil. The Onera-M6 is a swept tapered wing. The wing root chord is 0.8059 meters. Its tip length is 0.4533 meters implying a taper ratio of 0.56. The wing has a span of 1.1963 meters. Its sweep angle and aspect ratio are $26.7\ ^{\circ}$ and 3.8 respectively. In order to perform a set of validation test cases using the Onera-M6 wing as a benchmark, a geometry with the same experimental dimensions was used

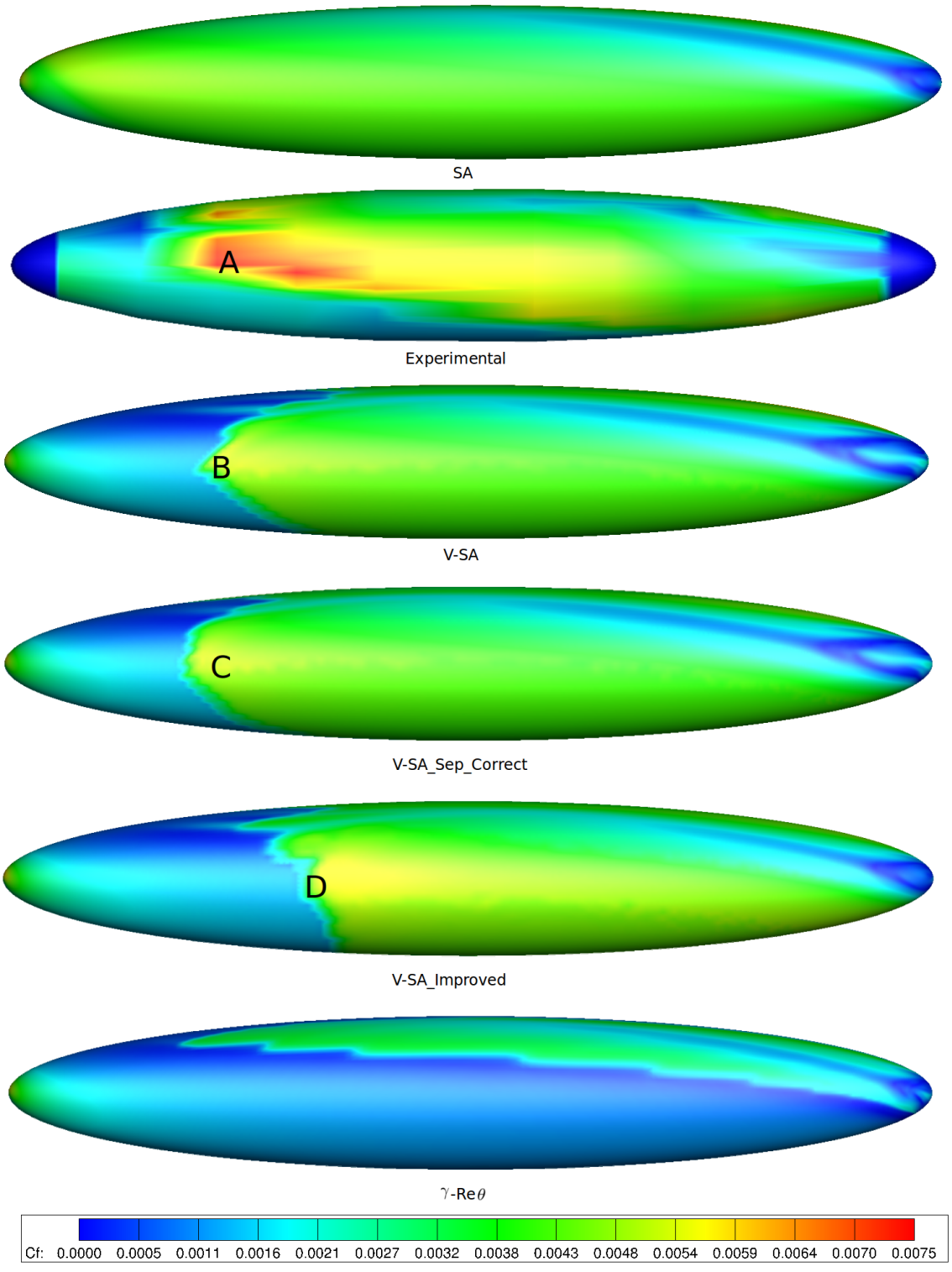

Figure 6.8: Comparison of experimental skin-friction coefficient contour map of 6:1 prolate-spheroid with AoA 15° with numerical results from the turbulence SA closure and the transition V-SA, V-SA-Sep-Correct, V-SA-Improved and γ-Re_{θ} models. In the regions marked by the letters A, B, C and D there is a severe cross-flow transition effect.

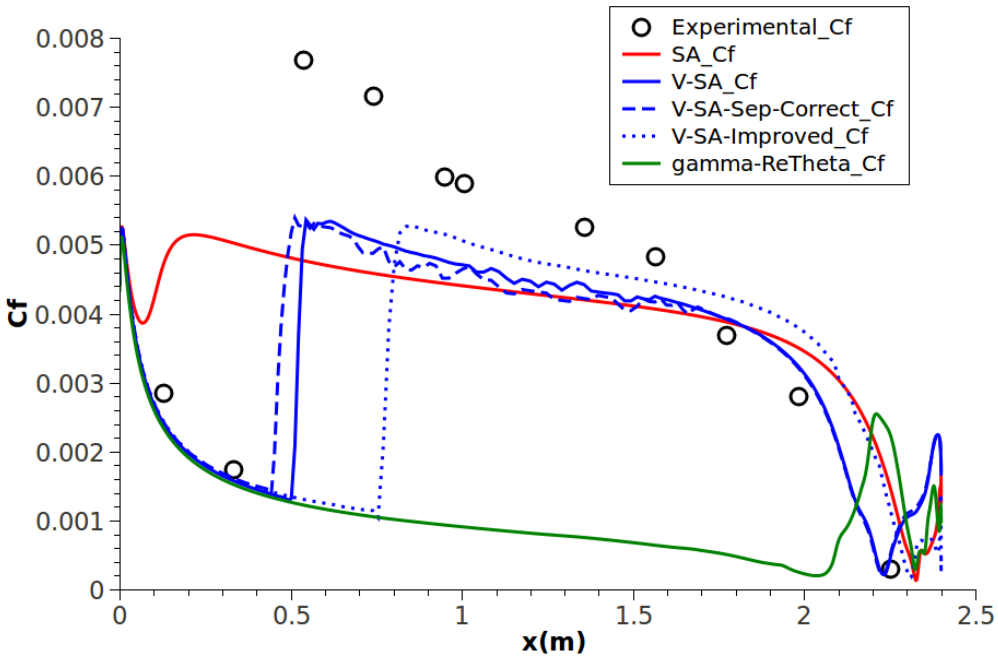

Figure 6.9: Comparison of experimental skin-friction coefficient along the X-Z cutting plane over the 6:1 prolate-spheroid with AoA 15° with numerical results from the turbulence SA closure and the transition V-SA, V-SA-Sep-Correct, V-SA-Improved and γ-Re_{θ} models.

Table 6.3: Onera-M6 Wing Test Conditions

AoA	$Tu(\%)$	Re
0°	0.2	5.6×10^6
5°	0.2	5.6×10^6
15°	0.2	5.6×10^6

for the computational mesh. This was computed using the SA turbulence closure, the separation corrected V-SA transition model, V-SA-Sep-Correct, and its improved version, the V-SA-Improved transition closure.

The used Onera-M6 wing test case experimental data was provided by Onera through the technical report in [182]. The experimental upstream conditions for these test cases are presented in table 6.3. The experimental test cases free-stream flow velocity was $90\,(m/s)$. For all of the experimentally tested Onera-M6 wing flow angles of attack, the root chord Reynolds number was 5.6×10^6. Therefore the experimental fluid kinematic viscosity was $\nu = 1.3 \times 10^{-5}\,(m^2/s)$. The performed validation based on the supplied experimental data, was conducted using the same fluid kinematic viscosity.

The computed Onera-M6 wing mesh was of unstructured nature, however it had y^+ values below 1 over the entire wing surface. Using a boundary layer mesh near the surface, the first layer of cells over the wing were distanced at 1×10^{-6} meters. The number of computational nodes over the Onera-M6 wing surface was 43760. The total number of mesh points is of 1.7 million. The Onera-M6 wing unstructured mesh is presented in Fig.6.14. A top view of the Onera-M6 wing unstructured surface mesh is shown in Fig.6.15.

A mesh validation with a 4 million cell grid was computed. The skin-friction coefficient contour plot is presented in Fig.6.16. As observed, the transition threshold regions are located at similar positions with the refined mesh predicting slightly larger laminar spots. Nevertheless,

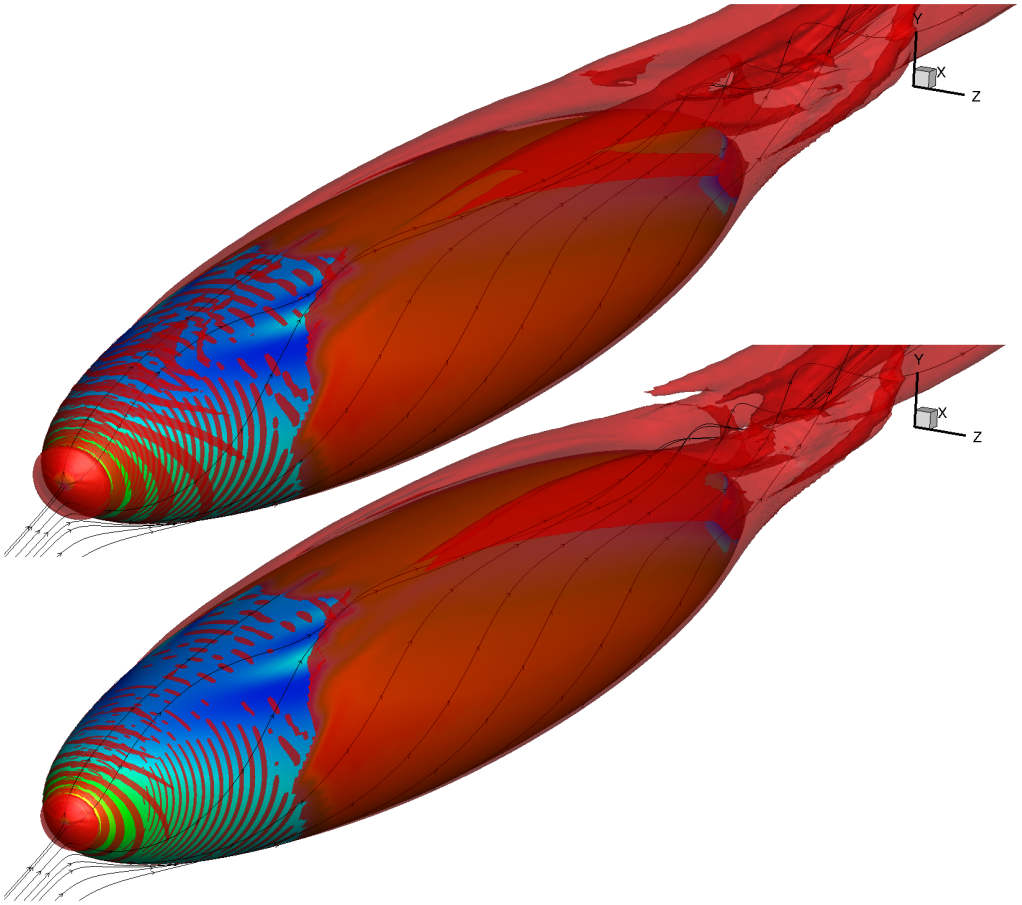

Figure 6.10: Prolate-spheroid pre-transitional instabilities. Side view of red colored transparent $\overline{u'v'}$ iso-surfaces with flow streamlines over the 6:1 prolate-spheroid with AoA 15°. Top image represents the $\overline{u'v'}$ iso-surface equal to -0.02. Bottom image represents the $\overline{u'v'}$ iso-surface equal to -0.03. The V-SA transition model calculated skin-friction coefficient contour map is used as surface contour.

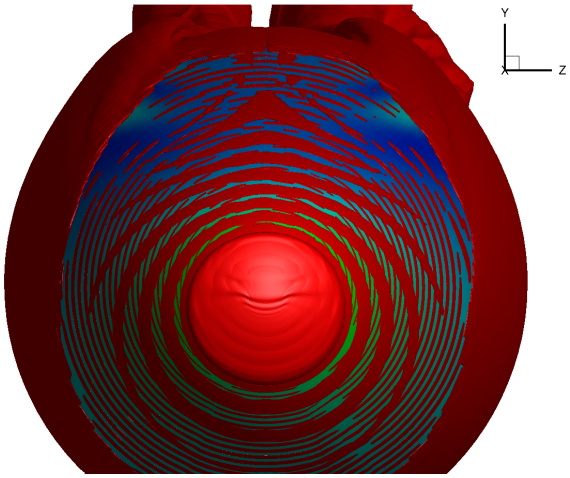

Figure 6.11: Front view of red colored non-transparent $\overline{u'v'}$ iso-surfaces over the 6:1 prolate-spheroid with AoA 15°. The image represents the $\overline{u'v'}$ iso-surface equal to -0.03. The V-SA transition model calculated skin-friction coefficient contour map is used as surface contour.

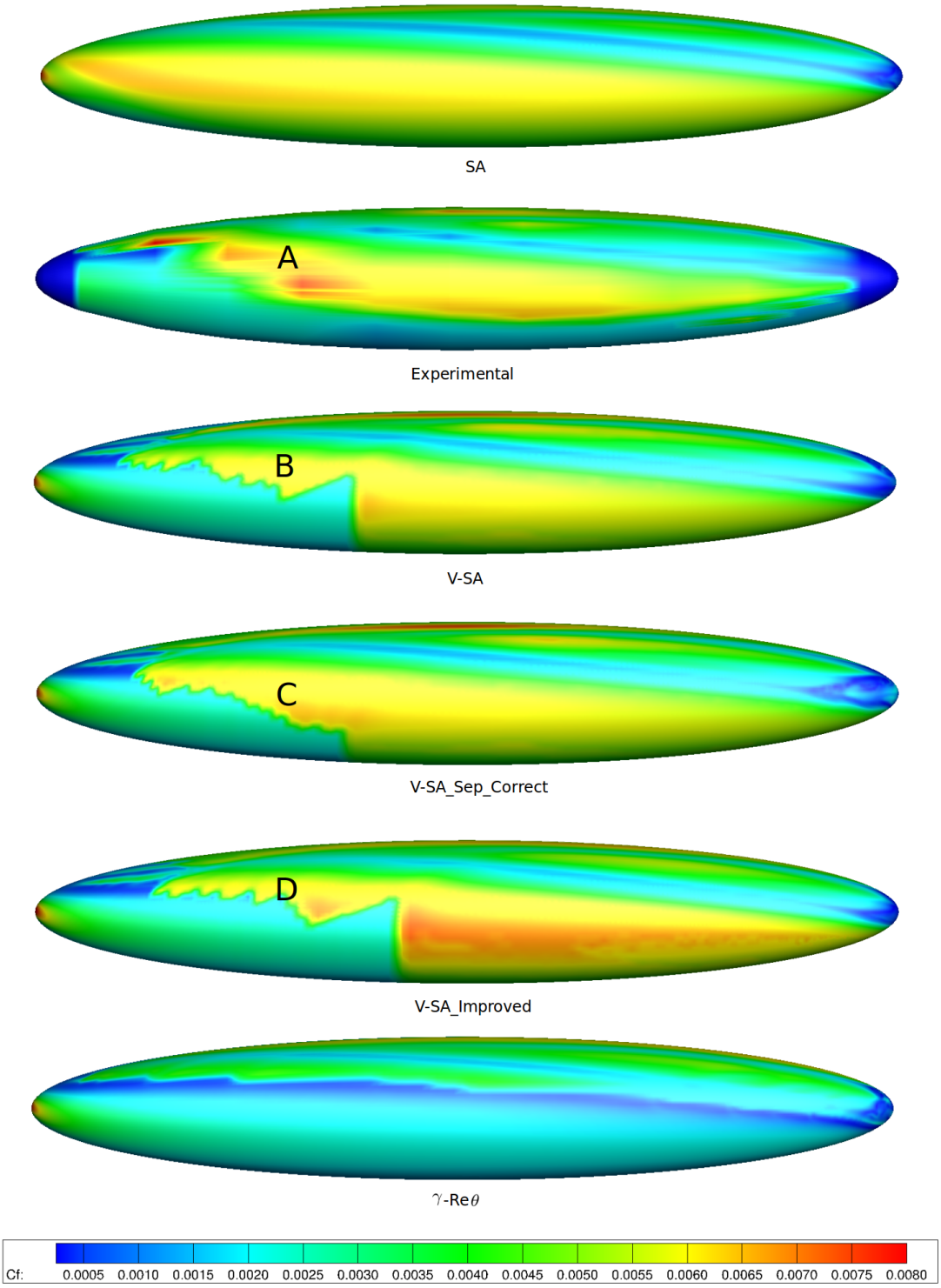

Figure 6.12: Comparison of experimental skin-friction coefficient contour map of 6:1 prolate-spheroid with AoA 30° with numerical results from the turbulence SA closure and the transition V-SA, V-SA-Sep-Correct, V-SA-Improved and γ-Re_θ models. In the regions marked by the letters A, B, C and D there is a severe cross-flow transition effect.

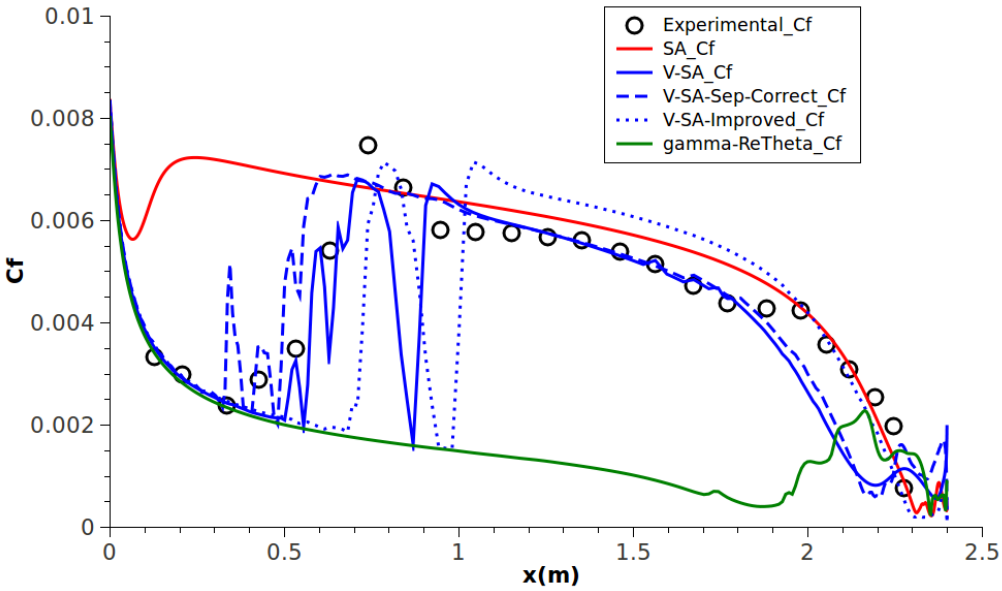

Figure 6.13: Comparison of experimental skin-friction coefficient along the X-Z cutting plane over the 6:1 prolate-spheroid with AoA 30° with numerical results from the turbulence SA closure and the transition V-SA, V-SA-Sep-Correct, V-SA-Improved and γ-Re_{θ} models.

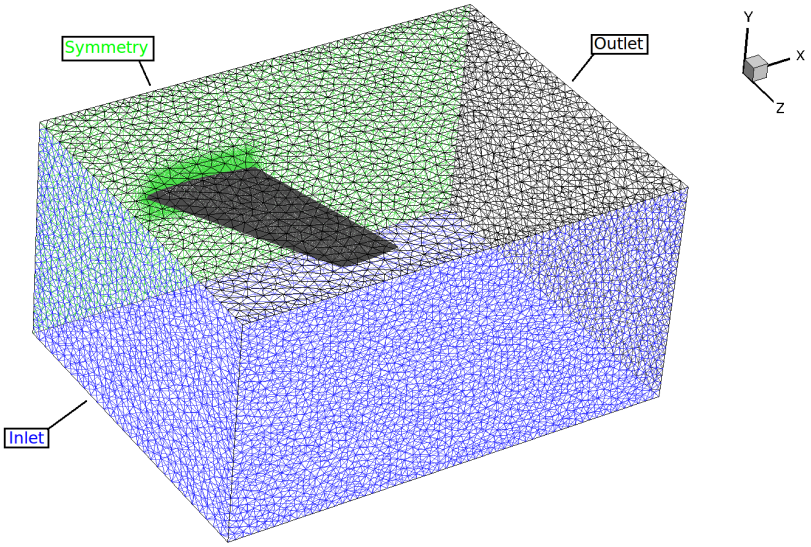

Figure 6.14: General overview of the Onera-M6 wing mesh. The inlet, outlet and symmetry surfaces are indicated and colored with the corresponding surface name color. The wing computational grid has a total number of 1700000 mesh points.

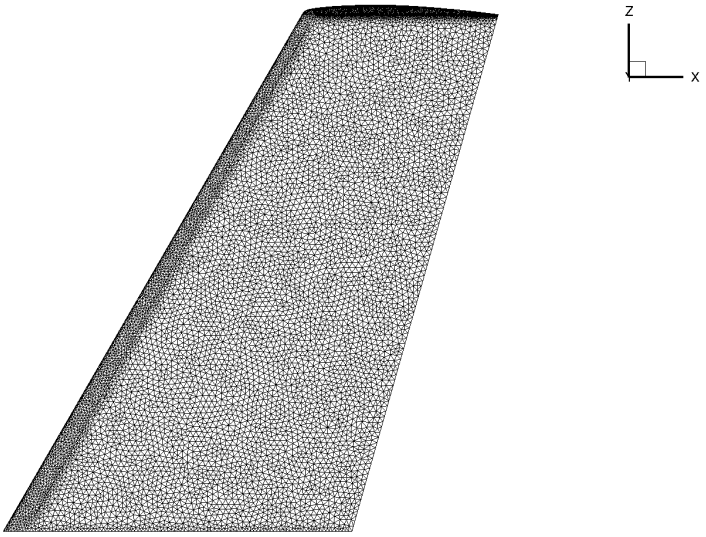

Figure 6.15: Onera-M6 wing mesh top view. The Onera-M6 has 43760 nodes over its surface.

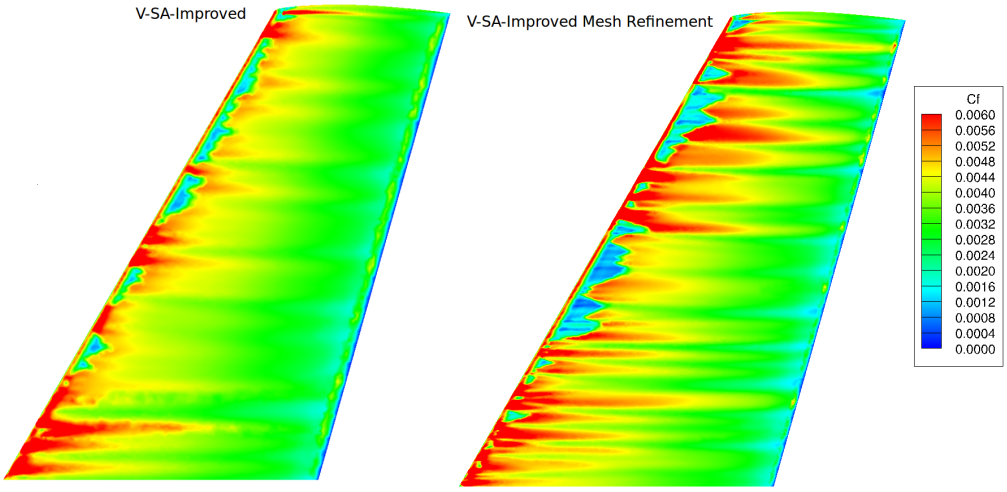

Figure 6.16: Onera-M6 wing mesh independence validation with AoA 0°. The V-SA-Improved transition model calculated skin-friction coefficient contour map is used as surface contour. The left contour represents the 1.7 million cells mesh result and the right contour shows the refinement effect of the usage of a 4 million cell mesh.

Table 6.4: Onera-M6 Wing Inlet Boundary Conditions

Model	$U(m/s)$	$k_p(m^2/s^2)$	$\tilde{\nu_t}(m^2/s)$
SA	90	N/A	1×10^{-6}
V-SA-Sep-Correct	90	0.0486	1×10^{-6}
V-SA-Improved	90	0.0486	1×10^{-6}

the computed results can be considered to be mesh independent.

The used inlet boundary conditions for the Onera-M6 wing validation are presented in table 6.4. The experimental photos capturing transition threshold regions over the upper and lower surfaces of the Onera-M6 wing at 0°, 5° and 15° AoA, were compared to the skin-friction coefficient contour plots obtained with the SA and V-SA models. The case of zero angle of attack with respect to the wing upper surface is presented in Fig.6.17. The experimental laminar regions are depicted in the photo as white zones. The fully turbulent flow regions are shown as fully dark zones. It can be seen that the experimentally obtained laminar wing area is mostly constant along the leading edge of the wing and has a short chord-wise extension. The V-SA-Sep-Correct skin-friction coefficient contour plot presents blue zones near the leading edge of the wing. These are relatively small laminar regions predicted by the transition model. The shown laminar spots occur almost over the whole wing leading edge span. However, near the wing root, the V-SA-Sep-Correct closure presents a transition threshold predicted too early when compared to the experimental picture. Also the calculated laminar regions are not constantly distributed and do not extend in the chord direction as long as the presented laminar regions in the experimental data. The V-SA-Improved transition model presents a similar behavior to the V-SA-Sep-Correct closure. The SA turbulence model apparently computes a transition region that resembles that of the V-SA models. Although there are regions near the leading edge which present a local depression of skin-friction coefficient, featuring a less turbulent flow extension, these spots have higher values of skin friction coefficient than those predicted by both V-SA models.

The following upper surface experimental data of the Onera-M6 wing for 5° AoA test case is presented in Fig.6.18. It can be seen that the experimental fully turbulent transition line moves forward towards the leading edge of the Onera-M6. Almost all of the wing's upper surface is under fully turbulent regime. Nonetheless, near the root of the wing there is a small laminar region. This can also be observed very near the leading edge of the wing close to its tip region. The SA turbulence model predicts transition onset from the leading edge of the wing throughout the whole wing span. Both the separation corrected V-SA and the V-SA-Improved transition models are able to capture the small laminar region near the leading edge within the wing's root zone. They also capture laminar zones in the tip region close to the wing's leading edge. Nevertheless, the V-SA models predict a thin transition region over the wing's leading edge in its mid span area. This transition pattern is not observed in the experimental photo.

The final Onera-M6 upper surface transition pattern experimental photo for flow at 15° AoA is disclosed in Fig.6.19. Similar to the case of the wing under 5° AoA, the experimentally recorded photo shows that the Onera-M6 wing upper surface is fully turbulent. The exceptions are again the near leading edge root and tip regions of the wing. The V-SA-Sep-Correct transition model captures again the laminar spot on the wing's leading edge near root region. The latter chord length is slightly bigger than the previous test case. Thus, it is also larger than the experimental disclosed laminar region. The transition model predicts a laminar region in the leading edge tip region of the wing. However, it also predicts a distribution of skin-friction coefficient in this tip region that is not in accordance with the experimental data. The V-SA-Sep-Correct transition

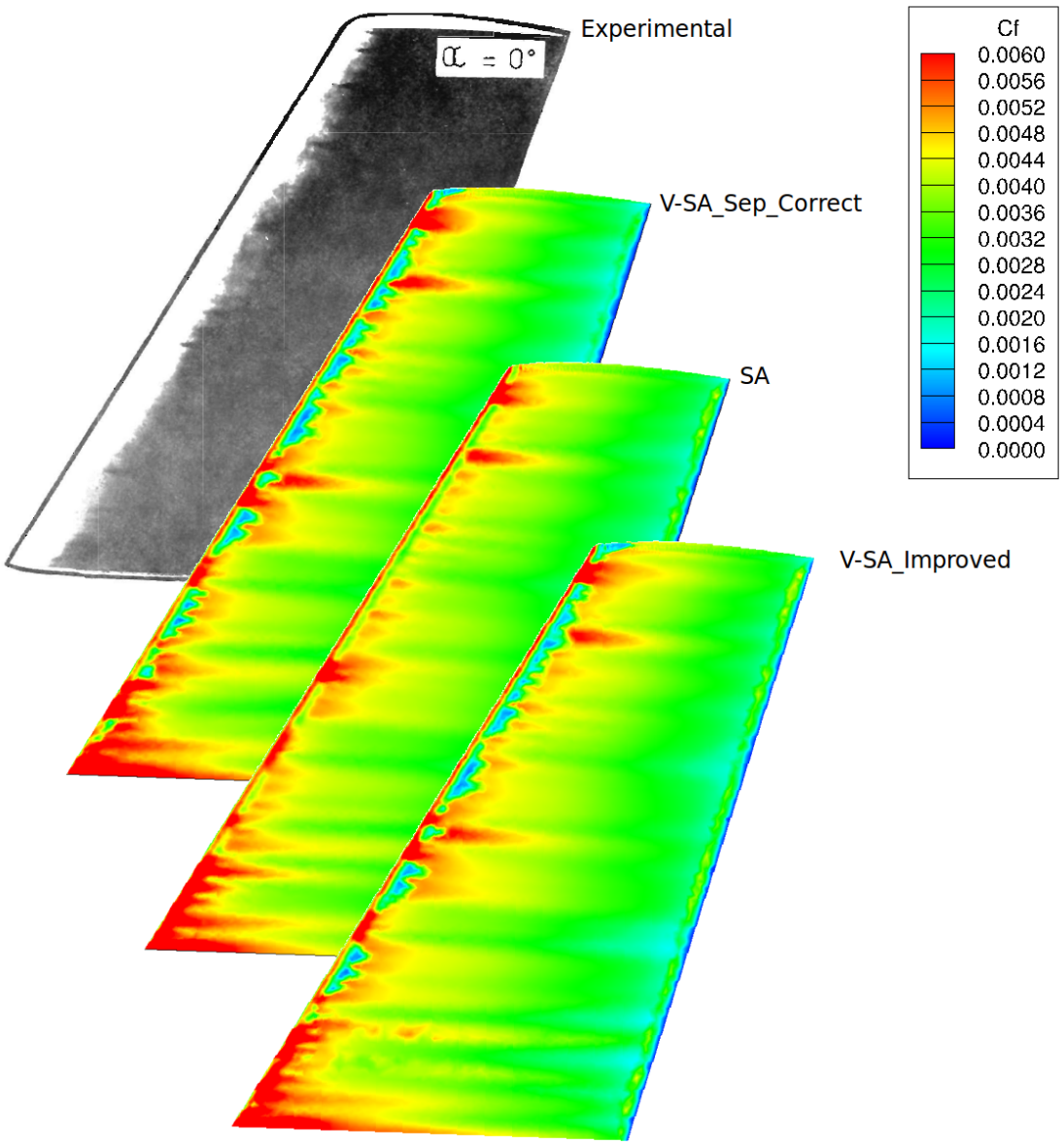

Figure 6.17: Onera-M6 wing upper surface experimental transition regions for 0° AoA. Comparison of experimental photo with skin-friction coefficient contour plots computed with the turbulence SA closure and the transition V-SA-Sep-Correct and V-SA-Improved models.

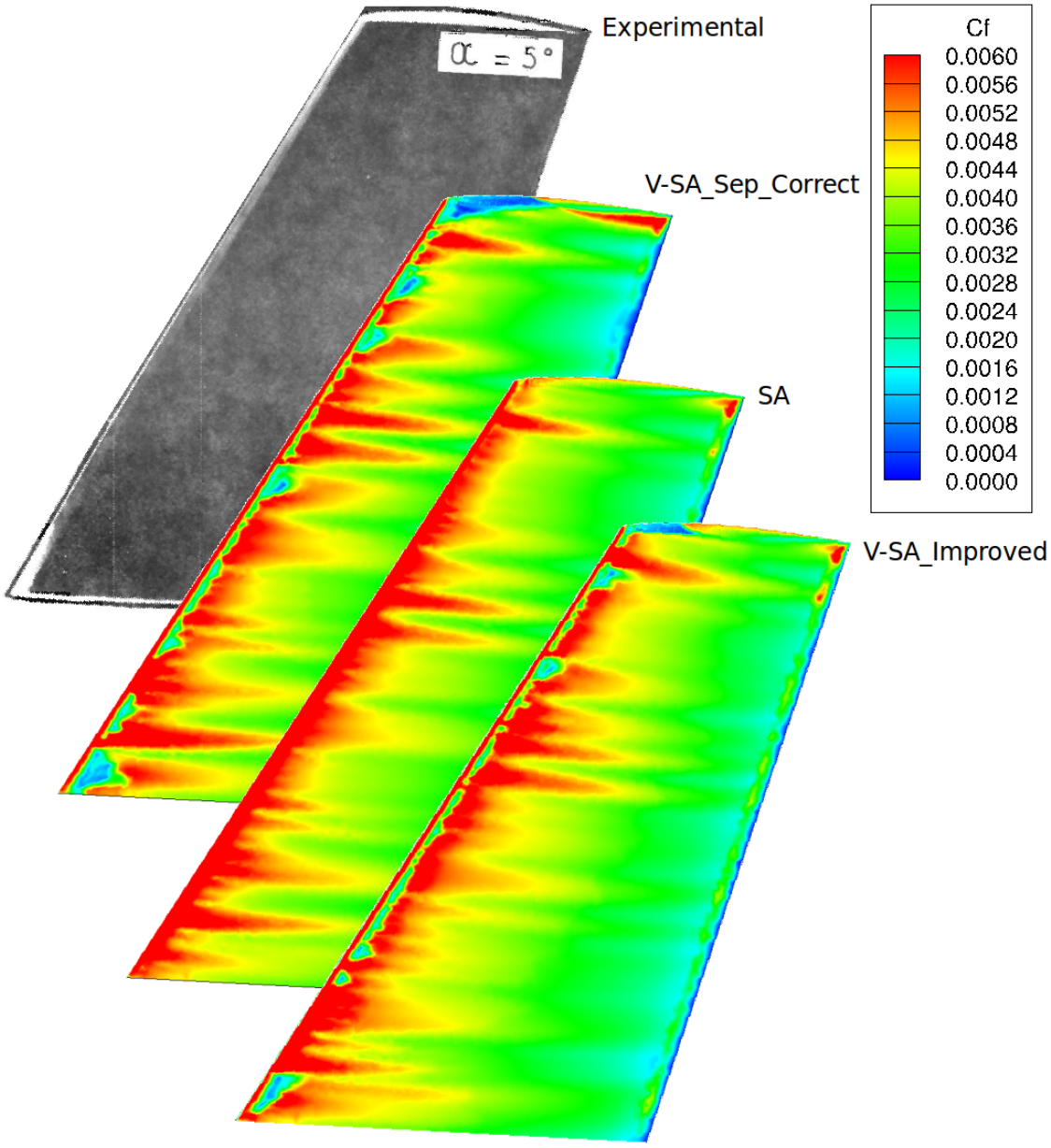

Figure 6.18: Onera-M6 wing upper surface experimental transition regions for 5° AoA. Comparison of experimental photo with skin-friction coefficient contour plots computed with the turbulence SA closure and the transition V-SA-Sep-Correct and V-SA-Improved models.

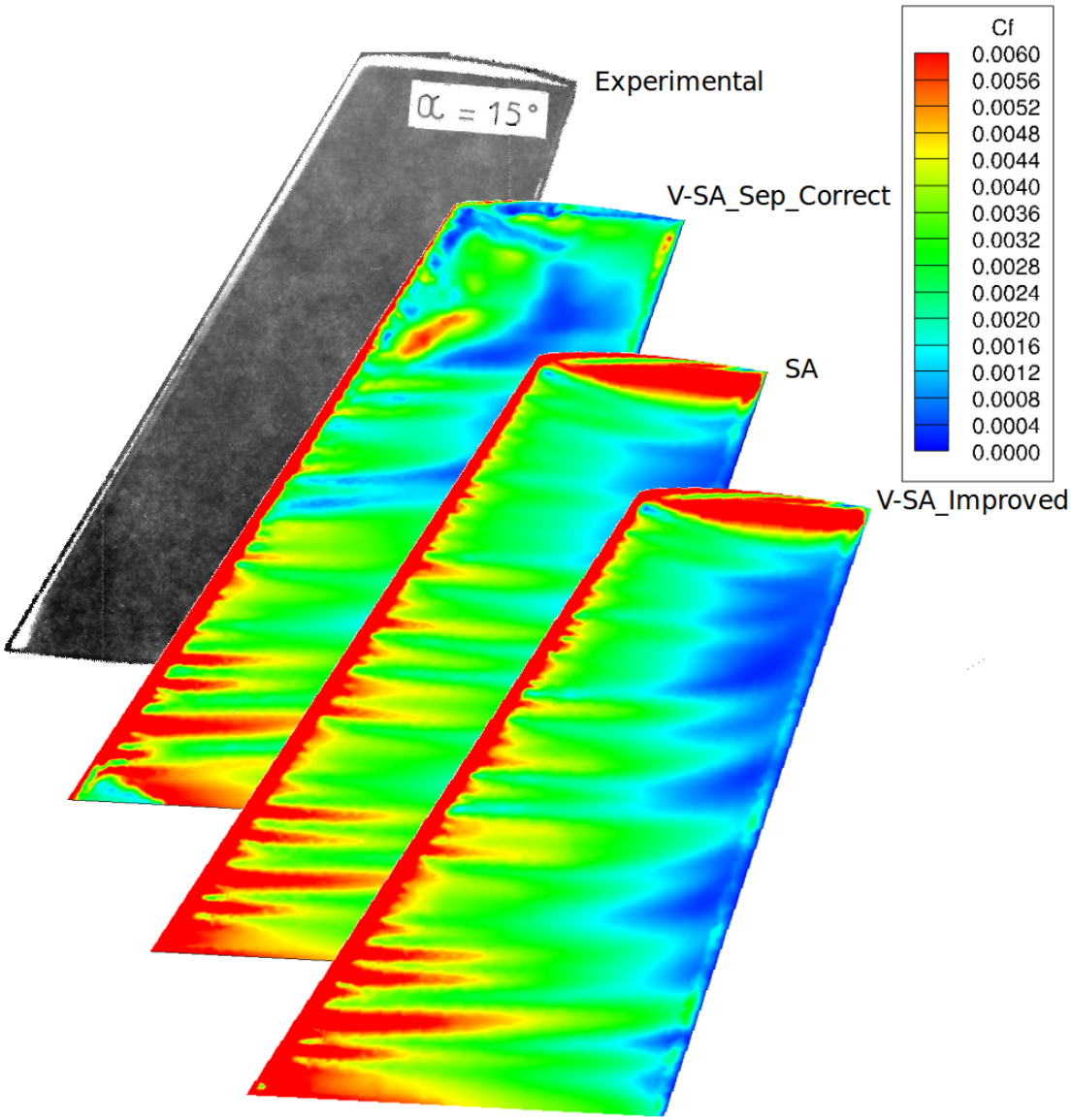

Figure 6.19: Onera-M6 wing upper surface experimental transition regions for 15° AoA. Comparison of experimental photo with skin-friction coefficient contour plots computed with the turbulence SA closure and the transition V-SA-Sep-Correct and V-SA-Improved models.

closure computes flow separation within the wing's tip region. Although the SA turbulence closure does not predict the root and tip laminar regions over the wing, it correctly calculates the attached flow over the wing's upper surface tip zone. The V-SA-Improved transition model shows a dramatic improvement on the tip region of the wing. The improved V-SA closure is able to compute fully attached flow over the wing's upper surface, similar to the SA turbulence model. However, the model does not predict the small laminar regions near the wing's root and tip zones.

Even though the next presented experimental data is similar to the upper surface case, the lower surface transition pattern of the Onera-M6 wing for 0° AoA is also presented in Fig.6.20. Since the Onera-M6 wing is symmetrical, similar conclusions can be withdrawn from the presented numerical results comparison with the experimental photo. However, this is not the case for the Onera-M6 lower surface at 5° AoA. This is shown in Fig.6.21. The experimental distribution of the laminar leading edge regions is not constant. There is a color variation from laminar white zones to gray and fully turbulent black regions. As such, moving from the near root zone of the wing's lower surface towards the tip of the wing, this is initially fully laminar close to the leading edge. In the neighboring area, the photo is gray, which can be interpreted as an early turbulent zone. Afterwards the surface is again totally white, thus implying laminar flow conditions. There after the surface presents a gray spike between the tip and mid span sections of the wing. After this spike the wing's leading edge surface is again white, therefore fully laminar. The SA turbulence closure computes fully turbulent flow regime over the entire lower surface of the wing. The separation corrected V-SA transition model predicts a non-uniform transition threshold pattern along the wing's span. In the root area, close to the leading edge the flow is laminar. Next to this flow region in the spanwise direction, the V-SA-Sep-Correct closure predicts a fully turbulent flow spike that reaches the wing's leading edge. This resembles with the experimentally observed gray zone near the wing's root leading edge area. However, this spike is not as wide as the experimental gray zone. Similar to the experimental transition data photo, within the leading edge mid and tip sections of the Onera-M6 wing, the V-SA-Sep-Correct model predicts a second turbulent spike that reaches the wing's leading edge. The V-SA-Improved model transition pattern resembles the V-SA-Sep-Correct closure and the disclosed experimental photo transition shape.

The last Onera-M6 transition pattern photo of the wing's lower surface is shown in Fig.6.22. The experimental leading edge transition region appears to be more regular in shape. Nevertheless, the color distribution within this transition leading edge region is not totally white nor constant. The wing's leading edge root region is again laminar. Along the wing's span direction this initial laminar region is turned into a darker zone, thus a turbulent region. Afterwards it presents an intermittent variation between dark and light gray regions up until the tip of the wing. The latter region is fully laminar. For this case the SA closure predicts intermittent and very small laminar spots along the leading edge region. The V-SA-Sep-Correct transition model predicts a large laminar region near the wing's root leading edge. This is larger than what can be perceived by the experimental photo. Nonetheless, along the wing's spanwise direction, the transition closure is able to predict an intermittent laminar region with an approximate chordwise size close to the experimentally observed transition region. At the wing's tip area, the V-SA-Sep-Correct model predicts a laminar region similar to the disclosed experimental data. Although the predicted transition shape is not identical to the experimental recorded pattern, again the V-SA-Sep-Correct model predicts a reasonable approximation of the complex transition threshold pattern behavior. The V-SA-Improved transition model shows a laminar region near the wing's root leading edge with a similar size to the experimental data. With exception

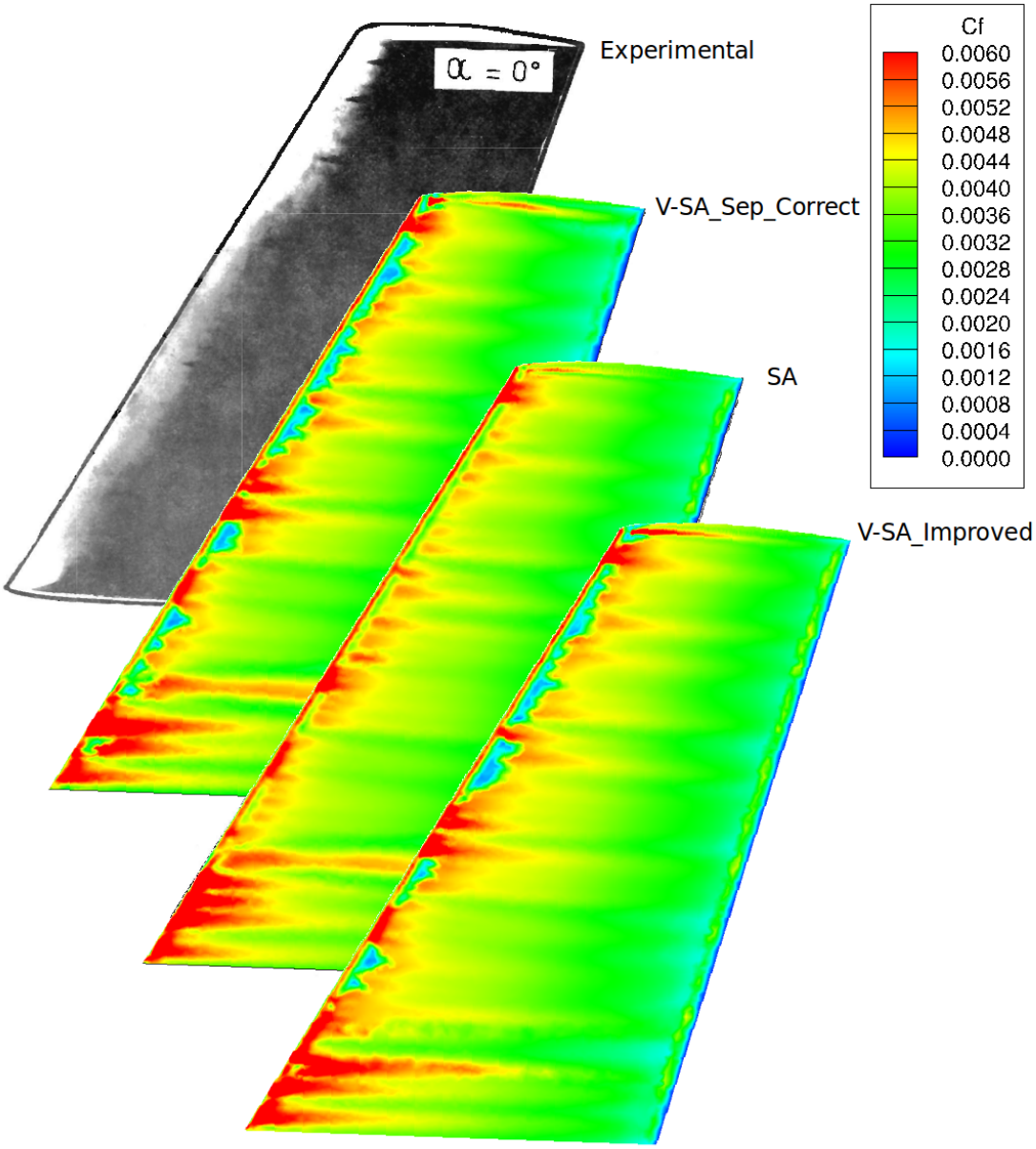

Figure 6.20: Onera-M6 wing lower surface experimental transition regions for 0° AoA. Comparison of experimental photo with skin-friction coefficient contour plots computed with the turbulence SA closure and the transition V-SA-Sep-Correct and V-SA-Improved models.

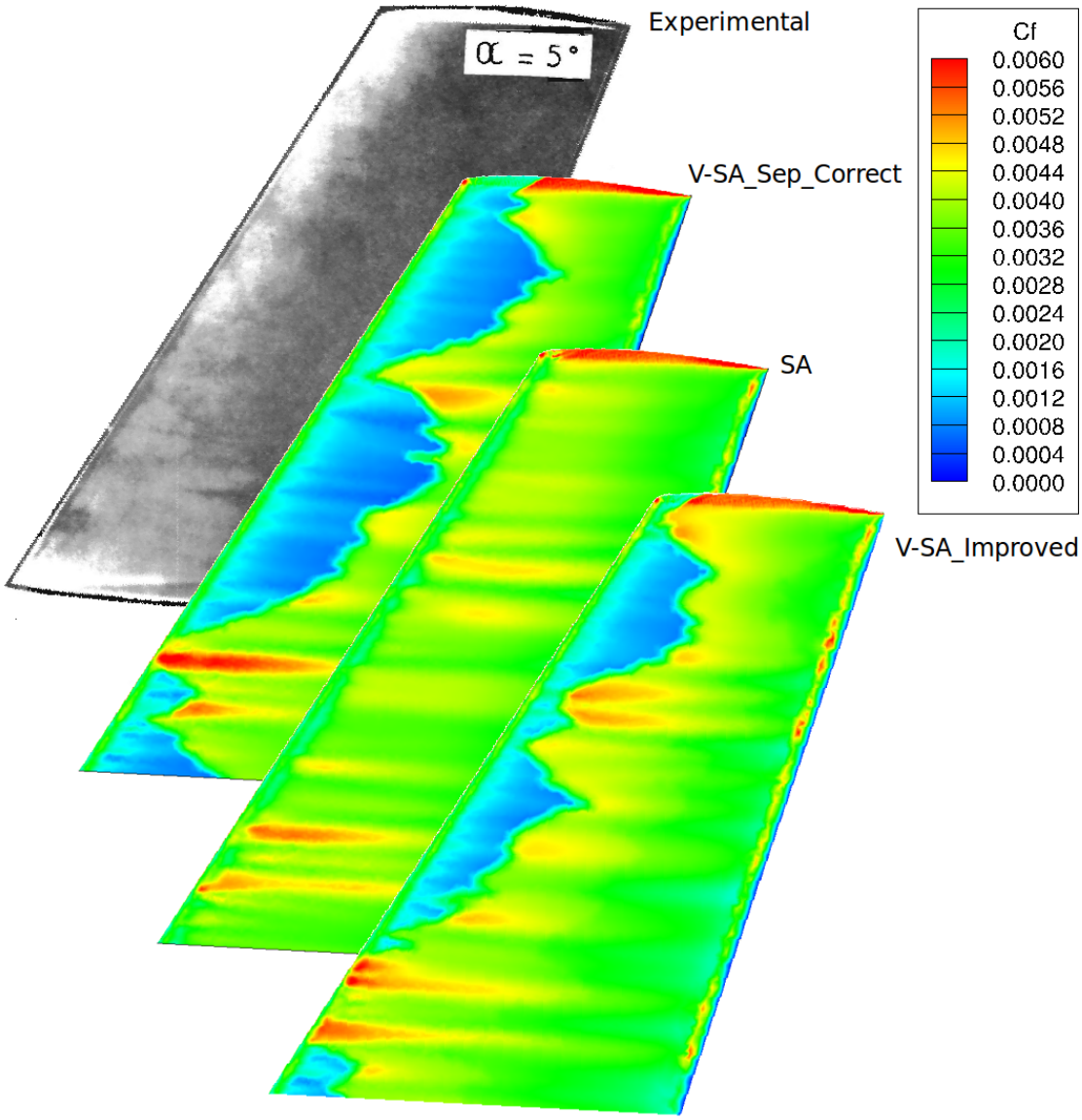

Figure 6.21: Onera-M6 wing lower surface experimental transition regions for 5° AoA. Comparison of experimental photo with skin-friction coefficient contour plots computed with the turbulence SA closure and the transition V-SA-Sep-Correct and V-SA-Improved models.

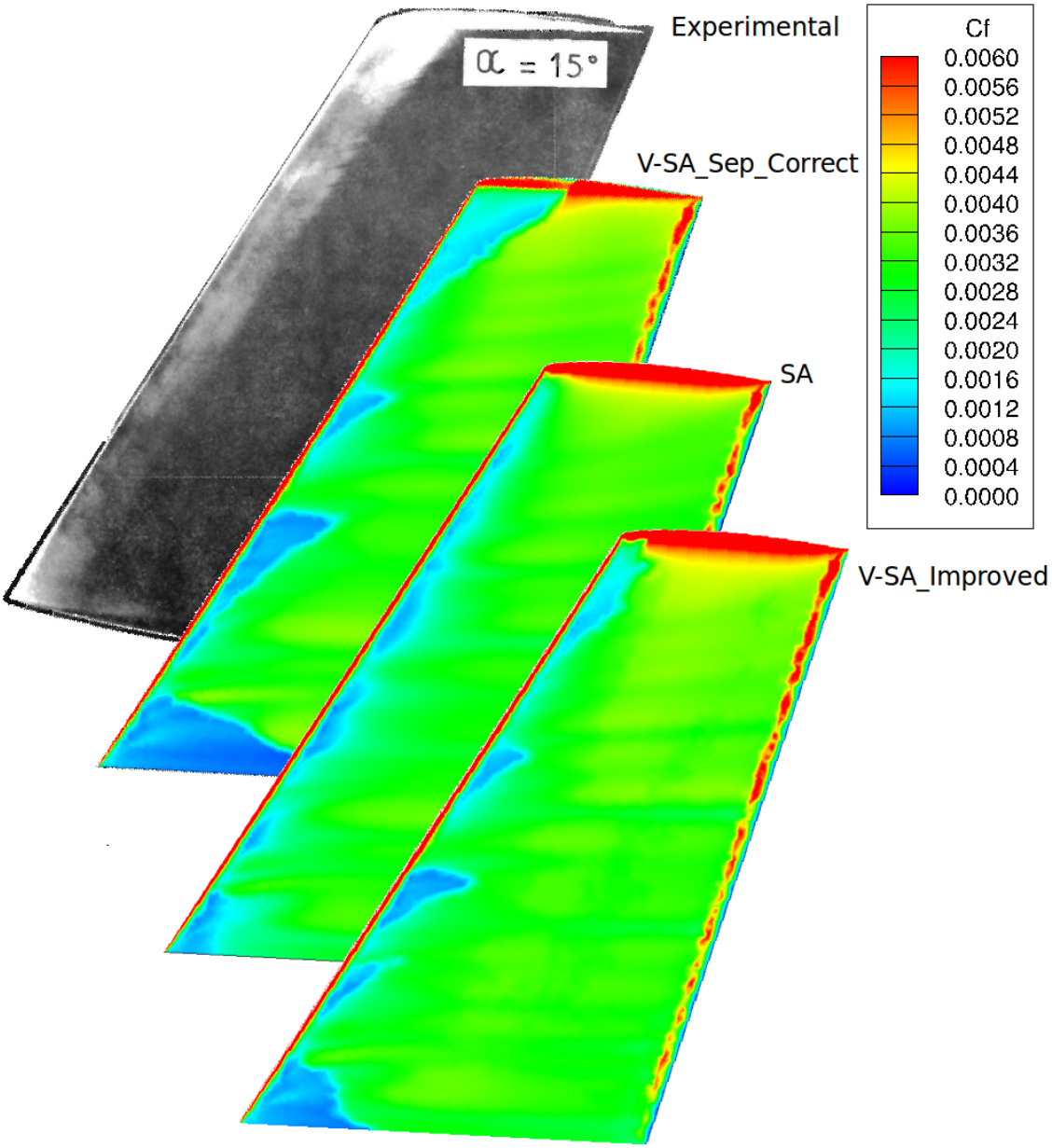

Figure 6.22: Onera-M6 wing lower surface experimental transition regions for 15° AoA. Comparison of experimental photo with skin-friction coefficient contour plots computed with the turbulence SA closure and the transition V-SA-Sep-Correct and V-SA-Improved models.

Table 6.5: DLR-F5 Wing Test Conditions

AoA	$Tu(\%)$	Re
0°	0.35	1.5×10^6
2°	0.35	1.5×10^6

Table 6.6: DLR-F5 Wing Inlet Boundary Conditions

Model	$U(m/s)$	$k_p(m^2/s^2)$	$\tilde{\nu_t}(m^2/s)$
SA	268.84	N/A	7.2×10^{-5}
V-SA-Sep-Correct	268.84	1.319	7.2×10^{-5}
V-SA-Improved	268.84	1.319	7.2×10^{-5}

of the near wing tip and root regions, the improved model version displays a similar transition behavior to the separation corrected transition closure.

6.1.3 The DLR-F5 wing test case

The final three-dimensional test case is the DLR-F5 wing under transonic flow conditions. This test case is fully documented within the report developed by Helmut Sobieczky [8]. The geometry is then a swept wing with an aspect ratio of 9.5 with 20° of swept angle, besides this, along the wing spanwise length there is no twist. Also, the root has a large fillet smoothing corner and the wing tip is rounded. The wing root chord is 0.359 meters and the wing tip has chord length of 0.058 meters, additionally the wing spanwise length is 0.649 meters. This wing was designed to avoid the development of vortices at the root's leading edge. The wing sections are based on a symmetrical NACA 0036 airfoil.

As described in the test case report, the dominant flow physics are laminar flow transition to turbulence and the presence of a shock-wave over the DLR-F5 wing. Therefore, the test case was conducted in the Transonic Wind-tunnel Göttingen (TWG) [183]. The tunnel stagnation pressure range is of 0.4 to 1.6 bar and its stagnation temperature is $310\ ^\circ K$. Also, the tunnel free-stream turbulence intensity is less than 0.35%. As detailed in Helmut Sobieczky report, the test conditions for the DLR-F5 wing are the flow angles of attack of 0 and 2 degrees. The flow Reynolds number was set to be 1.5×10^6 based on a mean chord value of 0.15 meters. The flow mach number is $M \simeq 0.82$. As such, the test conditions are disclosed in table 6.5.

This compressible DLR-F5 wing test case was computed with a density-based solver of Fluent using second order upwind discretization schemes. The V-SA-Sep-Correct and V-SA-Improved transition models Fluent implementation were applied for this case. Also, the SA turbulence model available within the Fluent software was used. The commercial software Ansys Fluent was selected to compute this case in order to have access to a fast implicit density based solver. The fluid viscosity was calculated using the Sutherland law. The applied stagnation temperature was $310\ ^\circ K$. The fluid density was calculated using the perfect gas law. The applied inlet conditions are presented in table 6.6.

The used computational mesh is then fully structured with y^+ values less than 1 over the entire DLR-F5 wing. This wing mesh had 200 computational nodes around its airfoil sections. Also, the spanwise length of the wing had 140 mesh points. The wing had 28000 computational points over its surface, with the first layer of cells over this wing surface with a wall normal distance of 1×10^{-6} meters. The total number of mesh points is 4 million. The DLR-F5 wing structured mesh is disclosed in Fig.6.23. A top view of the DLR-F5 wing structured surface mesh is presented in Fig.6.24. A mesh validation with an 8 million cell grid was computed.

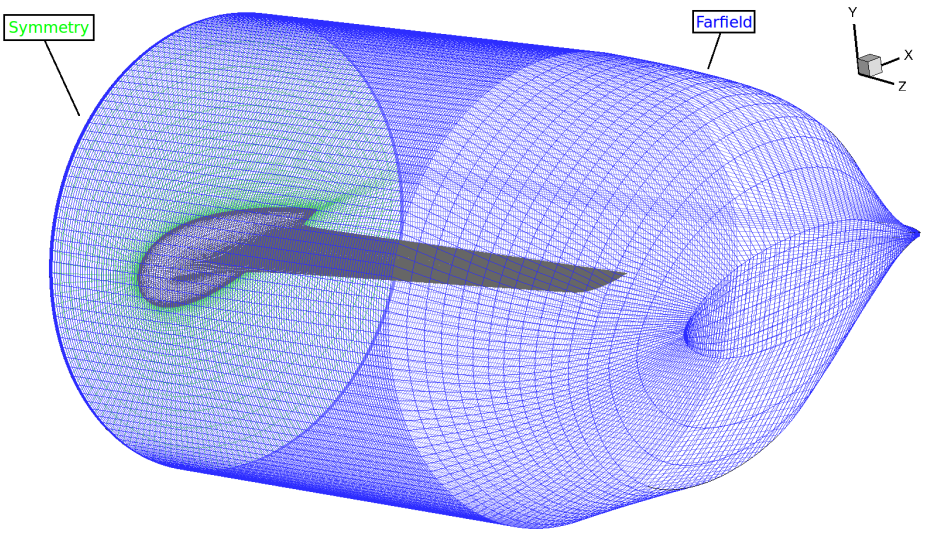

Figure 6.23: General overview of the DLR-F5 wing mesh. The far-field and symmetry surfaces are indicated and colored with the corresponding surface name color. The wing computational grid has a total number of 4000000 mesh points.

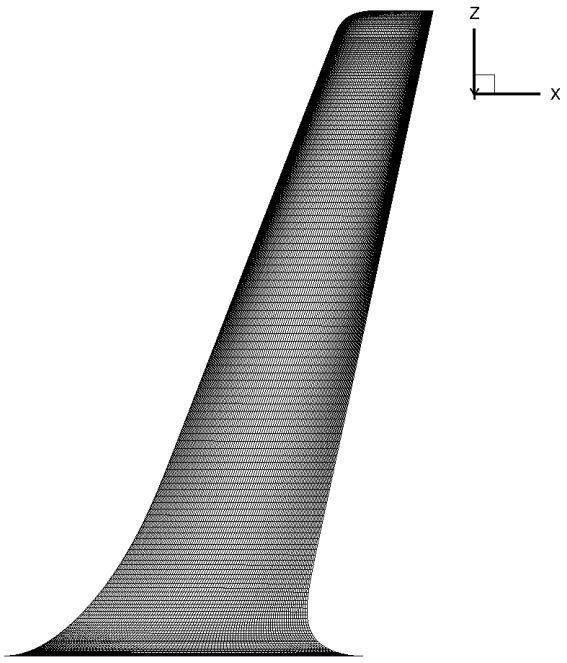

Figure 6.24: DLR-F5 wing mesh top view. The DLR-F5 has 28000 nodes over its surface.

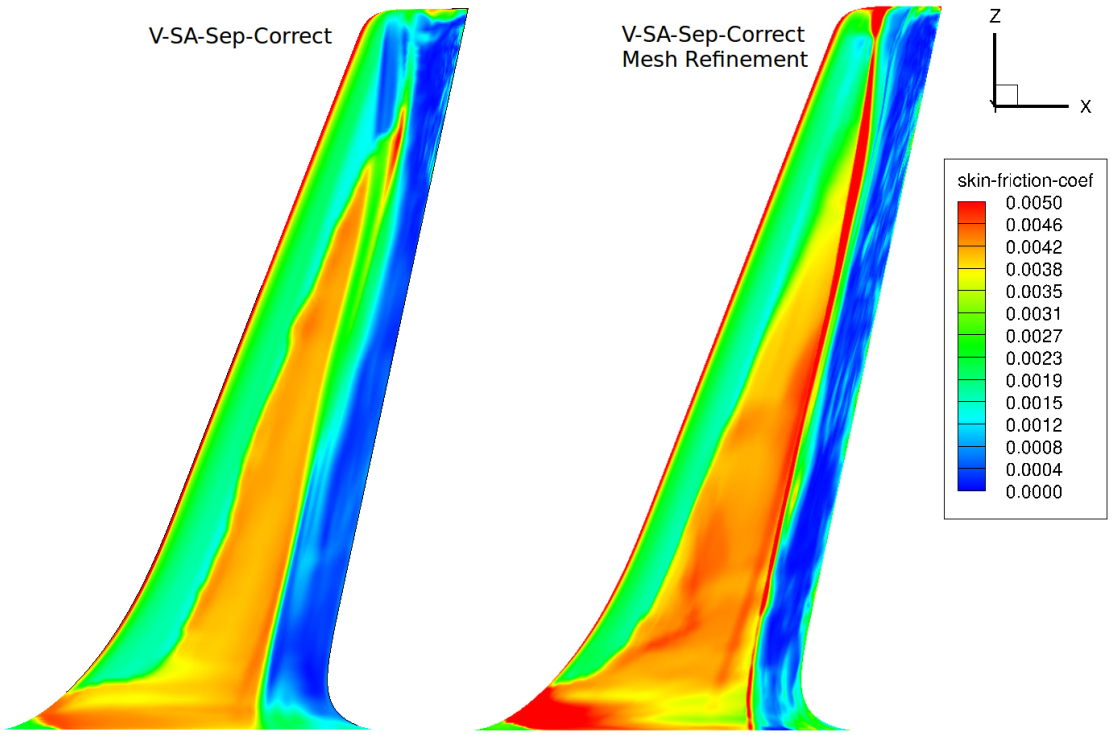

Figure 6.25: DLR-F5 wing mesh independence validation with AoA 0°. The V-SA-Sep-Correct transition model calculated skin-friction coefficient contour map is used as surface contour. The left contour represents the 4 million cells mesh result and the right contour shows the refinement effect of the usage of an 8 million cell mesh.

The skin-friction coefficient contour plot is presented in Fig.6.25. As can be seen, although the results are not identical, the general transition onset regions are similar with differences arising at the tip region of the wing. As such the obtained results can be considered to be mesh independent.

The pressure coefficient distribution along chordwise cross-sections of the wing under an AoA of $2^{\circ}$was analyzed. These are located at 1.64%, 33.77% and 80.02% of the wing spanwise length. The near root section distribution results are disclosed in Fig.6.26. The presented results show that both the turbulence and the transition models are able to capture the main features of the pressure distribution at this spanwise section of the wing. The shock-wave location on the upper surface of the wing is predicted slightly later by both closures. This improves on the lower surface case, where both the SA turbulence closure and the V-SA-Improved transition model predict the shock-wave presence closer to the experimental data than the V-SA-Sep-Correct closure. After the shock-wave there is a strong decay on the pressure coefficient. However, all models compute a steep decay compared to the experimental data. Nevertheless, for the lower surface the separation corrected V-SA transition closure predicts a pressure coefficient decay closer to the experimental data due to its delayed shock-wave position.

The mid wing section pressure coefficient plot results are disclosed in Fig.6.27. Similar to the former cross-section results, the pressure coefficient plots for the DLR-F5 wing lower surface are closer to the experimental data by the SA and both the V-SA models. On the upper-side of the wing, the numerically obtained results predict the occurrence of the transonic shock-wave earlier than what was experimentally recorded. After the shock-wave on the lower-surface side of the wing there are pressure oscillations. These are also present on the upper side of the

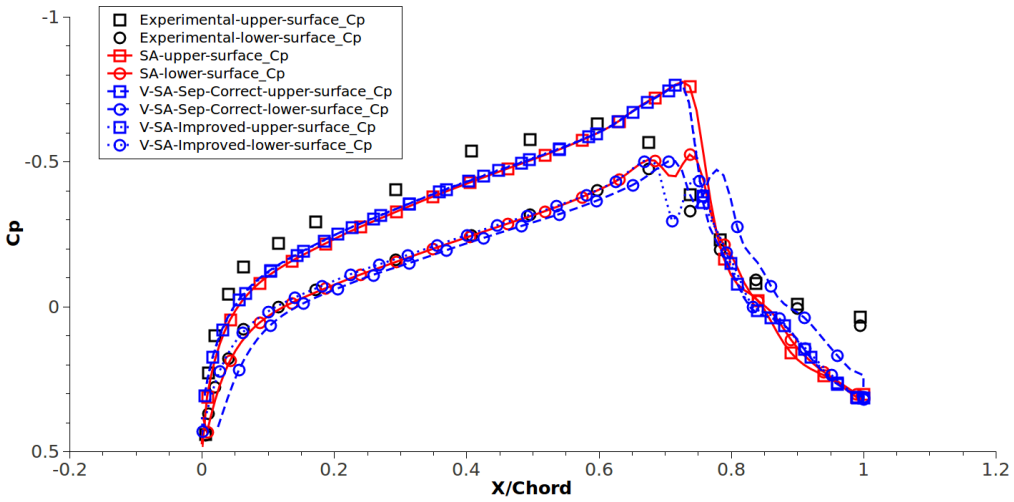

Figure 6.26: DLR-F5 wing pressure coefficient distribution along the chordwise cross-section at 1.64% of the wing spanwise length under 2° AoA. Comparison of experimental data on pressure coefficient plots with computed results from the turbulence SA closure and the transition V-SA-Sep-Correct and V-SA-Improved models.

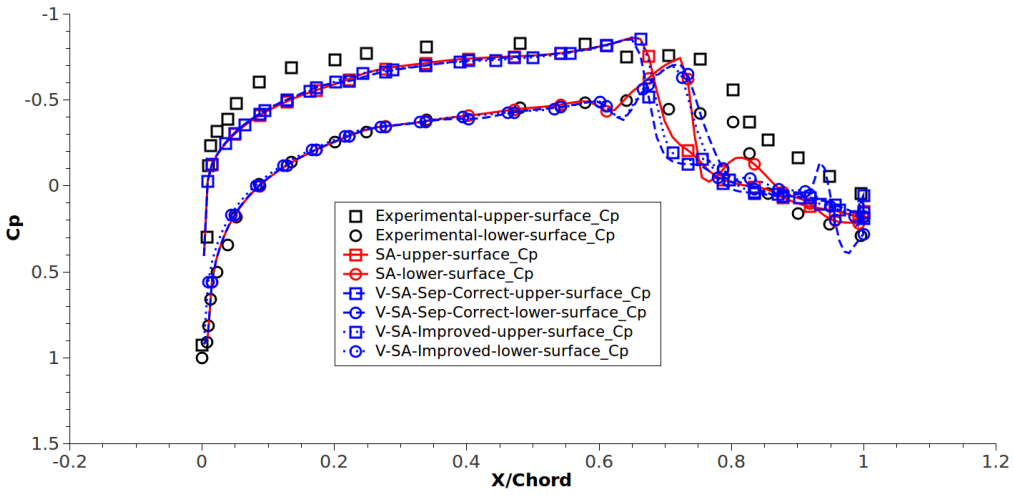

Figure 6.27: DLR-F5 wing pressure coefficient distribution along the chordwise cross-section at 33.77% of the wing spanwise length under 2° AoA. Comparison of experimental data on pressure coefficient plots with computed results from the turbulence SA closure and the transition V-SA-Sep-Correct and V-SA-Improved models.

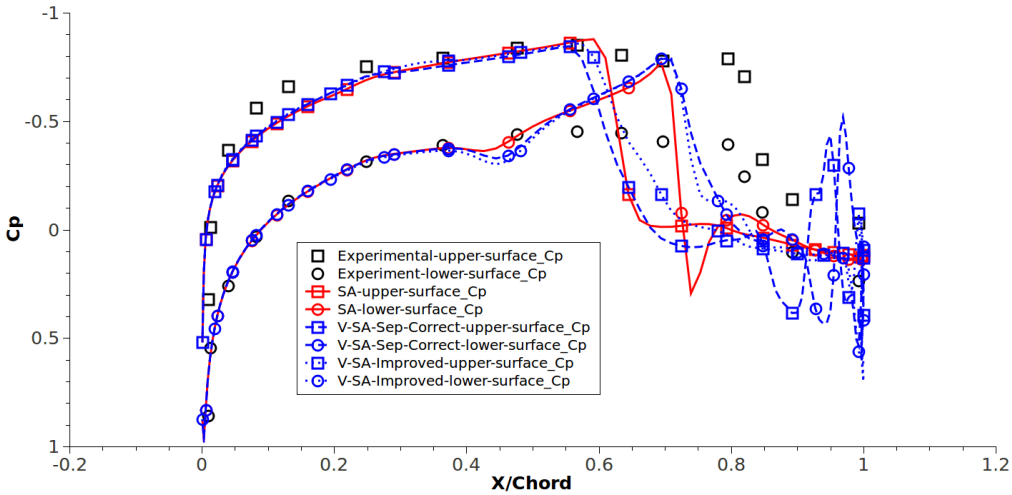

Figure 6.28: DLR-F5 wing pressure coefficient distribution along the chordwise cross-section at 80.02% of the wing spanwise length under 2° AoA. Comparison of experimental data on pressure coefficient plots with computed results from the turbulence SA closure and the transition V-SA-Sep-Correct and V-SA-Improved models.

wing, nevertheless with a smaller amplitude.

The near wing tip section pressure coefficient plot data is presented in Fig.6.28. It can be observed that the SA turbulence model and both the V-SA transition closures predict a very early pressure shock-wave on the upper surface of the wing. Also, the V-SA-Sep-Correct transition closure presents very intense pressure oscillations on the trailing edge of the wing after the shock-wave. These are due to the fact that the V-SA-Sep-Correct model computes flow separation in these regions on both sides of the wing. Both the V-SA-Improved and SA models improve on this issue, presenting a smoother pressure-coefficient development. Although the SA, V-SA-Sep-Correct and V-SA-Improved closures compute an earlier shock-wave location on the lower side of the wing, this is closer to the experimental data region than the upper side results.

In order to evaluate the experimentally recorded transition patterns over the DLR-F5 wing, a contour plot of the skin-friction coefficient over the wing was obtained for the SA and V-SA transition model versions. However, only the V-SA-Sep-Correct and V-SA-Improved transition models are directly compared to the experimental transition patterns. This is the case since the SA turbulence model does not predict any transition pattern, instead it assumes fully turbulent flow from the leading edge of the wing. Nevertheless, a comparison between the latter and the V-SA models is performed in order to expose this fact. As such, for an AoA of 0°, the comparison between the experimental transition patterns and the skin-friction coefficient contour plot is disclosed in Fig.6.29. For this transonic test case, the separation corrected V-SA transition model is able to capture the main transition features that occur over the DLR-F5 wing surface. The root leading edge region has a very small laminar extension due to the fact that the numerical simulation was performed using a symmetric boundary condition for the plane where the wing is recessed. In the experimental setup, this is a wall, which bleeds its turbulent boundary layer over the DLR-F5 wing root region. The used symmetry boundary will not affect turbulence transition since it does not impose any flow strain. The initial curved transition shape on the root is very closely predicted by the V-SA-Sep-Correct transition model

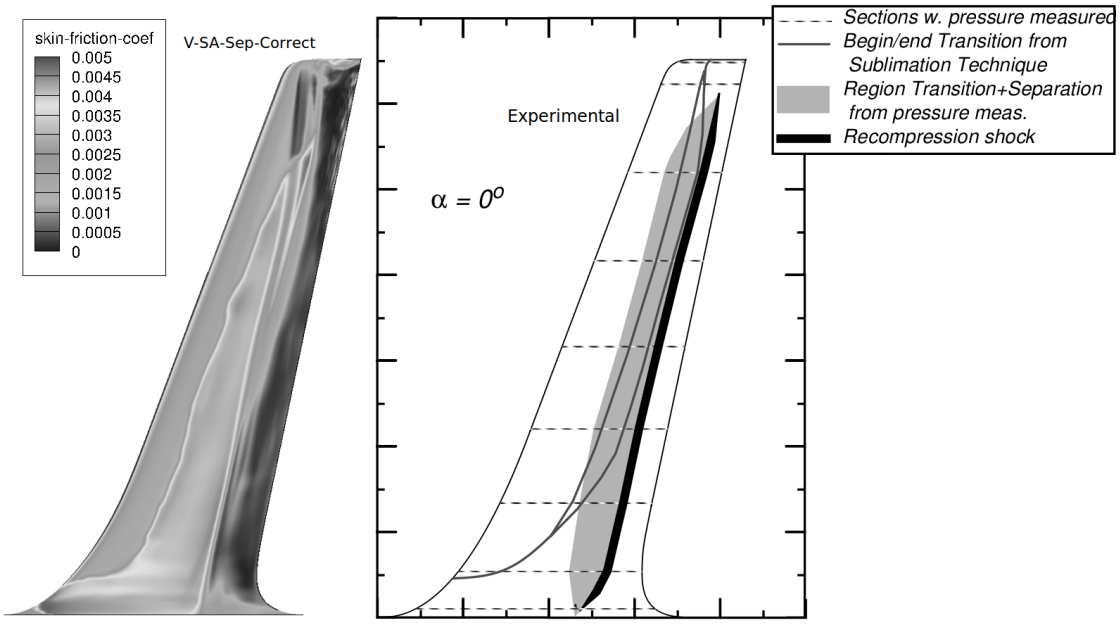

Figure 6.29: DLR-F5 wing experimental transition regions for 0° AoA. Comparison of experimental patterns with skin-friction coefficient contour plots computed with the separation corrected V-SA transition model.

when compared to the experimental pattern. The remaining spanwise length transition onset region is computed slightly earlier than the experimental data.

Although the near tip area presents an apparent transition shape resembling that of the experimental transition onset patterns, it is not clear and easily interpreted whether or not the computed transition threshold zones are correctly predicted. As such, an overlap of sections from the experimental transition patterns will be imposed on the skin-friction coefficient contour plots of both the V-SA-Sep-Correct and V-SA-Improved transition models. These are then used for the comparison with the obtained computational results from the SA turbulence model. This is presented in Fig.6.30. From these results it can be concluded that the SA turbulence model predicts a fully turbulent flow right from the leading edge of the wing. Even the near root leading edge region that was predicted to be laminar by the V-SA transition models is computed as fully turbulent flow by the SA closure. Also, it can be observed that the V-SA-Sep-Correct transition closure computes a slightly earlier transition threshold compared to the experimental data and a near tip area with an apparently correct transition shape close to the experimental pattern. The V-SA-Improved transition model presents a similar transition onset behavior to the V-SA-Sep-Correct closure. However, the V-SA-Improved model predicts a more accurate wing tip transition onset pattern. This can be observed in more detail in Fig.6.31.

The remaining experimental data on transition threshold patterns is for the case of the DLR-F5 wing under 2° AoA. The results from the upper surface side of the wing are then shown in Fig.6.32. For the case of the DLR-F5 wing upper surface under 2° AoA, the experimental transition patterns on the tip region slightly shift towards the leading edge. Additionally, the spanwise extension of the transition detection by pressure measurements is also extended towards the wing's tip. These two trends are also predicted by the V-SA-Sep-Correct transition model. Nevertheless, the transition shift onto the wing's leading edge is over-estimated in the mid sections of the DLR-F5. The V-SA-Sep-Correct transition model predicts an earlier transition onset than the experimental data in these regions.

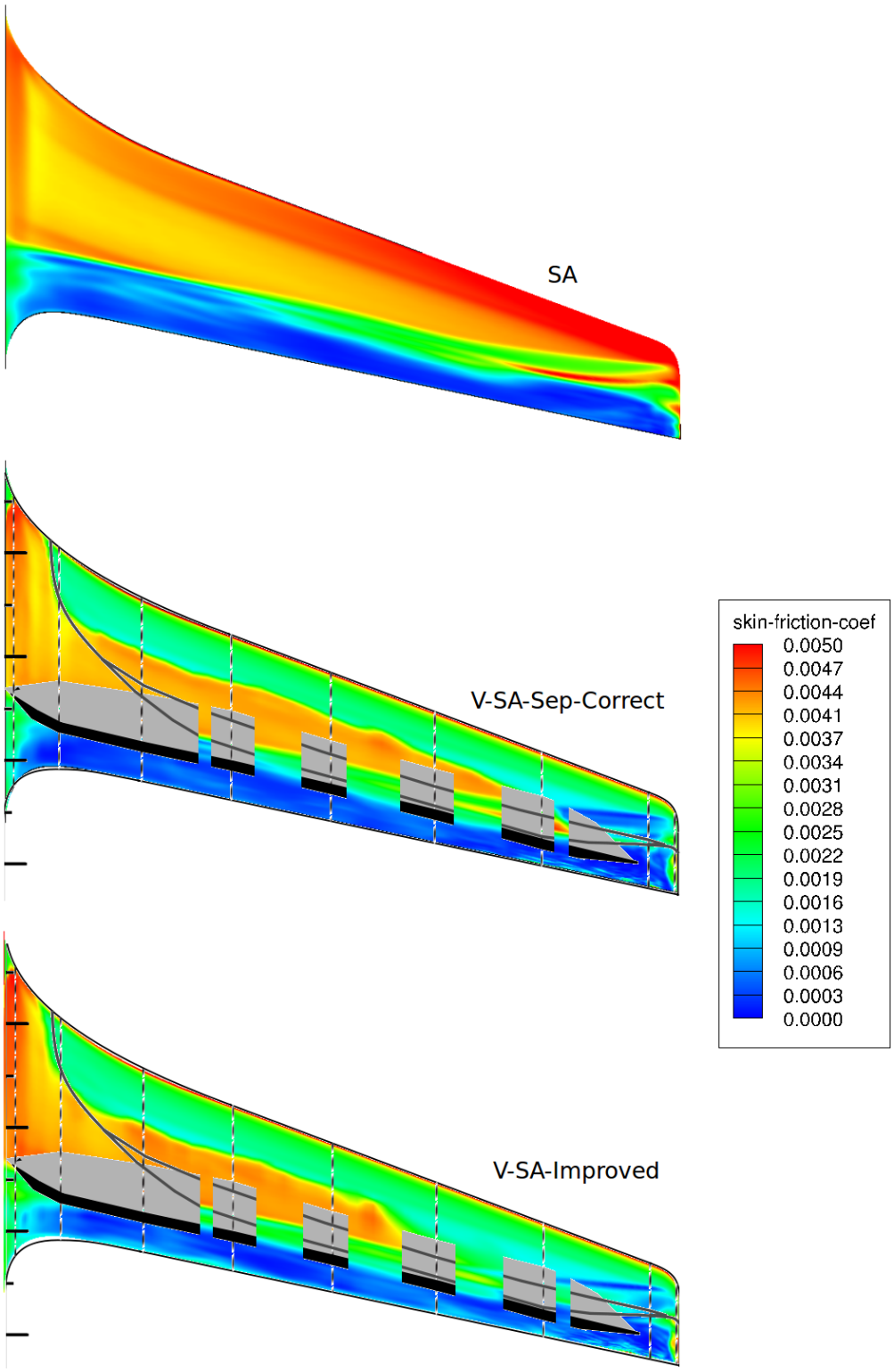

Figure 6.30: DLR-F5 wing skin-friction coefficient contour plot for 0° AoA. Comparison of computed results between the SA turbulence closure and the V-SA-Sep-Correct and V-SA-Improved transition models with overlapping experimental transition patterns.

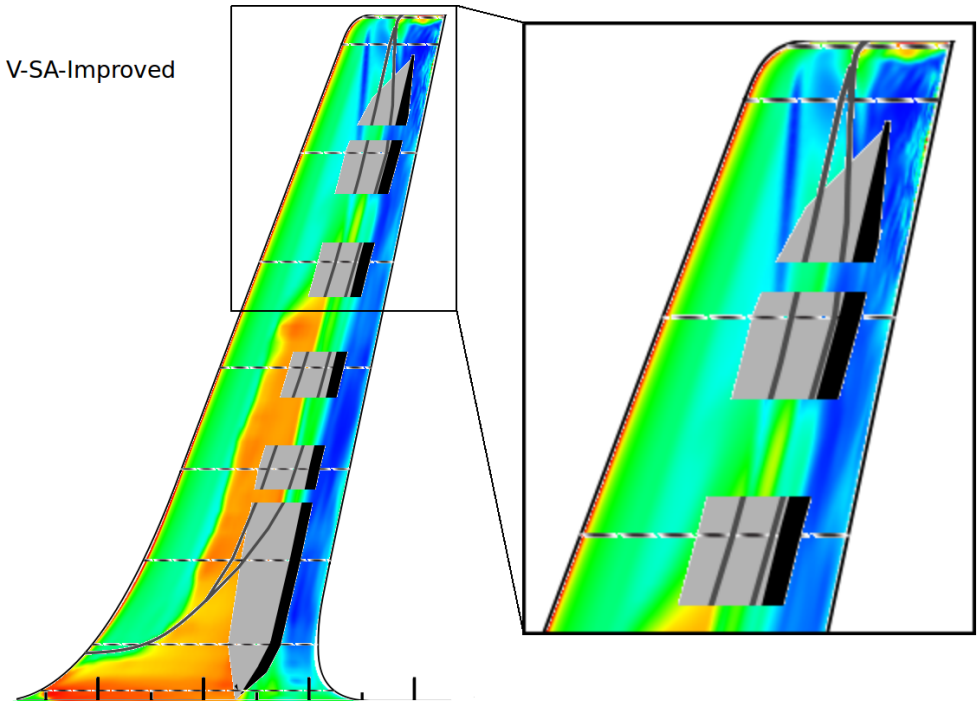

Figure 6.31: DLR-F5 wing skin-friction coefficient contour plot for 0° AoA with a wing tip region detail view. Comparison of computed results from the V-SA-Improved transition model with overlapping experimental transition patterns.

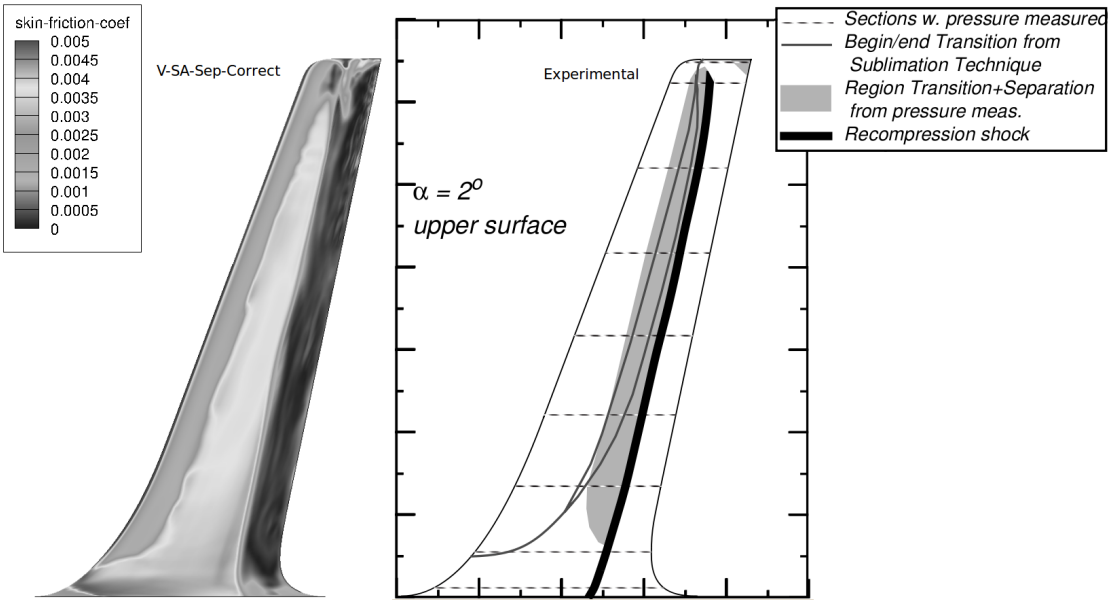

Figure 6.32: DLR-F5 wing upper surface experimental transition regions for 2° AoA. Comparison of experimental patterns with skin-friction coefficient contour plots computed with the separation corrected V-SA transition model.

The SA turbulence closure obtained results are compared with the separation corrected V-SA transition model and the V-SA-Improved closure in Fig.6.33. Again the SA turbulence closure predicts transition onset from the leading edge of the DLR-F5 wing. The experimental transition pattern overlap shows that the V-SA-Sep-Correct transition model computes a root transition region close to the experimental data, along side the wing tip region. However, within the spanwise mid zone of the wing, the transition closure predicts a transition onset earlier than the experimental data. Although the V-SA-Improved transition model results resemble those from the V-SA-Sep-Correct closure, these show a slightly more accurate transition pattern closer to the experimentally recorded data. It must be noted that the small wiggles, on the computed transition pattern lines, are to be expected. These small oscillations were also observed in the experimental photo from the Helmut Sobieczky report disclosed in Fig.6.34.

The experimental comparison, with the computed results from the lower surface side of the DLR-F5 wing under 2° AoA, is disclosed in Fig.6.35. These results show that the V-SA transition model captures the root region transition shape close to the experimental data. Although the remaining wing spanwise extension does not apparently display any transition onset, under a closer look it can be observed that this is actually predicted by the separation corrected V-SA transition model as shown in the following Fig.6.36. As can be seen, the SA turbulence model calculates fully turbulent flow from the leading edge of the DLR-F5 wing. The V-SA-Sep-Correct and V-SA-Improved transition closures are able to predict the transition onset regions close to the experimental data along the whole extension of the wing. Nevertheless, V-SA-Improved transition model discloses the most accurate transition onset pattern. This can be examined in more detail in Fig.6.37.

6.1.4 Summary of results

The strengths of the V-SA transition model are verified on the transition under cross-flow effects test cases of the three-dimensional 6:1 prolate-spheroid, the Onera-M6 wing and the DLR-F5 wing geometries. It was observed that although the free-stream turbulence intensity for these cases is very low, the 6:1 prolate-spheroid with Tu=0.1%, the Onera-M6 wing with Tu=0.2% and Tu=0.35% for the DLR-F5 wing, the model is able to predict transition onset patterns close to the experimental data.

However, the transition length of the model is short in some of the tested cases. For the 6:1 prolate-spheroid test case with a low angle of attack of 5°, the V-SA model predicts a short transition length. Although the reason for the latter is unclear, it is suspected that an excessive pre-transition turbulent kinetic energy diffusion inside the boundary layer might be the reason for such short transition length. The rate of turbulence intermittency diffusion into the transition boundary layer has a major role determining transition length as shown in the work of [12]. Also, the separation corrected version of the transition closure has an earlier prediction behavior compared to its base V-SA transition model. Nevertheless, the improved version of this model improves on this issue, however, for the AoA of 15° test case, the V-SA-Improved transition model shows a delayed transition onset compared to both the experimental and the numerical results of the remaining V-SA transition model versions. The V-SA-Improved closure predicted transition threshold patterns, for the test cases with an AoA of 5° and 30°, are in good agreement with the experimental data.

The most concerning issue of the V-SA-Sep-Correct model under adverse-pressure-gradient flow conditions, is its apparent lack of turbulent strength in the fully turbulent region. This is seen in the Onera-M6 wing test case upper surface tip zone for flow AoA of 15° and also in the

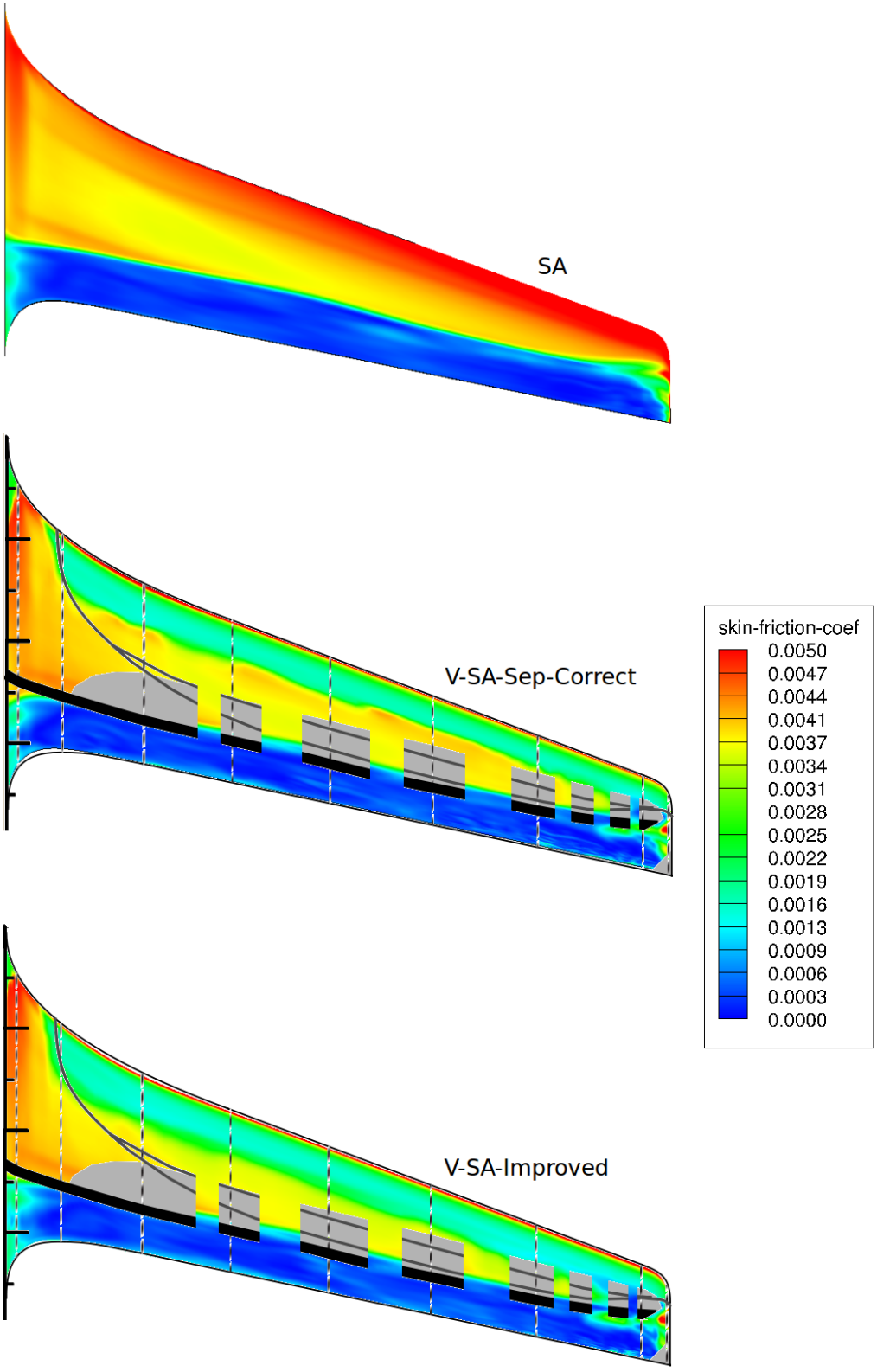

Figure 6.33: DLR-F5 wing upper surface skin-friction coefficient contour plot for 2° AoA. Comparison of computed results between the SA turbulence closure and the V-SA-Sep-Correct and V-SA-Improved transition models with overlapping experimental transition patterns.

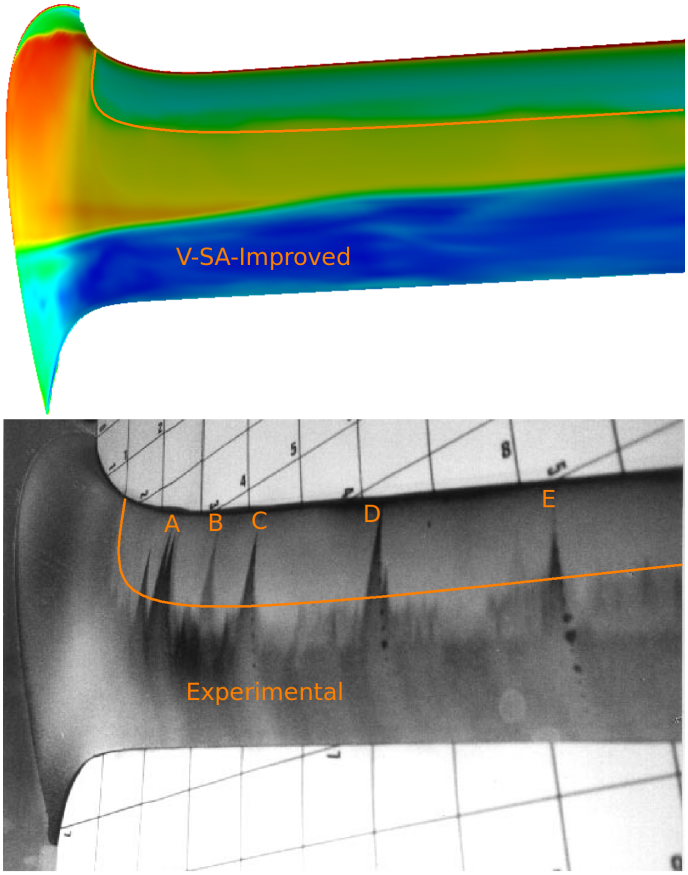

Figure 6.34: DLR-F5 wing upper surface sublimation turbulence transition detection technique for 2° AoA. Comparison of computed skin-friction coefficient results from V-SA-Improved model with experimental photo from technical report of Helmut Sobieczky [8]. The orange line highlights the transition onset location on both the experimental photo and the V-SA-Improved model computed transition pattern. The letters A, B, C, D, and E indicate the location of pressure probe stations.

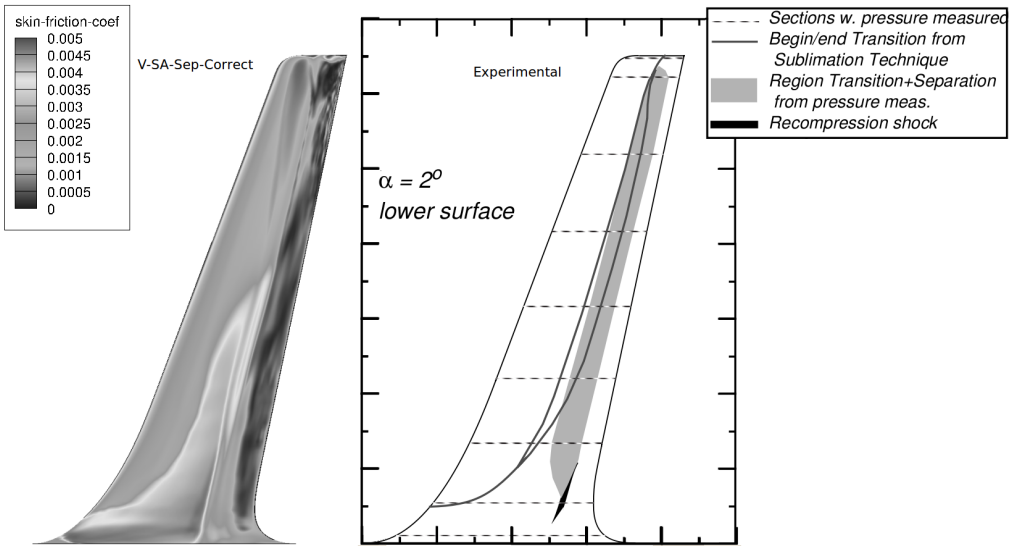

Figure 6.35: DLR-F5 wing lower surface experimental transition regions for 2° AoA. Comparison of experimental patterns with skin-friction coefficient contour plots computed with the separation corrected V-SA transition model.

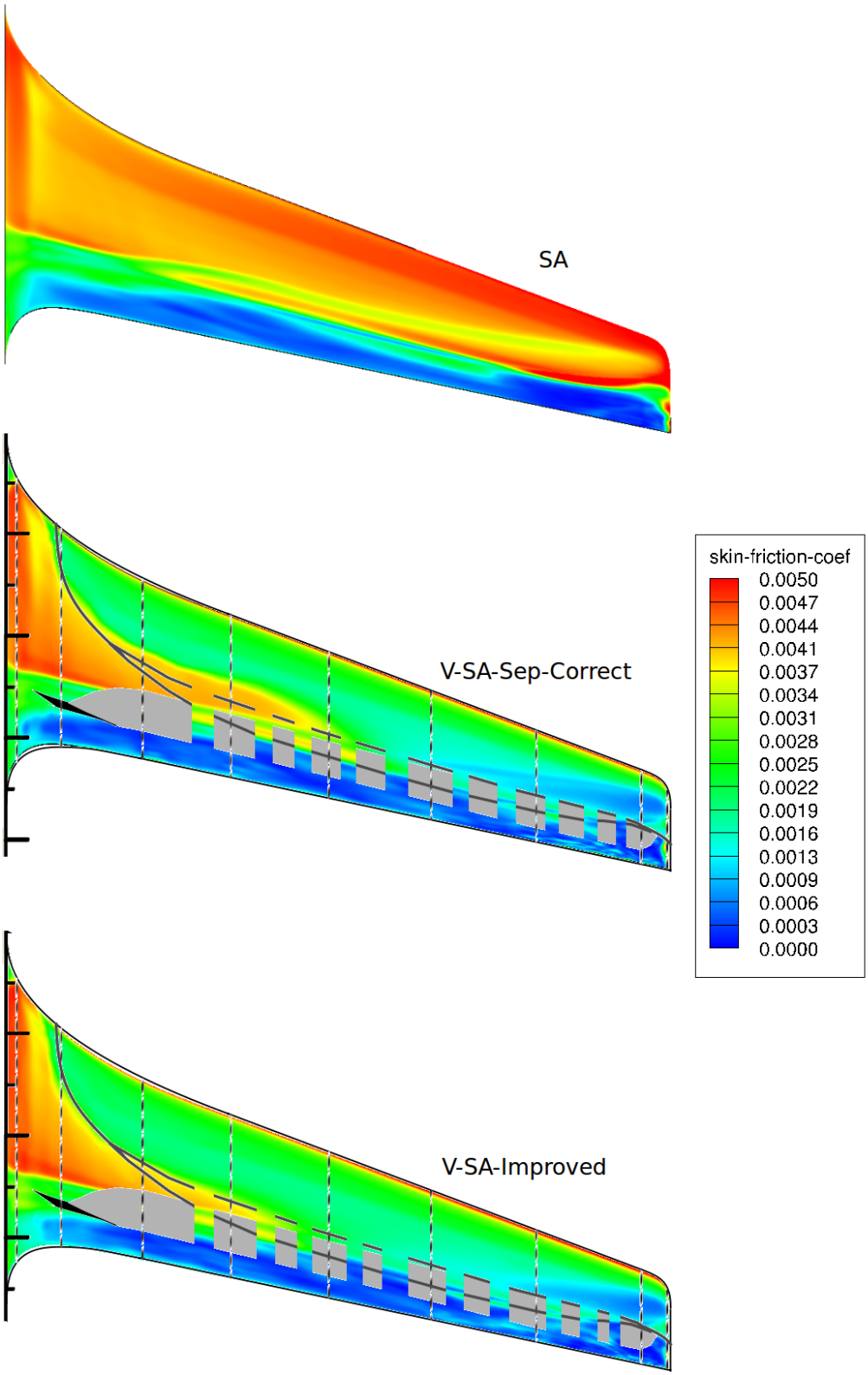

Figure 6.36: DLR-F5 wing lower surface skin-friction coefficient contour plot for 2° AoA. Comparison of computed results between the SA turbulence closure and the V-SA-Sep-Correct and V-SA-Improved transition models with overlapping experimental transition patterns.

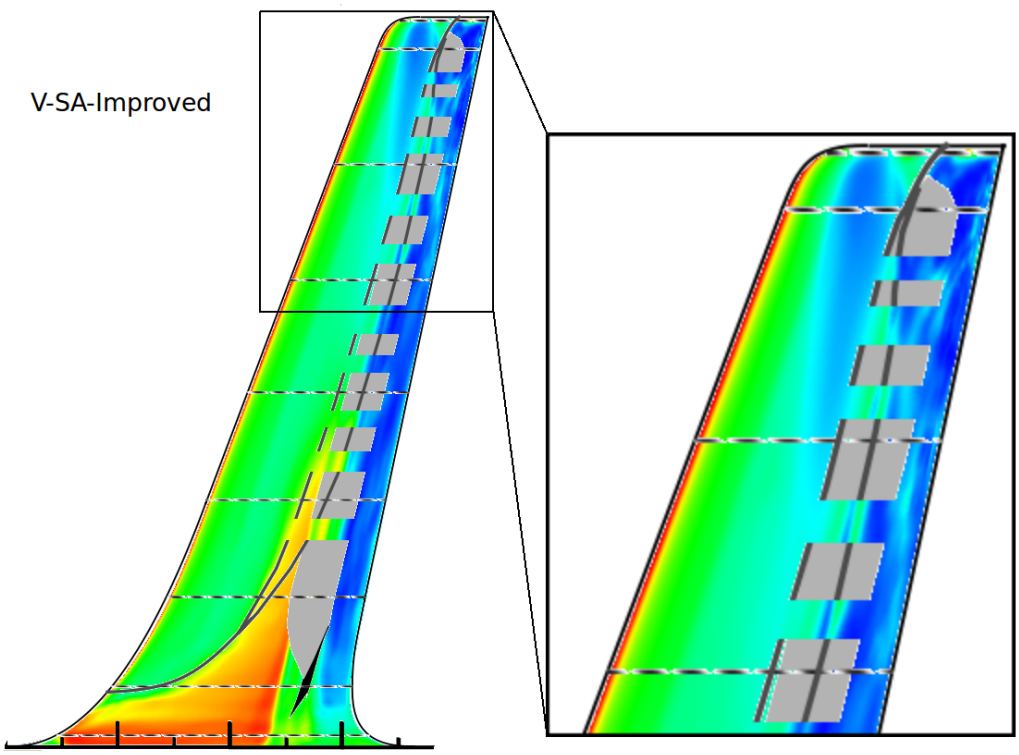

Figure 6.37: DLR-F5 wing lower surface skin-friction coefficient contour plot for 2° AoA with a wing tip region detail view. Comparison of computed results from the V-SA-Improved transition model with overlapping experimental transition patterns.

previous chapter test case of the Aerospatiale A-airfoil. For these cases the V-SA-Sep-Correct transition model computes flow separation earlier than expected. Nonetheless, the V-SA-Sep-Correct improved version, that is the V-SA-Improved, displays an outstanding enhancement on this issue. The V-SA-Improved transition model is able to maintain its transition onset prediction capabilities while correcting the aforementioned apparent lack of turbulent strength in the fully turbulent region. Thus, computations under adverse-pressure-gradient conditions, show no premature flow separation when compared to the V-SA transition model original Spalart-Allmaras turbulence closure.

The transonic DLR-F5 wing test case showed the full capacity of the model to predict complex transition patterns under transonic flow conditions with compressible effects on the transition behavior. Although some of the transition patterns were predicted slightly earlier, the comparison between the SA turbulence closure and the V-SA transition models show a clear distinction between using a low-Reynolds turbulence closure and a physics based transition model to compute a transonic transition test case. The low-Reynolds turbulence models are not fit for computations of compressible external flows with significant transition effects. On the other hand, and as shown by the V-SA-Improved transition model, the experimental DLR-F5 transonic wing test case transition patterns were accurately predicted by the performed computations using the V-SA transition models.

Chapter 7

Conclusions

7.1 Summary

During the present work, the main objective of developing numerical models for prediction of laminar boundary layer transition to fully turbulent flow regime was accomplished. These tools were implemented in a RANS work-frame.

The modified phenomenological LKE transition model, k-k_l-ω-mod, is also a RANS turbulence model since it is embedded within a k-ω turbulence model. The initial objective for the implementation of the phenomenological k-k_l-ω transition model, was its modification for improvement. However, when attempting to validate the implemented model according to the original published model formulation, the obtained results were systematically incorrect. Also, these presented different results and did not follow the same trend as the closed commercial model version.

As such, the initial objective of improving an existing transition RANS closure was changed to obtain a more correct model formulation. This was then performed in order to mimic the behavior of the commercial software Ansys Fluent available phenomenological transition model, not its improvement. The model was then validated for existing flat-plate ERCOFTAC benchmark test cases for zero-pressure-gradient, for pressure-gradient and also for separation induced transition.

Based on the initial transition model modification work, a new concept for transition prediction was developed. The concept is a never before used mechanical approximation for the effects of mean flow shear over turbulence characteristics in the pre-transition zone. This was then numerically evaluated and developed in order to be a feasible transition model. The developed novel transition model was coupled to the RANS low-Reynolds turbulence model, the Spalart-Allmaras.

Afterwards, the created V-SA transition model was validated for the ERCOFTAC flat-plate benchmark test cases of zero-pressure-gradient, pressure-gradient and separation induced transition. The effect of transition induced by separation under low velocity and turbulence intensity has revealed a weakness of the V-SA transition model. A correction for the separation issue was devised and successfully applied on the transition model.

Besides the previous flow separation induced transition predicament, yet another circumstance related to flow separation was observed. For this case, the transition model computed a premature boundary layer separation on the fully turbulent region of the flow under adverse-pressure-gradient conditions. This was solved by modifying the coupling between the transition V-model and the Spalart-Allmaras turbulence closure.

Also, the model was further validated for airfoil geometries and finally the transition closure was validated for three-dimensional geometries such as the 6:1 prolate-spheroid, the Onera-M6 wing and the transonic DLR-F5 wing test case.

7.2 Concluding remarks

The effect of small changes to the flat-plate leading edge radius was studied with the developed transition models and existing RANS transition closures. The increase of the flat-plate leading edge radius will move the transition onset prediction closer to the flat-plate leading edge, thus the transition threshold Reynolds number is reduced.

The obtained results from the modified laminar kinetic energy transition model, k-k_l-ω-mod, reveal a significant improvement in comparison to the original published model formulation. In some cases the altered model presents slightly improved results when compared to the obtained computations from the k-k_l-ω. Therefore, it can be stated that the achieved modified transition model, k-k_l-ω-mod, corresponds to the proposed objectives.

Regarding the novel transition model, V-SA, the proposed mechanical approximation for the mean flow shear effect on the turbulence characteristics was validated. This was performed using the ERCOFTAC database of $\overline{u'v'}$ values within the pre-transitional region of the laminar boundary layer. Although the evolution of the distribution of $\overline{u'v'}$, along the flat-plate test cases of T3A and T3C2 was not in perfect accordance to the experimental data, it captures the experimental trend.

The proposed separation correction for the V-SA model improves the model robustness under separation induced transition. Additionally, the improved transition model version enhances the separation corrected transition closure under adverse-pressure-gradient flow conditions for the fully turbulent boundary layer region.

The V-SA model was also validated for more complex cases such as wind turbine airfoils. The transition onset for the multiple AoA values was captured very close to the experimental data. Also, a validation of the T106 turbine airfoil was performed. The main experimental characteristic pressure losses evolution of the linear turbine cascade as well as the transition onset behavior were predicted in accordance to the experimental data.

Finally, the model validation with three-dimensional geometries reveals that the transition closure is able to capture interesting transition onset features of these test cases, such as the experimental 6:1 prolate-spheroid test case transition patterns. It can be concluded that the V-SA transition model is a ready to use robust transition tool for industry use [14, 15].

7.3 Future works

For future works it is proposed the improvement of the modified LKE transition model k-k_l-ω-mod in what regards transition onset prediction accuracy. Also, the LKE concept of the model could be linked to other turbulence models.

For the V-SA transition model, this could incorporate pure natural transition mechanism components. The implementation of such functions was not feasible since the developed mechanical model analogy is not applicable to pure natural transition onset. This would improve the accuracy for some cases such as the example in the ERCOFTAC zero-pressure-gradient test case of T3A-.

The V-model transition closure could also be coupled to other turbulence models. Also, the V-model formulation was performed for isotropic turbulence conditions, a three-component turbulent kinetic energy transition model would be of interest to see the implications of such approach.

Finally, the V-model transition closure is not able by it-self to reproduce turbulence. It

would be very interesting to attempt the creation of a turbulence model based on the proposed mechanical approximation.

Bibliography

[1] V. Parezanović, J. C. Laurentie, C. Fourment, J. Delville, L. Cordier, and B. R. Noack, "Experimental study of open- and closed-loop control of a turbulent mixing layer," in *14Th European Turbulence Conference, Lyon, France*, pp. 1–2, 2013.

[2] C. Liu and L. Chen, "Parallel DNS for vortex structure of late stages of flow transition," *Computers & Fluids*, vol. 45, no. 1, pp. 129–137, 2011.

[3] P. Bradshaw, "Turbulence: the chief outstanding difficulty of our subject," *Experiments in Fluids*, vol. 16, no. 3, pp. 203–216, 1994.

[4] P. S. Klebanoff, "Effects of free-stream turbulence on a laminar boundary layer," *Bulletin. Am. Phys. Soc.*, vol. 16, p. 1323, 1971.

[5] D. M. Somers, "Design and experimental results for the S805 airfoil," tech. rep., NREL/SR-440-6918, 1997.

[6] L. Cutrone, P. D. Palma, G. Pascazio, and M. Napolitano, "Predicting transition in two- and three-dimensional separated flows," *International Journal of Heat and Fluid Flow*, vol. 29, no. 2, pp. 504–526, 2008.

[7] H.-P. Kreplin, H. Vollmers, and H. Meier, "Wall shear stress measurements on an inclined prolate spheroid in the DFVLR 3 m x 3 m low speed wind tunnel, Göttingen," tech. rep., DFVLR-AVA, 1985.

[8] H. Sobieczky, "DLR-F5: Test wing for CFD and applied aerodynamics," tech. rep., DLR German Aerospace Research Establishment, 1994.

[9] M. Matsubara and P. H. Alfredsson, "Disturbance growth in boundary layers subjected to free-stream turbulence," *Journal of Fluid Mechanics*, vol. 430, pp. 149–168, 2001.

[10] I. Hadzic and K. Hanjalic, "Separation-induced transition to turbulence: Second-moment closure modelling," *Flow, Turbulence and Combustion*, vol. 63, pp. 153–173, 1999.

[11] R. Langtry and F. Menter, *Overview of Industrial Transition Modelling in CFX*. ANSYS Germany GmbH, ANSYS CFX Staudenfeldweg 12, 83624 ed., 2006.

[12] P. Durbin, "An intermittency model for bypass transition," *International Journal of Heat and Fluid Flow*, vol. 36, no. 0, pp. 1–6, 2012.

[13] B. Aupoix, D. Arnal, H. Bézard, B. Chaouat, F. Chedevergne, S. Deck, V. Gleize, P. Grenard, and E. Laroche, "Transition and turbulence modeling," *Aerospace Lab Journal*, p. 13, 2011.

[14] G. Ilieva, J. Páscoa, A. Dumas, and M. Trancossi, "A critical review of propulsion concepts for modern airships," *Central European Journal of Engineering*, vol. 2, no. 2, pp. 189–200, 2012.

[15] M. Trancossi, A. Dumas, M. Madonia, J. Páscoa, and D. Vucinic, "Fire-safe airship system design," *SAE International Journal of Aerospace,*, vol. 5, no. 1, pp. 11–21, 2012.

[16] A. V. Popov, R. M. Botez, and M. Labib, "Transition point detection from the surface pressure distribution for controller design," *Journal of aircraft*, vol. 45, no. 1, pp. 23–28, 2008.

[17] C. Baxevanou and D. Fidaros, "Validation of numerical schemes and turbulence models combinations for transient flow around airfoil," *Engineering Applications of Computational Fluid Mechanics*, vol. 2, pp. 208–221, 2008.

[18] W. P. Wolfe and S. S. Ochs, "CFD calculations of S809 aerodynamic characteristics," *AIAA-97-0973*, p. 8, 1997.

[19] S. Gupta and J. Leishman, "Dynamic stall modeling of the S809 airfoil and comparison with experiments," *44th AIAA Aerospace Sciences Meeting and Exhibit*, 2006.

[20] W. A. Timmer, "Two-dimensional low-Reynolds number wind tunnel results for airfoil NACA 0018," *Wind Engineering*, vol. 32, no. 6, pp. 525–537, 2008.

[21] J. C. Lin, S. K. Robinson, and R. G. McGhee, "Separation control on high-lift airfoils via micro-vortex generators," *Journal of Aircraft*, vol. 31, no. 6, pp. 1317–1323, 1994.

[22] M. Franke, S. Wallin, and F. Thiele, "Assessment of explicit algebraic Reynolds-stress turbulence models in aerodynamic computations," *Aerospace Science and Technology*, vol. 9, pp. 573–581, 2005.

[23] G. J. v. Fossen and C. Y. Ching, "Measurements of the influence of integral length scale on stagnation region heat transfer," *NASA Technical Memorandum 106503*, 1994.

[24] R. W. Radomsky and K. A. Thole, "Detailed boundary layer measurements on a turbine stator vane at elevated freestream turbulence levels," *Journal of Turbomachinery*, vol. 124, no. 1, pp. 107–118, 2002.

[25] R. E. Mayle, "The role of laminar-turbulent transition in gas turbine engines," *Journal of Turbomachinery*, vol. 113, no. 4, pp. 509–536, 1991.

[26] R. J. Volino and T. W. Simon, "Boundary layer transition under high free-stream turbulence and strong acceleration conditions: Part 1—mean flow results," *Journal of Heat Transfer*, vol. 119, no. 3, pp. 420–426, 1997.

[27] R. J. Volino and T. W. Simon, "Boundary layer transition under high free-stream turbulence and strong acceleration conditions: Part 2—turbulent transport results," *Journal of Heat Transfer*, vol. 119, no. 3, pp. 427–432, 1997.

[28] F. R. Menter, M. Kuntz, and R. Langtry, "Ten years of industrial experience with the SST turbulence model," *Turbulence, Heat and Mass Transfer 4*, 2003.

[29] R. B. Langtry and F. R. Menter, "Transition modeling for general CFD applications in aeronautics," *AIAA 2005-522*, 2005.

[30] F. G. Schmitt, "About Boussinesq's turbulent viscosity hypothesis: historical remarks and a direct evaluation of its validity," *Comptes Rendus Mecanique*, vol. 335, no. 9, pp. 617–627, 2007.

[31] J. Boussinesq, "Théorie de l'écoulement tourbillant," *Mem. Présentés par Divers Savants Acad. Sci. Inst. Fr.*, vol. 23, pp. 46–50, 1877.

[32] O. Reynolds, *On the Dynamical Theory of Incompressible Viscous Fluids and the Determination of the Criterion*, vol. 186 of *A*. Philosophical Transactions of the Royal Society of London, 1895.

[33] J. C. Rotta, "Statistische theorie nichthomogener turbulenz," *Zeitschrift fur Physik*, vol. 129, pp. 547–572, 1951.

[34] L. Prandtl, "Über die ausgebildete turbulenz," *ZAMM*, vol. 5, pp. 136–139, 1925.

[35] M. Wolfshtein, "The velocity and temperature distribution in one-dimensional flow with turbulence augmentation and pressure gradient," *International Journal of Heat and Mass Transfer*, vol. 12, no. 3, pp. 301–318, 1969.

[36] W. P. Jones and B. E. Launder, "The prediction of laminarization with a two-equation model of turbulence," *International Journal of Heat and Mass Transfer*, vol. 15, pp. 301–314, 1972.

[37] P. Y. Chou, "On the velocity correlations and the solution of the equations of turbulent fluctuation," *Quart. Appl. Math.*, vol. 3, p. 38, 1945.

[38] B. I. Davidov, "On the statistical dynamics of an incompressible fluid," *Doklady AN. SSSR*, vol. 136, p. 47, 1961.

[39] F. H. Harlow and P. I. Nakayama, "Transport of turbulence energy decay rate," *Los Alamos Sci. Lab. University of California report LA-3854*, 1968.

[40] H. L. Dryden, "Air flow in the boundary layer near a plate," tech. rep., NACA, 1937.

[41] G. B. Schubauer and H. K. Skramstad, "Laminar-boundary-layer oscillations and transition on a flat plate," tech. rep., NACA, 1943.

[42] W. Tollmien, "Über die entstehung der turbulenz," *Nachr. Ges. Wiss. Göttingen*, vol. 1, pp. 21–24, 1929.

[43] H. Schlichting, "Zur entstehung der turbulenz bei der plattenströmung," *Nach. Gesell, d, Wiss. z. Göttingen, Math. Phys. Klasse*, pp. 181–208, 1933.

[44] M. Nishioka, S. Iida, and Y. Ichikawa, "Experimental investigation of the stability of plane poiseuille flow," *Journal of Fluid Mechanics*, vol. 72, no. 4, pp. 731–751, 1975.

[45] A. J. Strazisar, E. Reshotko, and J. M. Prahl, "Experimental study of the stability of heated laminar boundary layers in water," *Journal of Fluid Mechanics*, vol. 83, no. 2, pp. 225–247, 1977.

[46] D. Arnal and J. C. Juillen, "Contribution experimentale à l'étude de la receptivité d'une couche limite laminaire, à la turbulence de l'ecoulement general," *ONERA Rap. Tech. 1/5018 AYD.*, 1978.

[47] P. S. Klebanoff, K. D. Tidstrom, and L. M. Sargent, "The three-dimensional nature of boundary-layer instability," *Journal of Fluid Mechanics*, vol. 12, pp. 1–34, 1962.

[48] A. Craik, "A wave-interaction model for the generation of windrows," *Journal of Fluid Mechanics*, vol. 41, no. 4, pp. 801–821, 1970.

[49] T. Herbert, "Secondary instability of plane channel flow to subharmonic three-dimensional disturbances," *Physics of Fluids*, vol. 26, no. 4, pp. 871–874, 1983.

[50] V. V. Kozlov and M. P. Ramazanov, "Development of finite-amplitude disturbances in poiseuille flow.," *Journal of Fluid Mechanics*, vol. 147, pp. 149–157, 1984.

[51] W. S. Saric, V. V. Kozlov, and V. Y. Levchenko, "Forced and unforced subharmonic resonance in boundary-layer transition," in *AIAA 22nd Aerospace Sciences Meeting*, p. 10, 1984.

[52] W. S. Saric and A. S. W. Thomas, "Experiments on the subharmonic route to turbulence in boundary layers," in *Turbulence and Chaotic Phenomena in Fluids, Proceedings of the International Symposium*, pp. 117–122, 1984.

[53] S. J. Leib, D. W. Wundrow, and M. E. Goldstein, "Effect of free-stream turbulence and other vortical disturbances on a laminar boundary layer," *J. Fluid Mech*, vol. 380, pp. 169–203, 1999.

[54] G. I. Taylor, "Some recent developments in the study of turbulence," in *Fifth International Congress for Applied Mechanics. Cambridge, Massachusetts.*, 1939.

[55] J. M. Kendall, "Studies on laminar boundary layer receptivity to freestream turbulence near a leading edge," *Boundary Layer Stability and Transition to Turbulence, ASME FED*, vol. 114, p. 8, 1991.

[56] H. P. Bakewell and J. L. Lumley, "Viscous sublayer and adjacent wall region in turbulent pipe flow," *Physics of Fluids (1958-1988)*, vol. 10, no. 9, pp. 1880–1889, 1967.

[57] A. A. Townsend, "Equilibrium layers and wall turbulence," *Journal of Fluid Mechanics*, vol. 11, pp. 97–120, 1961.

[58] P. Bradshaw, "Inactive motion and pressure fluctuations in turbulent boundary layers," *Journal of Fluid Mechanics*, vol. 30, pp. 241–258, 1967.

[59] J. C. R. Hunt, P. A. Durbin, N. K.-R. Kevlahan, and H. J. S. Fernando, "Non-local effects of shear in turbulent flows," in *Sixth European Turbulence Conference, Lausanne, Switzerland*, 1996.

[60] R. G. Jacobs and P. A. Durbin, "Shear sheltering and the continuous spectrum of the Orr-Sommerfeld equation," *Phys. Fluids*, vol. 10, pp. 2006–2011, 1998.

[61] R. J. Volino and T. W. Simon, "Transfer functions for turbulence spectra," *Unsteady Flows in Aeropropulsion, ASME*, vol. 40, pp. 147–155, 1994.

[62] H. W. Liepmann, "Investigations on laminar boundary-layer stability and transition on curved boundaries," *NACA-WR-W-107, NACA-ACR-3H30*, 1943.

[63] L.-S. Lin, H.-W. Chang, and C.-A. Lin, "Multi relaxation time lattice Boltzmann simulations of transition in deep 2D lid driven cavity using GPU," *Computers & Fluids*, vol. 80, no. 0, pp. 381–387, 2013.

[64] R. G. Jacobs and P. A. Durbin, "Simulations of bypass transition," *Journal of Fluid Mechanics*, vol. 428, pp. 185–212, 2001.

[65] P. Durbin, R. Jacobs, and X. Wu, *DNS of Bypass Transition*. Closure Strategies for Turbulent and Transitional Flows, Cambridge University Press, 2002.

[66] P. Lu, Z. Wang, L. Chen, and C. Liu, "Numerical study on U-shaped vortex formation in late boundary layer transition," *Computers & Fluids*, vol. 55, no. 0, pp. 36–47, 2012.

[67] P. Lu, Y. Yan, and C. Liu, "Numerical investigation on mechanism of multiple vortex rings formation in late boundary-layer transition," *Computers & Fluids*, vol. 71, no. 0, pp. 156–168, 2013.

[68] J. W. Deardorff, "A numerical study of three-dimensional turbulent channel flow at large Reynolds numbers," *J. Fluid Mech*, vol. 41, pp. 453–480, 1970.

[69] J. Smagorinsky, "General circulation experiments with the primitive equations," *Monthly Weather Review*, vol. 91, pp. 99–164, 1963.

[70] P. Schlatter, *Large-eddy simulation of transition and turbulence in wall-bounded shear flow*. PhD thesis, ETH Zürich, 2005.

[71] X. Huai, R. Joslin, and U. Piomelli, "Large-eddy simulation of transition to turbulence in boundary layers," *Theoretical and Computational Fluid Dynamics*, vol. 9, pp. 149–163, 1997.

[72] P. Schlatter, S. Stolz, and L. Kleiser, "LES of transitional flows using the approximate deconvolution model," *Heat and Fluid Flow*, vol. 25, pp. 549–558, 2004.

[73] U. Piomelli, S. Radhakrishnan, and G. Prisco, "Turbulent eddies in the RANS/LES transition region," *Adv. in Hybrid RANS-LES Modelling*, pp. 21–36, 2008.

[74] S. Kim, P. Wilson, and Z.-M. Chen, "Effect of turbulence modelling on 3-D LES of transitional flow behind a circular cylinder," *Ocean Engineering*, vol. 100, pp. 19–25, 2015.

[75] M. Taeibi-Rahni, M. Ramezanizadeh, D. Ganji, A. Darvan, E. Ghasemi, S. Soleimani, and H. Bararnia, "Comparative study of large eddy simulation of film cooling using a dynamic global-coefficient subgrid scale eddy-viscosity model with RANS and Smagorinsky modeling," *International Communications in Heat and Mass Transfer*, vol. 38, no. 5, pp. 659–667, 2011.

[76] A. Savill, "Evaluating turbulence model predictions of transition," *Applied Scientific Research*, vol. 51, no. 1-2, pp. 555–562, 1993.

[77] D. Wilcox, *Turbulence modeling for CFD*. DCW Industries, Inc., 1994.

[78] K. C. Chang, W. D. Hsieh, and C. S. Chen., "A modified low-Reynolds-number turbulence model applicable to recirculating flow in pipe expansion," *ASME*, vol. 117, pp. 417–423, 1995.

[79] W. L. Chen, F. S. Lien, and M. A. Leschziner, "Non-linear eddy-viscosity modelling of transitional boundary layers pertinent to turbomachine aerodynamics," *International Journal of Heat and Fluid Flow*, vol. 19, pp. 297–306, 1998.

[80] T. J. Craft, B. E. Launder, and K. Suga, "Development and application of a cubic eddy-viscosity model of turbulence," *Int. J. Heat and Fluid Flow*, vol. 17, pp. 108–115, 1996.

[81] T. J. Craft, B. E. Launder, and K. Suga, "Prediction of turbulent transitional phenomena with a nonlinear eddy-viscosity model," *International Journal of Heat and Fluid Flow*, vol. 18, no. 1, pp. 15–28, 1997.

[82] T. J. Craft, “Developments in a low-Reynolds-number second-moment closure and its application to separating and reattaching flows,” *International Journal of Heat and Fluid Flow*, vol. 19, pp. 541–548, 1998.

[83] C. L. Rumsey, “Apparent transition behavior of widely-used turbulence models,” *International Journal of Heat and Fluid Flow*, vol. 28, no. 6, pp. 1460–1471, 2007.

[84] S. Dhawan and R. Narasimha, “Some properties of boundary layer flow during the transition from laminar to turbulent motion,” *Journal of Fluid Mechanics*, vol. 3, pp. 418–436, 1958.

[85] B. Abu-Ghannam and R. Shaw, “Natural transition of boundary layers -the effects of turbulence, pressure gradient, and flow history,” *Journal of Mechanical Engineering Science*, vol. 22, no. 5, pp. 213–228, 1980.

[86] N. H. Cho, X. Liu, W. Rodi, and B. Schönung, “Calculation of wake-induced unsteady flow in a turbine cascade,” *ASME Journal of Turbomachinery*, vol. 115, pp. 675–686, 1993.

[87] W. J. Solomon, G. J. Walker, and J. P. Gostelow, “Transition length prediction for flows with rapidly changing pressure gradients,” *ASME*, 1995.

[88] J. Steelant and E. Dick, “Modeling of laminar-turbulent transition for high freestream turbulence,” *Journal of Fluids Engineering*, vol. 123, no. 1, pp. 22–30, 2001.

[89] P. Andersson, M. Berggren, and D. S. Henningson, “Optimal disturbances and bypass transition in boundary layers,” *Phys. Fluids*, vol. 11, pp. 134–150, 1999.

[90] Y. B. Suzen and P. G. Huang, “Modeling of flow transition using an intermittency transport equation,” *Journal of Fluids Engineering*, vol. 122, no. 2, pp. 273–284, 2000.

[91] J. Steelant and E. Dick, “Modelling of bypass transition with conditioned navier-stokes equations coupled to an intermittency transport equation,” *International Journal for Numerical Methods in Fluids*, vol. 23, no. 3, pp. 193–220, 1996.

[92] J. R. Cho and M. K. Chung, “A k- epsilon- gamma equation turbulence model,” *Journal of Fluid Mechanics*, vol. 237, pp. 301–322, 1992.

[93] C. Wang and B. Perot, “Prediction of turbulent transition in boundary layers using the turbulent potential model,” *J. Turbulence*, vol. 3, p. 15, 2002.

[94] N. A. Denissen, D. A. Yoder, and N. J. Georgiadis, “Implementation and validation of a laminar-to-turbulent transition model in the wind-us code,” *NASA*, vol. 215451, 2008.

[95] J. J. Rodio, X. Xiao, and H. A. Hassan, “A physics-based transition/turbulence stress model,” *AIAA SciTech*, 2015.

[96] D. Wilcox, *Turbulence Modeling for CFD, 3rd Edition*. DCW Industries, Inc., 2006.

[97] R. E. Mayle and A. Schulz, “Heat transfer committee and turbomachinery committee best paper of 1996 award: The path to predicting bypass transition,” *Journal of Turbomachinery*, vol. 119, no. 3, pp. 405–411, 1997.

[98] C. C. Lin, “Motion in the boundary layer with a rapidly oscillating external flow,” *Proc. 9th Int. Congress Appl. Mech. Brussels*, vol. 4, pp. 155–167, 1957.

[99] E. Dyban, E. Epik, and T. T. Suprun, “Characteristics of the laminar boundary layer in the presence of elevated free-stream turbulence,” *Fluid Mech. - Soviet Res.*, vol. 5, pp. 30–36, 1976.

[100] K. H. Sohn and E. Reshotko, “Experimental study of boundary layer transition with elevated freestream turbulence on a heated plate,” tech. rep., NASA CR 187068, 1991.

[101] K. J. A. Westin, A. V. Boiko, B. G. B. Klingmann, V. V. Kozlov, and P. H. Alfredsson., “Experiments in a boundary layer subjected to free stream turbulence. Part 1. boundary layer structure and receptivity,” *J. Fluid Mech.*, vol. 281, pp. 193–218, 1994.

[102] D. Zhou and T. Wang, “Effects of elevated free-stream turbulence on flow and thermal structures in transitional boundary layers,” *Journal of Turbomachinery*, vol. 117, no. 3, pp. 407–417, 1995.

[103] S. Lardeau, M. Leschziner, and N. LI, “Modelling bypass transition with low-Reynolds-number nonlinear eddy-viscosity closure,” *Flow, Turbulence and Combustion*, vol. 73, pp. 49–76, 2004.

[104] D. K. Walters and J. H. Leylek, “A new model for boundary layer transition using a single-point RANS approach,” *Journal of Turbomachinery*, vol. 126, no. 1, pp. 193–202, 2004.

[105] Z. Vlahostergios, K. Yakinthos, and A. Goulas, “Separation-induced boundary layer transition: Modeling with a non-linear eddy-viscosity model coupled with the laminar kinetic energy equation,” *International Journal of Heat and Fluid Flow*, vol. 30, pp. 617–636, 2009.

[106] R. J. Volino, “A new model for free-stream turbulence effects on boundary layers,” *Journal of Turbomachinery*, vol. 120, no. 3, pp. 613–620, 1998.

[107] J. R. Edwards, C. J. Roy, F. G. Blottner, and H. A. Hassan, “Development of a one-equation transition / turbulence models (aiaa paper 2000-0133),” *AIAA Journal*, vol. 39, no. 9, pp. 1691–1698, 2001.

[108] E. S. Warren and H. A. Hassan, “Transition closure model for predicting transition onset,” *Journal of Aircraft*, vol. 35, no. 5, pp. 769–775, 1998.

[109] E. J. Walsh, D. M. M. Eligot, L. Brandt, and P. Schlatter, “Entropy generation in a boundary layer transitioning under the influence of freestream turbulence,” *Journal of Fluids Engineering*, vol. 133, no. 6, p. 10, 2011.

[110] D. K. Walters and D. Cokljat, “A three-equation eddy-viscosity model for Reynolds-Averaged Navier–Stokes simulations of transitional flow,” *Journal of Fluids Engineering*, vol. 130, no. 12, p. 121401, 2008.

[111] J. Fürst, M. Islam, J. Prihoda, and D. Wood, “Towards pressure gradient sensitive transitional k-kl-w model: The natural transition for low Re airfoils,” *Topological Problems of Fluid Mechanics, Prague, 2015*, 2015.

[112] W. Tollmien, “The production of turbulence,” *NACA TM 609*, 1931.

[113] W. Tollmien, “General instability criterion of laminar velocity distributions,” *NACA TM 792*, 1936.

[114] H. Schlichting, "Über die entstehung der turbulenz in einem rotierenden zylinder," *Nach. Gesell, d, Wiss. z. Göttingen, Math. Phys. Klasse*, vol. 2, pp. 160–198, 1932.

[115] S. A. Orszag and A. T. Patera, "Secondary instability of wall-bounded shear flows.," *Journal of Fluid Mechanics*, vol. 128, pp. 347–385, 1983.

[116] A. M. O. Smith and N. Gamberoni, "Transition, pressure gradient and stability theory," tech. rep., Douglas Aircraft Company, Technical Report ES-26388, 1956.

[117] J. L. van Ingen, "A suggested semi-empirical method for the calculation of the boundary layer transition region," tech. rep., Delft University, Report VTH-71, 1956.

[118] M. Drela and M. B. Giles, "Viscous-inviscid analysis of transonic and low Reynolds number airfoils," *AIAA*, vol. 25, no. 10, pp. 1347–1355, 1987.

[119] J. M. M. Sousa and L. M. G. Silva, "Transition prediction in infinite swept wings using Navier-Stokes computations and linear stability theory," *Computers and Structures*, vol. 82, pp. 1551–1560, 2004.

[120] J. L. van Ingen, "The e^n method for transition prediction: historical review of work at TU Delft," in *38th Fluid Dynamics Conference and Exhibit, AIAA 2008-3830*, p. 49, 2008.

[121] N. Krimmelbein and R. Radespiel, "Transition prediction for three-dimensional flows using parallel computation," *Computers & Fluids*, vol. 38, pp. 121–136, 2009.

[122] N. Krimmelbein and A. Krumbein, "Automatic transition prediction for three-dimensional configurations with focus on industrial application," *JOURNAL OF AIRCRAFT*, vol. 48, no. 6, pp. 1878–1887, 2011.

[123] F. Menter, R. Langtry, and S. Völker, "Transition modelling for general purpose CFD codes," *Flow, Turbulence and Combustion*, vol. 77, pp. 277–303, 2006.

[124] R. B. Langtry, *A Correlation-Based Transition Model using Local Variables for Unstructured Parallelized CFD Codes*. PhD thesis, Universität Stuttgart, Holzgartenstr. 16, 70174 Stuttgart, 2006.

[125] R. B. Langtry, F. R. Menter, S. R. Likki, Y. B. Suzen, P. G. Huang, and S. Völker, "A correlation-based transition model using local variables—Part ii: Test cases and industrial applications," *Journal of Turbomachinery*, vol. 128, no. 3, pp. 423–434, 2006.

[126] F. R. Menter, R. B. Langtry, S. R. Likki, Y. B. Suzen, P. G. Huang, and S. Völker, "A correlation-based transition model using local variables—Part i: Model formulation," *Journal of Turbomachinery*, vol. 128, no. 3, pp. 413–422, 2006.

[127] E. R. Van Driest and C. B. Blumer, "Boundary layer transition: Freestream turbulence and pressure gradient effects," *AIAA Journal*, vol. 1, pp. 1303–1306, 1963.

[128] F. R. Menter, T. Esch, and S. Kubacki, "Transition modelling based on local variables," in *5th International Symposium on Engineering Turbulence Modelling and Measurements, Mallorca, Spain*, pp. 555–564, 2002.

[129] F. R. Menter, "Two-equation eddy-viscosity turbulence models for engineering applications," *AIAA*, vol. 32, pp. 1598–1605, 1994.

[130] K. Suluksna and E. Juntasaro, "Assessment of intermittency transport equations for modeling transition in boundary layers subjected to freestream turbulence," *International Journal of Heat and Fluid Flow*, vol. 29, no. 1, pp. 48–61, 2008.

[131] K. Suluksna, P. Dechaumphai, and E. Juntasaro, "Correlations for modeling transitional boundary layers under influences of freestream turbulence and pressure gradient," *International Journal of Heat and Fluid Flow*, vol. 30, no. 1, pp. 66–75, 2009.

[132] P. Malan, K. Suluksna, and E. Juntasaro, "Calibrating the γ-Reθ transition model for commercial CFD," in *47th AIAA Aerospace Sciences Meeting Including The New Horizons Forum and Aerospace Exposition, AIAA 2009 -1142*, p. 20, 2009.

[133] W. Piotrowski, W. Elsner, and S. Drobniak, "Transition prediction on turbine blade profile with intermittency transport equation," *Journal of Turbomachinery*, vol. 132, p. 10, 2010.

[134] R. B. Langtry and F. R. Menter, "Correlation-based transition modeling for unstructured parallelized computational fluid dynamics codes," *AIAA Journal*, vol. 47, no. 12, pp. 2894–2906, 2009.

[135] J. Y. You and O. J. Kwon, "Blending of SAS and correlation-based transition models for flow simulation at supercritical Reynolds numbers," *Computers & Fluids*, vol. 80, no. 0, pp. 63–70, 2013.

[136] S. Gorji, M. Seddighi, C. Ariyaratne, A. E. Vardy, T. O'Donoghue, D. Pokrajac, and S. He, "A comparative study of turbulence models in a transient channel flow," *Computers & Fluids*, vol. 89, pp. 111–123, 2014.

[137] B. Launder and B. Sharma, "Application of the energy-dissipation model of turbulence to the calculation of flow near a spinning disc," *Letters in Heat and Mass Transfer*, vol. 1, pp. 131–137, Jan. 1974.

[138] R. J. Volino, "An investigation of the scales in transitional boundary layers under high free-stream turbulence conditions," *Experiments in Fluids*, vol. 38, pp. 516–533, 2005.

[139] R. W. Moss and M. L. G. Oldfield, "Effect of free-stream turbulence on flat-plate heat flux signals: spectra and eddy transport velocities," *J Turbomach*, vol. 118, pp. 461–467, 1996.

[140] K. A. Thole and D. G. Bogard, "High freestream turbulence effects on turbulent boundary layers," *J Fluids Eng*, vol. 118, pp. 276–284, 1996.

[141] R. J. Volino and T. W. Simon, "Spectral measurements in transitional boundary layers on a concave wall under high and low free-stream turbulence," *J Turbomach*, vol. 122, pp. 450–457, 2000.

[142] L. Cutrone, P. D. Palma, G. Pascazio, and M. Napolitano, "An evaluation of bypass transition models for turbomachinery flows," *International Journal of Heat and Fluid Flow*, vol. 28, no. 1, pp. 161–177, 2007.

[143] D. K. Walters and J. H. Leylek, "Computational fluid dynamics study of wake-induced transition on a compressor-like flat plate," *J. Turbomach.*, vol. 127, no. 1, pp. 52–63, 2005.

[144] Z. T. Reza, M. Salary, and A. Kolaei, "Prediction of boundary layer transition based on modeling of laminar fluctuations using RANS approach," *Chinese Journal of Aeronautics*, vol. 22, pp. 113–120, 2009.

[145] D. D. Sanders, W. F. O'Brien, R. Sondergaard, M. D. Polanka, and D. C. Rabe, "Predicting separation and transitional flow in turbine blades at low Reynolds numbers-Part i: Development of prediction methodology," *Journal of Turbomachinery*, vol. 133, no. 3, pp. 031011–10, 2011.

[146] D. D. Sanders, W. F. O'Brien, R. Sondergaard, M. D. Polanka, and D. C. Rabe, "Predicting separation and transitional flow in turbine blades at low Reynolds numbers-Part ii: The application to a highly separated turbine blade cascade geometry," *Journal of Turbomachinery*, vol. 133, no. 3, pp. 031012–7, 2011.

[147] M. S. Genç, Ünver Kaynak, and H. Yapici, "Performance of transition model for predicting low aerofoil flows without/with single and simultaneous blowing and suction," *European Journal of Mechanics - B/Fluids*, vol. 30, no. 2, pp. 218–235, 2011.

[148] D. S. Holloway, D. K. Walters, and J. H. Leylek, "Prediction of unsteady, separated boundary layer over a blunt body for laminar, turbulent, and transitional flow," *Int. J. Numer. Meth. Fluids*, vol. 45, pp. 1291–1315, 2004.

[149] C. Turner and R. Prosser, "The application of laminar kinetic energy to laminar-turbulent transition prediction," *Turbulence, Heat and Mass Transfer 6*, p. 4, 2009.

[150] C. Bernardini, M. Carnevale, M. Manna, F. Martelli, D. Simoni, and P. Zunino, "Turbine blade boundary layer separation suppression via synthetic jet: an experimental and numerical study," *Journal of Thermal Science*, vol. 21, pp. 404–412, 2012.

[151] C. Turner, *Laminar Kinetic Energy Modelling for Improved Laminar-Turbulent Transition Prediction*. PhD thesis, University of Manchester, 2012.

[152] B. Shome, "Numerical study of oscillating boundary layer flow over a flat plate using k-kl-ω turbulence model," *International Journal of Heat and Fluid Flow*, vol. 42, pp. 131–138, 2013.

[153] P. Bradshaw, *An Introduction to Turbulence and its Measurement*. Pergamon Press, 1971.

[154] T.-H. Shih and J. Zhu, "A new Reynolds stress algebraic equation model," tech. rep., NASA, 1994.

[155] T.-H. Shih, W. W. Liou, A. Shabbir, Z. Yang, and J. Zhu, "A new k-epsilon eddy viscosity model for high Reynolds number turbulent flows: Model development and validation," *Comput. Fluids*, vol. 24, pp. 227–238, 1995.

[156] P. R. Viswanath, R. Narasimha, and A. Prabhu, "Visualization of relaminarizing flows," *J. Indian Inst. Sci.*, vol. 60, no. 3, pp. 159–165, 1978.

[157] A. Noorani, G. K. El Khoury, and P. Schlatter, "Evolution of turbulence characteristics from straight to curved pipes," *International Journal of Heat and Fluid Flow*, vol. 41, pp. 16–26, 2013.

[158] P. R. Spalart and S. R. Allmaras, "One-equation turbulence model for aerodynamic flows," *Recherche aerospatiale*, vol. 1, no. 1, pp. 5–21, 1994.

[159] C. L. Rumsey, D. O. Allison, R. T. Biedron, P. G. Buning, T. G. Gainer, J. H. Morrison, S. M. Rivers, S. J. Mysko, and D. P. Witkowski, "CFD sensitivity analysis of a modern civil transport near buffet-onset conditions," *NASA/TM-2001-211263*, 2001.

[160] J. Coupland, "ERCOFTAC special interest group on laminar to turbulent transition and retransition T3A and T3B test cases," tech. rep., ERCOFTAC, 1990.

[161] J. Coupland, "ERCOFTAC special interest group on laminar to turbulent transition and retransition T3C test cases," tech. rep., ERCOFTAC, 1990.

[162] J. Coupland and D. Brierley, "Transition in turbomachinery flows," tech. rep., BRITE/EURAM Project AERO-CT92-0050., 1996.

[163] J. L. Tangler and D. M. Somers, "NREL airfoil families for HAWTs," tech. rep., NREL/I'P-442-7109, 1995.

[164] R. Eppler and D. M. Somers, "A computer program for the design and analysis of low-speed airfoils," *NASA TM-8021O*, 1980.

[165] R. Eppler and D. M. Somers, "Supplement to: A computer program for the design and analysis of low-speed airfoils," *NASA TM-81862*, 1980.

[166] J. L. van Ingen, L. M. M. Boermans, and J. J. H. Blom, "Low-speed airfoil section research at Delft University of Technology. leas-80-1o.1, Munich, oct. 1980," *ICAS-80-1O.1*, 1980.

[167] D. M. Somers, "Design and experimental results for the S809 airfoil," tech. rep., NREL/SR-440-6918, 1997.

[168] R. R. Ramsay, M. J. Hoffmann, and G. M. Gregorek, "Effects of grit roughness and pitch oscillations on the S809 airfoil," tech. rep., NREL/TP-442-7817, 1995.

[169] R. R. Ramsay, J. M. Janiszewska, and G. M. Gregorek, "Wind tunnel testing of three S809 aileron configurations for use on horizontal axis wind turbines," tech. rep., NREL, 1996.

[170] S. Schmidt and F. Thiele, "Detached eddy simulation of flow around A-airfoil," *Flow, Turbulence and Combustion*, vol. 71, pp. 261–278, 2003.

[171] E. Chaput, "Aerospatiale-A airfoil. contribution in ECARP- European Computational Aerodynamics Research Project: Validation of CFD codes and assessment of turbulence models," *Notes on Numerical Fluid Mechanics*, vol. 58, pp. 327–346, 1997.

[172] P. Gendre, "Maximum lift for a single-element airfoils - experimental results A-airfoil ('CERFACS' contribution in task 2.1 to EUROVAL) EUROVAL - A European initiative on validation of CFD codes," *Notes on Numerical Fluid Mechanics*, vol. 42, 1992.

[173] C. Gleyzes, "Opération décrochage - résultats de la 2éme campangne d'essais à F2 - mésures de pression et vélocimétrie laser," tech. rep., Technical Report RT-DERAT 55/5004, ONERA, 1989.

[174] R. Huddeville, O. Piccin, and D. Cassoudesalle, "Opération décrochage - mesurement de frottement sur profiles as 239 et a 240 à la soufflerie F1 du CFM," *Technical Report RT-OA 19/5025 (RT-DERAT 19/5025 DN), ONERA*, 1987.

[175] W. Haase, F. Brandsma, E. Elsholz, M. Leschziner, and D. E. Schwamborn, "EUROVAL - a european initiative on validation of CFD codes," *Notes on Numerical Fluid Mechanics*, vol. 42, 1992.

[176] W. Haase, E. Chaput, E. Elsholz, M. Leschziner, and U. E. Müller, "ECARP - European Computational Aerodynamics Research Project: Validation of CFD codes and assessment of turbulence models," *Notes on Numerical Fluid Mechanics*, vol. 58, 1997.

[177] I. Mary and P. Sagaut, "Large eddy simulation of flow around an airfoil near stall," *AIAA J.*, vol. 36, no. 1, pp. 1139–1145, 2001.

[178] S. Dahlström and L. Davidson, "Large eddy simulation applied to a high-Reynolds flow around an airfoil close to stall," *AIAA 2003-776 41st Aerospace Sciences Meeting and Exhibit*, 2003.

[179] H. Hoheisel, R. Kiock, H. J. Lichtfuss, and L. Fottner, "Influence of free-stream turbulence and blade pressure gradient on boundary layer and loss behavior of turbine cascades," *Journal of Turbomachinery*, vol. 109, pp. 210–219, 1987.

[180] H. H. Hebbel, "Über den einfluss der machzahl und der reynoldszahl auf die aerodynamischen beiwerte von turbinenschaufelgittern bei verschiedener turbulenz der strömung," *Forschg. im Ing.-Wesen*, vol. 30, pp. 65–77, 1964.

[181] C. Seyfert and A. Krumbein, "Correlation-based transition transport modeling for three-dimensional aerodynamic configurations," *Journal of Aircraft*, vol. 50, no. 5, pp. 1533–1539, 2013.

[182] V. Schmitt and J. Cousteix, "Boundary layers on a swept wing up to high angles of attack," tech. rep., Office National d'Etudes et de Recherches Aérospatiales, ONERA, 92320 Châtillon, France, 1999.

[183] T. Hottner and W. Lorenz-Meyer, "Der transsonische windkanal der aerodynamischen versuchsanstalt Göttingen (zweite ausbaustufe)," *Jahrbuch 1968 dr DGLR*, pp. 234–244, 1968.

Appendix A

A1 - Publications prepared during the thesis work

Journal:

- R. Vizinho, J. Páscoa and M. Silvestre, "Turbulent transition modeling through mechanical considerations", Applied Mathematics and Computation, vol. 269, pp. 308-325, 2015.
- R. Vizinho, J. Morgado, J. Páscoa and M. Silvestre, "Analysis of transitional flow in 3D geometries using a novel phenomenological model", Aerospace Science and Technology, vol. 45, pp. 431-441, 2015.
- R. Vizinho, J. Páscoa and M. Silvestre, "High Altitude Transitional Flow Computation for a Propulsion System Nacelle of MAAT Airship," SAE Int. J. Aerosp., vol. 6, no. 2, pp. 714-720, 2013.
- J. Morgado, R. Vizinho, M. Silvestre and J. Páscoa, "XFOIL vs CFD performance predictions for high lift low Reynolds number airfoils", Aerospace Science and Technology, vol. 52, pp. 207-214, 2016.

Conferences:

- R. Vizinho, J. Páscoa and M. Silvestre, "Turbulent transition modeling through mechanical considerations", in Proc. 4th European Seminar on Computing-ESCO, Pilsen, Czech Republic, p. 20, 2014.
- R. Vizinho, J. Páscoa and M. Silvestre, "High altitude transitional flow computation for a propulsion system Nacelle of MAAT airship", in Proc. SAE Aerotech Congress & Exhibition, Montréal, Canada, paper no 2013-01-2268, p. 7, 2013.
- R. Vizinho, J. Páscoa and M. Silvestre, "By-pass transition effects in propulsion components of high-altitude airships", in Proc. European Conference for Aero-Space Sciences-EUCASS, Munich, Germany, p. 9, 2013.
- R. Oliveira, J. Páscoa and M. Silvestre, "Preliminary assessment of transitional flow modeling using low-Re turbulence closures", in Proc. IV Conferência Nacional de Mecânica dos Fluidos, Termodinâmica e Energia-MEFTE, Lisboa, Portugal, paper no 59, p. 10, 2012.

Submitted to journal:

- "A phenomenological turbulence transition model improvement for flow under adverse-pressure-gradient", p. 25, Computers & Fluids.
- "Development and validation of a transition model based on the concept of laminar kinetic energy", p. 10, Aeronautical Journal.